UNIVERSITY OF LIVERPOOL

Search for a heavy CP-odd Higgs Boson A decaying to a Z boson and a heavy CP-even Higgs boson H with $\ell\ell bb$ final state in 13 TeV pp Collisions with the ATLAS Detector

A thesis submitted in accordance with the requirements of
the University of Liverpool
for the degree of Doctor of Philosophy
by

Wai Yuen Chan

under the supervision of

Dr. Nikolaos Rompotis & Prof. Andrew Mehta

Department of Physics,
Oliver Lodge Laboratory
University of Liverpool

September 2021

Abstract

This thesis presents a search for a heavy neutral Higgs boson, A, decaying into a Z boson and another heavy Higgs boson, H, using a data sample corresponding to an integrated luminosity, initially, of 36.5 fb^{-1} and, subsequently, increased to 139 fb^{-1} from proton-proton collisions at $\sqrt{s} = 13$ TeV recorded by the ATLAS detector at the LHC. The search considers the Z boson decaying into electrons or muons and the H boson into a pair of b-quarks. The mass range considered is 230–800 GeV for the A boson and 130–700 GeV for the H boson. The data are in good agreement with the background predicted by the Standard Model, and 95% confidence-level upper limits on $\sigma(A) \times BR(A \to ZH) \times BR(H \to bb)$ are set. The upper limits are in the range 14–830 fb and 0.0062–0.380 pb for the data sample corresponding to an integrated luminosity of 36.5 fb^{-1} and 139 fb^{-1}, respectively. An interpretation of the results in the context of two-Higgs-doublet models is also given.

The principle of science, the definition, almost, is the following:

The test of all knowledge is experiment.

Experiment is the sole judge of scientific "truth".

- Richard Feynman

Acknowledgements

I have been fortunate to have an opportunity to studying at the University of Liverpool in the past decade, thanks for all the support from the department of physics. I still remember that I start getting interested in the particle physics in my second year, and choose a HEP related master project in my master year. Eventually, I have a chance to contribution into the ATLAS experiment during my PhD course at the University of Liverpool.

First and foremost, I would like to express my sincere appreciation to my supervisors, Nickolaos Rompotis and Andrew Mehta, who constantly support my work and being an invaluable source of knowledge and advice. Thank you for guiding me to become a professional researcher in the past years. I am extremely grateful to Nickolas for always spending time to help me in the past years. I wound not be able to finish my PhD and this thesis without his countless suggestions.

I also wish to thank the rest of the Liverpool ATLAS group and the HEP group. I learnt a lot from all the experts in the group and I will always remember that I was a part of this wonderful group. Outside the Liverpool HEP community, I am grateful to have all the collaborators of the $A \rightarrow ZH$ analysis group: Xiaohu Sun, Flavia Dias, Dainel Nielsen, Shyam Balaji and of course my supervisors. This analysis cannot be finished without any of your contribution. Besides the $A \rightarrow ZH$ analysis, I would like to thank Federico Sforza, Akanksha Vishwakarma, Angela Maria, Jonathan Shlomi and Emily Graham who helped me a lot in the simulation adjustment method. I could not finish the task without your support. I would also like to thank all the experts from CERN who have be bothered by me via email or Skype in the past years, thank you for spending time with me to explain all the details related to your expertise.

I am so thankful for having a good time with all the PostDoc and PhD students I know from the Liverpool HEP group. Thank you for being friendly, always forgive my annoying behaviour and of course discuss physics with me all the time. A huge thank you especially to Michael O'Keefe, Adam Jaspan, Hanna Borecka-Belska, Matthew Sullivan, Jordan Zhiyuan Li, Adam Ruby, Ka Ming Tsui and Ting Fung Lee. Wish all of you keep shinning in your field in the future.

A special thanks to all of my friends from Hong Kong and Japan, who help me to hold tight while I am having the depression during the pandemic. Especially all the people I know from Sagara Mayu's community. Thank you for holding a wonderful place across the internet for me to relax in the spare time. I am always encouraged by all the stories behind you guys and grateful to become a part of the community. I am looking forward to meeting all of you in person one day.

Lastly, I would like to thank my family and my girlfriend from Hong Kong, who support my study unconditionally . I am so grateful my parents respect my choice to engage with HEP research, while most of the parents in Hong Kong wish their children to work with anything related to stock marketing and economy. I am so lucky to have my girlfriend who is brave enough to have a long distance relationship with me. Although it is hard to meet in person due to the CoVID situation, I believed that we are about the reunite very soon.

Declaration

This thesis is the result of my own work, except where explicit reference is made to the work of others, and has not been submitted for another qualification to this, or any other, university. This thesis does not exceed the word limit for the respective Degree Committee.

Wai Yuen Chan

02-09-2021

Contents

CHAPTER 1

Theoretical Background and Motivation

The standard model of particle physics (SM) successfully describes the properties of all known elementary particles and their non-gravitational interactions. A particle with mass approximately equal to 125 GeV, which has observed properties compatible with those of the final missing elementary particle of the SM, was discovered in July 2012 at the Large Hadron Collider (LHC) [1, 2]. This particle is a Higgs boson, that is a scalar particle associated with the Brout-Englert-Higgs-Guralnik-Hagen-Kibble mechanism (Higgs mechanism) [3–5], which is an important feature of the SM since it explains the apparent breaking of the electroweak symmetry. However, it is possible that this particle is not the only Higgs boson. It is still possible to have other heavier or lighter Higgs bosons in the context of theories beyond the SM. In this thesis, the search for two heavy Higgs bosons is performed with LHC data recorded by the ATLAS detector with proton-proton collision energy at 13 TeV with total luminosity 36 fb^{-1} initially, and subsequently increased to 139 fb^{-1}. The theoretical background and the motivation is the subject of this chapter.

1.1 The Standard Model

The standard model of particle physics describes the fundamental particles and their interactions. It is constructed by the quantum field theories of electromagnetic, strong and weak nuclear interactions [6, 7]. These interactions are described by a product of three local gauge symmetry groups: $SU(3)_C \times SU(2)_L \times U(1)_Y$. The $SU(3)_C$ is the symmetry group of quantum chromodynamics (QCD) which governs the strong interactions, and it is also known as the symmetry group of colour charge. The group product $SU(2)_L \times U(1)_Y$ describes the symmetry of the electroweak (EW) interaction, which gives rise to electromagnetism and weak interactions at lower energies. $SU(2)_L$ represents the weak isospin and $U(1)_Y$ represents the weak hyprecharge. There are two types of particles in the SM, which

are divided by their spin quantum number: fermions, which have half-integer spin; and bosons, which have integer spin. The particles contained in the SM are summarised in Figure 1.1 and listed in the following:

- **Quarks** are fermions with spin = $\frac{1}{2}$ which interact with all 4 forces. There are 6 quarks with 3 different colours (plus their antiparticles), namely *up* (u), *down* (d), *strange* (s), *charm* (c), *top* (t) and *bottom* (b).
- **Leptons** are fermions with spin = $\frac{1}{2}$ which do not interact with the strong force. Similar to the quarks, there are 6 leptons plus their antiparticles. They are electrons(e), muons(μ), tau leptons(τ), electron neutrinos(ν_e), muon neutrinos(ν_μ) and tau neutrinos(ν_τ).
- **Gauge bosons**: Also known as force-carrying bosons or vector (Spin 1) bosons due to their properties. The interactions between the elementary particles are governed by the gauge bosons, they are gauge-invariant under a continuous group of local transformations. Photons (γ) and gluons (g) are responsible for the electromagnetic and strong forces, respectively; while the $W^{\pm}$ and Z^0 bosons are responsible for the weak force.
- **Higgs boson**: The only elementary scalar (spin 0) boson in the SM, it is related to the mass-giving mechanism of the $W^{\pm}$and Z^0 bosons, and even some fermions.

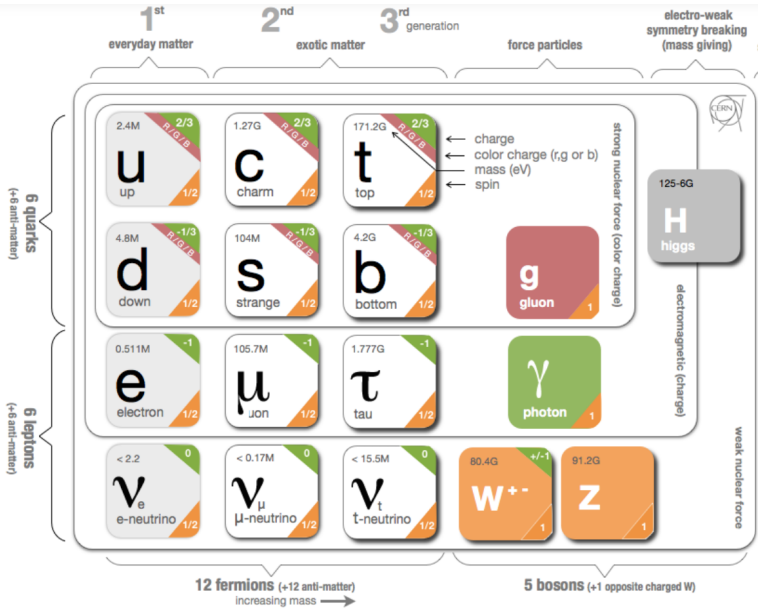

Figure 1.1: The Standard Model of elementary particles. From ref.[8]

1.1.1 Electroweak interaction & Higgs Mechanism

The electroweak interaction give rise to the electromagnetism and weak interaction at lower energies. It was first proposed by Glashow [9], Weinberg [10] and Salam [11]. The theory is based on the invariance with respect to the local gauge transformations of the symmetry group $SU(2)_L \times U(1)_Y$, as introduced above. The corresponding gauge fields are the three isospin fields from $SU(2)_L$: $W^i_\mu (i = 1,2,3)$; and the weak hypercharge field from $U(1)_Y$: B_μ. The weak interaction couples differently to the left-handed and right-handed chiral particles and anti-particles. The right-handed particle and left-handed anti-particle have isospin singlets with weak isospin, $I_W = 0$. For example, the right-handed electron and the right-handed neutrino are weak isospin singlets, denoted as e_R and ν_R, respectively. The left-handed particle and right-handed anti-particle are composed as the weak isospin doublet. For example, left-handed electron and its neutrino are composed as:

$$\begin{pmatrix} \nu_e \\ e \end{pmatrix}_L ,$$

where the upper member of the doublet always differs by $+1$ electric charge relative to the lower member of the doublet. The upper member and lower member of the doublet always have the third component of weak isospins $I^{(3)}_W = +1/2$ and $I^{(3)}_W = -1/2$, respectively. The weak hypercharges of the particles in the weak isospin doublet has to be the same in order to be invariance under the $SU(2)_L$ and $U(1)_Y$ gauge transformation. The hypercharge can be expressed as the combination of the electric charge and the third component of weak isospins: $Y = 2(Q - I^{(3)}_W)$, where Q is the electric charge. Therefore, the weak hypercharge is different between each type of fermions. For example, the hypercharge of the left-handed charged leptons are $Y = -1$, while it is $Y = -2$ for the right-handed charged leptons.

The physical states for $\mathrm{W}^\pm$, Z^0 bosons and photon can be constructed by the combination of these fields:

$$\begin{aligned} W^\pm_\mu &= \frac{1}{\sqrt{2}}(W^1_\mu \mp W^2_\mu), \\ Z_\mu &= W^3_\mu \cos\theta_w - B_\mu \sin\theta_w, \text{ and} \\ A_\mu &= W^3_\mu \sin\theta_w + B_\mu \cos\theta_w, \end{aligned} \tag{1.1}$$

where θ_w is the weak mixing angle, which can be expressed by the weak (g) and electromagnetic (g')

coupling constants:

$$\sin\theta_w = \frac{g'}{\sqrt{g^2+g'^2}} \text{ and } \cos\theta_w = \frac{g}{\sqrt{g^2+g'^2}}. \tag{1.2}$$

Although the theory successfully summarised the electromagnetic and weak nuclear interaction, it is not possible to give the mass terms for the $W^{\pm}$ and Z^0 boson, which are observed to be massive in the experiment. In order to obtain the masses of the weak gauge bosons, the electroweak symmetry breaking is needed in the theory. This can be achieved by the Higgs mechanism, which introduced a new complex doublet field that has a non-zero vacuum expectation value (VEV) but it is symmetric under the gauge transformations. In this case, the symmetry of the Lagrangian remain unchanged while the vacuum state of the field does not respect the symmetry. This is also known as "spontaneous symmetry breaking". After the spontaneous symmetry breaking, there are four degrees of freedom in the complex scalar field, three non-physical massless Goldstone bosons and a massive Higgs boson is given by the field. These Goldstone bosons are absorbed by the $W^{\pm}$ and Z bosons, leading them to acquire masses terms. The Higgs mechanism in the SM is achieved by introducing a weak isospin doublet of complex scalar fields with hypercharge = $+1$:

$$\phi = \begin{pmatrix} \phi^+ \\ \phi^0 \end{pmatrix} = \frac{1}{\sqrt{2}} \begin{pmatrix} \phi_1 + i\phi_2 \\ \phi_3 + i\phi_4 \end{pmatrix}, \tag{1.3}$$

where $\phi^{+(0)}$ has a positive (neutral) electric charge, all ϕ_i are real fields. The corresponding Lagrangian for this field is

$$\mathscr{L}_{Higgs} = (D_\mu\phi)^\dagger(D^\mu\phi) - V(\phi^\dagger\phi), \tag{1.4}$$

where D_μ is the covariant derivative, which is given by

$$D_\mu = \partial_\mu - \frac{i}{2}gW_\mu^a \cdot \sigma^a - \frac{i}{2}g'B_\mu, \tag{1.5}$$

where the σ^a,$a = 1,2,3$ are the usual Pauli matrices. The minimum potential, V, is renormalisable and satisfying the gauge symmetry, can be expressed as:

$$V(\phi) = \mu^2(\phi^\dagger\phi) + \lambda(\phi^\dagger\phi)^2, \tag{1.6}$$

where $\mu^2 < 0$ and $\lambda > 0$ are required in order to have a minimum in the potential which is not symmetric without breaking the electroweak symmetry, which is the condition of the spontaneous symmetry breaking. Also, one can choose the direction of minimum among the infinite number of

degenerate minima such that three components of ϕ are zero. In order to fulfill the requirement that the photon remains massless, the usual choice is $\phi_1, \phi_2, \phi_4 = 0$ and hence $\phi_3 = |\phi_0|$, which leads to the non-zero VEV, v, defined by:

$$< \phi >= \frac{1}{\sqrt{2}} \begin{pmatrix} 0 \\ v \end{pmatrix}, v = \sqrt{\frac{-\mu^2}{|\lambda|}}, \tag{1.7}$$

where the VEV in the SM is approximately 246 GeV [6, 7]. Under the local gauge transformation which eliminated the Goldstone bosons, the field can be writen as an expansion about this minimum,

$$\phi = \frac{1}{\sqrt{2}} \begin{pmatrix} 0 \\ v + H \end{pmatrix}, \tag{1.8}$$

where H is the physical Higgs boson, oscillating around the vacuum. Substituting this expression back into the $(D_\mu \phi)^\dagger (D^\mu \phi)$ term in the Lagrangian of the Higgs field, one will have the gauge bosons masses:

$$m_W = \frac{gv}{2}, \; and \;\; m_Z = \frac{1}{2}\frac{gv}{\cos\theta_w}. \tag{1.9}$$

More importantly, the mass for the Higgs boson is given by $m_h = \sqrt{-2\mu^2}$, which is a free parameter of the theory. The Higgs mechanism can also be used to generate masses of the fermions in the SM. After the spontaneous symmetry breaking, the fermion masses are generated by their interaction with the Higgs field, which can be expressed by:

$$\mathscr{L}_{f-Higgs} = -y_f \frac{v}{\sqrt{2}}(\overline{f_L} f_R + \overline{f_R} f_L) - y_f \frac{H}{\sqrt{2}}(\overline{f_L} f_R + \overline{f_R} f_L), \;\; m_f = y_f \frac{v}{\sqrt{2}}, \tag{1.10}$$

where the y_f is known as the Yukawa coupling for fermion f, f_L is the weak isospin doublet of the left-handed fermions; and f_R is the weak isospin singlet of the right-handed fermions.

In 2012, 50 years after the first proposal of the Higgs mechanism, ATLAS and CMS experiment discovered a SM Higgs-like boson [1, 2], h, with mass, $m_h = 125.10 \pm 0.14$ GeV [12]. After subsequent studies, this discovered boson has been found to be compatible with the description of Higgs boson in SM such as the value of the intrinsic spin and the couplings to the gauge bosons [13–16].

1.1.2 SM Higgs production and decay in LHC

The SM Higgs-like boson was discovered by ATLAS and CMS experiment through $h \to \gamma\gamma$ and $h \to ZZ \to 4\ell$ channels at $\sqrt{s} = 7$ and 8 TeV [1, 2]. There are four main production mechanisms for the Higgs boson in the LHC [17]: gluon fusion (ggh), vector boson fusion process (VBF), Higgs-strahlung (Vh) and $t\bar{t}$-associated production (tth). Figure 1.2 shows example Feynman diagrams for these production mechanisms in the LHC.

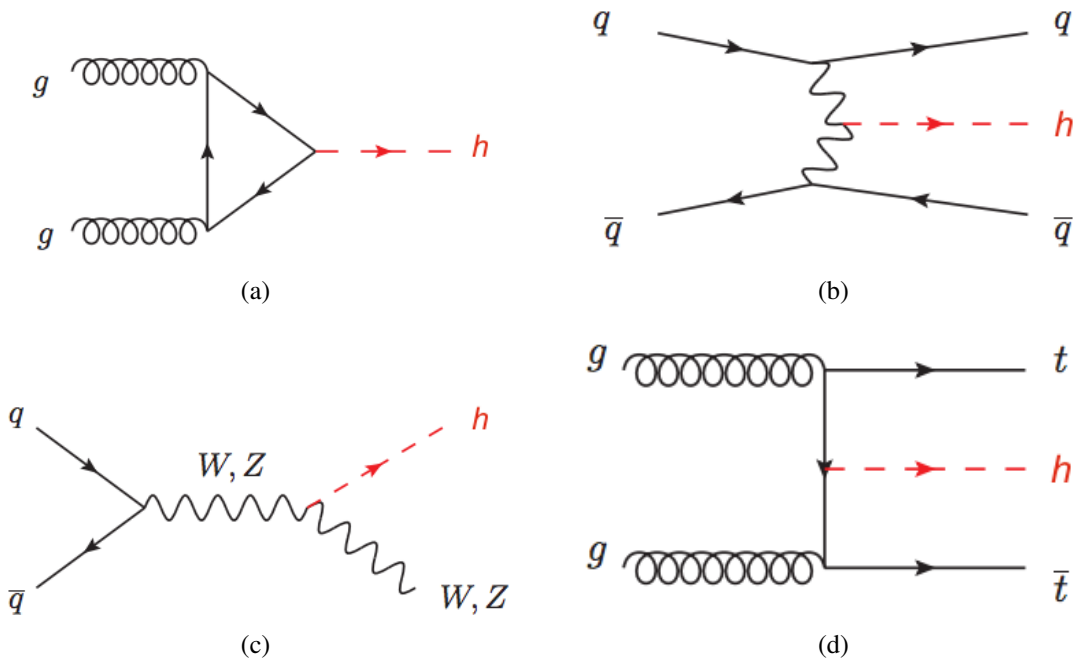

Figure 1.2: Higgs production at the LHC [17], (a) gluon fusion (ggh), (b) vector boson fusion process (VBF), (c) Higgs-strahlung (Vh) and (d) $t\bar{t}$-associated production (tth).

The Higgs boson at the LHC is mainly produced via gluon fusion and vector boson fusion. The SM Higgs boson cross sections for $m_h = 125$ GeV at $\sqrt{s} = 13$ TeV are shown in Table 1.1 and the SM Higgs branching ratio near $m_h = 125$ GeV is shown at figure 1.3. The $h \to b\bar{b}$ is the main decay channel of SM Higgs boson. However, due to the large QCD background in the LHC, the Higgs boson was discovered by searching at $h \to ZZ \to 4\ell$ and $h \to \gamma\gamma$ channels [1, 2].

Production mechanism	ggh	VBF	Wh	Zh	tth
Production cross sections [pb]	$48.6^{+4.6\%}_{-6.7\%}$	$3.78^{+2.2\%}_{-2.2\%}$	$1.37^{+2.6\%}_{-2.6\%}$	$0.88^{+4.1\%}_{-3.5\%}$	$0.50^{+6.8\%}_{-9.9\%}$

Table 1.1: LHC Higgs production cross sections for $m_h = 125$ GeV at $\sqrt{s} = 13$ TeV [12, 17].

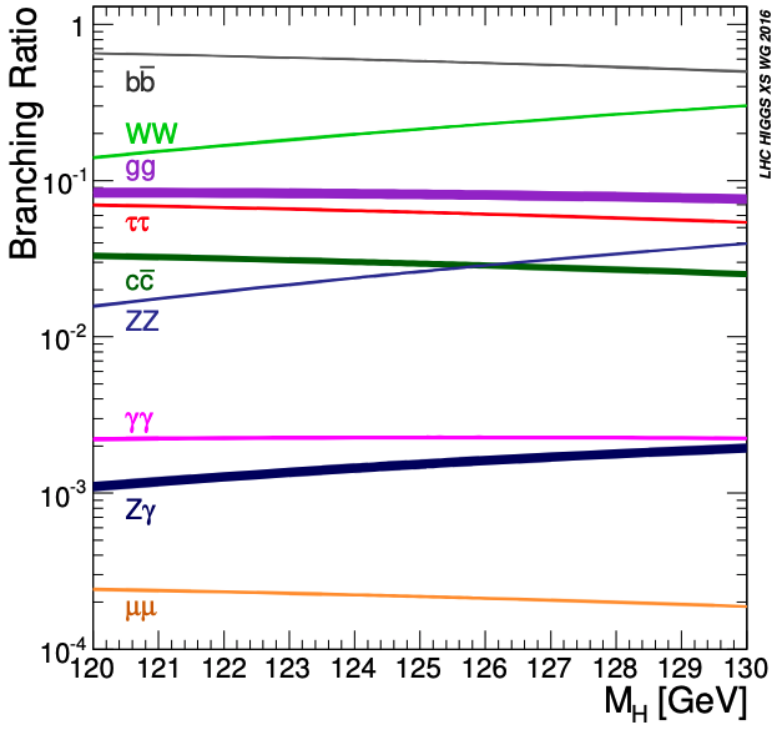

Figure 1.3: The branching ratios for the main decays of the SM Higgs boson near $m_h = 125$ GeV [12]. The theoretical uncertainties are indicated as bands.

In the LHC, several SM Higgs decay channels are also being studied. The discovery channels, $h \to ZZ \to 4\ell$ and $h \to \gamma\gamma$, has been studied with more data collected after 2012 at $\sqrt{s} = 13$ TeV [18–21], other channels such as the $h \to \tau\tau$ decay had been observed in 2017 [22, 23], the $h \to b\bar{b}$ decay via Vh production mode has been seen in 2018 [24, 25]. A hint of the $h \to \mu\mu$ decay has been observed in both CMS and ATLAS experiment in 2020 [26, 27]. The $h \to cc$ channels are also being searched for [28, 29]. Also, the coupling between t and h has been measured in 2018 with the confirmation of tth production mode [30, 31].

1.1.3 Problems with the SM

Although most of the observations in particle physics can be described by the SM, there are still some that cannot be accommodated [6, 7]. For instance, the gravitational interaction is a well-known physical phenomenon which does not fit into the SM. Another unexplained observation is the asymmetry between matter and anti-matter in our universe.

There is a well-known problem with the SM called “Hierarchy problem”, which is related to the energy scales of the elementary particles. In particle physics, there are different energy scales. For example, the electroweak scale, which is related to the eletroweak physics, consider the energy at 100

GeV level; and the Plank scale, which is important for the physics related to the Gravity, at 10^{19} GeV level. However, the origin of the difference between these scales is not known. Another problem related to the energy scale is the radiation correction on the spin 0 particle mass. These correction works fine at the electroweak scale. However, they will become very large at such high mass scale as the Plank scale. Eventually, it is hard to keep the mass of the SM Higgs boson at the electroweak scale of 100 GeV. One can apply a fine-tuned cancellation to solve this problem, while a more natural solution can be provided by supersymmetry (SUSY). In SUSY, SM particles have their corresponding super-partners "sparticle" which differs by the spin [32]. Therefore, the loop of SM particles can be exactly cancelled by the loop of the corresponding sparticles if they had the same masses as the corresponding SM particles. Another issue related to the particle masses in the SM is that the Higgs boson give mass to fermions such as quarks, but there are mass difference between different type of fermions. For example, the mass of up quark and top quark are $2.16^{+0.49}_{-0.26}$ MeV and 172.76 ± 0.30 GeV, respectively [17]. More studies are needed in order to understand the origin of this difference.

Another well-known problem is the "Strong CP problem", which is related to the CP-violation of the strong interaction. In the SM, it is possible to have a strong CP term in the QCD Lagrangian, but the relevant parameter is zero. Peccei and Quinn [33, 34] shows that this can be explained by introducing an extra U(1) symmetry. Under their assumption, the parameter becomes a dynamical variable, and it is zero at the minimum of the potential. Weinberg [35] and Wilczek [36] even predicted that spontaneous breaking of this symmetry leads to the generation of a new particle called "axion" with mass ranging in 10^{-5} to 10^{-2} eV, depending on the energy scale of the extra U(1) symmetry.

The above examples show that some problems with the SM can be explained or solved by extending the SM with an extra degree of freedom. One of the simplest extensions of SM is the Two-Higgs-Doublet-Model (2HDM). In 2HDM, an extra doublet has been added into the Higgs sector and hence there are additional Higgs bosons [37]. The existence of these additional Higgs bosons has a great potential to answer the unanswered question from the SM. For example, the minimum implementation of the SUSY has the structure of 2HDM. Generally, a more complicated Higgs sector is needed in the SUSY model.

1.2 Two-Higgs-Doublet-Model

The SM Higgs mechanism is the simplest way to give $W^{\pm}$ and Z boson masses with only one weak isospin doublet. In the 2HDM, there are two weak isospin doublets: Φ_1 and Φ_2. Each of them has four degrees of freedom. After the spontaneous symmetry breaking, three of them corresponding to the $W^{\pm}$ and Z boson longitudinal polarisation degrees of freedom, leaving five Higgs bosons. In most of the phenomenological studies, the model is simplified by assuming CP conservation in the Higgs sector. In this case, the most general scalar potential is given by [37]:

$$\begin{aligned} V(\Phi_1\Phi_2) = m_{11}^2\Phi_1^\dagger\Phi_1 + m_{22}^2\Phi_2^\dagger\Phi_2 + m_{12}^2(\Phi_1^\dagger\Phi_2 + \Phi_2^\dagger\Phi_1) + \frac{\lambda_1}{2}(\Phi_1^\dagger\Phi_1)^2 + \frac{\lambda_2}{2}(\Phi_2^\dagger\Phi_2)^2 \\ +\lambda_3\Phi_1^\dagger\Phi_1\Phi_2^\dagger\Phi_2 + \lambda_4\Phi_1^\dagger\Phi_2\Phi_2^\dagger\Phi_1 + \frac{\lambda_5}{2}[(\Phi_1^\dagger\Phi_2)^2 + (\Phi_2^\dagger\Phi_1)^2], \end{aligned} \tag{1.11}$$

where all the parameters are taken to be real. The potential minimum corresponding to the CP-conserving vacua are:

$$< \Phi_1 >= \frac{1}{\sqrt{2}}\begin{pmatrix} 0 \\ v_1 \end{pmatrix}, \qquad < \Phi_2 >= \frac{1}{\sqrt{2}}\begin{pmatrix} 0 \\ v_2 \end{pmatrix}, \tag{1.12}$$

where the v_1 and v_2 are VEVs of Φ_1 and Φ_2, respectively. The relation between v_{SM} (VEV from SM Higgs doublet), v_1 and v_2 are given by: $\sqrt{v_1^2 + v_2^2} = v_{SM} = 246$ GeV. Also, the ratio between the VEVs is customary to be expressed as the notation [37]:

$$\tan\beta \equiv \frac{v_2}{v_1}. \tag{1.13}$$

Similar to the Higgs mechanism in the SM, the weak isospin doublets with hypercharge = $+1$ are:

$$\phi_1 = \begin{pmatrix} \phi_1^+ \\ \frac{(v_1+\rho_1+i\eta_1)}{\sqrt{2}} \end{pmatrix}, \qquad \phi_2 = \begin{pmatrix} \phi_2^+ \\ \frac{(v_2+\rho_2+i\eta_2)}{\sqrt{2}} \end{pmatrix}. \tag{1.14}$$

There are eight degrees of freedom after spontaneous symmetry breaking. As in the SM, three of them are eliminated in order to generate the masses of the weak gague bosons, leaving five Higgs bosons including a charged scalar($H^{\pm}$), two neutral scalars (h, H), and a pseudoscalar (A). The physical

neutral Higgs bosons can be written as:

$$\begin{aligned} h &= \rho_1 \sin\alpha - \rho_2 \cos\alpha, \\ H &= -\rho_1 \cos\alpha - \rho_2 \sin\alpha, \text{ and} \\ A &= \eta_1 \sin\beta - \eta_2 \cos\beta, \end{aligned} \tag{1.15}$$

where the angle $\beta \equiv \arctan v_2/v_1$, and the angle α is also known as the Higgs mixing angle, which is the mixing angle after diagonalising the mass matrix for the neutral scalars. The neutral scalars are also called "CP-even Higgs" since their CP structure does not change during the interaction with other particles. On the other hand, the pseudoscalar is also called "CP-odd Higgs" since the CP structure will change during the interaction with other particles. In general, there are 7 physical parameters in the 2HDM: Higgs boson masses (m_h, m_H, m_A, $m_{H^\pm}$), potential parameter m_{12}^2, $\tan\beta$ and α. A combination of parameters is often used in the 2HDM analysis: $\cos(\beta-\alpha)$, the closer this parameter to zero, the more the coupling of the h act like the SM Higgs. The coupling of h will be the same as the couplings of the SM Higgs boson when $\cos(\beta-\alpha) \to 0$, this condition is also known as "weak decoupling limit" [38] or the "alignment limit" [39]. Another limit, the "strong decoupling limit", required the additional Higgs boson to be much heavier than the SM Higgs.

There are several ways to arrange the Yukawa couplings in CP conserving 2HDM. If the flavour-changing neutral currents are absent at tree level, there will be four possible arrangements [40] and hence 4 types of model in CP-conserving 2HDM: Type-I, Type-II, lepton-specific and flipped. The arrangement of the couplings between the fermions and the doublet is different in these models. In Type-I, all charged fermions couple only to Φ_2. In Type-II the up-type quarks couple to Φ_2 and down-type quarks couple to Φ_1. The lepton-specific model is similar to Type-I but has charged leptons coupling to Φ_1. Lastly, in the "flipped" model is similar to Type-II but has charged leptons coupling to Φ_2. The Yukawa couplings coefficient with respect to the SM Yukawa coupling in each of the models depends on the combination of the α and β [38], as summarised in Table 1.2.

As the couplings depends on the parameters in the 2HDM, the choices of parameter (benchmark scenarios) will affect the results from interpretation or searches for the 2HDM Higgs bosons decay. There are two main 2HDM benchmark scenarios used in the LHC: (a) The Higgs couplings measurement and interpretation; and (b) The standard 2HDM searches. In the Higgs coupling measurement [42], the m_h is fixed at 125 GeV, where other Higgs bosons are assumed to be heavy enough

Coupling	Type-I	Type-II	lepton-specific	flipped
huu	$s_{\beta-\alpha}+c_{\beta-\alpha}/t_\beta$	$s_{\beta-\alpha}+c_{\beta-\alpha}/t_\beta$	$s_{\beta-\alpha}+c_{\beta-\alpha}/t_\beta$	$s_{\beta-\alpha}+c_{\beta-\alpha}/t_\beta$
hdd	$s_{\beta-\alpha}+c_{\beta-\alpha}/t_\beta$	$s_{\beta-\alpha}-c_{\beta-\alpha}\cdot t_\beta$	$s_{\beta-\alpha}+c_{\beta-\alpha}/t_\beta$	$s_{\beta-\alpha}-c_{\beta-\alpha}\cdot t_\beta$
$h\ell\ell$	$s_{\beta-\alpha}+c_{\beta-\alpha}/t_\beta$	$s_{\beta-\alpha}-c_{\beta-\alpha}\cdot t_\beta$	$s_{\beta-\alpha}-c_{\beta-\alpha}\cdot t_\beta$	$s_{\beta-\alpha}+c_{\beta-\alpha}/t_\beta$
Huu	$c_{\beta-\alpha}-s_{\beta-\alpha}/t_\beta$	$c_{\beta-\alpha}-s_{\beta-\alpha}/t_\beta$	$c_{\beta-\alpha}-s_{\beta-\alpha}/t_\beta$	$c_{\beta-\alpha}-s_{\beta-\alpha}/t_\beta$
Hdd	$c_{\beta-\alpha}-s_{\beta-\alpha}/t_\beta$	$c_{\beta-\alpha}+s_{\beta-\alpha}\cdot t_\beta$	$c_{\beta-\alpha}-s_{\beta-\alpha}/t_\beta$	$c_{\beta-\alpha}+s_{\beta-\alpha}\cdot t_\beta$
$H\ell\ell$	$c_{\beta-\alpha}-s_{\beta-\alpha}/t_\beta$	$c_{\beta-\alpha}+s_{\beta-\alpha}\cdot t_\beta$	$c_{\beta-\alpha}+s_{\beta-\alpha}\cdot t_\beta$	$c_{\beta-\alpha}-s_{\beta-\alpha}/t_\beta$
Auu	$1/t_\beta$	$1/t_\beta$	$1/t_\beta$	$1/t_\beta$
Add	$-1/t_\beta$	t_β	$-1/t_\beta$	t_β
$A\ell\ell$	$-1/t_\beta$	t_β	t_β	$-1/t_\beta$

Table 1.2: Yukawa coupling coefficient with respect to the SM Yukawa coupling for h, H and A Higgs bosons coupling to up-type quark (u); down-type quark (d) and charged leptons (ℓ) [41]. The shorthand notations are defined as: $s_i \equiv \sin i$, $c_i \equiv \cos i$ and $t_i \equiv \tan i$; where $i = \beta$ or $(\beta-\alpha)$. These coefficients are defined such that the Yukawa Lagrangian terms are $-(m_f/v)\bar{f}f\phi$ and $i(m_f/v)\bar{f}\gamma_5 fA$, where $f = u,d,\ell$ and $\phi = h,H$.

that their radiation corrections do not affect the measurement to the h. The measurement sets constraints on the $(\cos(\beta-\alpha), \tan\beta)$ plane and hence $\cos(\beta-\alpha)$ and $\tan\beta$ are free parameters. For the standard 2HDM searches, for example the search for $A \to Zh$ [43], the masses of A, H and $H_\pm$ are assumed to be equal to each other while the $m_h = 125$ GeV is required. The $\cos(\beta-\alpha)$ and $\tan\beta$ are free parameters, their range is varying depends on which part of the parameter space was probed by the searches.

The perviously mentioned benchmark scenarios are not suitable for the search described in this thesis since the $A \to ZH$ decay require the mass difference between the A and H. In this search, the following benchmark is required: $\cos(\beta-\alpha) \simeq 0$, $m_h = 125$ GeV, $(m_A - m_H) \geq 100$ GeV, $m_A \leq 800$ GeV, $m_H \geq 130$ GeV. Figure 1.4(a) and (b) shows an example of branching ratio of the A boson and the H boson as a function of m_H under the benchmark used in the search. Two scenarios depends on the $\cos(\beta-\alpha)$ values in the Type-I 2HDM are shown in this figure. The production cross section of the A boson also vary across the 2HDM parameter space, Figure 1.4(c)–(e) demonstrated the production cross section of the A boson as a function of $\tan\beta$ under the gluon-gluon fusion and b-associated production mechanisms. The production cross sections in Type-I and Type-II 2HDM are also compared. Figure 1.4(c) and (d) shows that the production cross section of the A boson generally dropped when the $\tan\beta$ becomes larger. However, there is an exception as shown in Figure 1.4(e): In Type-II 2HDM, the production cross section of the b-associated produced A boson increase with the $\tan\beta$. In Figure 1.5, the ratio of the width and the mass of the A boson, Γ_A/m_A, is shown as the number in percentage in each bins along the m_A and m_H spectra in Type-I 2HDM with $\tan\beta = 1$, 5 and 10.

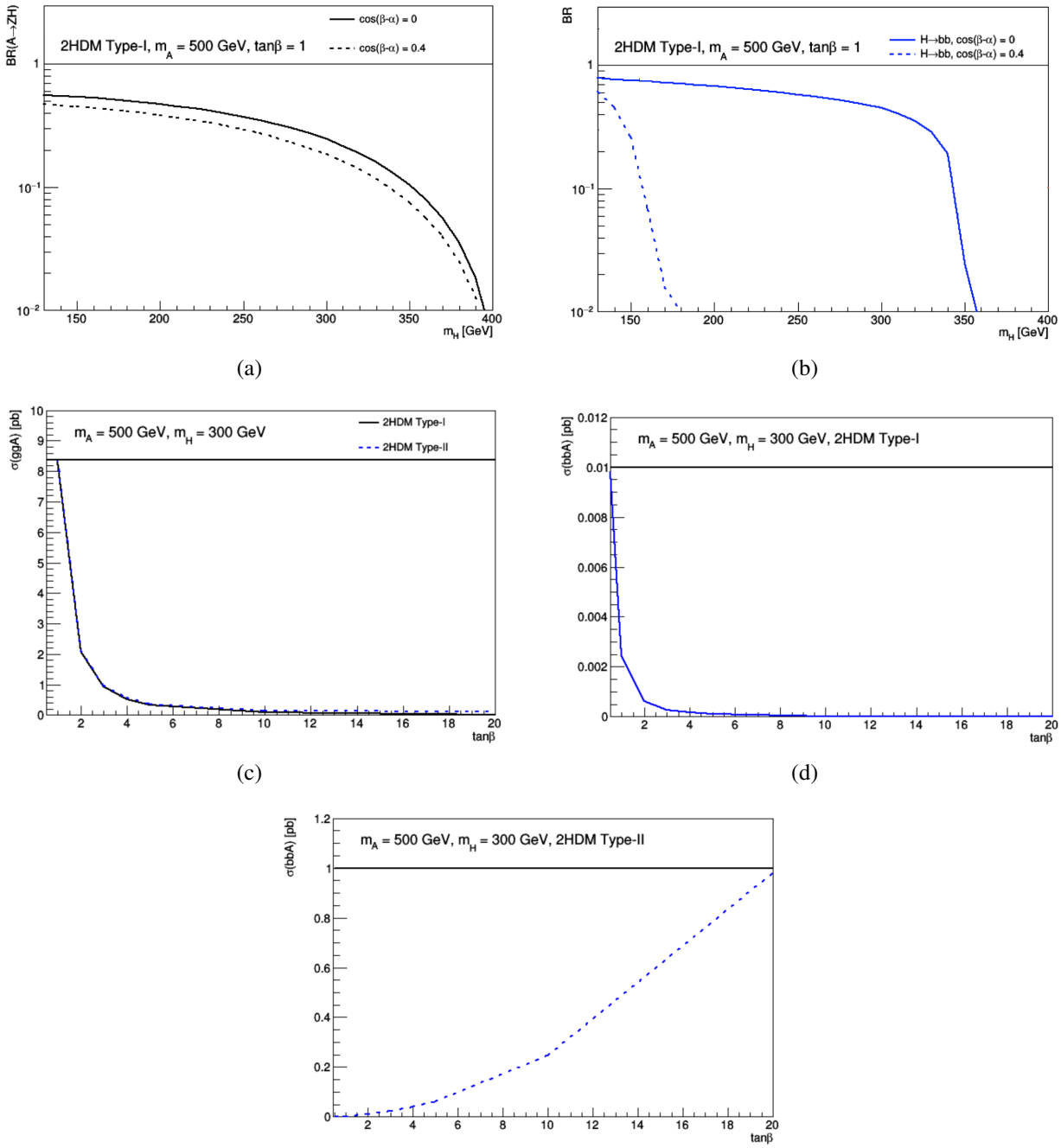

Figure 1.4: Example branching ratios of the $A \to ZH$ decay (left) and $H \to b\bar{b}$ decay (right) as a function of m_H in 2 scenarios: $\cos(\beta-\alpha) = 0$ (Solid lines) and $\cos(\beta-\alpha) = 0.4$ (dotted lines) in the Type-I 2HDM. Other parameters, m_A and $\tan\beta$ are fixed. Example production cross section of the A with $m_A = 500$ GeV and $m_H = 300$ GeV. The cross section of the A boson produced by both (c) gluon-gluon fusion in Type-I and Type-II 2HDM and b-associated production in (d) Type-I and (e) Type-II 2HDM are shown [44].

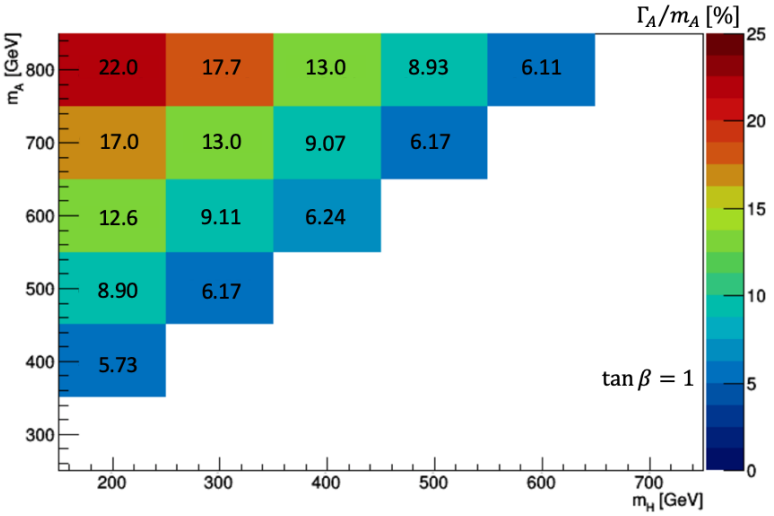

(a)

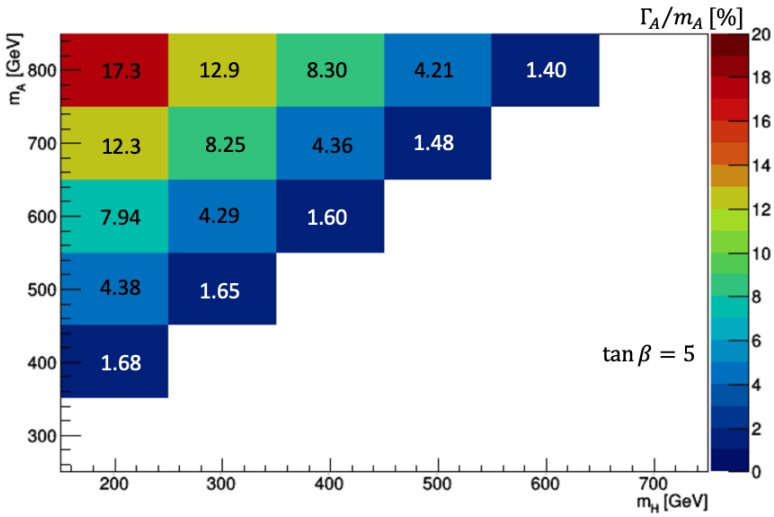

(b)

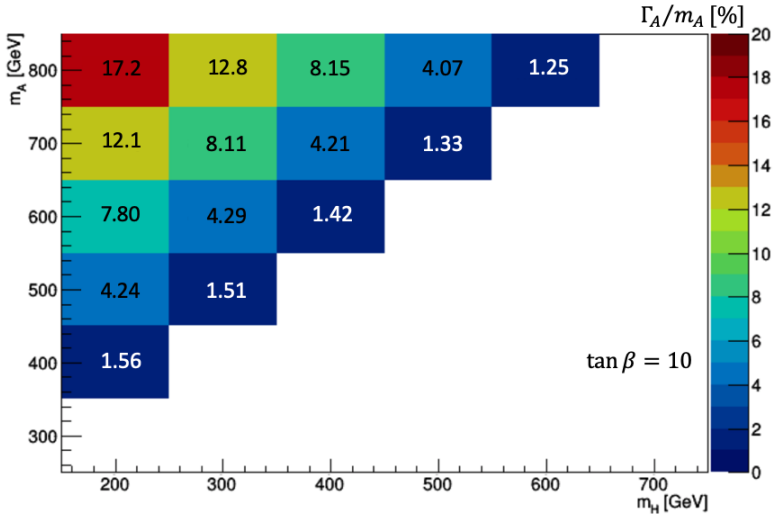

(c)

Figure 1.5: The ratio of the width and the mass of the A boson, Γ_A/m_A, along the m_A and m_H spectra in Type-I 2HDM with (a)$\tan\beta = 1$, (b) $\tan\beta = 5$ and (c) $\tan\beta = 10$. The ratio Γ_A/m_A is shown as the number in each bins [44].

1.2.1 2HDM Higgs production and decay in LHC

The production mechanisms of the 2HDM Higgs bosons are similar to the SM Higgs boson in the LHC. All the neutral Higgs bosons can be produced via gluon fusion and a production in association with a top or bottom quark. Only the CP-even Higgs boson can be produced by the VBF and the Higgs-strahlung production modes since there is no such couplings for the CP-odd Higgs boson at tree-level.

The decay modes of the 2HDM Higgs bosons are much complicated compare to the production mechanisms described above. It is due to the fact that the branching ratio of the heavy Higgs boson decays is depending on the choice of the 2HDM parameters. There are several searches for 2HDM Higgs bosons decay at the LHC in the past include $H \to WW/ZZ$ [45–49], $H \to hh$ [50, 51], $A \to Zh$ [43, 52], $A/H \to \tau\tau/b\bar{b}$ [53–55]. In this thesis, the A boson is considered to decay into another H boson associated with a Z boson; while the H boson will further decay into a pair of b quarks. This channel has been studied by the CMS collaboration in 2016 [56]. The very first study of this channel in the ATLAS collaboration is described in Section 5, the result of this search is published in Ref. [57]. The search was improved in Ref. [58] with more data collected by ATLAS detector, which is also discussed in Section 6. The benchmark used in this search is described in the previous section.

1.2.2 Electroweak-baryogenesis and 2HDM

Another motivation of the search is called “baryogenesis”, which is a mechanism proposed to explain the origin of the matter-antimatter asymmetry in our universe. In the standard cosmological model [59], the amounts of matter and antimatter were equal in the very early universe. The way of transition between this matter-antimatter balance universe to the matter dominated universe is still one of the unanswered questions in both particle physics and cosmology. The condition of baryogenesis as stated by Sakharov [60] are the following:

1. Non-conservation of baryon number.
2. Breaking of C and CP invariance.
3. Deviation from thermal equilibrium.

There are several scenarios of baryogenesis. For instance, the $A \to ZH \to llb\bar{b}$ search is motivated by the scenario called “electroweak brayogenesis”, which can be realised via the Higgs sector

at the energy scale of LHC. In order to have electroweak baryogenesis, following conditions are required [61]:

- The temperature evolution of the Higgs potential must be such that there are two degenerate vacua at some critical temperature, and the electroweak phase transition proceeds through the formation of bubbles of the new vacuum that gradually increase and fill the whole space.
- New sources of CP violation are needed in order to create the matter–antimatter asymmetry close to the bubble walls.
- The critical temperature must be low enough compared to the Higgs vacuum expectation value in order to violate the baryon numbers.

The electroweak baryogenesis does not require a more complicated Higgs sector than what we have in the SM. However, in order to reach the conditions of electroweak baryogenesis with SM alone, the mass of SM Higgs boson has to be lower than 80 GeV [61], which is already excluded by the searches for the Higgs boson [62], as well as the LHC Higgs boson discovery. However, it is still possible to have electroweak baryogenesis with more complicated Higgs sector such as 2HDM [61]. In order to have the electroweak baryogenesis happenning in the LHC energy scale, the study in Ref. [61] suggested that $(m_A - m_H) \geq v$ and $m_A \leq 1$ TeV are required. This paper shows that the A boson with mass between 230 to 800 GeV; and the H boson with mass between 130 to 700 GeV is more responsible for the realisation of the baryogenesis. In addition, the mass splitting between A and H is required to satisfy the condition $m_A - m_H > 100$ GeV. Therefore, the mass range of the m_A and m_H used in this search follow these conditions. The search for this channel was investigated at the LHC in 2016 [56] by CMS collaboration. This is the first time for this channel to be investigated with the data collected from the ATLAS experiment.

In the following chapters, the search is performed with LHC data recorded by the ATLAS detector with proton-proton collision energy at 13 TeV with total Luminosity 36 fb^{-1} and 139 fb^{-1} in Chapter 5 and 6, respectively. Next chapter, the experimental apparatus including the structure of the LHC and the ATLAS detector will be discussed. The data handling and the analysis software will also be introduced in the next chapter.

CHAPTER 2

Experimental Apparatus

Scientific theories require empirical evidence which is provided by experiments. There are several types of particle physics experiments. In this thesis the focus is on collider experiments. In a particle collider, charged particles like electrons and protons are accelerated and brought into collision in given points. The particle detectors then record the outcome of the collisions, so that it can be further analysed. In this thesis, the search for $A \to ZH \to \ell\ell b\bar{b}$ is performed with the collision data in the ATLAS detector, which is one of the detectors at the Large Hadron Collider. This chapter will introduce the Large Hadron Collider and give a description of the ATLAS detector.

2.1 The Large Hadron Collider

The Large Hadron Collider (LHC) is currently the world's largest particle collider [63]. It is located at CERN (Conseil Européen pour la Recherche Nucléaire) near Geneva, Switzerland. The LHC was constructed between 1998 and 2008 inside a 27 km long circular tunnel, which is located around 100 m below ground level, crossing the border between Switzerland and France. Both protons and heavy ions can be accelerated in opposite directions within the LHC beam pipes. In proton-proton (pp) collision mode, proton beams are accelerated up to the energy of 6.5 TeV per beam. The protons are first extracted off hydrogen atoms, and then they are accelerated using a linear accelerator named Linac 2. The beam is subsequently injected into the Proton Synchrotron Booster (PSB) and Proton Synchrotron (PS), then further accelerated at the Super Proton Synchrotron (SPS) and transferred to the two beam pipes of the LHC. The proton beam is discontinuously transferred into LHC as a series of proton bunches, which nominally have around 10^{11} protons each, with a nominal bunch spacing of 25 ns, which means that the nominal crossing frequency is 40 MHz. The beams are guided by superconducting dipole magnets and accelerated by radio frequency cavities. The beams

cross at 4 interaction points around the ring, and the collision products are recorded by four particle detectors: ATLAS (A Toroidal LHC ApparatuS)[64], CMS (Compact Muon Solenoid)[65], LHCb (Large Hadron Collider beauty experiment)[66] and ALICE (A Large Ion Collider Experiment)[67], which surround these interaction points. ATLAS and CMS are multipurpose detectors, which are used to perform a wide range of searches and measurements. The LHCb is optimised to the B-hadron precision physics and ALICE is specialised for the measurement of heavy-ion collisions. The LHC accelerator complex is shown in Figure 2.1.

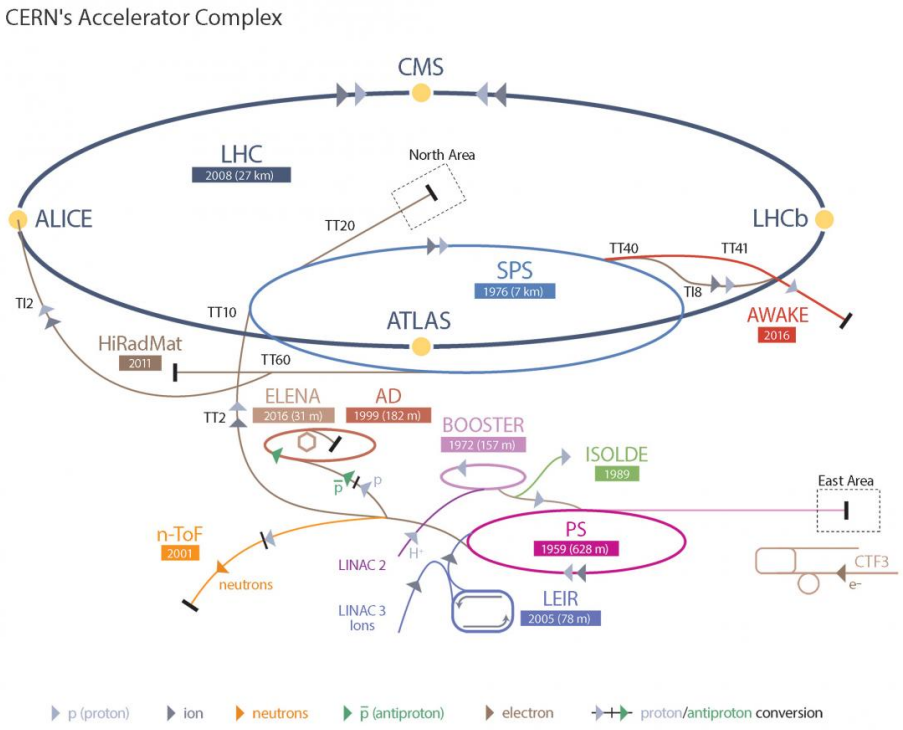

Figure 2.1: A schematic view of the CERN accelerator complex [68].

2.2 Luminosity

The energy is not the only important feature of high-energy particle collisions. Especially for rare processes, like those that are of interest in the LHC, the number of collisions per unit time is of paramount importance for the eventual physics performance. This feature is quantified in the concept of luminosity, which is discussed in more detail in the following.

The instantaneous luminosity, $\mathscr{L}$, for a proton-proton collision in LHC is defined with the following formula [69]:

$$\mathscr{L} = \frac{N_b^2 n_b f_{rev} \gamma_r}{4\pi\varepsilon_n \beta_*} F, \tag{2.1}$$

where N_b is the number of protons in a bunch and n_b is the number of bunches per beam. The revolution frequency of the particles is denoted by f_{rev}, the γ_r is the relativistic gamma factor, the normalised transverse beam emittance is denoted by ε_n, the beta function at the collision point is given by β_*, and the geometric luminosity reduction factor F, which is due to the crossing angle of the beams at the interaction point. Table 2.1 list the peak luminosities of the LHC during the 2015 to 2018 running period.

Running period	2015	2016	2017	2018
Peak luminosity [10^{33}cm^{-2}s^{-1}]	5.0	13.8	20.9	21.0

Table 2.1: Peak luminosities of the LHC during the 2015 to 2018 running period [70].

The number of events per second of a given process, $pp \to X$ with cross section, $\sigma_{pp\to X}$, is given by

$$\frac{dN_{pp\to X}}{dt} = \mathscr{L}\sigma_{pp\to X}, \tag{2.2}$$

where the total number of events, $N_{pp\to X}$, is given by integrating the above expression over time. The cross section, $\sigma_{pp\to X}$, is time-independent but depends on the incoming and outgoing particles as well as the centre-of-mass energy, such that $N_{pp\to X}$ is directly proportional to the "integrated luminosity", L, which is the time integral of the instantaneous luminosity. Thus, the $N_{pp\to X}$ in the pp collision is given by:

$$N_{pp\to X} = \sigma_{pp\to X} L = \sigma_{pp\to X} \int \mathscr{L} dt. \tag{2.3}$$

2.3 Pileup

Multiple pp collisions sometimes occur within the same bunch crossing. This is referred to as "pileup" and it is a serious challenge for the physics analysis at the LHC. Two major components of pileup in the LHC are "in-time pileup" and "out-of-time pileup"[71]. When there are more than one inelastic pp collision taking place within the same bunch crossing is known as in-time pileup. On the other hand, if the interactions occurs in different bunch crossings during the time taken by the detector to process a single event are known as out-of-time pileup. Out-of-time pile-up is depending on the

detector time resolution. The average number of pileup interactions per event, $<\mu>$, is related to the centre of mass energy of the collision, the number of bunches in the beam and the beam condition, such as the number of protons per bunch.

2.4 The ATLAS Detector

The ATLAS detector is one of the two general purpose detectors at the LHC [64]. The particles that come out of the collisions are detected by several sub-detector systems, which are sensitive to different particle properties. A schematic picture of the ATLAS detector is shown in Figure 2.2. The sub-system which is closest to the beam pipe is the inner detector system. It provides an electronic signal when charged particles pass through. Surrounding the inner detector system, the ATLAS calorimeter detects particles by stopping them and absorbing their energy. There are two types of calorimeters in ATLAS: the electromagnetic calorimeter and the hadronic calorimeter. The outermost layer of ATLAS is the muon spectrometer. The events are examined by a dedicated trigger system, about whether they are interesting for the ATLAS physics programme or not. Only events that the trigger system decides that they are interesting are stored permanently. Details of each sub-detector system and trigger system are provided in the following sections.

Each sub-system is responsible for the measurement of specific particles. Figure 2.3 shows the interaction of various particles with different sub-systems of ATLAS. Each particle type has its own signature in the detector:

- Charged particles, for example electrons and charged pions, are detected both in the tracking system and the calorimeters.
- Neutral particles, for instance unconverted photons and neutrons, are not detectable in the tracking system. Neutrons are detected by the energy deposit in the hadronic calorimeter, while unconverted photons are detected by the electromagnetic calorimeter.
- Muons are very penetrating, being the only charged particles that regularly exit the calorimeters. They are reconstructed by the signals from the muon spectrometer at the outermost layer of the detector and the inner tracker.
- Neutrinos do not provide any signal in any of the sub-system in ATLAS since they rarely interact with matter. However, the presence of neutrinos can be inferred can be inferred indirectly

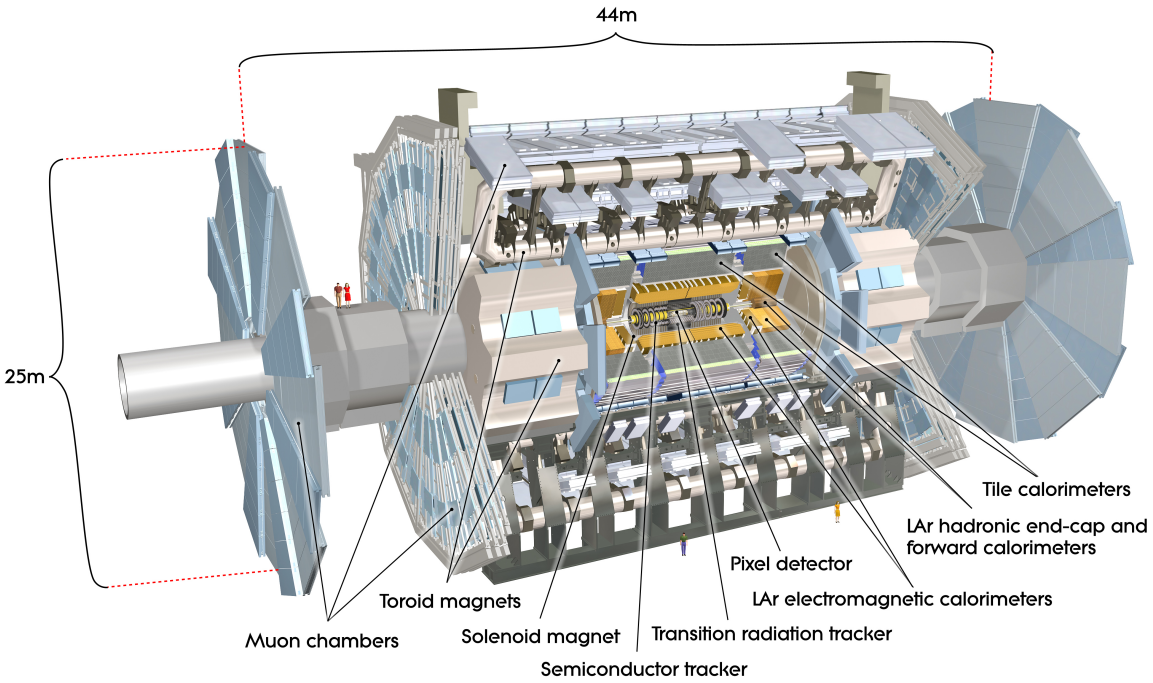

Figure 2.2: An overview of the ATLAS detector and its sub-detectors [64].

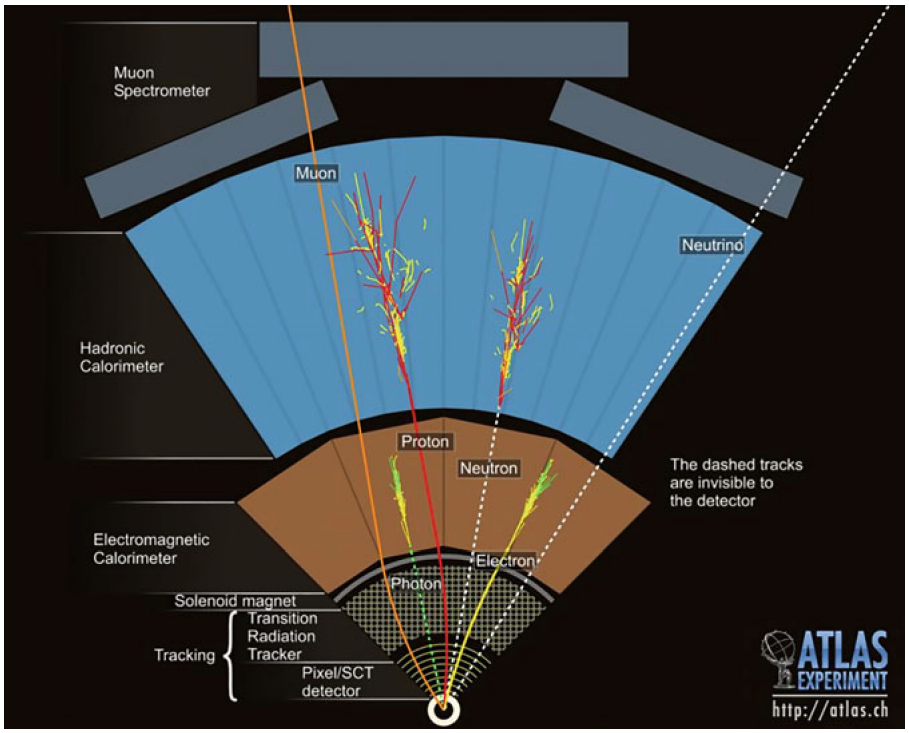

Figure 2.3: Diagram of the detection of different type of particles going from the interaction point through the whole ATLAS detector. Figure taken from [72].

by using the conservation of momentum to calculate the missing momentum in the final decay products. Details of the calculation of the missing momentum are discussed in Section 2.4.1.

2.4.1 ATLAS Coordinate System

ATLAS uses a right-handed coordinate system with the z-axis along the beam pipe and the origin at the interaction point, which is the centre of the detector as shown in Figure 2.4. The positive x-axis points towards the centre of the LHC ring, and the y-axis points upwards. Cylindrical coordinates (ρ,ϕ) are applied in the transverse (xy) plane, where ϕ is the azimuthal angle around the beam pipe, ranging between $-\pi$ and $+\pi$ with respect to the x-axis, and ρ is a measure of the radial distance from the interaction point. Instead of the polar angle θ, which is the angle between the particle three-momentum and the positive z-axis, the pseudo-rapidity, η, is often being considered. Pseudo-rapidity is defined in terms of θ as:

$$\eta = -\ln\tan(\frac{\theta}{2}). \tag{2.4}$$

Table 2.2 shows the corresponding pseudo-rapidity values as a function of θ.

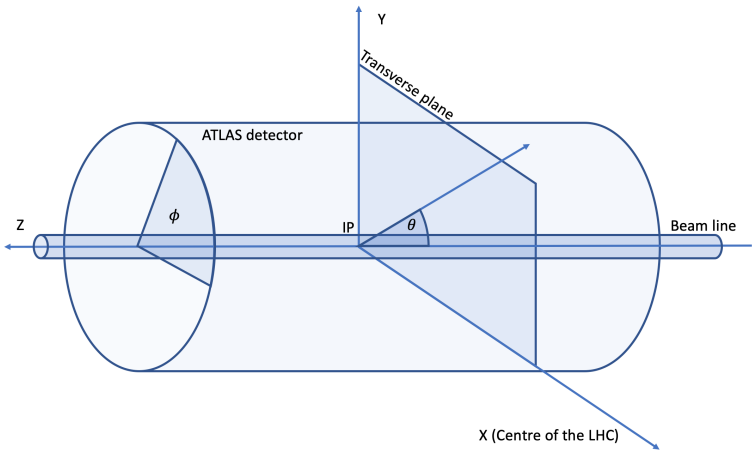

Figure 2.4: The ATLAS coordinate system, where IP is the interaction point.

θ	0°	5°	10°	20°	30°	45°	60°	80°	90°
η	∞	3.13	2.44	1.74	1.31	0.88	0.55	0.18	0

Table 2.2: Pseudo-rapidity versus polar angle values, where $\theta = 0°$ and $\theta = 90°$ lies on z-axis and xy-plane of ATLAS coordinate system, respectively.

The angular separation (ΔR) between objects is defined as:

$$\Delta R = \sqrt{(\Delta\phi)^2 + (\Delta\eta)^2}, \tag{2.5}$$

where $\Delta\phi$ and $\Delta\eta$ are the ϕ and η separation between the objects, respectively.

The projection of variables on the transverse plane with respect to the beam direction are often being used. For instance, the transverse momentum and transverse energy of an object is denoted as P_T and E_T, respectively:

$$P_T = P\sin\theta, \qquad E_T = E\sin\theta. \tag{2.6}$$

These transverse quantities are often used for the object reconstruction.

2.4.2 Inner detector

The inner detector (ID) is the closest sub-system to the interaction point. It has a cylindrical geometry: 6.2 m in length and 2.1 m in diameter. It is immersed in a 2 T magnetic field produced by the surrounding solenoid magnet. The magnetic field is needed in order to bend charged particles for the momentum measurement. The ID is comprised of four detection systems, as shown at Figure 2.5. These are (from nearest to furthest from the beam pipe): the insertable B-layer (IBL), the Pixel detector, the Semiconductor tracker (SCT), and the Transition Radiation Tracker (TRT). SCT and TRT are covering $|\eta| < 2.5$ and $|\eta| < 2.0$, respectively. While a charged particle is travelling though the ID, it leaves a track, which is formed by the hits on silicon or the gas, along its trajectory.

The IBL is the closest sub-detector to the beam pipe. It was installed during the long shutdown 1 (LS1), which was the period between LHC Run-1 and Run-2 (2013 to 2014), to improve tracking and vertexing performance due to the fact that in Run-2 the instantaneous luminosity was doubled with respect to Run-1 [73]. The IBL consists of 14 staves arranged around the beam axis. The staves are flat and arranged at a 14° tilt with respect to the beam axis, as seen in Figure 2.6. Each stave consists of 20 sensor modules distributed along the z-axis. The pixel resolution of the IBL in the $\rho - \phi$,z direction is $8 \times 40\ \mu\text{m}^2$.

Immediately after the IBL is the Pixel detector, which is composed of 3 concentric cylindrical barrels with 3 disks at each endcap. When a charged particle passes though, it leaves a hit on each

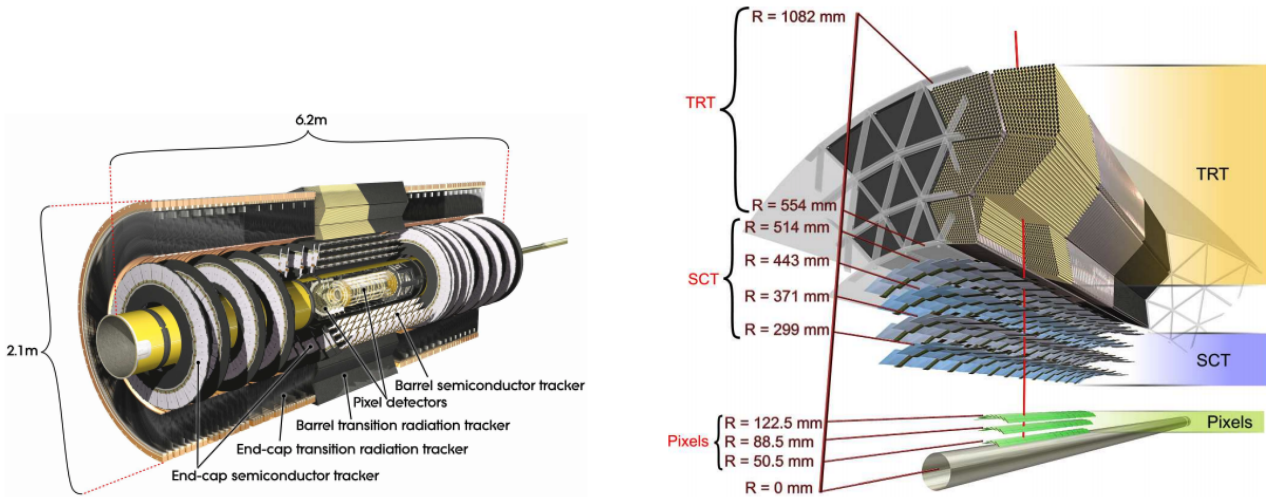

(a) (b)

Figure 2.5: The layout of the ATLAS inner detector with its subsystems labelled in the (a) longitudinal view [64] and (b) the cross-sectional view [64].

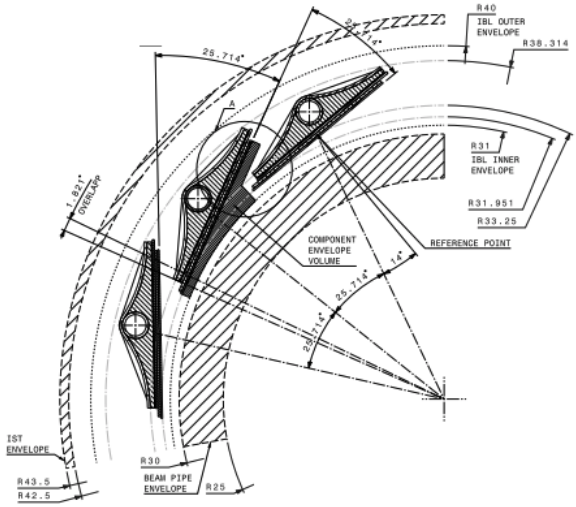

Figure 2.6: IBL structure in transverse plane [73].

pixel layer. The Pixel detector has a resolution of 10 μm in ρ-ϕ plane, 115 μm in z-direction for the barrel region, and 115 μm in ρ for the endcaps.

Surrounding the Pixel detector is the SCT, which is composed of 4 cylindrical layers in the barrel and 9 disks at each endcap. Each barrel layer contains 2 strip layers with different orientations: one parallel to the beam axis, another one offset by 40 mrad. This geometrical arrangement allows for a 2-dimensional coordinate measurement at each layer. A similar setup is applied in the endcap where one strip is radially aligned while the other one is offset by 40 mrad. These layers are arranged in a way that a charged particle would leave 4 hits in the SCT. The design resolution of SCT is 17 μm in

the transverse plane, 580 μm along the z-axis and 580 μm in ρ direction at the endcaps.

The outermost sub-detector system of the ID is the TRT. It is a straw tube tracker of around 300,000 drift tubes, each with a 4 mm diameter. The tubes in the barrel region are 144 cm long and arranged parallel to the beam axis over 73 layers. In the endcaps, the tubes are 37 cm long and arranged over 160 straw plane. The position per straw is 30 μm, and refers only to the transverse plane. The layers of straws are interleaved with polypropylene fibres and foils in the barrel and endcaps, respectively. These material will emit X-rays radiation when ultra-relativistic charged particle passes through them. The X-ray is absorbed by the gas mixture within the tube, which contain 70% of Xenon, 27% of CO_2 and 3% of O_2. Though the resolution is lower than the SCT and Pixel, the TRT is able to make more measurements per track over a longer length, which is beneficial to particle identification, especially in the discrimination of pions against electrons.

2.4.3 Calorimeter

The ATLAS calorimeter system consists of the electromagnetic calorimeter (ECAL) and the hadronic calorimeter (HCAL). The energy of electrons and photons is measured in the ECAL, while HCAL contains the energy deposed by hadronic showers. Each calorimeter system has a barrel region, which is central around the inner tracking system and cylindrical, and two endcap regions, which provide full coverage in ϕ. In order to maximise the coverage of electromagnetic and hadronic showers, the thickness of the ATLAS calorimeter system is required to have at least 10 interaction lengths (λ), which is defined as the average distance required for the energy of particle to reduce by a factor of $\frac{1}{e}$ via hadronic interactions. This requirement ensures a good measurement of the missing energy and also reduce the noise in the muon spectrometer which surrounds the calorimeter system.

The ECAL is a lead-liquid Argon detector, which uses liquid Argon (LAr) as the active medium, with barrel ($|\eta| < 1.475$) and endcap ($1.375 < |\eta| < 3.2$) components. It is placed just outside the ID and surrounded by the HCAL. ECAL, as its name suggested, measures the energy deposited by the electromagnetically interacting particles. It has 1.53 mm and 1.7 – 2.2 mm thick lead absorber plates in barrel and endcaps, respectively. The calorimeter has two to three layers depending on the η range with the 2 mm thick active LAr layer in $|\eta| < 1.8$. The total thickness of the barrel region is approximately equal to 24 radiation lengths (X_0)[1] [74].

[1] One radiation lengths (X_0) is defined as the average distance required for the energy of particle to reduce by a factor of $\frac{1}{e}$ via electromagnetic interactions.

The barrel HCAL is a tile calorimeter, which contains a central barrel for the range $|\eta| < 1.0$ and two extended barrels in the region $0.8 < |\eta| < 1.7$. The sampling material is scintillating plastic tiles and the absorber is steel. The tile calorimeter extends from 2.28 m to 4.25 m radially, and divided in 64 modules along the ϕ direction. The barrel is segmented in three layers with interaction lengths (λ)[2] of approximately 1.5, 4.1 and 1.8 for a total thickness of 7.4 λ at $\eta = 0$ [75].

The hadronic calorimeter in the endcap region is located directly behind the electromagnetic calorimeter. It uses LAr as sampling medium and copper as the absorbers. It contains two independent coaxial wheels on each side of the endcap, each wheel is built from 32 wedge-like copper plate modules and cover the $1.5 < |\eta| < 3.2$ region.

There is another calorimeter located at the endcap region, which is known as the Forward Calorimeter. It covers the range $3.1 < |\eta| < 4.9$ and contains three modules 10 X_0 deep. The first module has copper absorber for electromagnetic measurements, while the outer two modules are made of tungsten 2.6 λ deep.

2.4.4 Muon Spectrometer

The muon spectrometer (MS) is the outermost part of the ATLAS detector. It is because the muons are very penetrating and pass through the whole detector. The muons passing through the MS chambers are deflected by a magnetic field, where the field lines are concentric with the beam axis. The field is generated by three large air-core superconducting toroid magnets, one in the barrel and two in the endcaps regions. The barrel toroid provides 0.5 T magnetic field in the range $|\eta| < 1.4$, while two endcap magnets provide 1T magnetic field in the range $1.6 < |\eta| < 2.7$. Both barrel and endcap toroids provide a relatively low magnetic field in the "transition region", which is the region within the range $1.4 < |\eta| < 1.6$. The barrel MS is constructed by three cylindrical layers parallel to the beam axis, while the endcap contain three disk-shaped layers parallel to the transverse plane.

There are four types of components in the MS and all of them are gas detectors [64, 76]: Monitored Drift Tubes (MDTs), Cathode Strip Chambers (CSCs), Resistive Plate Chambers (RPCs) and the Thin Gap Chambers (TGCs). The MDTs provide tracking measurements in both barrel and endcap regions, with 35 μm z-resolution per tube. The gas mixture used in the MDTs is mixed by 93% of Ar and

[2]Interaction length (λ) is defined as the average distance required for the energy of particle to reduce by a factor of $\frac{1}{e}$ via hadronic interactions

7% of CO_2. The CSCs are located at the first endcap layers, covering the region $2.0 < |\mu| < 2.7$ and providing extra tracking power. The gas mixture used in the CSCs is mixed by 80% of Ar and 20% of CO_2. The resolution of CSCs is 40 μm in ρ and 5 mm in ϕ direction. RPCs and TGCs are used as the muon trigger in the barrel and endcap regions, respectively. They are optimised for time and position resolution. RPCs measure the ϕ and z components of muon with a spatial resolution of 1 cm, while TGCs measure ρ and ϕ components with resolution of 2-3 mm and 3-7 mm, respectively. The gas mixture used in RPCs consists 94.7% of $C_2H_2F_4$, 5% of Iso-C_4H_{10} and 0.3% of SF_6; while the gas in TGCs is mixed by 55% of CO_2 and 45% of n-C_5H_{12} (n-pentane). The time resolution is 1 ns in PRCs, and 4 ns in TGCs.

2.4.5 Trigger system

The LHC beam bunches contain up to 10^{11} protons colliding with the design bunch-crossing rate of 40 MHz. A typical ATLAS event occupies a few MB of disk space and, hence, it is not realistic to store every one of them. In addition, most of the events correspond to well-known processes that are of no interest to the ATLAS physics program. In order to keep events with potential physics interest with the limited amount of storage, a trigger system is employed.

The ATLAS Trigger system consists of a hardware-based level-1 (L1) trigger [77], and a software-based Higher level trigger (HLT) [78]. The L1 trigger searches for events with early reconstructed physical objects based on the measurements from muon trigger chambers and calorimeters then make a decision in less than 2.5 μs. For the needs of the L1 operation, the detector is split in Regions of Interest (ROIs) in η and ϕ, in order to locate the regions of the detector where particle candidates are observed. Once the event has been identified as potentially interesting by the L1 trigger system, its ROI information will be then passed to the HLT. The HLT trigger investigates the ROIs with the full detector geometry, including the tracks from the ID as well as the ROI information from L1 triggers. It takes roughly 40ms to make that decision. The event that passed both L1 and HLT will go offline and further decision will be made in EF, with the processing time about 4 seconds. Eventually, the output rate of the ATLAS Trigger system is about 1 kHz, depending on the data taking period and conditions.

2.5 ATLAS offline software

The analysis of the ATLAS experiment data highly depends on reliable computing, including storage and analysis software. The hardware requirements of the offline computing system are demanded by the high amount of data produced (at ~PB level). All these data have to be stored. Provisions must be made not only for storage, but also for a system that allows collaborators to access the data from around the world. Equally important is the offline software system, which is responsible for the reconstruction of the physical objects, their calibration and the physics analysis. This section represents a brief overview of the ATLAS storage and analysis framework.

2.5.1 The Computing Grid

The Worldwide LHC Computing Grid (WLCG) [79] is used to store and process the large amounts of simulated and recorded data which are produced by the ATLAS detector. The WLCG is divided into three different types of computing sites: Tier 0, Tier 1 and Tier 2. Tier 0 is the centre of the WLCG. Any collision event passing the trigger(s) of an LHC experiment will be sent to the Tier 0 facility at CERN. The Tier 0 will execute a first-pass processing of the detector data (RAW data) using experiment-specific reconstruction algorithms. The reconstructed datasets, often called "AOD" (Analysis Object Data), are subsequently distributed among the Tier 1 sites to make them available for user analysis and reprocessing like calibration. Once the primary AOD is fully calibrated and aligned, it would be derived into smaller subset called "DAOD" (derived AOD datasets). Specific events of interest are selected to store into the DAOD, any unnecessary information are dropped. It can effectively reduce the number of events and reduce the event size to run over during the analysis. Also, DAODs are more tuned into specific physics or detector projects, for instance electron identification calibration. Tier 1 facilities provide access to reconstructed detector data as well as simulated event data. Each Tier 1 site stores some fraction of the AOD, and it will be responsible for reprocessing this data in a reprocessing campaign. The UK Particle Physics Grid (GridPP) [80] is one of the Tier 1 facilities across the UK. Tier 2 Facilities are mainly used to process physics analysis and simulation jobs. About 170 Tier 2 sites are currently being hosted by various institutes around the world. Tier 2 sites differ in size an capacity and thus each site has a specific role which will differ from the roles of other Tier 2 sites. An institute hosting a Tier 2 site that is also involved in a particular physics analysis, will usually use their local Tier 2 to process and store the corresponding analysis jobs and

DAODs. For instance, University of Liverpool is one of the institutes hosting the Tier 2 facilities which is shared between institutes across the northern England.

2.5.2 Analysis Software: Athena

Athena is the ATLAS common analysis software, which provide a wide range of physics data-processing applications [81]. It is based on the GAUDI framework [82], which is a software architecture is originally developed for LHCb. Athena has a component[3]-based architecture which allows flexibility in developing both a range of shared components and, where appropriate, components that are specific to the particular experiment and better meet its particular requirements. Beside the usage in the main analysis, Athena can be used in event generation, the High Level Trigger, detector environment simulation and DAOD generation.

2.5.3 Detector Simulation

The detector simulation is needed for the physics analysis in order to simulate the ATLAS detector response. At this stage, interactions of final state particles with the detector are simulated, including displaced vertices for long-lived particles, shower evolution in the calorimeters and pileup. There are two types of simulations in ATLAS, a full simulation and a fast simulation. The full simulation is performed using GEANT4 [83], which is a toolkit used for the simulation of the passage of particles through matter. The tool uses a complete description of the detector and models the trajectories of every particles passing through the detector. The fast simulation aims to speed up the slowest part of the full simulation. To achieve this, the low energy electromagnetic particles are removed from the calorimeter and replaced with pre-simulated showers stored in memory [84]. In this thesis, both full simulation and fast simulation of the ATLAS detector are used.

[3]Component: a block of software

CHAPTER 3

Data, Simulation, Object Reconstruction and Object Identification

The data collected by ATLAS detector do not come from a single process. In order to understand what kind of processes are included in the collected data, simulated samples for both the signal and background processes are employed. In the search preformed in this thesis, $A \rightarrow ZH \rightarrow \ell\ell bb$ is the signal process while the standard model processes with $\ell\ell bb$ final state are considered as background.

In addition, the elementary particles that are used in LHC physics results are not directly observed in the ATLAS detector. The particles are detected though their interaction to the sub-systems of the ATLAS detector. The unstable collision products almost instantly decay into relatively stable particles, which pass through the sub-systems of the ATLAS detector and leave indications of their passage. In order to search for the particles which are produced in the collision, effective reconstruction and identification algorithms are needed.

The aim of this chapter is to describe the simulated samples that are used to understand the data collected by the ATLAS detector and are employed in this thesis. The algorithms that are used to reconstruct physics objects using these data are also discussed.

3.1 Data and simulated samples

The data samples used in this thesis as well as an overview of the Monte Carlo (MC) generators used to produce simulated samples for signal and background processes is given in this section. All simulated background samples are passed through the full simulation of the ATLAS detector produced in GEANT4 [83], with both the data and simulated samples reconstructed using the same software.

The simulated $A \to ZH \to \ell\ell bb$ signal samples with different m_A and m_H were passed through the ATLAS fast simulation framework[85].

In the search for $A \to ZH \to \ell\ell bb$, the main sources of backgrounds are Z+jets and top-quark-pair production ($t\bar{t}$). Other background processes, including diboson (VV), single top, the SM Higgs boson production in association with a Z boson (Vh), and the top-quark-pair production in association with a vector boson (ttV), are also considered.

3.1.1 Data

The data used for the analysis in Chapter 5 was collected by the ATLAS detector during the 2015 and 2016 running periods, with the LHC operating at a centre-of-mass energy of $\sqrt{s} = 13$ TeV. The cumulative integrated luminosity versus time delivered by the LHC and recorded by ATLAS during the periods are shown in Figure 3.1. The selected data events were required to have all the relevant components of the ATLAS detector running in good working condition. They correspond to a total integrated luminosity of 36.1 fb^{-1}. This data are also used in the flavour tagging calibration study in Chapter 4. For the analysis described in Chapter 6, the data was collected by the ATLAS detector at the LHC between 2015 and 2018 running periods, corresponding to an integrated luminosity of 139 fb^{-1} as shown in figure 3.1(c).

Besides the luminosity, the number of interactions per bunch crossing also increases after combining data collected during 2017 and 2018. The number of interactions per bunch crossing, $< \mu >$, corresponds to the mean of the Poisson distribution of the number of interactions per crossing calculated for each bunch. Figure 3.2 shows the $< \mu >$ value for the data which is collected by the ATLAS detector at the LHC during the 2015 to 2016 running period and the 2015 to 2018 running period. The $< \mu >$ value is 23.7 for data collected during the 2015 to 2016 running period, while it is 33.7 after combined the 2017 and 2018 data.

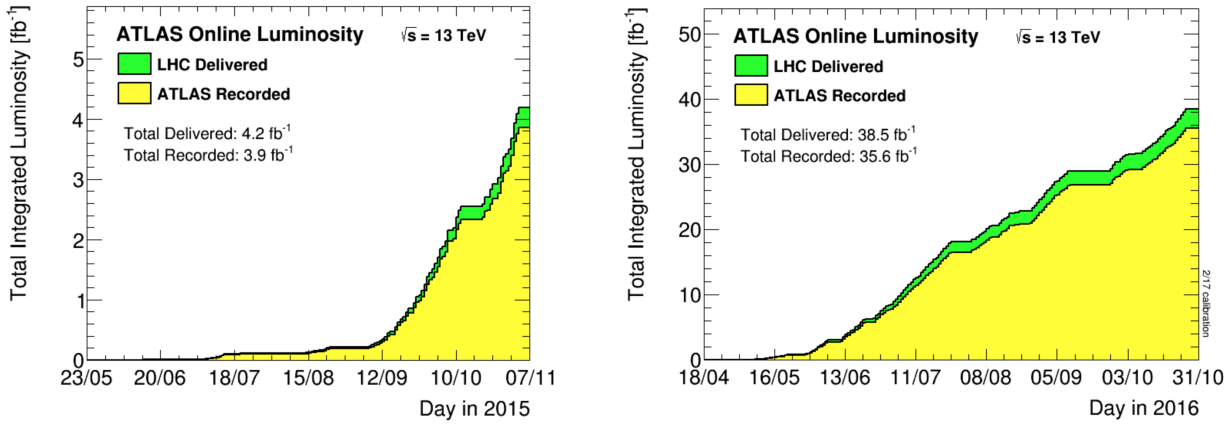

(a) (b)

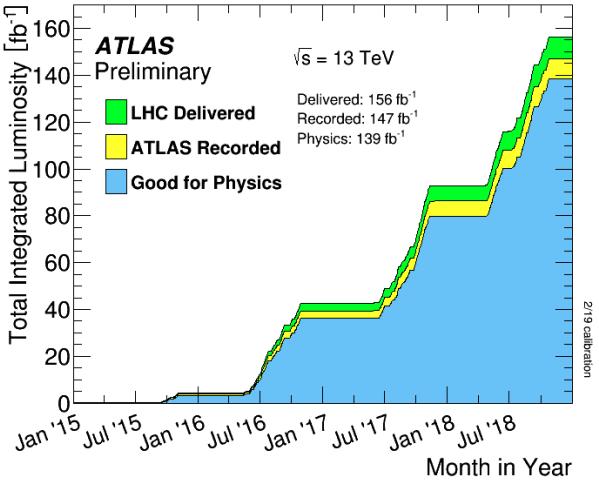

(c)

Figure 3.1: The cumulative luminosity versus time delivered by the LHC (green) and recorded by ATLAS (yellow) for (a) 2015 [86] and (b) 2016 [87]. In (c), the cumulative integrated luminosity is shown versus time delivered by the LHC (green), recorded by ATLAS (yellow) and good quality data (blue) for data in the 2015 to 2018 running period.

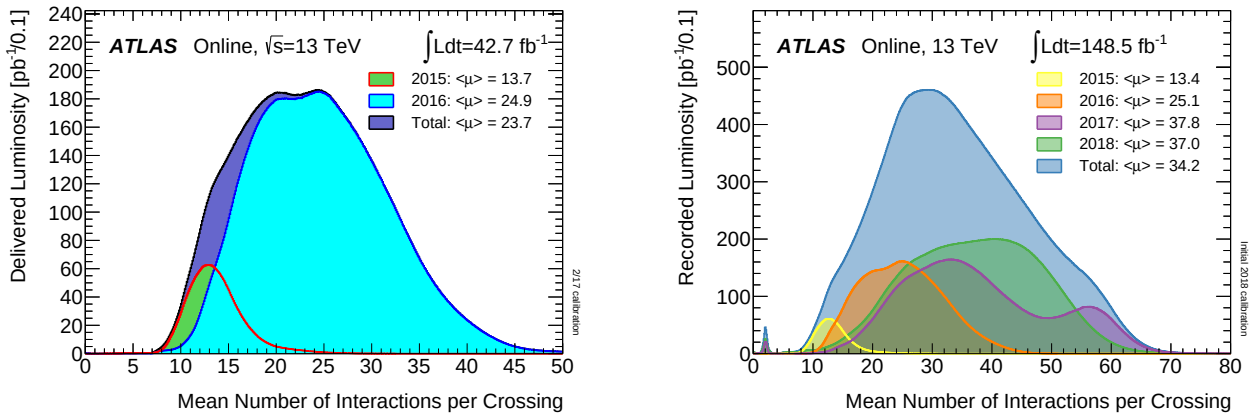

(a) (b)

Figure 3.2: The number of interactions per bunch crossing in the data collected by the ATLAS detector at the LHC during the (a) 2015 to 2016 running period and (b) 2015 to 2018 running period. Taken from Ref. [70].

3.1.2 Simulated samples

The simulation of signal and background processes is performed using Monte Carlo methods over a series of stages of computation. There are two main steps in the Monte Carlo simulation:

1. Simulation of the hard interactions. The hard interaction is simulated by calculating the matrix element at either leading order (LO) or next-to-leading order (NLO) in perturbation theory. The intermediate particles are decayed according to their branching ratios.

2. Parton showering. This is a process which the coloured partons radiate further partons and end up with colorless hadrons. It is necessary in order to see how the resulting partons evolve after the hard interactions.

Signal samples for $A \to ZH \to \ell\ell bb$

The heavy boson A that is searched for here is mainly produced via gluon-gluon fusion (ggA) and b-associated production (bbA). Examples of the lowest order Feynman diagrams for these processes are shown in Figure 3.3. Subsequently, the A boson decays to a Z boson and an H boson. Finally, the Z boson further decays into the dilepton system, $\ell\ell$, and the H boson further decays into bb. The signal samples are generated assuming various choices for m_A and m_H. The mass range is 230 GeV – 800 GeV for m_A and 130 GeV – 700 GeV for m_H. The m_A, m_H values of the simulated signal points are shown in figure 3.4. The ggA samples are generated using Madgraph5 [88] while the bbA

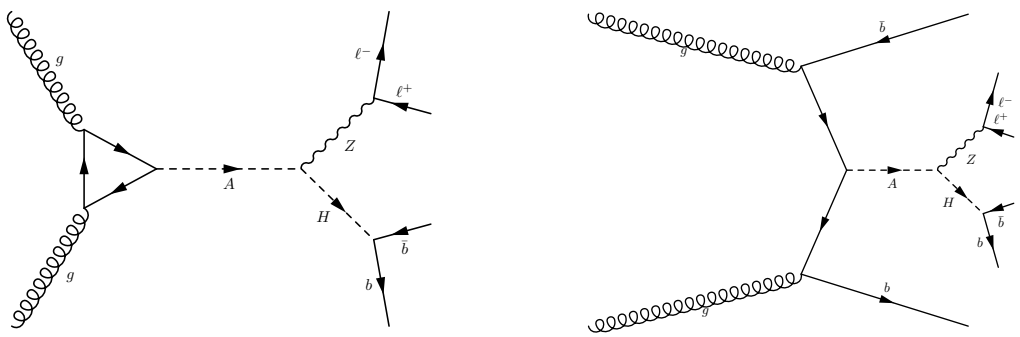

Figure 3.3: The examples of the lowest order Feynman diagrams for (a) gloun-gloun fussion (ggA) and (b) b-associated production (bbA).

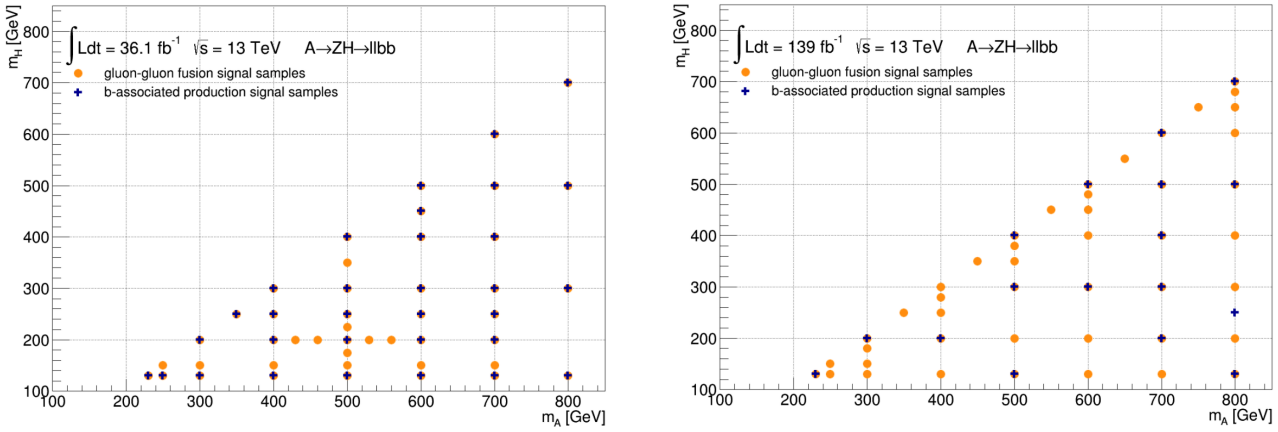

Figure 3.4: The simulated m_A and m_H signal points probed in the analysis for both ggA and bbA mechanism with total integrated luminosity of (a) 36.1 fb^{-1} and (b) 139 fb^{-1}.

samples are generated using a dedicated implementation of the process in MG5_aMC@NLO [89]. The showering and hadronization has been done using Pythia8 [90]. Both narrow and large width ggA samples are generated. For the large width samples the width choices are 5%, 10% and 20% as a fraction of mA. Such widths are relevant in the decoupling limit, with $\tan\beta$ values in the range from 1 to 20.

Background simulated samples

In the $A \to ZH \to \ell\ell bb$ analysis which will be discussed in Chapters 5 and 6, the event generation for $W/Z+$ jets processes employ Sherpa 2.2.1 [91] with the NNPDF3.0NNLO PDF set [92]. Top-quark pair production, $t\bar{t}$, is simulated with PowHeg-BOX v2 [93–95] framework and the CT10nlo PDF set [96]. The single-top-quark production is simulated with PowHeg-BOXv1 and CT10nlo_f4

PDF set [96] for all the three production modes (t-channel, Wt-channel and s-channel). The parton shower is performed with Pythia 6.428 [97] using the Perugia 2012 set of tuned parameters [98]. The ttV processes are simulated using Madgraph5_aMC@NLO 2.2.3 and the NNPDF3.0NLO PDF set, whereas PYTHIA8.186 is used for the parton shower. VV processes are simulated using Sherpa2.1 and the NNPDF3.0NNLO PDF set. The production of Vh is generated using Pythia8 with POWHEG-BOX and the NNPDF3.0NLO PDF set, whereas the parton shower is performed with Pythia 8.186 using the AZNLO tune [99]. Figure 3.5 shows the colour code used for the background simulated samples in the pre-fit plots in Chapter 5 and 6. Pileup events are simulated using the soft QCD processes implementation in Pythia8 with the A2 tune [100] and the MSTW2008LO PDF set [101]. Finally, an event-level re-weighting is performed to ensure that the distribution of the number of interactions per bunch crossing in data matches the one in simulation.

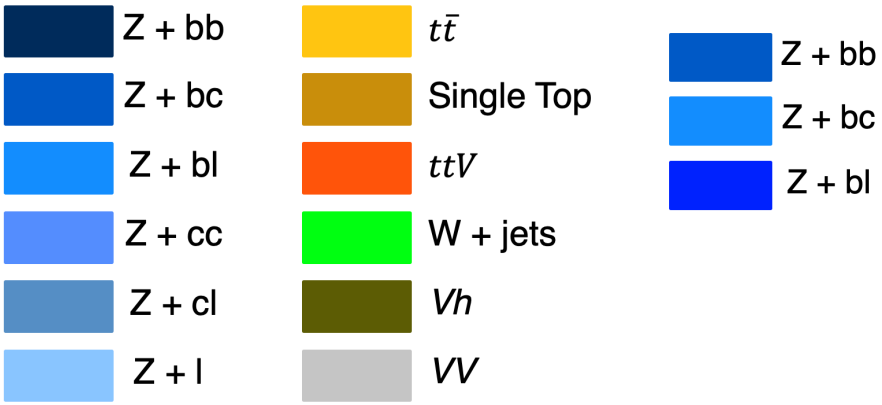

(a) (b)

Figure 3.5: Colour code for the background simulated samples in the pre-fit plot shown in Chapter 5 and 6. (a) The colour code used in Chpater 5, (b) The colour code for simulated Z+bb, Z+bc and Z+bc samples used in Chapter 6, while other simulated samples are using the same colour code as shown in (a).

3.2 Track and Vertex Reconstruction

Tracks are one of the most basic elements used for particle reconstruction in ATLAS. They are reconstructed from hits in the inner detector. Pixel and SCT hits are clustered to improve the accuracy of the position measurement and to reduce the noise. After cluster creation, the track-finding algorithm searches for three-point tracks in the silicon detectors [102]. These are extrapolated into the outer regions of the tracking detector by iteratively associating new clusters to the track and updating the

track parameters. This algorithm is designed to find charged particles emanating from the collision point. The hits from the TRT are combined in an opposite direction, as they are extrapolated towards the silicon detectors by a back-tracking algorithm. This algorithm finds tracks which do not originate from the interaction region. The tracks reconstructed by the track-finding algorithm are required to have transverse momentum $p_T > 400$ MeV. The space coordinates of a track are also important. They are described by the shortest distance in transverse and longitudinal direction between the interaction point and the track. These are also known as the transverse and longitudinal impact parameters, which are respectively denoted as d_0 and z_0.

Another basic element used for particle reconstruction in ATLAS are vertices. The point where the hard scattering occurred is the primary vertex. If the particles produced in the primary vertex are long lived to decay further away, a secondary vertex is formed. Vertices are reconstructed using an iterative vertex finding algorithm [103]. Vertex reconstruction proceeds by calculating the crossing point of several tracks and iteratively adding or discarding all tracks that are respectively compatible or incompatible with originating from this crossing point. In this process, the vertex position is updated with each change of the track association. Primary vertices are always within the interaction region, whereas secondary vertices are usually not. Secondary vertices are crucial information for heavy flavour identification, since heavy flavoured hadrons usually have long lifetimes, such that they can decay several millimetres from the collision point. The SCT secondary vertex radial resolution is typically around 0.2 to 0.3 mm. This is designed to reach the expected mean decay length for long-lived particles. The lifetime of a B_0 meson is about $\tau = 1.520 \times 10^{-12}$s [17]. For a B_0 meson with mass $= 5279.58$ MeV and a momentum of $p = 10$ GeV, the expected flight length is expected to be about 0.8 mm, which is a measurable distance through the detector before decaying. This distance can be seen in Figure 3.6, where it is labelled as L_{xy}.

The impact parameter often classified by their sign, which is called “signed impact parameter”. The sign of the impact parameter is based on the angular momentum projection on the z axis. In the case with the jet axis, the sign can be determined by the angle between the jet and the line between the primary vertex and the point of the closest approach of the track, as shown in Figure. 3.7. In this sketch, “1. Vertex” is the primary vertex, and the $|\delta|$ is the impact parameter. The sign of this impact parameter is decided by the angle α. The signed impact parameter is one of the key elements for heavy flavour identification, which will be discussed in section 3.5.

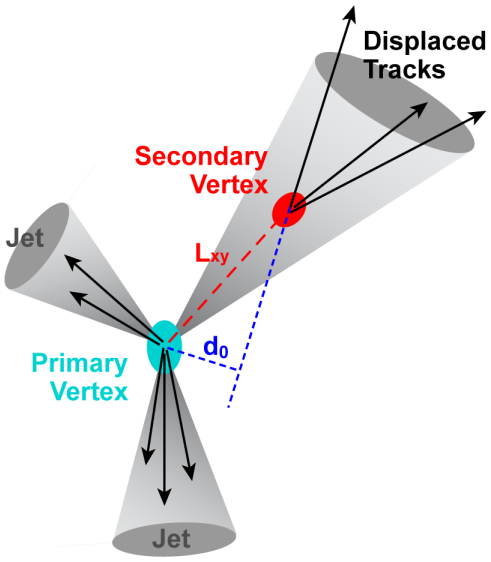

Figure 3.6: Diagram of an event with a secondary vertex. The long-lived particle decay occurs at the secondary vertex at a distance L_{xy} from the primary vertex. The distance labelled d_0 is the transverse impact parameter; this has a large value for B_0 meson. Taken from Ref. [104].

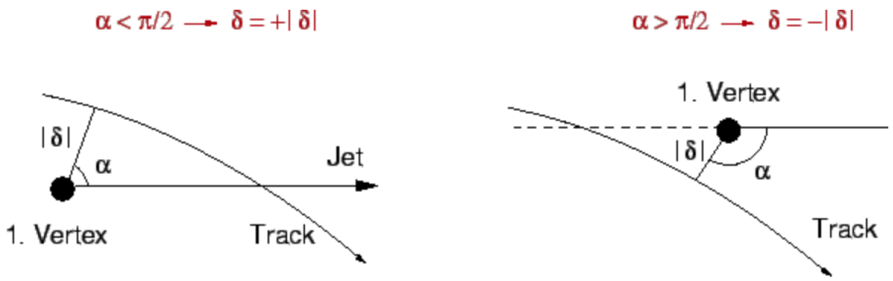

Figure 3.7: Sketch of the impact parameter reconstruction. The sign of the impact parameter is based on the angle between the jet and the line between the primary vertex and the point of the closest approach of the track. The two cases for (left) a positive sign and (right) a negative sign are shown. Taken from Ref.[104].

3.3 Electrons and Muons

Electrons are reconstructed by matching energy deposits in the ECAL with tracks in the inner detector. A likelihood method is applied on several variables derived from calorimeter clusters, tracking and combined cluster-tracking information in order to define three levels of electron identification [105]. These identification levels are denoted as Loose, Medium and Tight, and have progressively higher background rejection power at a cost to electron efficiency. Only candidates within $|\eta| < 2.47$ (excluding the crack region[1]) with $p_T > 7$ GeV are considered. All electrons must at least satisfy the

[1]Crack region is the transition region between the barrel and endcup calorimeters, within $1.37 < |\eta| < 1.52$.

loose identification criteria in the analysis outlined in this thesis. Figure 3.8 shows the electron identification efficiency measured with $Z \to ee$ events using 2016 data as a function of E_T and η for all identification levels are shown. The identification efficiency varies from 55% at E_T = 4.5 GeV to 90% at E_T = 100 GeV for the Tight operating point. For the Loose operating point, the identification efficiency varies from 85% at E_T = 20 GeV to 96% at E_T = 100 GeV.

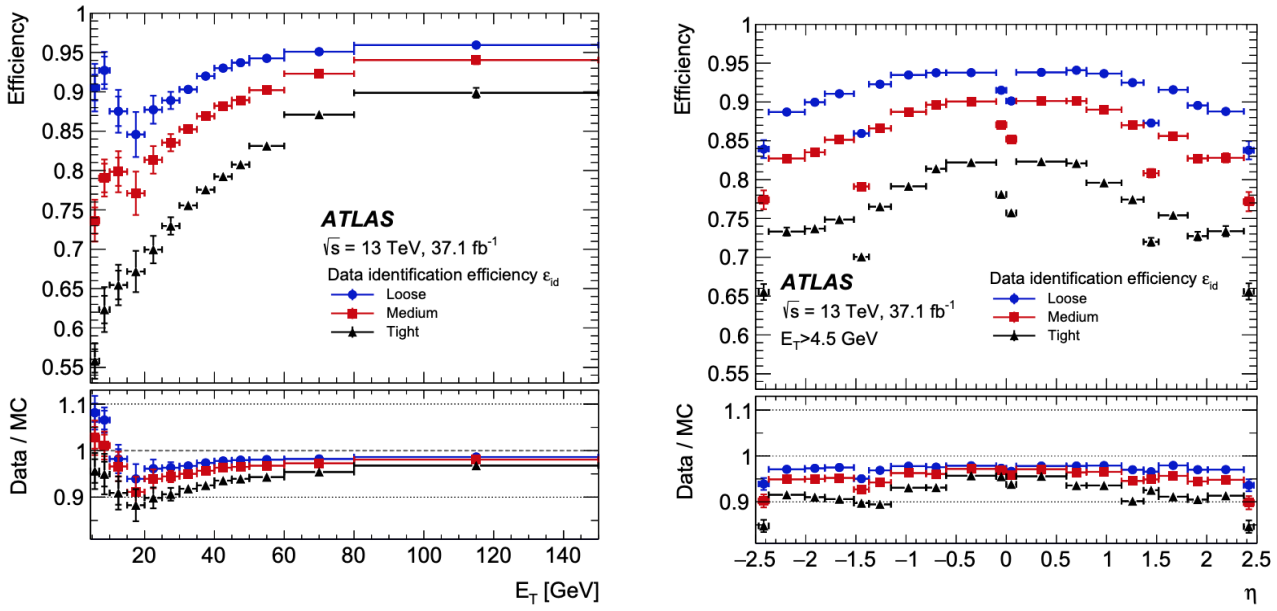

(a) (b)

Figure 3.8: Measured electron identification efficiencies in $Z \to ee$ events for the Loose (blue circle), Medium (red square), and Tight (black triangle) operating points as a function of E_T (a) and η (b). The vertical uncertainty bars (barely visible because they are small) represent the statistical (inner bars) and total (outer bars) uncertainties. For both plots, the bottom panel shows the data-to-simulation ratios. Reproduced from Ref.[105].

Muons are identified by matching tracks in the ID with tracks in the MS. Muon identification is performed by applying quality requirements in order to suppress backgrounds, mainly the pion and kaon decays in flight, while selecting muons with a robust momentum measurement. There are four identification working points recommended in Ref. [106]: Loose, Medium, Tight and High-p_T. All muons must at least satisfy the loose identification criteria with $p_T > 7$ GeV in the analysis outlined in this thesis. Figure 3.9 shows the muon identification efficiencies at medium and loose working points as a function of η. The identification efficiency varies from 60% at $|\eta| < 0.1$ to around 99% in $0.1 < |\eta| < 2.5$ for the Medium operating point, while the efficiency for Loose operating point is 96% at $|\eta| < 0.1$ [106].

In addition to the identification requirements, electron and muon isolation requirements are applied to reject electrons and muons originating from hadronic decays, narrow jets or hadrons that pass through the calorimeters so that to leave tracks in the MS. The isolation requirement consists of a restriction on the sum of the calorimetric energy deposits around the candidate muon track relative to the muon transverse momentum. The efficiency for Loose operating point is 99% [105].

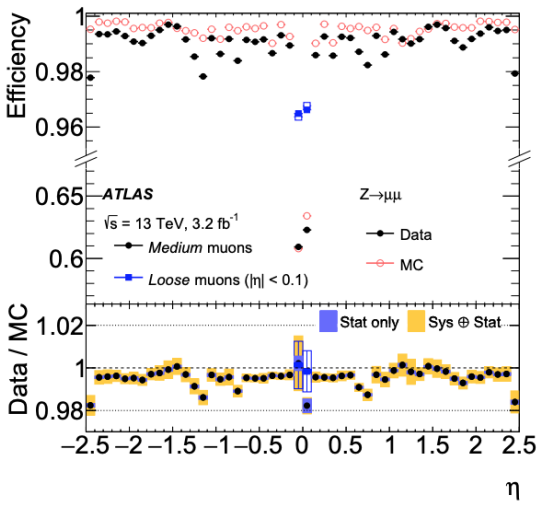

Figure 3.9: Muon reconstruction efficiency as a function of η measured in $Z \to \mu\mu$ events for muons with $p_T > 10$ GeV shown for Medium (black dots) and Loose (blue squares) muon operating points. The error bars on the efficiencies indicate the statistical uncertainty. The bottom panel shows the ratio of the measured to predicted efficiencies, with statistical and systematic uncertainties [106].

3.4 Jets

The term jet refers to the group of collimated particles resulting from the fragmentation and hadronization of gluons and quarks. Jets are reconstructed using the anti-k_T algorithm with distance parameter R = 0.4 [107]. Jets from the decay of heavy-flavour B-hadrons, C-hadrons and from the decay of light-flavour hadrons are defined as b-jets, c-jets and light-jets, respectively. Different types of input objects are used in the anti-k_T algorithm to reconstruct different types of jets. In ATLAS, calorimeter jets (calo-jets) are reconstructed using topological clusters and PFlow jets using particle flow objects.

3.4.1 Calorimeter Jets

The reconstruction of calo-jets requires topological clusters [108], which are collections of calorimeter cell signals calibrated at the electromagnetic (EM) energy scale[2]. The cluster formation begins with a seed cell and builds a cluster by iteratively adding neighbouring cells, providing these cells have significant energy relative to the expected noise. This is performed by an algorithm that uses the ratio of the cell signal to the average noise to decide the threshold of seed (ratio = 4), growth (ratio = 2) and boundary (ratio = 0) of one cluster. Once the seed cell is located, the ratio of every cells nearby the seed cells are examined. This process is repeated until all topologically connected cells passing the seed, growth and boundary conditions criteria are found. Individual clusters represent the full or fractional response to a single particle (full shower or shower fragment), the merged response of several particles, or a combination of merged full and partial showers, depending on the incoming particle types, energies, spatial separations and cell signal formation.

The calo-jets are reconstructed by using topological clusters as the input of anti-k_T algorithm with a jet radius parameter of 0.4 [107]. The measured jet energies are corrected based on the area of the jet to reduce the effects due to additional proton-proton interactions in the same or neighbouring bunch crossings (pileup) and the underlying event.

The jet energy at the hadronic scale is then obtained by applying calibration factors depending on transverse momentum and pseudorapidity. Inner detector tracks are associated with the calorimeter jets based on their distance in (η, ϕ) space. Calo-jets entering the analysis outlined in this thesis are required to have a transverse momentum $p_T^{jet} > 20$ GeV and to be within the acceptance of the inner detector, limited to $|\eta^{jet}| < 2.5$, where tracking is possible.

In order to reduce the contamination of jets arising from additional pileup interactions, the jet-vertex tagger tool (JVT)[109], building a 2-dimensional likelihood from tracking and vertexing information, is used. For calo-jets, the JVT output score is required to be greater than the 0.59 with conditions $p_T^{jet} < 60$ GeV and $|\eta^{jet}| < 2.4$, which corresponds to the medium JVT working point [109].

[2]This scale reconstructs the energy deposited by electrons and photons correctly but does not include any corrections for the loss of signal for hadrons in the ATLAS calorimeters [108]

3.4.2 Particle Flow Jets

Particle flow (PFlow) objects can be used as an alternative input for jet reconstruction instead of topological clusters. Unlike the topological clusters, the PFlow algorithm reconstructs the particles in an event such as electrons, muons and hadrons. In order to produce a PFlow object, both tracks and topological clusters are used as an input to the PFlow algorithm in order to produce a new set of clusters, PFlow clusters, using a procedure that is summarised in figure 3.10 and Ref.[110].

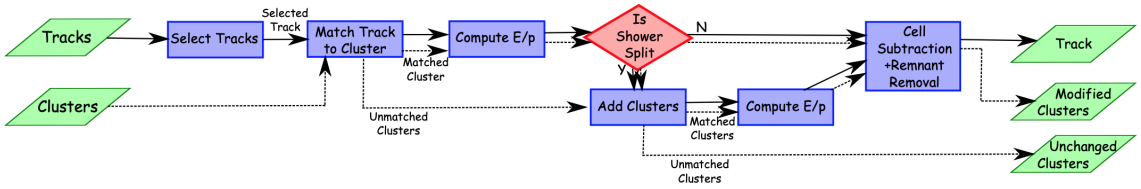

Figure 3.10: A flow chart of how the particle flow algorithm proceeds. E/p is the ratio between energy of the cluster and the momentum of the tracks. Taken from [110].

The PFlow jets are reconstructed employing the anti-k_T algorithm with $R = 0.4$ taking both tracks and calorimeter measurements as input. The energy deposited in the calorimeter by all the charged particles is removed, and then the jet reconstruction is performed on the PFlow objects. These objects consist of the remaining calorimeter energy and tracks which are matched to the hard interaction. For any particle whose track measurement has been used, the corresponding energy must be subtracted from the calorimeter measurement.

The track information also contributes to the pile-up rejection since the tracks considered in the reconstruction, it is possible to search for the existence of its associated vertex. Therefore, the effect of the additional particles in the pile-up interactions can be reduced by examining their vertices. In addition, the JVT also applied to the PFlow jets with the JVT output greater than 0.5 for jets with $p_T^{jet} < 60$ GeV and $|\eta^{jet}| < 2.4$ [109].

3.5 Identification of b-jets

A jet that contains a B-hadron is defined as a b-jet. The process of b-jet identification (b-tagging) in the ATLAS experiment is based on a set of basic b-tagging algorithms relying on the reconstruction of track impact-parameters, secondary vertices, and decay chain multi-vertices. The output of these

basic algorithms is then combined into a multivariate discriminant, trained for the optimal separation between b-jets and the jets originating from the other flavours [111]. The output of the algorithm is also used to select samples that are enriched in light or c-jets. The calibration of the b-tagging efficiency will be discussed in Chapter 4.

In order to achieve a better discrimination than any of the basic algorithms can exploit individually, a Boosted Decision Tree (BDT) algorithm, referred as MV2 in the following, using the ROOT Toolkit for Multivariate Data Analysis (TMVA) [112], is employed. The distribution of the input variables are shown in Figure 3.11, 3.12 and 3.13. The most commonly used version for ATLAS analyses during 2015 to 2016 is labelled as MV2c10 used 90% light- and 10% c-jets in the training. The performance of the b-tagging algorithm is characterised by the b-tagging efficiency (ε_b), which is the probability of tagging a b-jet correctly, with the mis-tagging efficiency of c-jets (ε_c) and light-jets (ε_{light}), which is the probability of mistakenly tagging a c-jet and light-jet as a b-jet, respectively. Several working points are defined with different b-tagging efficiencies, as shown in Table 3.1. In this table, the rejection rates for light-flavour jets and c-jets are defined as the inverse of the efficiency for tagging a light-flavour jet or a c-jet as a b-jet, respectively. Figure 3.14 shows the MV2c10 BDT performance which is calibrated with respect to the $t\bar{t}$ events from the 2016 ATLAS dataset [111]. For the analysis outlined in this thesis, the 70% b-tagging efficiency working point is used.

Working Point	MV2c10 score	ε_b [%]	c rejection rate	light rejection rate
85%	0.11	85.23	2	28
77%	0.64	77.53	4	113
70%	0.83	70.84	8	313
60%	0.94	61.14	22	1204

Table 3.1: MV2c10 working points with the corresponding MV2c10 score, which is the discriminant from MV2 algorithm, b-tag efficiency, c-jet rejection rate and light-jet rejection rate. Results based on the calo-jet from $t\bar{t}$ process [113].

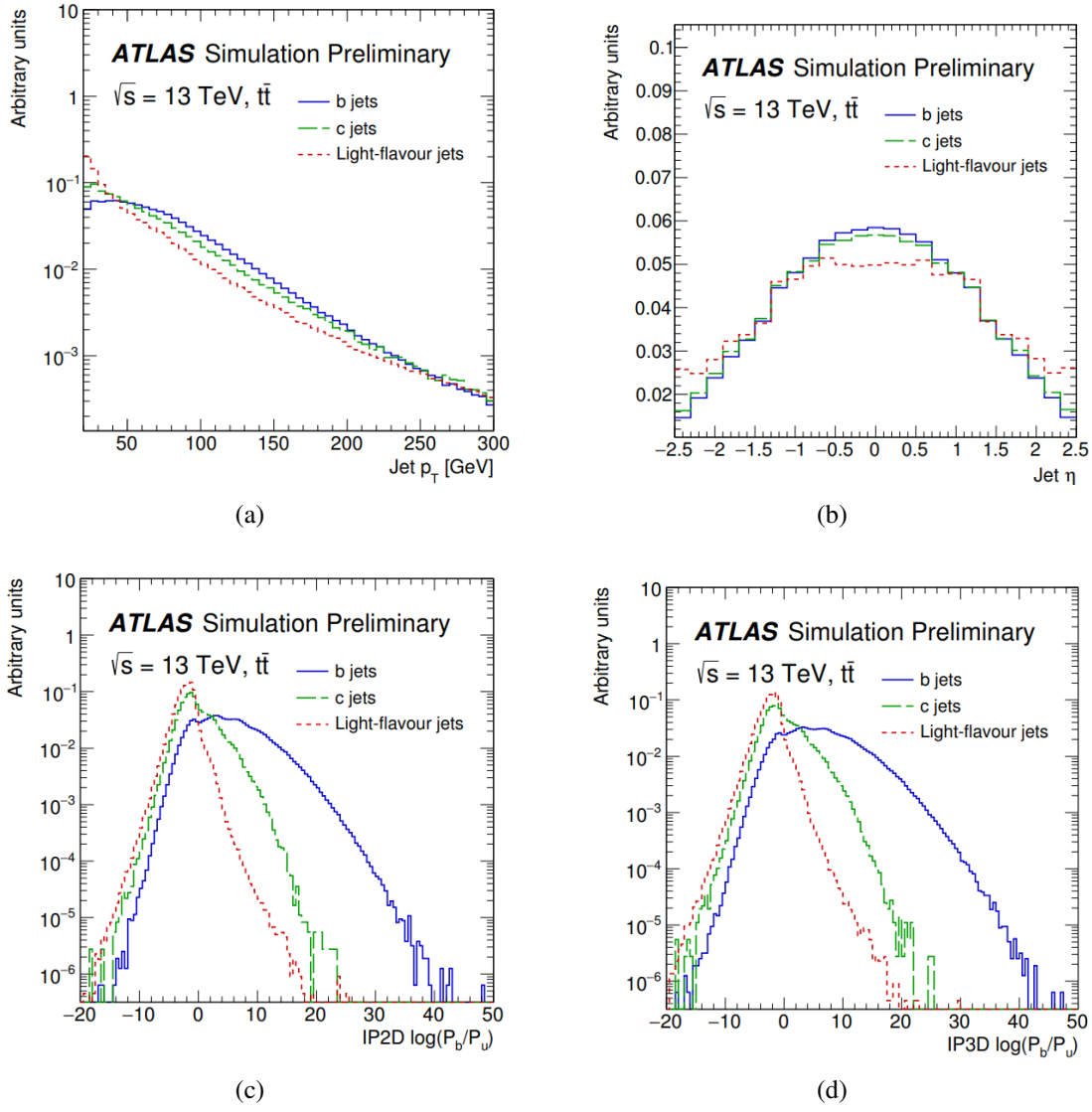

Figure 3.11: The distribution of MV2c10 BDT input: (a) The p_T and (b) η distributions of the jet, the log-likelihood ratio for the basic b-tagging algorithm which based on the (c) 2D and (d) 3D reconstruction of track impact-parameters. Distribution from b-jet, c-jet and light-jet are shown. Reproduced from [111].

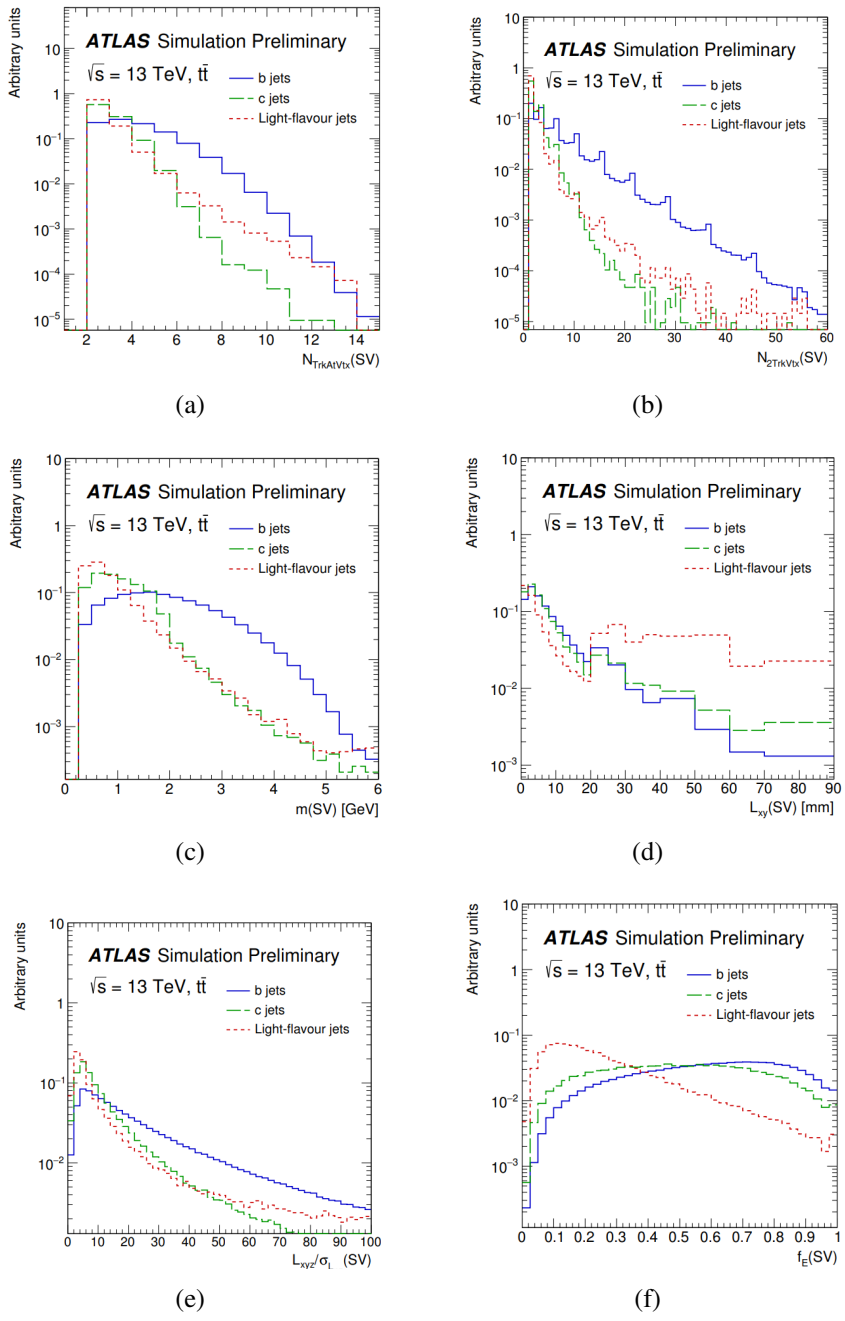

Figure 3.12: The distribution of MV2c10 BDT input: (a) The number of tracks, (b) the number of two-track vertices reconstructed within the jet, (c) the invariant mass, (d) the transverse decay length, (e) the 3D decay length significance and (f) the energy fraction, defined as the energy of the tracks in the displaced vertex relative to the energy of all tracks reconstructed within the jet. Distribution from b-jet, c-jet and light-jet are shown. All these variables are used in the secondary vertices-based algorithm. Reproduced from [111].

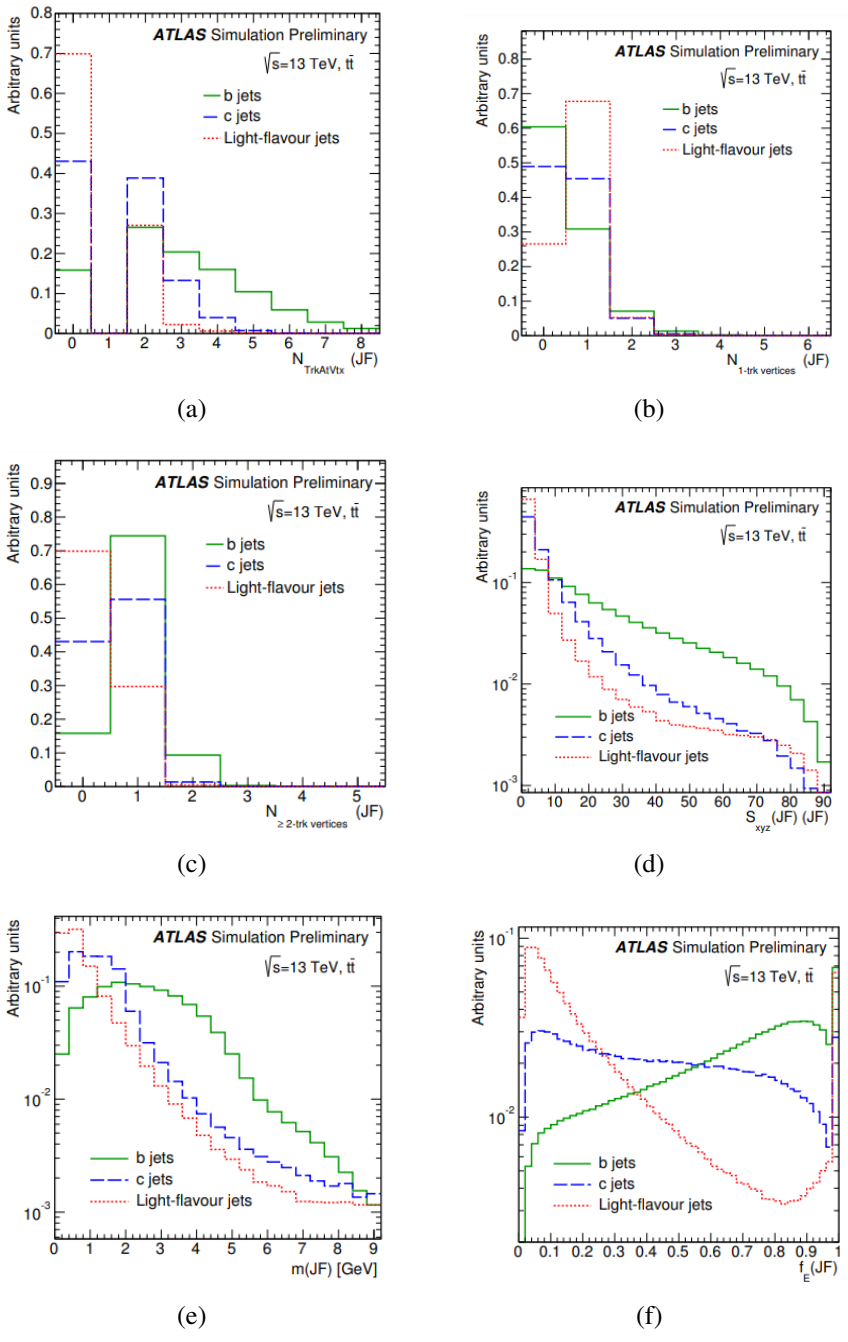

Figure 3.13: The distribution of MV2c10 BDT input: (a) The number of tracks from vertex, (b) the number of 1-track vertices, (c) the number of tracks from vertices with at least two tracks , (d) the average flight length significance of the reconstructed vertices, (e) the invariant mass of tracks fitted to one or more displaced vertices and (f) the energy fraction. Distribution from b-jet, c-jet and light-jet are shown. All these variables are used in the decay chain multi-vertices based algorithm. Reproduced from [111].

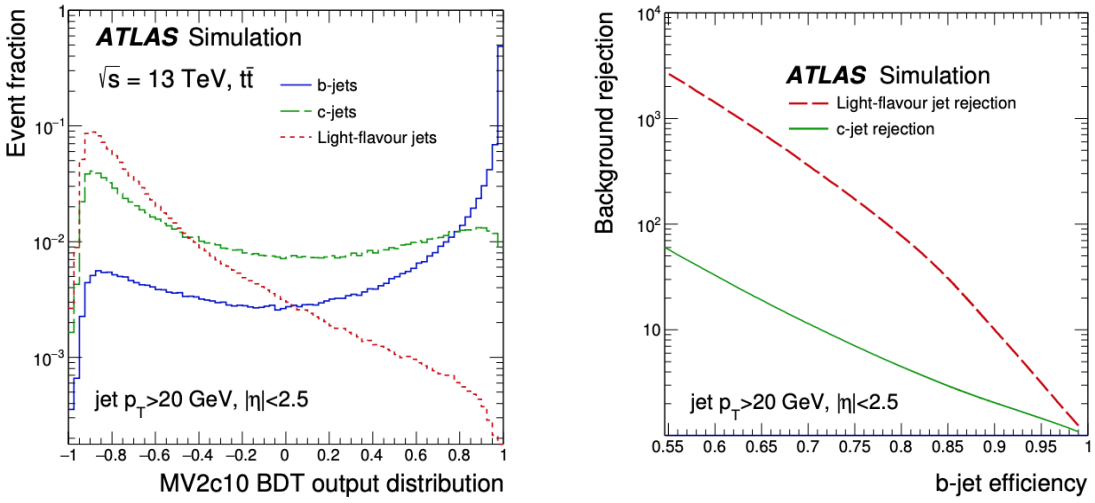

(a) (b)

Figure 3.14: (a) MV2c10 BDT output for b- (solid blue), c- (dashed green) and light-flavour (dotted red) jets evaluated with $t\bar{t}$ events. (b) The light-flavour jet (dashed line) and c-jet rejection factors (solid line) as a function of the b-jet tagging efficiency of the MV2c10 b-tagging algorithm. Reproduced from [111].

3.6 Missing Transverse Energy

Conservation of momentum in the plane transverse implies that the vector transverse momenta of the collision products should sum to zero. An imbalance in the sum of visible transverse momenta is known as missing transverse momentum, denoted as E_T^{miss}. This is a quantity which makes use of the conservation of 4-momentum to indirectly measure any particles which do not deposit any energy within the detector. In the ATLAS experiment, the E_T^{miss} reconstruction is calculated as the sum of a number of components [114]:

$$E_{x(y)}^{miss} = E_{x(y)}^{miss,e} + E_{x(y)}^{miss,\gamma} + E_{x(y)}^{miss,\tau} + E_{x(y)}^{miss,jets} + E_{x(y)}^{miss,\mu} + E_{x(y)}^{miss,soft}, \tag{3.1}$$

where each term is given by the negative vector sum of the momenta of the respective calibrated objects: electrons (e), photons (γ), hadronically decaying τ-leptons, jets, muons (μ) and soft term [3]. The magnitude of E_T^{miss} is then combined as:

$$E_T^{miss} = \sqrt{(E_x^{miss})^2 + (E_y^{miss})^2}. \tag{3.2}$$

[3]The soft term is composed of reconstructed tracks that are not associated with any physical objects

3.7 Overlap Removal

Since the objects are reconstructed and identified separately and independently, there might be an object passing the reconstruction criteria of multiple object types. An overlap removal procedure, which prioritises some objects in favour of others, is therefore applied among objects with a geometric overlap to avoid double counting. The criterion to define which objects overlap is based on the angular space (ΔR) between 2 objects. Object removal criteria for the analysis outlined in this thesis are defined as follow [115]:

- **electron-muon**: Remove the electron if it shares the same track with a muon.
- **electron-jet 1**: Remove jets within $\Delta R = 0.2$ of any surviving electron.
- **electron-jet 2**: Remove electrons within $\Delta R = \min(0.4, 0.04\text{+}10\ \text{GeV}/p_T^{electron})$ of the surviving jet that passes JVT requirement as introduced above.
- **muon-jet 1**: Remove jets within $\Delta R = 0.2$ of any surviving muon if the jet contain lass than 3 tracks.
- **muon-jet 2**: Remove muons within $\Delta R = \min(0.4, 0.04\text{+}10\ \text{GeV}/p_T^{\mu})$ of the surviving jet that passes JVT requirement as introduced in section 3.4.

Event with object passed above criteria will be further selected in order to improve the discrimination between the signal and backgrounds. The event selection criteria are described at Chapter 5 and 6.

Events from both the simulation and data are all reconstructed using the same algorithm which described in this chapter. However, their performance are not necessarily matched to each other. Therefore, the calibration is needed in order to reduce the difference between the recorded data and the simulated samples before examined by the object removal criteria. The calibration method of one of the parameters which related to the b-jet selection criteria will be discuss in the next chapter.

CHAPTER 4

Calibration of Light Flavour Jet b-tagging Efficiency in ATLAS

This chapter focuses on the calibration of the "light jet mistagging efficiency", ε_{light}, which is the probability of a light jet to pass the b-jet selection criteria that are described in Section 3.4. Ideally, the simulated samples describe in a prefect way the data and no calibration is needed. However, this is not the case. Additional calibration is often needed to account for differences between data and simulation. Such differences may be originating, for instance, from an imperfect detector response description or from limitations in the modelling of the underlying particle physics process, as in the case of the modelling of the kinematics of the jets produced in association with a Z boson. Effects like the ones described in the previous sentence may explain the differences between data and simulation as shown in Figure 4.1, which shows the MV2c10 algorithm output (see also Section 3.5).

There are two calibration methods used in the ATLAS experiment in order to correct the light jet mistagging efficiency: the adjusted simulation method and the negative tag method. The adjusted simulation method will be described in this chapter in more detail. It is a new method which relies on the data-driven calibrations of track related quantities and propagating them into the calibration of the light jet mistagging efficiency. On the other hand, the negative-method based on the comparison of the light jet mistagging efficiency between simulation and data in a light flavour enriched data set, which is selected by altering the tag requirement of the b-tagging algorithm.

The negative-tag method relies on an assumption that the light jets are mistagged as b-jets because of the finite resolution of the reconstructed impact parameters. Under this assumption, the signed impact parameter (see Section 3.2) of the tracks associated with light jets are symmetric around zero. On the other hand, the tracks associated with b- and c- jets will have a larger tail at large positive values

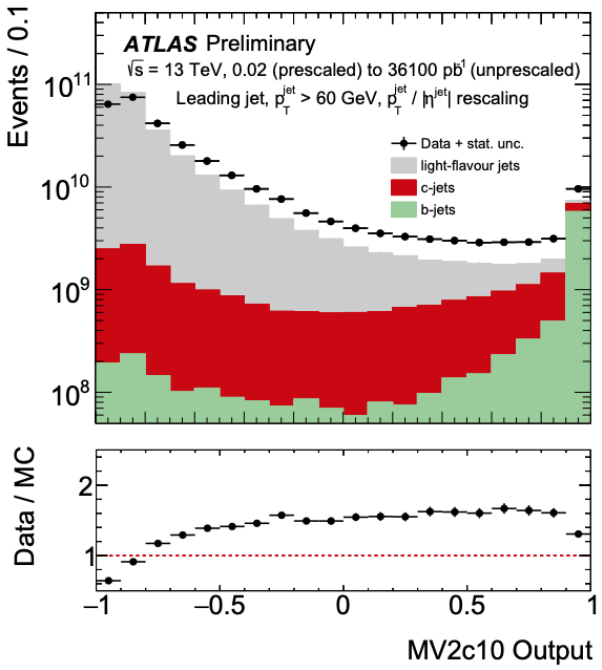

Figure 4.1: MV2c10 output distribution for data and simulated multijet events. The simulated events are split by jet flavour. The number of simulated events is scaled to the total number of data events in different $p_T^{jet}, |\eta^{jet}|$ bin considered in the measurement regardless of the jet flavour. The MV2c10 output of the highest p_T jet is shown for jets with $p_T > 60$ GeV. The difference between data and simulation samples at the bottom plane indicated that the calibration of *b*-tagging efficiency is needed. Reproduced from [116].

due to their longer lifetime as shown in Figure 4.2. This difference is one of the key discriminating properties used in the b-tagging algorithm. However, there are no such tails for b- and c-jets in the negative values while the distribution of the light jets remains the same. Therefore, flipping the sign of this parameter would largely reduce the acceptance for b-jets without altering the acceptance of light-jets. Eventually, the negative tag method approximates the light jet mistagging efficiency as the b-tagging efficiency found when running the lower level algorithm after reversing the sign of the impact parameter of the jet tracks. The combined algorithm of these lower level algorithm are noted as "MV2c10Flip", the output of MV2c10 and MV2c10Filp is shown in Figure 4.3.

In the following section, the adjusted simulation method is described in more detail. Both this method and the negative tag method are used for the calibrations used in the ATLAS experiment data analyses up to 2017. Although adjusted simulation method in principle would have smaller systematic uncertainties in comparison to the negative-tag method, since it is only relying on the tracking parameter calibration, only negative tag method has been used for the final ATLAS calibration since 2018. This is due to the high amount of computational resources needed for the adjusted simulation

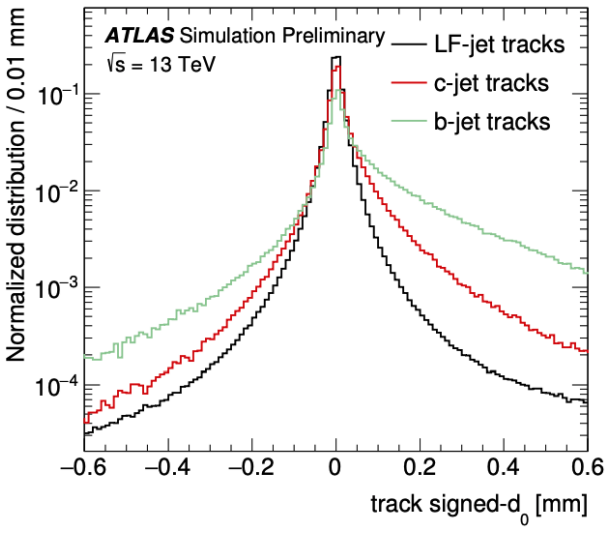

Figure 4.2: Signed transverse impact parameter, signed-d_0 distributions for tracks associated to light jets, c-jets and b-jets in simulated events. Reproduced from [116].

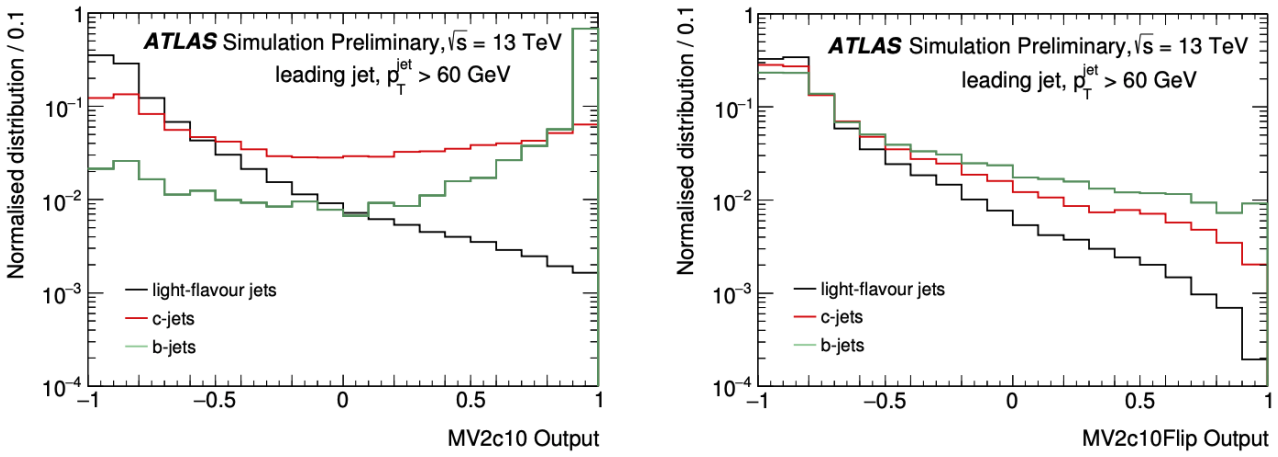

(a) (b)

Figure 4.3: The (a) MV2c10 and (b) MV2c10Flip output distribution for light jets, c-jets and b-jets in simulated events. The highest p_T jet in the event is shown, when this jet satisfies $p_T^{jet} > 60$ GeV. Reproduced from [116].

method. This is because the method requires comparisons of the calibrated track parameters along with their systematic uncertainties, which can be done only using multiple copies of derived AODs. The study presented here requires milti-TB level of storage and uses only 2015 and 2016 data. The required disk space would increase by several times, should the complete set of Run-2 data is used.

4.1 Adjusted simulation method

The adjusted simulation calibration method relies on data-driven calibrations of track related quantities, which are provided by the ATLAS tracking group. These quantities are used as input to the b-tagging algorithm output evaluation. The adjusted simulation calibration method uses these quantities as an input to re-run the b-tagging algorithm. Therefore, this method is well suited for the calibration of the mistag rate due to the effects related to mismodelling of track impact parameters or the existence of fake tracks, which are defined as reconstructed tracks that do not have a majority of their hits associated with a single charged particle, associated to a light jet. The light jet mistagging efficiency is largely determined by the properties of tracks, where differences between simulation and data result in different b-tagging performance [116]. The light jet calibration scale factors can be obtained by comparing the distribution of the original simulated sample, denoted as "nominal", and the calibrated track parameters, denoted as "adjusted". This calibration scale factors are multiplicative factors that are applied on the simulation in bins of jet p_T.

The baseline mistag efficiencies for light jets in the standard simulated sample, $\varepsilon_{light}^{Nominal}$, are derived separately for each of the MV2c10 algorithm working points: 60%, 70%, 77% and 85% as listed in Table 3.1. The MV2c10 distribution is re-evaluated after adjusting the simulation to account for several individual effects which might induce b-tagging performance differences between data and simulation. Each of these "adjusted" distribution is used to derive "adjusted" light jet mistag efficiencies, $\varepsilon_{light}^{adjusted}$. The effects that have been considered here are those that have been shown to have the largest impact: the track impact parameter resolution, which will be discussed in Section 4.1.1, and the fake track reconstruction rate, which will be discussed in Section 4.1.2. The calibration of these parameters are studied by the ATLAS tracking group, with the calibration method and results are recorded in Ref. [117]. Other effects, which have smaller impact on the calibration compared to the impact parameter resolution and fake track reconstruction rate, are not considered in the study performed in this chapter. However, they have been investigated in a previous study [116] and including the following:

- The fraction of long-lived strange-hadrons, such as K_s and Λ_s, is underestimated in Pythia 8 simulation.
- The non-Gaussian tails in the impact parameter distribution, which are difficult to reproduce accurately in the simulation.
- The choice of the parton-shower model. This effect can be tested by comparing the MV2c10 output distribution of light flavour jets to alternative parton-shower implementations, such as Ptyhia8 against Herwig++.

The procedure to adjust the simulated samples is the following:

1. Track parameters, such as track impact parameter resolution, fake-rate, track reconstruction efficiency are determined in both data and simulation by the ATLAS tracking group [117].
2. The simulated track parameters are then "adjusted" based on the corresponding result from the data-driven calibration (see Section 4.1.1 and 4.1.2 for details) to reproduce the track parameter distributions observed in the data.
3. The b-tagging algorithm is applied to the adjusted simulation samples to extract a new mistag efficiency, $\varepsilon_{light}^{adjusted}$. The light jet calibration scale factor, SF_{LF}, with respect to the standard simulated sample is calculated in bins of p_T^{jet} as:

$$SF_{LF} = \frac{\varepsilon_{light}^{adjusted}}{\varepsilon_{light}^{Nominal}}. \tag{4.1}$$

The systematic uncertainties originated from the calibration of simulated track parameters will be propagated into the final light jet calibration scale factor. More details are given in Section 4.1.3.

The standard simulated sample used in the calibration is the top pair ($t\bar{t}$) events which is defined in Chapter 3. Events with at least one jet with transverse energy above 100 GeV are selected for both the data and the simulated $t\bar{t}$ sample using a single jet trigger. The calibration is performed for jets with $p_T \geq 20$ GeV and $|\eta| \leq 2.5$. The simulated $t\bar{t}$ events have the advantage that the inclusive b-jets can be probed. Calibration based on both calorimeter jets and particle flow jets is performed with the corresponding JVT requirements, mentioned in Section 3.4. The resulting calibration scale factor can be used to weight the simulated jets, in order to provide a better agreement with the data.

4.1.1 Track Impact Parameter Resolution

The impact parameter resolution is the key element of this calibration method as well as the b-tagging performance in general. The study of the track impact parameter resolution is done by the ATLAS tracking group. In this section, the method they used would be described. Eventually, the correction terms of the impact parameter resolution is obtained and used as an input of the adjusted simulation method.

The impact parameter of the charged particle tracks with $p_T \approx 1$ (20) GeV reconstructed by ATLAS tracking system with a resolution of the order of 100 (10) μm, respectively [116]. This results from a convolution of several effects; for instance: intrinsic single-hit resolution, alignment of the tracking components, multiple scattering inside the detector material and the accuracy of track reconstruction algorithms. These effects are difficult to simulate and, as a result, the track impact parameter reconstruction performance in simulation may need additional tuning [118] to reproduce the data adequately. The transverse and longitudinal track impact parameter resolutions, denoted as $\sigma(d_0)$ and $\sigma(z_0)$, respectively, are measured using samples of simulated di-jet, minimum-bias [1] and $Z \to \mu\mu$ events. Events are required to have a reconstructed primary vertex with at least 10 tracks in the di-jet sample, and to have a pair of opposite-sign reconstructed muons with invariant mass, $m_{\mu\mu}$, in the window $60 < m_{\mu\mu} < 120$ GeV in the $Z \to \mu\mu$ sample. Tracks from these samples with different p_T ranges are extracted for the impact parameter resolution measurement. Simulated di-jet samples with $p_T < 110$ GeV are used in the study. In the $Z \to \mu\mu$ sample, tracks with $p_T > 20$ GeV have been used. Finally, tracks with $0.4 < p_T < 10$ GeV are extracted from minimum-bias events.

The impact parameter resolution is studied in bins of p_T and η. The resolution of track impact parameter measurements is directly related to the capability of single-track reconstruction of the ATLAS inner detector. However, the resolution of the event-by-event reconstructed primary vertex is also convoluted with the measurement. The contribution from the primary vertex resolution, which is the order of 10 μm in the transverse plane, is sizeable for p_T^{track} above a few GeV and the effect from it needs to be removed to determine the track intrinsic impact parameter resolution. This process is often called “unfolding”. The track impact parameter resolution after it has been corrected for the effect of the vertex resolution is described as “unfolded”. The unfolding procedure uses an iterative

[1] Minimum-bias: It is a selection of inelastic events with the minimum possible requirements necessary to ensure that an inelastic collision occurred. Typically, minimum bias events are dominated by soft interactions, with low transverse momentum and low particle multiplicity [119].

algorithm to deconvolute the primary vertex resolution in both data and simulation. This procedure is described in detail in Ref. [117] as demonstrated in the following.

The unfolding procedure starts with the core of the impact parameter resolution for the reconstructed impact parameter, $d_{0,reco}$, which can be described by the function:

$$R(d_{0,reco}) = \int \exp\left[-\frac{1}{2}\frac{d_{0,reco}^2}{\sigma^2(d_{0,track}) + \sigma^2(d_{0,PV})}\right] P(\sigma(d_{0,PV}))d\sigma(d_0, PV), \tag{4.2}$$

where the Gaussian function has a width equal to the sum in quadrature of the reconstructed track resolution $\sigma(d_{0,track})$ and the primary vertex resolution projected along the impact parameter direction $\sigma(d_{0,PV})$. The integral runs on all possible primary vertex resolutions, $P(\sigma(d_{0,PV}))$, corresponding to all the considered tracks. The dependence on the primary vertex resolution can be removed by using the change of variables:

$$d_{0,reco} = d_{0,unfold}\sqrt{\frac{\sigma^2(d_{0,track}) + \sigma^2(d_{0,PV})}{\sigma^2(d_{0,track})}}. \tag{4.3}$$

Substituting this into Equation 4.2 allows the integral to be factorised and a Gaussian distribution of width $\sigma(d_{0,track})$ can be obtained.

Since the method in Equation 4.3 relies on the knowledge of the unknown observable of interest, $\sigma(d_{0,track})$. The iterative method described in ref. [117] allows to obtain the approximate value of $\sigma(d_{0,track})$ starting from the $d_{0,reco}$ variable. For each track the reconstructed impact parameter $d_{0,reco}$ is corrected with the unfolding factor:

$$d_{0,unfold,(i)} = d_{0,reco}\sqrt{\frac{K_{(i-1)}^2\sigma^2(d_{0,reco})}{K_{(i-1)}^2\sigma^2(d_{0,reco}) + K_{PV}^2\sigma^2(d_{0,PV})}}, \tag{4.4}$$

where the index (i) indicates the i-th iteration, and the $d_{0,reco}$ is the value of the original impact parameter before the first iteration and the errors $\sigma(d_{0,reco})$ and $\sigma(d_{0,PV})$ are taken, track-by-track, from the nominal track and vertex fits. The corection factor, $K_{(i)}$, is extracted using a iterative Gaussian fit of the 1.5σ core of the distribution of $d_{0,unfold,(i)}$ and $d_{0,reco}$ for a set of tracks of given p_T and η. For the first iteration the original $d_{0,reco}$ is used as $d_{0,unfold}$. The correction factor of primary vertex resolution, K_{PV}, has been set to 1.25 ± 0.08, where the uncertainty accounts for differences between the reconstructed and expected primary vertex resolution [117].

The uncertainty sources of the impact parameter resolution are the following [116]: (1) propagation of the unfolding statistical uncertainty, (2) variation of the definition of core of fits, (3) propagation of the K_{PV} uncertainty, (4) track-density effects, which is evaluated by comparing the standard impact parameter resolution and the one in the region where ΔR between a track and jet axis less than 0.02. In addition, the impact parameter resolution measurement extracted in $Z \to \mu\mu$ and minimum-bias samples is used as a source of systematic uncertainty by taking the difference with respect to the di-jet measurement.

The reconstructed track impact parameter resolution is found to be stable with $K_{(i)} \approx 1$ after two iterations and the results are summarised in Figure 4.4, showing the result of data and simulation, as a function of track p_T.

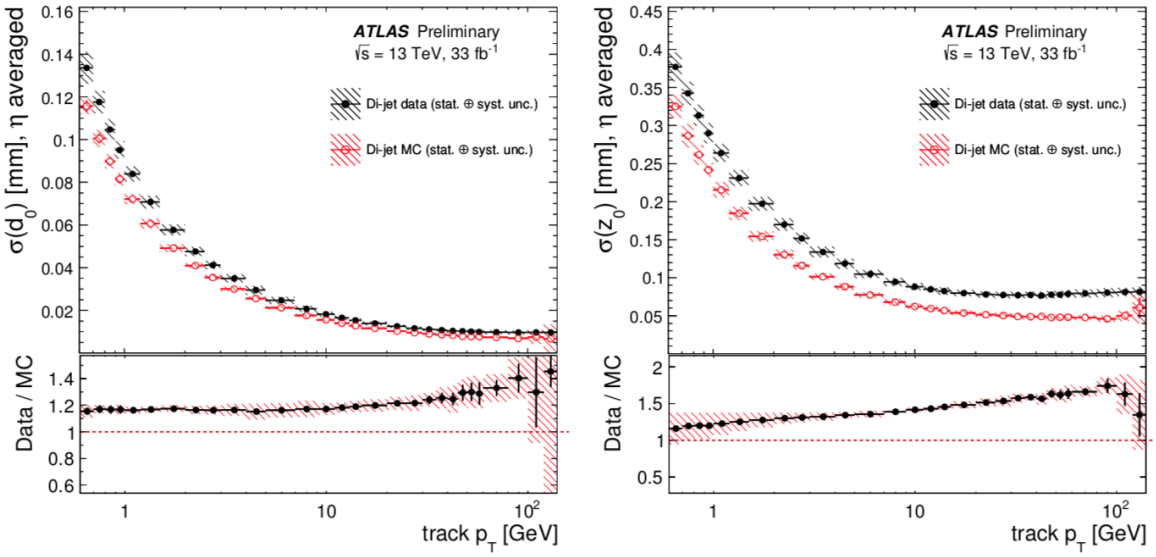

Figure 4.4: Reconstructed track impact parameter resolution in the transverse direction (left) and in the longitudinal direction (right). The top panels show the results for data (black) and simulation (red) as a function of the track p_T, after averaging the 2-dimensional $p_T - \eta$ distribution along η. Systematic plus statistic uncertainties are shown as a dashed area. The bottom panels show the ratio between data and simulation with corresponding uncertainties. Reproduced from ref.[116].

The simulation can be corrected to match the impact parameter resolution in data by using the bin-by-bin quadrature difference between data and simulated resolutions, which is given by the following equation:

$$\sigma^{cor}(d_0) = \sqrt{(\sigma^{data}(d_0))^2 - (\sigma^{MC}(d_0))^2} \tag{4.5}$$

where $\sigma^{cor}(d_0)$ and $\sigma^{cor}(z_0)$ are the correction terms to be added to the simulation of the track transverse and longitudinal impact parameter value, respectively. The correction is obtained with a smearing procedure where a random value extracted from a Gaussian distribution of zero mean and width equal to $\sigma^{cor}(d_0)$ and $\sigma^{cor}(z_0)$. The correction terms are added to the d_0 and z_0 of each simulated track while all the other track parameters are left unchanged [116]. Figure 4.5 shows the distribution of $\sigma^{cor}(d_0)$ and $\sigma^{cor}(z_0)$ in the (p_T , η) parameter space.

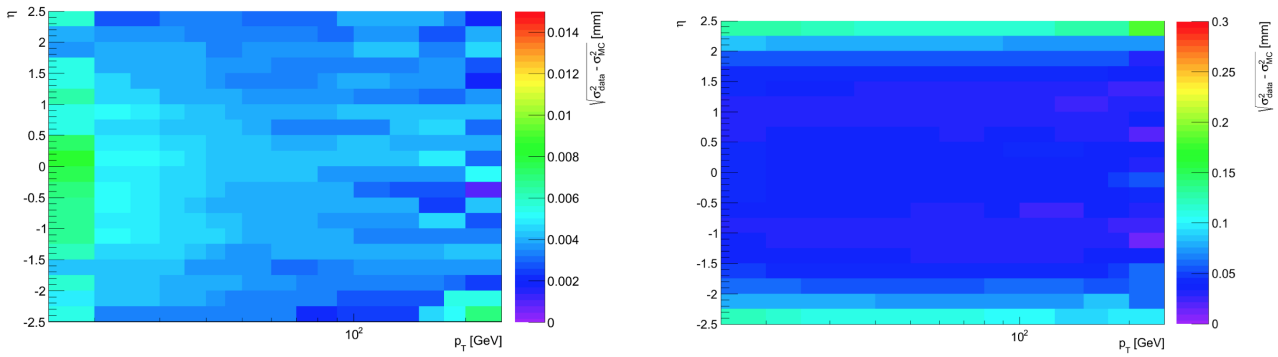

(a) $\sigma^{cor}(d_0)$ (b) $\sigma^{cor}(z_0)$

Figure 4.5: The (a) $\sigma^{cor}(d_0)$ and (b) $\sigma^{cor}(z_0)$ distribution across the (p_T , η) parameter space. Only di-jet events with $20 < p_T < 300$ GeV and $|\eta| < 2.5$ are considered.

In the adjusted simulation method, the correction is applied to the simulated tracks based on the distribution of $\sigma^{cor}(d_0)$ and $\sigma^{cor}(z_0)$, shown in Figure 4.5. After the correction is applied, the corresponding primary vertex is reconstructed. After that, the b-tagging algorithm would be re-run with these corrected tracks. Although the jet is not reconstructed again using these corrected tracks and primary vertex, the jet energy calibration and JVT are re-applied after the b-tagging. This adjustment is done separately in d_0 and z_0. The systematic uncertainties of the impact parameter resolution as mentioned above are propagated into this adjustment, which is considered as a uniform $\pm 1\sigma$ Gaussian uncertainty for each of the corrected tracks.

Figure 4.6 shows the light jet mistagging efficiency after the calibration on $\sigma^{MC}(d_0)$ and $\sigma^{MC}(z_0)$ as a function of jet p_T. The bottom panel shows the difference between calibrated and nominal impact parameter resolutions. The adjustment of $\sigma^{data}(d_0)$ and $\sigma^{data}(z_0)$ in general has a similar effect on the light-jet mis-tag efficiency. However, comparing the difference between the adjusted and nominal samples, a bigger difference from $\sigma^{cor}(d_0)$ has been found in the high jet p_T (> 1000 GeV) region. Systematic uncertainties are propagated from the correction of the impact parameter resolutions, as mentioned above. The correlation between $\sigma^{cor}(d_0)$ and $\sigma^{cor}(z_0)$ is considered as an systematic uncertainty in the combined calibration scale factor, which is described at Section 4.1.3.

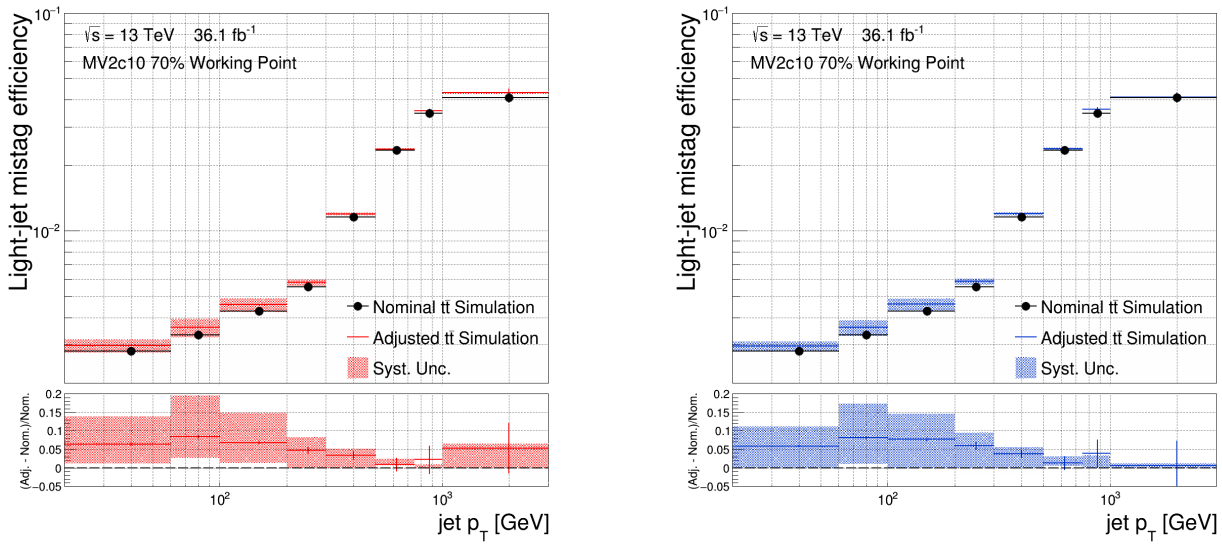

(a) Calibration on $\sigma^{MC}(d_0)$

(b) Calibration on $\sigma^{MC}(z_0)$

Figure 4.6: The calibrated light jet mis-tag efficiency with respected to (a) $\sigma^{MC}(d_0)$ and (b) $\sigma^{MC}(z_0)$. The nominal light jet mis-tag efficiency is overlaid. The difference between adjusted and nominal impact parameter resolutions are shown at the bottom panel. Figures for these distributions with different MV2c10 working points can be found in Appendix A.

4.1.2 Fake track reconstruction rate

As mentioned before, fake tracks are defined as reconstructed tracks that do not have a majority of their hits associated with a single charged particle. They are reconstructed in the inner tracker due to pile up, high track multiplicity and high density of hits on the inner detectors. The number of fake tracks has a large uncertainty stemming from several sources. For instance, the interactions between particles and detector components or dead sensors can produce incomplete track information leading to fake tracks. The uncertainty on the number of fake tracks must be taken into account when calculating the light jet mis-tag efficiency. To provide a cross-check on the modelling of the tracking fake rate, an estimate of this quantity is made by assuming that the number of real tracks is to first order proportional to the number of pile-up interactions. Any deviation from linearity is therefore assumed to be due to fakes [120]. In Ref. [120], a study is performed with two sets of track selection: "Loose" and "Tight primary". The Loose tracks are required to have at least 7 hits in the Pixel and SCT detectors. The Tight Primary required to have at least 9 hits in the Pixel and SCT detectors if $|\eta| \leq 1.65$, or 11 hits if $|\eta| > 1.65$. Data used in this study is recorded by ATLAS detector between September and November 2015 and corresponding to an integrated luminosity of around 1.74 fb^{-1}. Simulation events from minimum-bias di-jet sample are used to evaluate the track reconstruction

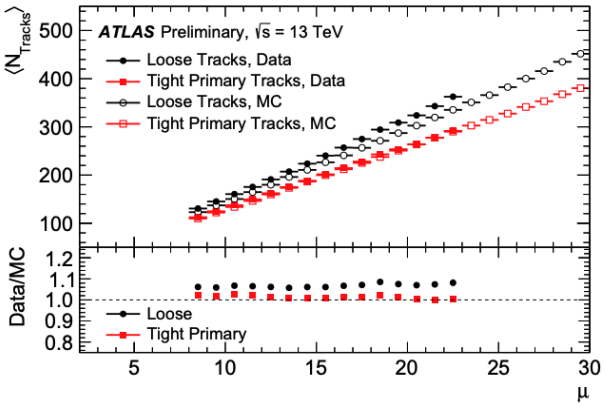

(a) $< N_{tracks} >$

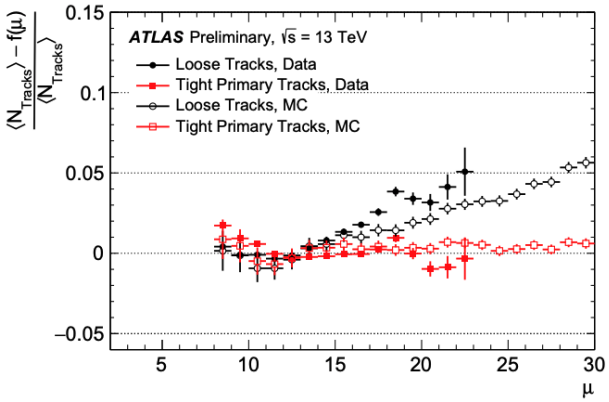

(b) $\frac{<N_{tracks}>(\mu)-f(\mu)}{<N_{tracks}>(\mu)}$

Figure 4.7: (a) Average number of reconstructed tracks as a function of μ for data and simulated di-jet events, applying the Loose and Tight Primary selections. (b) An estimation of the tracking fake rate, derived from the relative deviation from the linear fit to $<N_{tracks}>$ as a function of μ. Reproduced from ref.[120]

efficiency and to compare against the data. The average number of tracks, $< N_{tracks} >$, passing the Loose and Tight Primary selections, as a function of the average number of interactions per bunch crossing, μ, is shown in Figure 4.7(a). The estimation of the fake rate is provided by relative deviation from the linear fit, which can be expressed as:

$$\frac{< N_{tracks} > (\mu) - f(\mu)}{< N_{tracks} > (\mu)}, \tag{4.6}$$

where the $f(\mu)$ is a linear function which fitted the data from figure 4.7(a) in the region $10 \leq \mu \leq 15$. In this region, both data and simulation demonstrate approximately linear behaviour. Figure 4.7(b) shows the relative deviation as a function of μ.

Another study demonstrated a method to estimate the fake tracks in real data by fitting a fake tracks enriched control regions, see Ref. [121] for more details. The result of this study suggested that the number of fake tracks in simulation is usually less than what is observed in data. For simulated fake tracks passing the loose requirement, the study suggested increasing the amount by 27% in order to match the number observed in data. This result agreed with the difference between data and simulation in Figure 4.7(a). Both of them indicated that the number of fake tracks can be one of the possible parameters that can be used in the adjusted simulation method for light-jet calibration. Since it is not possible to create new tracks in a simulated event, in order to mimic the difference between the data and the simulated sample the adjustment is done by randomly removing 27% of the tracks wihch passed the loose selection. This approach mirrors the effect from the study mentioned above, and

therefore the impact has to be symmetrised. The symmetrisation with respect to the nominal sample is done for each bin in the jet p_T spectrum. Difference between the adjusted and nominal samples are first calculated. If the difference is positive, the absolute value of the difference is subtracted from the nominal value of that bin. If the difference is negative, its absolute value is added to the nominal value of that bin. The uncertainty of this adjustment is estimated by repeating the adjustment with the tight primary fake tracks. Since the study in Ref. [121] suggests increasing the amount pf tracks by 124% in order to match the observation in the data for the tight primary fake tracks, 100% of the tracks which passed the tight selection has been removed in the adjustment. As a consequence of this procedure, only tracks which is not passed the tight selection has been used and this uncertainty estimate is very conservative.

4.1.3 Combination of the tracking performance adjustments and calibration result

The final calibration of the simulated samples is obtained assuming the effect of the impact parameter resolution and the fake tracks to be uncorrelated. Under this assumption, the combined calibration scale factor, SF_{LF}, is given by:

$$SF_{LF} = \prod_i \frac{\varepsilon_{light}^{adjusted,i}}{\varepsilon_{light}^{nominal}} = \prod_i SF_{LF}^{adjustment,i} = SF_{LF}^{d_0} \cdot SF_{LF}^{z_0} \cdot SF_{LF}^{Fake}, \tag{4.7}$$

where the product is over the adjustments in d_0, z_0 and number of fake tracks. Figure 4.8 shows the impact of each of the terms in Equation 4.7 on the MV2c10 output score. In the same figure, the bottom panel shows the difference between the adjusted and nominal simulated samples. Figure 4.9 shows the breakdown of SF_{LF} as a function of jet p_T for calorimeter and particle flow jets. In general, the SF_{LF} and its breakdown have a similar distribution up to the jet in both calorimeter and particle flow jets. However, the distribution of $SF_{LF}^{d_0}$ and $SF_{LF}^{z_0}$ in particle flow jet SF_{LF} has a different behaviour compare to the calorimeter jet SF_{LF} in the high jet p_T region. Thus, the particle flow jet combined scale factor in this region is lower in comparison to the one used for the calorimeter jets.

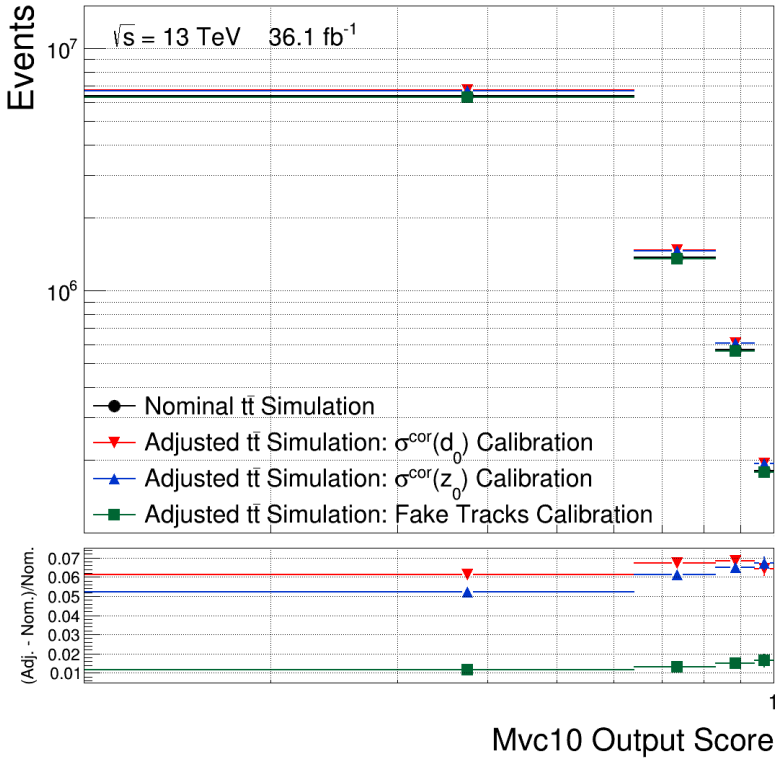

Figure 4.8: The MV2c10 output under different adjustment in calorimeter jet. The difference between adjusted and nominal samples are shown at the bottom panel.

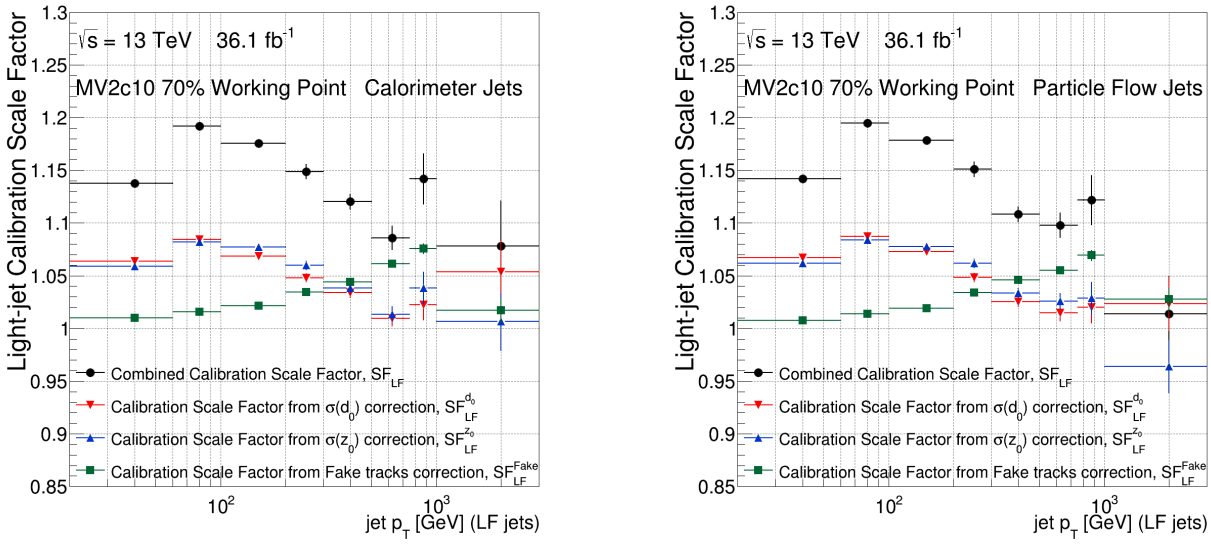

(a) Calorimeter jets

(b) Particle flow jets

Figure 4.9: The combined calibration scale factor with its components as mentioned in Equation 4.7. Distributions in both (a) calorimeter and (b) particle flow jets are shown. Figures for these distributions with different MV2c10 working points can be found in Appendix A.

The following uncertainties for the combined calibration scale factor are considered:

- The statistical uncertainty associated with the simulated samples. This uncertainty is stemming from the finite number of events in the simulated sample. This uncertainty becomes larger as the jet p_T increases.
- Uncertainties propagated from the track impact parameter resolution measurements. This is covered by a uniform Gaussian 1σ confidence intervals for both $\sigma^{cor}(d_0)$ and $\sigma^{cor}(z_0)$ as mentioned in Section 4.1.1.
- The uncertainty of adjusting the number of fake tracks. The adjustment is repeated with the tight primary fake tracks. The effect on the final scale factor is estimated by replacing the SF_{LF}^{Fake} in Equation 4.7 with the adjustment of tight primary fake tracks. The difference with respect to the SF_{LF} in Equation 4.7 is used to evaluate a corresponding uncertainty.
- The uncertainty arising from correlations between the d_0 and z_0 corrections. This is due to the mis-measurement that simultaneously degrades the impact parameter resolution in the longitudinal and transverse plane.

The breakdown of the different systematic uncertainties, as a function of jet p_T, is shown in Figure 4.10. The largest systematic uncertainty comes from the adjustment on number of fake tracks. The systematic uncertainties related to the impact parameter resolutions are similar in both calorimeter and particle flow jets, except from the fact that the uncertainty of $\sigma^{cor}(z_0)$ with jet $p_T > 1000$ GeV in particle flow jets is larger than the one in calorimeter jets. Figure 4.11 shows the SF_{LF} for both calorimeter and particle flow jets, with the total systematic uncertainties are shown as the envelope. The difference between SF_{LF} of calorimeter and particle flow jets is shown at the bottom panel. Except from the very last jet p_T bin in this plot, the SF_{LF} is compatible between calorimeter and particle flow jets, with difference about 2% according to the bottom panel. The difference in the last jet p_T bin with jet $p_T > 1000$ GeV is about 6 % with a large statistic uncertainty. This originates from the different behaviour of $SF_{LF}^{z_0}$ in calorimeter and particle flow jets, as shown in Figure 4.9 and discussed above. The overall combined scale factor is about 1.15 for both calorimeter and particle flow jets.

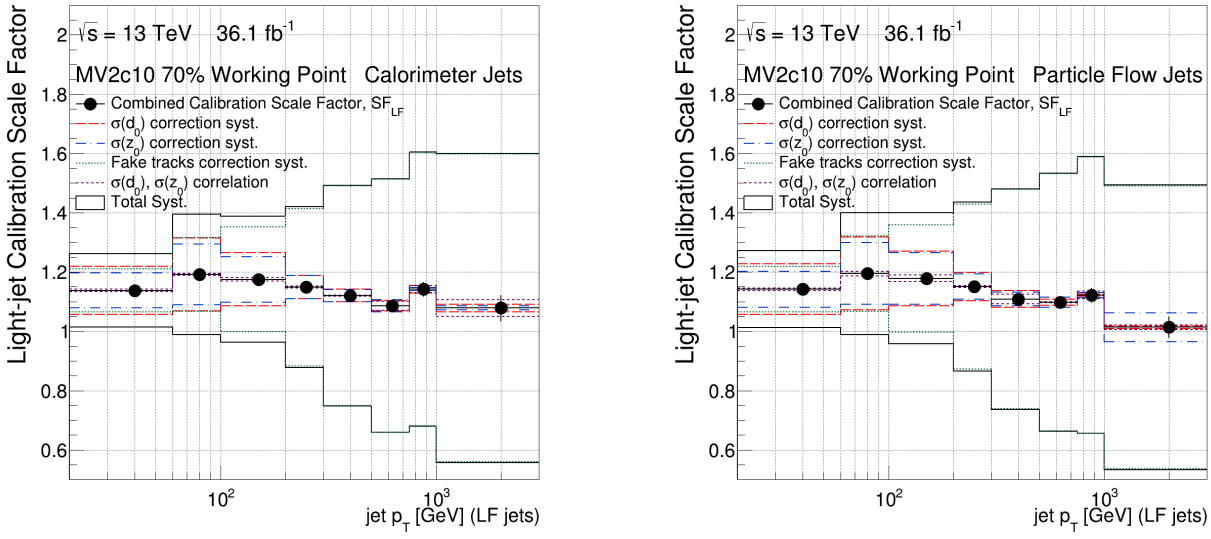

(a) Calorimeter jets (b) Particle flow jets

Figure 4.10: The combined calibration scale factor with components of systematic uncertainties. Distributions of (a) calorimeter and (b) particle flow jets are shown. Figures for these distributions with different MV2c10 working points can be found in Appendix A.

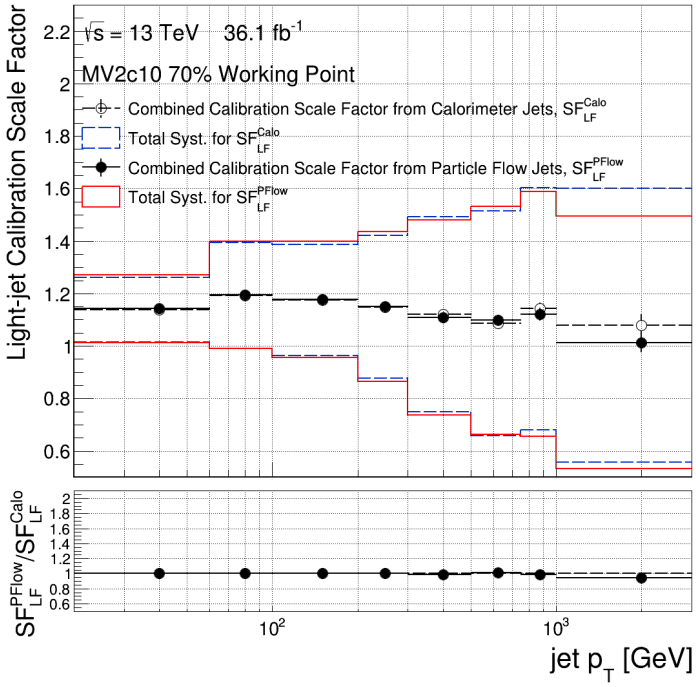

Figure 4.11: The combined calibration scale factor for calorimeter and particle flow jets with total systematic uncertainties. The difference between the calibration scale factor for calorimeter and particle flow jets are shown in the bottom panel. Figures for this distribution with different MV2c10 working points can be found in Appendix A.

As mentioned at the beginning of this chapter, the negative tag method is the official light jet mistagging efficiency calibration method in the ATLAS experiment. Figure 4.12 compares the calibration result from adjusted simulation method and the negative tag method in both calorimeter and particle flow jets. The bottom panel shows the difference of the calibration result and the combined calibration scale factor, provided by two methods. Overall, the result from the adjusted simulation method agrees with the negative tag method, with the best agreement being observed in the particle flow jets.

The results from the adjusted simulation method agree very well with the negative tag method. Given that the particle flow jets would be the default method in future analyses, the adjusted simulation method can be used as a cross-check of the result from the negative tag method with respect to the 2017 and 2018 data, which is not included here.

The following improvements can be considered in a possible future study with this method. The choice of the track selection using fewer constraints as the source of systematic uncertainty in the adjustment of fake tracks. By reducing this largest uncertainty, the SF_{LF} from the adjusted simulation method would have a much narrower and less conservative total systematic uncertainty. Another improvement can be done by increasing the number of generated events in the simulated sample, in order to gain more events in the high jet p_T region. As shown in Figure 4.9, the scale factor has a relatively large statistical uncertainty in the region with jet $p_T \geq 1000$ GeV. A more precise scale factor can also be estimated by increasing the number of events in that region. For example, the number of generated events for simulated multi-jet samples dropped from around 1,900,000 to around 400,000 after the region with jet $p_T \geq 3200$ GeV. This sample can provide enough statistical power for the adjusted simulation method to work well up to jet p_T of 3 TeV. In addition, since the negative tag method does not use $t\bar{t}$ events, the comparison in Figure 4.12 can be improved by introducing an additional systematic uncertainty by considering the difference between the simulated samples.

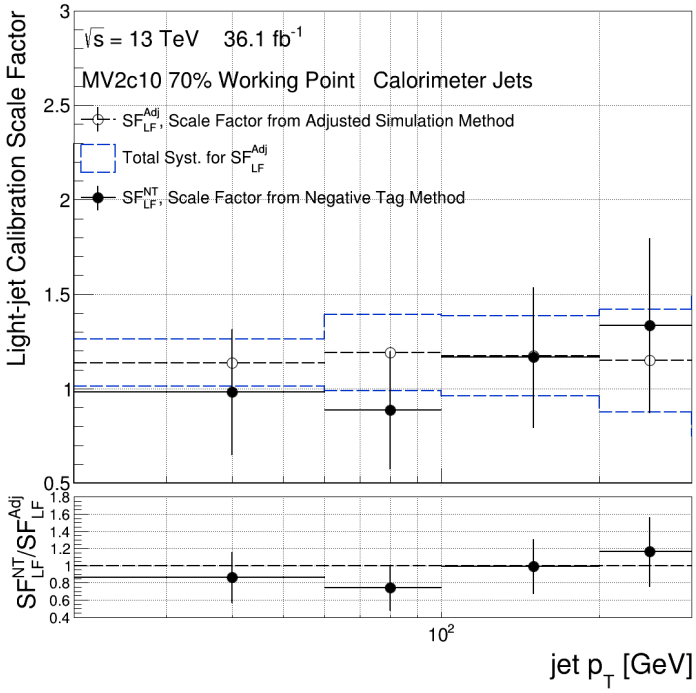

(a) Calorimeter jets

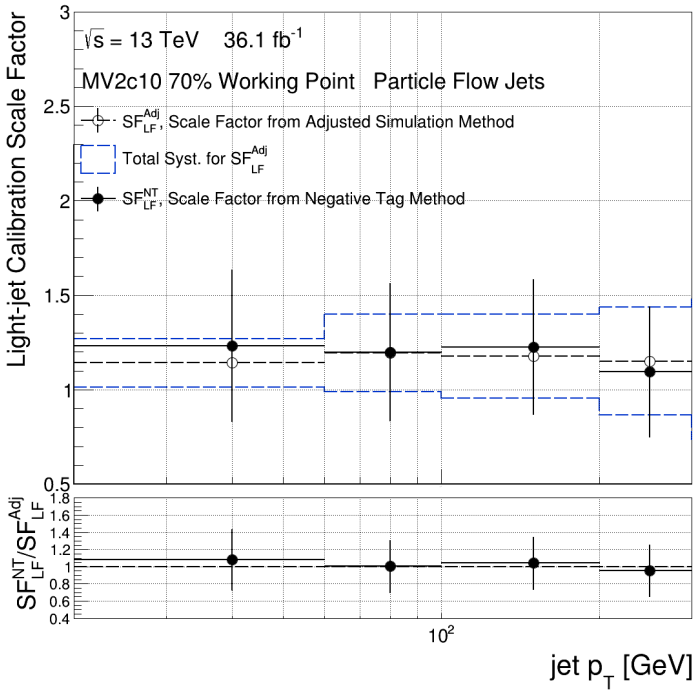

(b) Particle flow jets

Figure 4.12: The light jet calibration scale factors from adjusted simulation and negative-tag method for (a) calorimeter and (b) particle flow jets. The difference between the results of two methods is shown in the bottom panel. Figures for these distributions with different MV2c10 working points can be found in Appendix A.

CHAPTER 5

Search for $A \to ZH \to \ell\ell bb$ with 36 fb^{-1}

In this chapter, the search discussed in this thesis, $A \to ZH \to \ell\ell b\bar{b}$, is introduced. The result was published in Physics Letters B, see Ref. [57]. The search is performed with a proton-proton collision data sample collected by the ATLAS detector, which corresponds to integrated luminosity of 36 fb^{-1}. The signal signature being searched for consists of a $b\bar{b}$ pair that comes from an H boson decay, where the H boson has mass $130 < m_H < 600$ GeV, and an $\ell\ell$ pair ($\ell = e$ or μ) that comes from a Z boson decay. Also, a resonance forms in the $\ell\ell b\bar{b}$ system coming from $A \to ZH$ decay, where $200 < m_A < 800$ GeV. An additional b-jet may be present if the signal is produced via the b-associated production mechanism. Since the final implementation of this analysis is an effort of a larger group in the ATLAS collaboration, this chapter will focus on aspects that were studied the most during the work for this thesis.

5.1 Event selection

The selection criteria are applied in order to improve the discrimination between signal and background in the final signal extraction. Events in this search are initially selected by the single-lepton triggers. These triggers are fired by electrons or muons satisfying several combinations of p_T thresholds, identification and isolation requirements that depend on the data taking period. These combinations are optimised such that the efficiency to select events with prompt electrons or muons is maximised, taking also into account the limitations on the HLT bandwidth. In particular, the single-electron trigger requirements are detailed in the following [122]:

- At least one electron with $p_T > 24$ GeV satisfying the Medium identification criteria with isolation requirements ($p_T > 26$ GeV and Tight identification criteria in later data-taking periods).

- At least one electron with $p_T > 60$ GeV satisfying the Medium identification criteria.
- At least one electron with $p_T > 120$ or 140 GeV, depending on the data-taking period, satisfying the Loose identification criteria.

The single-muon trigger requirements are detailed in the following:

- At least one muon with $p_T > 24$ or 26 GeV, depending on the data-taking period, satisfying the isolation requirements as mentioned in Chapter 3.
- at least one muon with $p_T > 50$ GeV.

Since this search has two leptons coming from the $Z \to \ell\ell$ decay, events are required to have two same flavour leptons, i.e., ee or $\mu\mu$, where at least one of these leptons is required to match the lepton that fired the trigger. These events are requited to satisfy the loose identification requirements, as well as the isolation criterion described in Chapter 3. In addition to these requirements, at least one of these leptons must have $p_T > 27$ GeV. Also, for events that contain $\mu\mu$ pair are required to have opposite charge muons. The mass of the $\ell\ell$ system ($m_{\ell\ell}$) is constrained in the range $80 < m_{\ell\ell} < 100$ GeV, in order to compatible with the Z mass. The events are also required to contain at least 2 b-jets, since the signal process contains the decay $H \to b\bar{b}$. The leading b-jet [1] is required to have $p_T > 45$ GeV, in order to be compatible with the b-jets that are found in the signal, which tend to have high p_T due to the large mass of H,which is at least 130 GeV. In addition, a E_T^{miss} significance cut is applied to reduce the top-quark pair production, which is defined as follows:

$$E_T^{miss}\text{significance} = E_T^{miss}/\sqrt{(\Sigma p_T^{\text{e}} + \Sigma p_T^{\mu} + \Sigma p_T^{\text{jet}})} < 3.5.$$

Figure 5.1 shows the E_T^{miss} before and after the E_T^{miss} significance cut.

Subsequently, two categories are defined: the $n_b = 2$ category, which contains events with exactly two b-jets, and the $n_b \geq 3$ category, which contains events with three or more b-jets. The $n_b \geq 3$ category is important for the b-associated production signals due to the existence of the associated b-jets. In the $n_b \geq 3$ category, it is important to choose the correct pair of b-jets which coming from the $H \to b\bar{b}$ decay from the many b-jets that are in the event. By default, the $b\bar{b}$ system is reconstructed by the two highest p_T b-jets, since it is expected that the b-jets that are produced in association with the A boson have lower p_T in comparison with the b-jets from the H boson decay. It is still possible

[1] leading b-jet: The b-jet with the highest p_T.

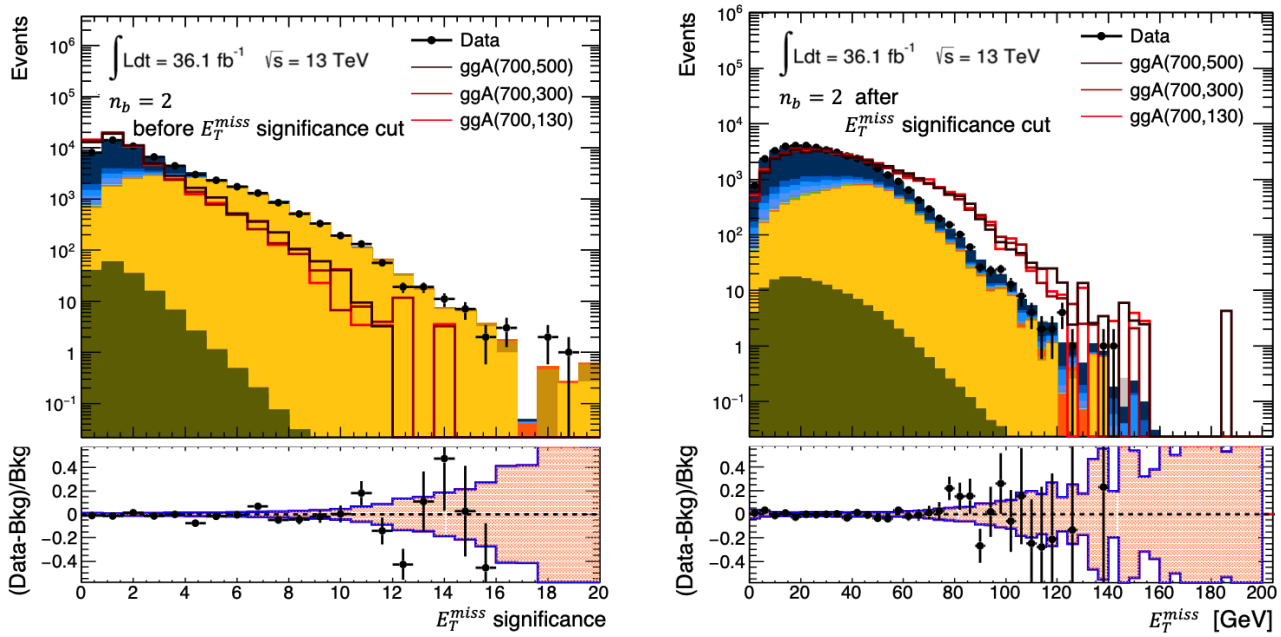

(a) E_T^{miss} significance

(b) E_T^{miss} after E_T^{miss} significance cut

Figure 5.1: The (a) E_T^{miss} significance and the (b) E_T^{miss} distribution after the E_T^{miss} significance cut. Only events that contain exactly 2 b-jets and at least 2 jets, with only the statistical uncertainty shown. For the background simulated samples, color code shown in Figure 3.5 has been used. At the bottom panel, the filled area represents the statistical uncertainties, while the blue line shows the combined uncertainty from statistical and shape uncertainties. Figures for these distributions with event that contain at least 3 b-jets can be found in Appendix B.

that the associated b-jet has higher p_T than the b-jets from the H boson. In this scenario, the choice of the two highest p_T b-jets fails to identify the $H \to b\bar{b}$ decay b-jets. In order to evaluate the effect of wrong pairings, two studies were performed. In the first study, the $b\bar{b}$ system is reconstructed by the pair of b-jets which minimise the $|m_{bb} - m_H|$. In most of the cases, the $m_{\ell\ell bb}$ distributions does not improve. In the second study, kinematic variables including the p_T^{jet} and the ΔR are used as an input of the neural-network based algorithm. The output of this algorithm improved the tail region of the $m_{\ell\ell bb}$ distribution of signals. However, the background rejection around the peak of the distribution dropped by 20% compare to the default method. Therefore, the original approach is eventually used to reconstruct the $b\bar{b}$ system.

For the gluon fusion production, depending on the assumed m_A and m_H, 94%–97% of the events passing the E_T^{miss} significance criterion. From those events, 36%–62% of them are classified in the $n_b = 2$ category, and 1%–4% are falling into the $n_b \geq 3$ category, which contains events with three or more b-jets. On the other hand, for b-associated production signal has 89%–94% probability to pass the E_T^{miss} significance criterion. From there, 40%–45% and 15%–24% of b-associated production

signal events are classified in the $n_b = 2$ and $n_b \geq 3$ category, respectively. In both $n_b = 2$ and $n_b \geq 3$ category, a requirement on the following variable is applied:

$$\sqrt{\Sigma p_T^2}/m_{\ell\ell bb} > 0.4,$$

where:

$$\Sigma p_T^2 = (p_T^{\ell 0})^2 + (p_T^{\ell 1})^2 + (p_T^{b0})^2 + (p_T^{b1})^2.$$

The $p_T^{\ell 0}$ and $p_T^{\ell 1}$ denote the p_T of the leading and sub-leading leptons, while the p_T^{b0} and p_T^{b1} represent the p_T of the leading and sub-leading b-jets. Figure 5.2 shows the distribution of $\sqrt{\Sigma p_T^2}/m_{\ell\ell bb}$ and $m_{\ell\ell bb}$ after the $\sqrt{\Sigma p_T^2}/m_{\ell\ell bb} > 0.4$ cut in the $n_b = 2$ category. The numerator of the variable, $\sqrt{\Sigma p_T^2}$, separate the signals from the Z+jets backgrounds since the jets are not forming the resonance in the Z+jets events and hence the variable is softer. The denominator, $m_{\ell\ell bb}$, separate the signals from the Z+jets background in the similar way as the $m_{\ell\ell bb}$ of the signals are much higher than the Z+jets backgrounds.

Finally, the invariant mass of the two leading b-jets, m_{bb}, must be compatible with the assumed H boson mass by satisfying the requirement of $0.85 \cdot m_H - 20$ GeV $< m_{bb} < m_H + 20$ GeV for the $n_b = 2$ category, and $0.85 \cdot m_H - 25$ GeV $< m_{bb} < m_H + 50$ GeV for the $n_b \geq 3$ category. The region after the application of the m_{bb} window is the signal region. The event selection is summarised in Figure 5.3. The $\sqrt{\Sigma p_T^2}/m_{\ell\ell bb}$ cut, and the boundaries of the m_{bb} windows have been optimised as described in Section 5.3.

In this search, the mass distribution of the $\ell\ell b\bar{b}$ system, $m_{\ell\ell bb}$, for each signal hypothesis is used to extract the signal after the corresponding m_{bb} window is applied. To improve the resolution of the $\ell\ell b\bar{b}$ spectrum, the four momentum of the $\ell\ell$ and $b\bar{b}$ system is scaled by $m_Z/m_{\ell\ell}$ ($m_Z = 91.187$GeV [17]) and m_H/m_{bb} (m_H is the assumed H boson mass for each signal region), respectively. As a result, the resolution can be improved by a factor of two without distorting the background distributions. Figure 5.4 shows the $m_{\ell\ell bb}$ distribution before and after the mass scaling in one of the signal regions. The improvement of reconstructed A mass resolution after applying the mass scaling is demonstrated by signal samples with $m_A = 500$ GeV and $m_H = 250$ GeV in Figure 5.5.

The effect of the selection criteria on the signal acceptance is shown in Table 5.1 for both signal production mechanisms and for various selection stages for a selection of the of signal (m_A, m_H) pairs used in this search before the $\sqrt{\Sigma p_T^2}/m_{\ell\ell bb}$ cut is applied. The signal acceptance is defined as

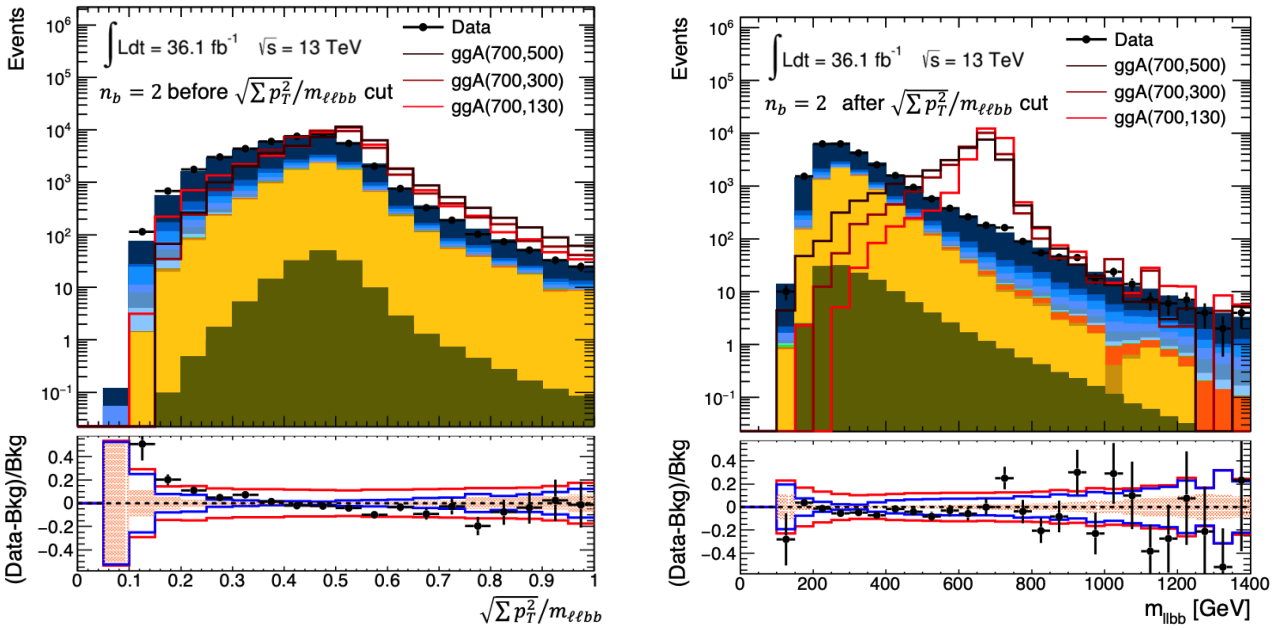

(a) $\sqrt{\Sigma p_T^2}/m_{\ell\ell bb}$ (b) $m_{\ell\ell bb}$ after $\sqrt{\Sigma p_T^2}/m_{\ell\ell bb}$ cut

Figure 5.2: The (a) $\sqrt{\Sigma p_T^2}/m_{\ell\ell bb}$ distribution and the (b) $m_{\ell\ell bb}$ distribution after the $\sqrt{\Sigma p_T^2}/m_{\ell\ell bb}$ cut. Only events in $n_b = 2$ category are shown. For the background simulated samples, color code shown in Figure 3.5 has been used. At the bottom panel, the filled area represent the statistical uncertainties, while the blue line shows the combined uncertainty from statistical and shape uncertainties. The total uncertainty which combines statistical and systematic uncertainties are also shown as a red line. Figures for these distributions in the $n_b \geq 3$ category can be found in Appendix B.

the number of signal events after the selection divided by the number of generated signal events. In Table 5.1, the first column refer to the stage before the E_T^{miss} significance < 3.5 selection, while second column refer to the stage after the E_T^{miss} significance < 3.5 selection. The last two columns show the signal acceptance in the $n_b = 2$ and $n_b \geq 3$ categories, respectively. The effect of the selection criteria in the signal acceptance after the $\sqrt{\Sigma p_T^2}/m_{\ell\ell bb}$ cut and in the corresponding signal regions are shown in Table 5.2.

The signal region that is used to extract the final result of the fit is defined for each m_H hypothesis after the m_{bb} window requirement. In each of these windows, the $m_{\ell\ell bb}$ distribution, after the improvement in the resolution using the technique described previously, is fitted assuming different m_A hypotheses. The fit uses the data distributions and the background estimation described in Section 5.2.

In order to avoid bias, the optimization of the selection requirement described in this section has been preformed without considering the data in the signal region. During the development of the selection strategy, data is masked in any region after the m_{bb} window requirement in the $n_b = 2$ and $n_b \geq 3$ categories.

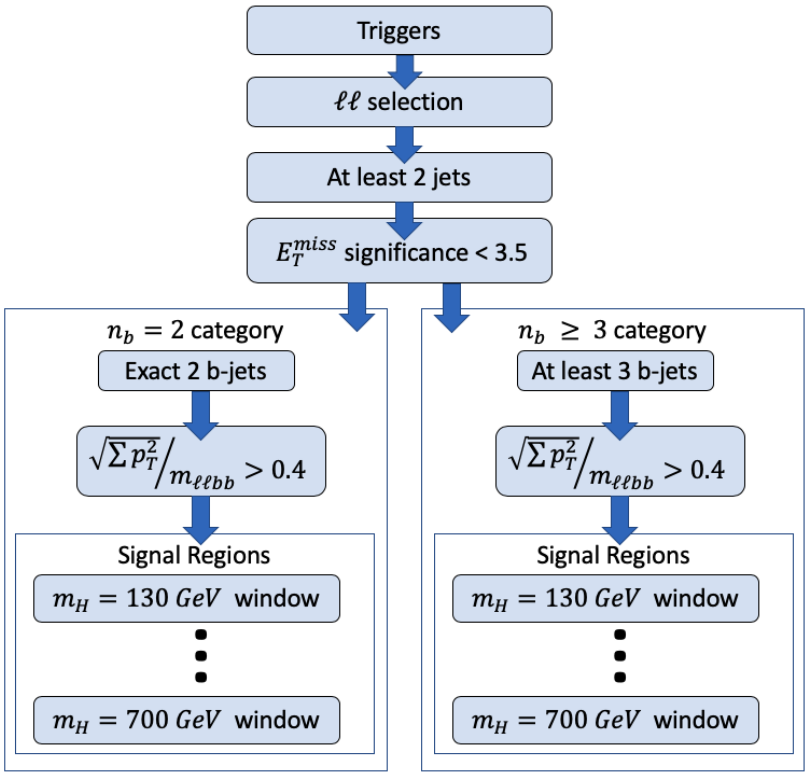

Figure 5.3: The sketch of selection processes for $A \to ZH \to \ell\ell b\bar{b}$ analysis.

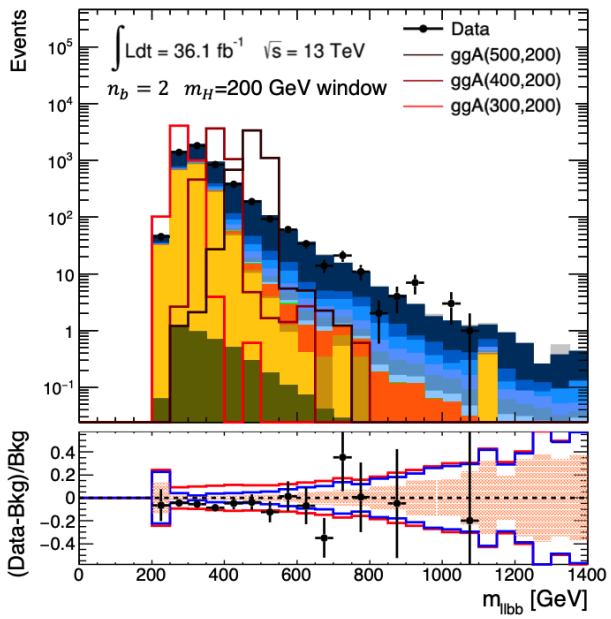

(a) $m_{\ell\ell bb}$, passed $m_H = 200$ GeV window

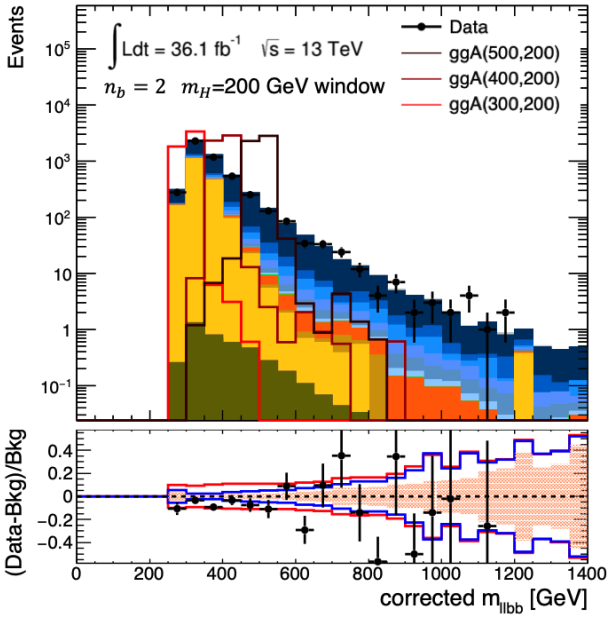

(b) $m_{\ell\ell bb}$ with mass scaling, passed $m_H = 200$ GeV window

Figure 5.4: The $m_{\ell\ell bb}$ distribution (a) without and (b) with the mass scaling in the signal regions after the $\sqrt{\Sigma p_T^2}/m_{\ell\ell bb}$ cut and the m_{bb} window in the $n_b = 2$ category. For the background simulated samples, color code shown in Figure 3.5 has been used. At the bottom panel, the filled area represent the statistical uncertainties, while the blue line shows the combined uncertainty from statistical and shape uncertainties. The total uncertainty which combines statistical and systematic uncertainties are also shown as a red line. Figures for these distributions in the $n_b \geq 3$ category can be found in Appendix. B.

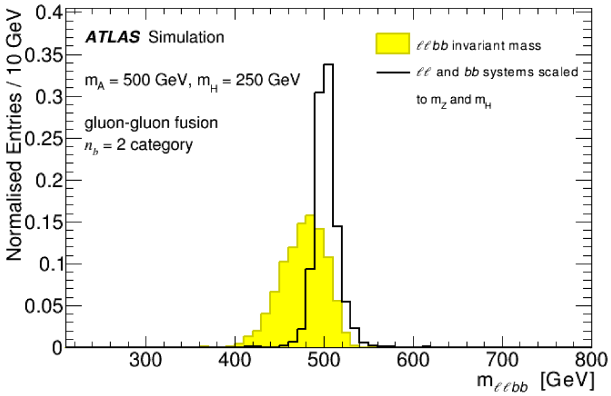

(a) $n_b = 2$ category

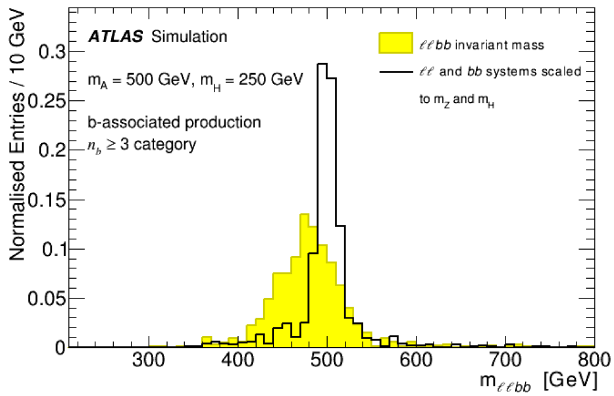

(b) $n_b \geq 3$ category

Figure 5.5: The signal $m_{\ell\ell bb}$ distribution shapes calculated by taking the mass of the $\ell\ell b\bar{b}$ system (filled histograms) and after scaling the $b\bar{b}$ and $\ell\ell$ systems with respected to the hypothetic H boson mass and the Z boson mass (lines) for (a) the gluon-gluon fusion in the $n_b = 2$ category and (b) b-associated production in the $n_b \geq 3$ category of a A boson assuming $m_A = 500$ GeV and $m_H = 250$ GeV.

Signal acceptance: gluon-gluon fusion samples					
m_A (GeV)	m_H (GeV)	before E_T^{miss} significance cut	after E_T^{miss} significance cut	$n_b = 2$ category	$n_b \geq 3$ category
230	130	0.2030 ± 0.0033	0.1926 ± 0.0033	0.0721 ± 0.0011	0.00208 ± 0.00021
250	130	0.2441 ± 0.0036	0.2325 ± 0.0035	0.0857 ± 0.0012	0.00310 ± 0.00026
300	130	0.2992 ± 0.0038	0.2852 ± 0.0038	0.1036 ± 0.0014	0.00338 ± 0.00025
300	200	0.2615 ± 0.0037	0.2456 ± 0.0036	0.1113 ± 0.0014	0.00347 ± 0.00029
400	130	0.3631 ± 0.0040	0.3434 ± 0.0040	0.1322 ± 0.0016	0.00449 ± 0.00029
400	200	0.3606 ± 0.0040	0.3390 ± 0.0039	0.1437 ± 0.0017	0.00568 ± 0.00033
500	130	0.3906 ± 0.0041	0.3637 ± 0.0040	0.1423 ± 0.0016	0.00526 ± 0.00033
500	200	0.4018 ± 0.0041	0.3746 ± 0.0040	0.1596 ± 0.0017	0.00705 ± 0.00044
500	300	0.3775 ± 0.0040	0.3501 ± 0.0040	0.1562 ± 0.0017	0.00821 ± 0.00048
500	400	0.2956 ± 0.0038	0.2671 ± 0.0037	0.1264 ± 0.0015	0.00609 ± 0.00038
700	130	0.4227 ± 0.0041	0.3833 ± 0.0040	0.1563 ± 0.0017	0.00677 ± 0.00044
700	200	0.4288 ± 0.0041	0.3904 ± 0.0041	0.1665 ± 0.0018	0.00801 ± 0.00045
700	300	0.4366 ± 0.0041	0.3973 ± 0.0041	0.1716 ± 0.0018	0.00954 ± 0.00044
700	400	0.4214 ± 0.0041	0.3818 ± 0.0040	0.1717 ± 0.0018	0.00865 ± 0.00043
700	500	0.3994 ± 0.0041	0.3563 ± 0.0040	0.1591 ± 0.0017	0.01001 ± 0.00052
Signal acceptance: b-associated production samples					
m_A (GeV)	m_H (GeV)	before E_T^{miss} significance cut	after E_T^{miss} significance cut	$n_b = 2$ category	$n_b \geq 3$ category
230	130	0.2174 ± 0.0034	0.2022 ± 0.0033	0.0816 ± 0.0021	0.0327 ± 0.0013
250	130	0.2502 ± 0.0036	0.2333 ± 0.0035	0.0955 ± 0.0022	0.0347 ± 0.0013
300	130	0.2904 ± 0.0038	0.2719 ± 0.0037	0.1076 ± 0.0025	0.0457 ± 0.0015
300	200	0.2849 ± 0.0038	0.2654 ± 0.0037	0.1193 ± 0.0026	0.0485 ± 0.0017
400	130	0.3410 ± 0.0039	0.3153 ± 0.0039	0.1281 ± 0.0027	0.0555 ± 0.0017
400	200	0.3401 ± 0.0039	0.3157 ± 0.0039	0.1362 ± 0.0028	0.0584 ± 0.0018
400	300	0.3065 ± 0.0038	0.2793 ± 0.0037	0.1229 ± 0.0027	0.0622 ± 0.0018
500	130	0.3744 ± 0.0040	0.3449 ± 0.0040	0.1391 ± 0.0028	0.0656 ± 0.0019
500	200	0.3678 ± 0.0040	0.3406 ± 0.0039	0.1429 ± 0.0029	0.0695 ± 0.0020
500	300	0.3530 ± 0.0040	0.3267 ± 0.0039	0.1421 ± 0.0029	0.0736 ± 0.0020
500	400	0.3167 ± 0.0039	0.2840 ± 0.0038	0.1248 ± 0.0027	0.0671 ± 0.0019
700	130	0.3958 ± 0.0041	0.3587 ± 0.0040	0.1472 ± 0.0030	0.0763 ± 0.0021
700	200	0.3978 ± 0.0041	0.3605 ± 0.0040	0.1481 ± 0.0030	0.0804 ± 0.0022
700	300	0.3930 ± 0.0041	0.3585 ± 0.0040	0.1524 ± 0.0030	0.0813 ± 0.0023
700	400	0.3889 ± 0.0041	0.3509 ± 0.0040	0.1500 ± 0.0030	0.0808 ± 0.0023
700	500	0.3625 ± 0.0040	0.3240 ± 0.0039	0.1378 ± 0.0029	0.0747 ± 0.0022

Table 5.1: Signal acceptance for gluon fusion and b-associated production samples in early selection stages. Only some of the signal samples are shown in this table. Only uncertainties due to the finite number of generated events in the simulated samples are considered.

Signal acceptance: gluon-gluon fusion samples					
m_A	m_H	$n_b = 2$ category		$n_b \geq 3$ category	
(GeV)	(GeV)	after $\sqrt{\Sigma p_T^2}/m_{\ell\ell bb}$ cut	signal regions	after $\sqrt{\Sigma p_T^2}/m_{\ell\ell bb}$ cut	signal regions
230	130	0.0667 ± 0.0010	0.0578 ± 0.0009	0.00152 ± 0.00017	0.00087 ± 0.00014
250	130	0.0786 ± 0.0012	0.0682 ± 0.0011	0.00250 ± 0.00023	0.00169 ± 0.00021
300	130	0.0888 ± 0.0013	0.0769 ± 0.0012	0.00261 ± 0.00022	0.00148 ± 0.00018
300	200	0.0991 ± 0.0014	0.0732 ± 0.0012	0.00302 ± 0.00028	0.00189 ± 0.00024
400	130	0.1106 ± 0.0015	0.0947 ± 0.0014	0.00324 ± 0.00024	0.00163 ± 0.00018
400	200	0.1218 ± 0.0015	0.0895 ± 0.0013	0.00462 ± 0.00030	0.00245 ± 0.00023
500	130	0.1186 ± 0.0015	0.1019 ± 0.0014	0.00409 ± 0.00030	0.00248 ± 0.00023
500	200	0.1317 ± 0.0016	0.0993 ± 0.0014	0.00564 ± 0.00034	0.00312 ± 0.00025
500	300	0.1335 ± 0.0016	0.0854 ± 0.0012	0.00696 ± 0.00045	0.00352 ± 0.00031
500	400	0.1080 ± 0.0014	0.0639 ± 0.0011	0.00534 ± 0.00035	0.00264 ± 0.00025
700	130	0.1272 ± 0.0016	0.1110 ± 0.0014	0.00538 ± 0.00035	0.00345 ± 0.00027
700	200	0.1337 ± 0.0016	0.1034 ± 0.0014	0.00603 ± 0.00040	0.00315 ± 0.00029
700	300	0.1414 ± 0.0016	0.0914 ± 0.0013	0.00737 ± 0.00038	0.00398 ± 0.00028
700	400	0.1429 ± 0.0016	0.0867 ± 0.0013	0.00717 ± 0.00040	0.00326 ± 0.00026
700	500	0.1325 ± 0.0016	0.0736 ± 0.0011	0.00842 ± 0.00048	0.00357 ± 0.00035
Signal acceptance: b-associated production samples					
m_A	m_H	$n_b = 2$ category		$n_b \geq 3$ category	
(GeV)	(GeV)	after $\sqrt{\Sigma p_T^2}/m_{\ell\ell bb}$ cut	signal regions	after $\sqrt{\Sigma p_T^2}/m_{\ell\ell bb}$ cut	signal regions
230	130	0.0658 ± 0.0019	0.0498 ± 0.0017	0.0240 ± 0.0011	0.0191 ± 0.0010
250	130	0.0743 ± 0.0019	0.0550 ± 0.0017	0.0233 ± 0.0011	0.0184 ± 0.0010
300	130	0.0797 ± 0.0021	0.0551 ± 0.0018	0.0307 ± 0.0012	0.0217 ± 0.0010
300	200	0.0940 ± 0.0023	0.0566 ± 0.0018	0.0379 ± 0.0015	0.0266 ± 0.0013
400	130	0.0944 ± 0.0023	0.0620 ± 0.0019	0.0381 ± 0.0015	0.0245 ± 0.0012
400	200	0.1039 ± 0.0025	0.0605 ± 0.0019	0.0419 ± 0.0016	0.0277 ± 0.0013
500	130	0.1034 ± 0.0024	0.0648 ± 0.0019	0.0463 ± 0.0016	0.0274 ± 0.0013
500	200	0.1074 ± 0.0025	0.0629 ± 0.0019	0.0503 ± 0.0017	0.0299 ± 0.0013
500	300	0.1132 ± 0.0026	0.0555 ± 0.0018	0.0575 ± 0.0018	0.0330 ± 0.0014
500	400	0.0961 ± 0.0024	0.0411 ± 0.0016	0.0553 ± 0.0018	0.0304 ± 0.0013
700	130	0.1087 ± 0.0026	0.0653 ± 0.0021	0.0548 ± 0.0018	0.0334 ± 0.0014
700	200	0.1136 ± 0.0026	0.0631 ± 0.0020	0.0578 ± 0.0019	0.0338 ± 0.0015
700	300	0.1156 ± 0.0026	0.0557 ± 0.0019	0.0595 ± 0.0020	0.0356 ± 0.0015
700	400	0.1178 ± 0.0027	0.0498 ± 0.0017	0.0640 ± 0.0020	0.0352 ± 0.0015
700	500	0.1076 ± 0.0025	0.0410 ± 0.0016	0.0589 ± 0.0020	0.0319 ± 0.0014

Table 5.2: Signal acceptance after the $\sqrt{\Sigma p_T^2}/m_{\ell\ell bb}$ cut and for the signal regions in both $n_b = 2$ and $n_b \geq 3$ categories. Only some of the signal samples are shown in this table. Only uncertainties due to the finite number of generated events in the simulated samples are considered.

5.2 Background Estimation

The dominant background to the $A \to ZH \to \ell\ell b\bar{b}$ signal process comes from the production of a Z boson in association with jets, which will be referred to as "Z+jets production" in the following, and the top-quark pair ($t\bar{t}$) production. Figure 5.6 shows example Feynman diagrams of the Z+jets production and the $t\bar{t}$ production.

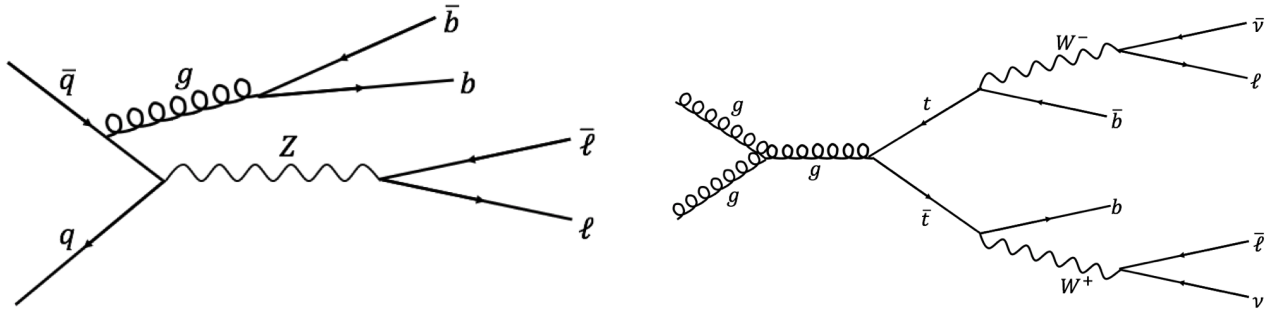

(a) Z+jets production (b) $t\bar{t}$ production

Figure 5.6: Example Feynman diagrams of the (a) Z+jets production and the (b) $t\bar{t}$ production.

The Z+jets production becomes more and more dominant as the lower end of the $m_{\ell\ell bb}$ spectrum is approached. The main source of this background in the $n_b = 2$ category originates from Z boson produced along with a pair of b-jets, which is estimated using simulation to be about 61% to 74% of the total Z+jets backgrounds, depending on the m_{bb} window. Similarly, in the $n_b \geq 3$ category, the main source of Z+jets production is from a Z boson produced in association with a pair of b-jets and another jet that passes the b-tagging requirement. The flavour composition of this additional jet after the events have passed the $\sqrt{\Sigma p_T^2}/m_{\ell\ell bb}$ requirement is about 74% of the time is a b-jet. In fact, the processes of Z production in association with several jets is a process that is difficult to estimate precisely the cross section in the simulation. Thus, using some control region to derive a normalisation would decrease the associated uncertainties. In addition, because it is difficult to have a dedicated control region that is orthogonal to all signal regions in this search, a sideband region is considered as the control region of Z+jets production for each of the signal region. The sideband region is defined by inverting the m_{bb} window ($m_{bb} < 0.85 \cdot m_H - 20$ GeV and $m_{bb} > m_H + 20$ GeV for the $n_b = 2$ category, $m_{bb} < 0.85 \cdot m_H - 25$ GeV and $m_{bb} > m_H + 50$ GeV for the $n_b \geq 3$ category). These regions may have significant contamination from $t\bar{t}$ background. However, this method will prove successful since the $t\bar{t}$ production can be controlled in a pure control region as explained in the following paragraph.

A top-quark pair decaying in the fully leptonic channel contains two b-jets and two leptons at the lowest order as shown in Figure 5.6(b). The flavour of the leptons can be identical (ee or $\mu\mu$ pairs) of different ($e\mu$ pairs). The $t\bar{t}$ background with same flavour leptons constitutes the source of background for the signal region, whereas when the two leptons have different flavour can form an excellent top control region that is naturally orthogonal to all signal regions. The $t\bar{t}$ background in the $n_b = 2$ category comes from the lowest order Feynman diagram directly, and hence it is expected to be well modelled by the simulation. It is relatively more important at higher m_{bb} windows as most of the $t\bar{t}$ events are peaked around $m_{\ell\ell bb} = 2m_t$ and the $t\bar{t}$ events which are peaked around $m_{bb} = m_t$, it is difficult to estimate precisely the cross section in the high m_{bb} (≥ 400 GeV) and $m_{\ell\ell bb}$ (≥ 600 GeV) region. On the other hand, in the $n_b \geq 3$ category this background is formed by the $t\bar{t}$ production in association with jets. This process is more difficult to simulate, and therefore larger differences with respect to the simulation are expected.

Before the final signal extraction, a scale factor has been used to compare the shape of the distributions in the plots and examine how well the cross section is estimated in simulation before and after the $\sqrt{\Sigma p_T^2}/m_{\ell\ell bb}$ cut. The scale factor of $t\bar{t}$ is calculated assuming that all non-$t\bar{t}$ contributions in the control region are predicted correctly by the simulation. The scale factor of Z+jets are calculated in a similar way after the $t\bar{t}$ scale factor has been applied. In order to calculate these scale factor, the shape of the backgrounds is taken directly from the simulated samples, and then it is compared against the data. These scale factors are only for demonstration in the plots before the fit. The fitted value will eventually being used in the final signal extraction, see Table 5.7.

5.2.1 Top background

The top control region, after the various m_{bb} window requirements, are applied along the corresponding signal region to determine the $t\bar{t}$ normalisation. The normalisation of the $t\bar{t}$ background has been checked before the m_{bb} window is applied. The scale factors before and after the $\sqrt{\Sigma p_T^2}/m_{\ell\ell bb}$ cut are shown in Table 5.3. The difference of the scale factors between $n_b = 2$ and $n_b \geq 3$ categories is expected. This is due to the fact that most of the events contain 2 b-jets from the $t\bar{t}$ decays in the $n_b = 2$ category of the top control region. In the $n_b \geq 3$ category, most of the events comes from the $t\bar{t}$ production in association with jets, which is difficult to simulate as mentioned before. Thus, the scale factor in this category is expected to be different from the one in $n_b = 2$ category.

Figure 5.7 shows the scale factor as a function of m_{bb} in $n_b = 2$ and $n_b \geq 3$ categories of the top control region, respectively. In this figure, the scale factors before and after $\sqrt{\Sigma p_T^2}/m_{\ell\ell bb}$ cut are shown as straight lines across the m_{bb} spectrum, while the scale factors after m_{bb} window with respect to different m_H assumptions are presented with statistical uncertainties across the corresponding m_{bb} window. The statistical uncertainties in the regions corresponding to higher m_H become larger because they contain relatively fewer events compare to other regions. Also, the scale factors in these regions are different with respect to the inclusive one, which is derived before the m_{bb} windows requirement is applied. This is due to the difficulty of modelling m_{bb} in such high m_{bb} region as mentioned in Section 5.2.

The m_{bb} and $m_{\ell\ell bb}$ distributions with and without mass scaling of the top control region in $n_b = 2$ category are shown in Figure 5.8. The corresponding scale factor has been applied. This control region after the m_{bb} window will be included in the final signal extraction. The $t\bar{t}$ background in $n_b = 2$ and $n_b \geq 3$ categories is fitted separately.

	Before $\sqrt{\Sigma p_T^2}/m_{\ell\ell bb}$ cut		After $\sqrt{\Sigma p_T^2}/m_{\ell\ell bb}$ cut	
	$n_b = 2$	$n_b \geq 3$	$n_b = 2$	$n_b \geq 3$
Data:	8464	365	6624	259
Rest:	20.553 ± 3.062	0.47 ± 0.20	13.91 ± 2.73	0.41 ± 0.20
Top:	8227.74 ± 60.45	264.00 ± 11.62	6520.12 ± 54.09	196.91 ± 10.16
Scale factor	1.027 ± 0.014	1.381 ± 0.095	1.014 ± 0.015	1.31 ± 0.11

Table 5.3: The number of events before and after the $\sqrt{\Sigma p_T^2}/m_{\ell\ell bb}$ cut used for the calculation of $t\bar{t}$ scale factor in the control region of $n_b = 2$ and $n_b \geq 3$ categories. Only uncertainties due to the finite number of generated events in the simulated samples are shown.

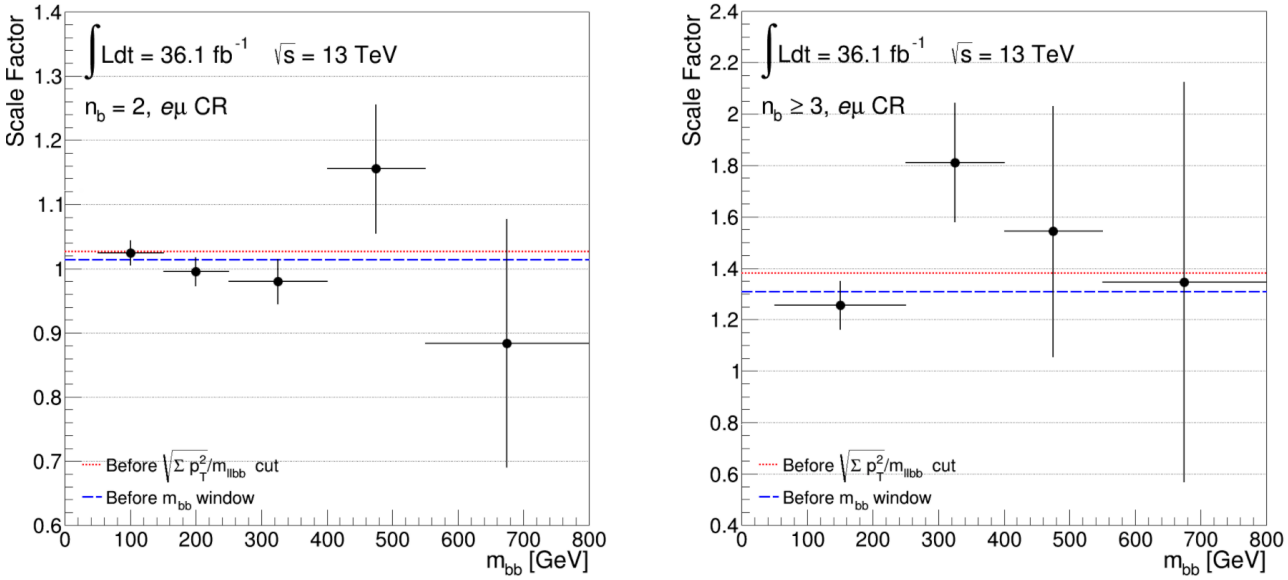

(a) $n_b = 2$ category

(b) $n_b \geq 3$ category

Figure 5.7: Scale factors of $t\bar{t}$ background as a function of m_{bb} in top control region of (a) $n_b = 2$ and(b) $n_b \geq 3$ categories for several selection requirements. This scale factor is not used in the fit, see Section 5.6 for more details. Statistical uncertainties from the data and systematic uncertainties that are due to the finite number of simulated events are considered.

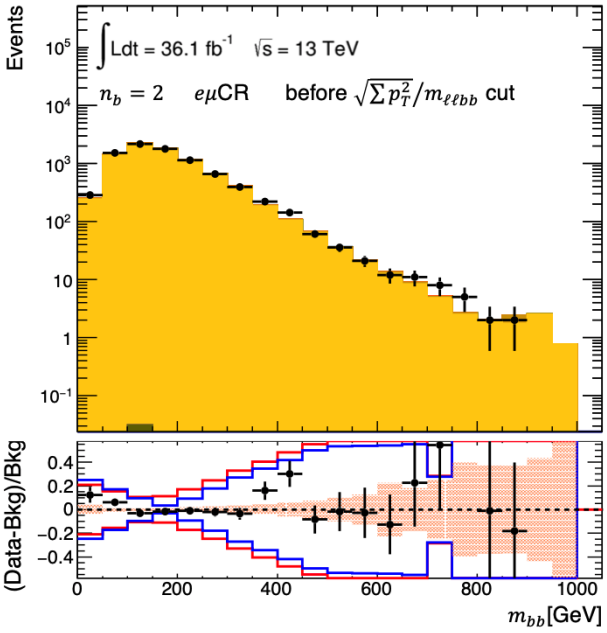

(a) m_{bb}

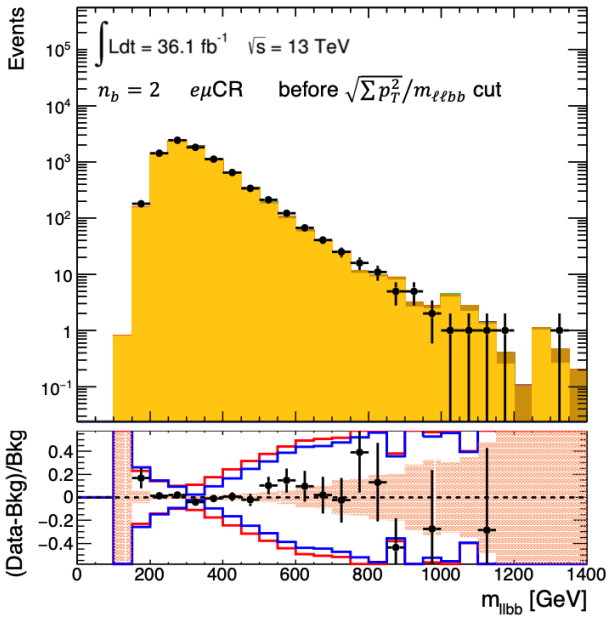

(b) $m_{\ell\ell bb}$

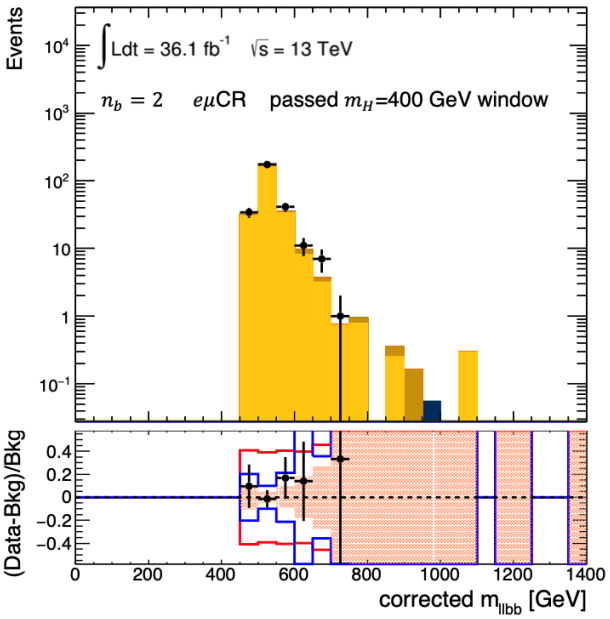

(c) $m_{\ell\ell bb}$ with mass scaling, passed $m_H = 400$ GeV window

Figure 5.8: The (a) m_{bb}, (b) $m_{\ell\ell bb}$ distributions before the $\sqrt{\Sigma p_T^2}/m_{\ell\ell bb} > 0.4$ cut and the (c) $m_{\ell\ell bb}$ with mass scaling for the top control region in the $n_b = 2$ category. For the background simulated samples, color code shown in Figure 3.5 has been used. At the bottom panel, the filled area represents the statistical uncertainties, while the blue line shows the combined uncertainty from statistical and shape uncertainties. The total uncertainty which combines statistical and systematic uncertainties is also shown as a red line. Figures for these distributions in the $n_b \geq 3$ category can be found in Appendix B.

5.2.2 Z+jets background

As mentioned in Section 5.2, it is not possible to define a dedicated Z+jets control region orthogonal to all the signal regions used in this search. Therefore, a sideband region for each signal region has been used. This region is defined as the region outside the m_{bb} window. During the development of the selection strategy, the normalisation of the Z+jets backgrounds is estimated by an inclusive scale factor before and after the $\sqrt{\Sigma p_T^2}/m_{\ell\ell bb}$ cut in order to check the description of the shapes in the simulation. These scale factors are shown in Table 5.4, which is calculated after corrected the normalisation of $t\bar{t}$ background. Figure 5.9 shows the scale factor as a function of m_{bb} in the $n_b = 2$ and $n_b \geq 3$ categories. In this figure, the scale factors before and after $\sqrt{\Sigma p_T^2}/m_{\ell\ell bb}$ cut are shown as straight lines across the m_{bb} spectrum, while the scale factors after m_{bb} window with respect to different m_H assumptions are presented with statistical uncertainties across the corresponding m_{bb} window. The m_{bb}, $m_{\ell\ell bb}$ and corrected $m_{\ell\ell bb}$ distributions in the $n_b = 2$ category after the application of $t\bar{t}$ and Z+jets scale factors are shown in Figure 5.10.

	Before $\sqrt{\Sigma p_T^2}/m_{\ell\ell bb}$ cut		After $\sqrt{\Sigma p_T^2}/m_{\ell\ell bb}$ cut	
Categories	$n_b = 2$	$n_b \geq 3$	$n_b = 2$	$n_b \geq 3$
Data:	41349	1403	25238	883
Rest:	9445.03 $\pm$ 63.64	442.52 $\pm$ 19.73	7345.56 $\pm$ 55.73	317.20 $\pm$ 16.40
Z:	25699.06 $\pm$ 133.59	833.39 $\pm$ 21.88	15016.60 $\pm$ 83.99 $\pm$ 84	477.84 $\pm$ 16.31
Scale factor	1.2411 $\pm$ 0.0069	1.152 $\pm$ 0.037	1.1916 $\pm$ 0.0076	1.184 $\pm$ 0.053
Z+jets sample break-up				
Zl + Zcl	504.91 $\pm$ 1.54	12.30 $\pm$ 10.82	262.17 $\pm$ 0.98	4.02 $\pm$ 4.24
Zcc	832.48 $\pm$ 4.88	21.47 $\pm$ 6.85	488.63 $\pm$ 3.23	14.88 $\pm$ 6.63
Zbl	1260.58 $\pm$ 56.15	91.15 $\pm$ 7.67	692.64 $\pm$ 37.66	44.56 $\pm$ 6.13
Zbc	1685.70 $\pm$ 38.61	145.694 $\pm$ 12.023	970.12 $\pm$ 26.57	77.80 $\pm$ 10.42
Zbb	21415.41 $\pm$ 114.79	562.78 $\pm$ 10.56	12603.04 $\pm$ 70.13	336.61 $\pm$ 7.61

Table 5.4: The number of events before and after the $\sqrt{\Sigma p_T^2}/m_{\ell\ell bb}$ cut used for the calculation of the Z+jets inclusive scale factor for the $n_b = 2$ and $n_b \geq 3$ categories. The normalisation of $t\bar{t}$ background is corrected before the calculation. Only uncertainties due to the finite number of generated events in the simulated samples are shown.

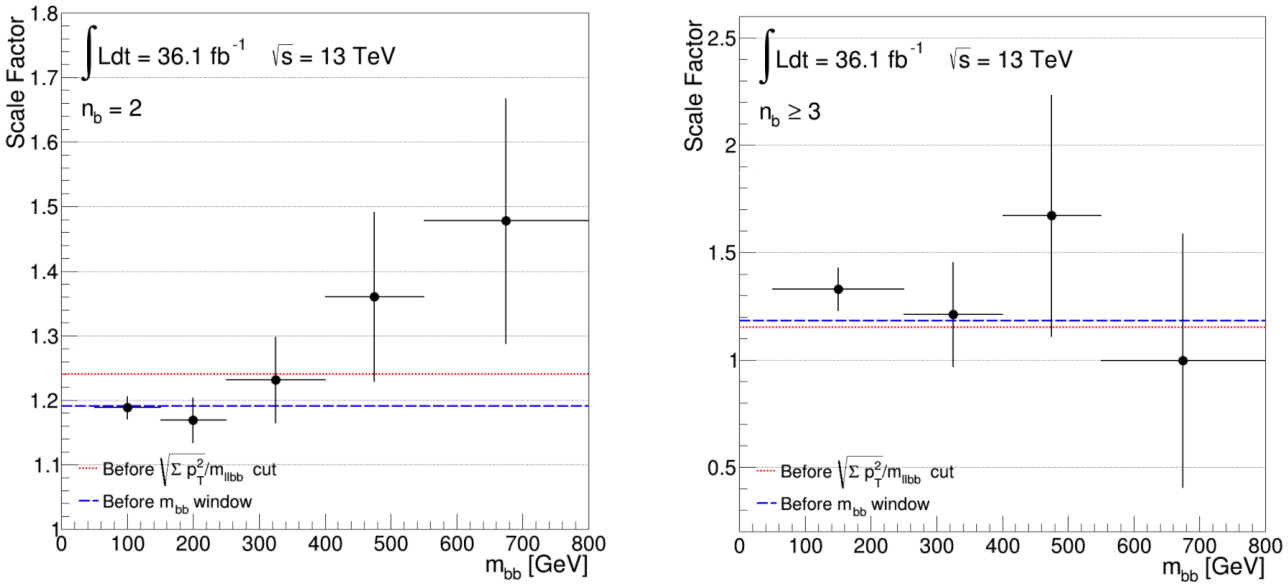

(a) m_{bb} in $n_b = 2$ category

(b) $n_b \geq 3$ category

Figure 5.9: Scale factors of Z+jets background as a function of m_{bb} in (a) $n_b = 2$ and (b) $n_b \geq 3$ categories for several selection requirements. This scale factor is not used in the fit, see Section 5.6 for more details. Statistical uncertainties from the data and systematic uncertainties that are due to the finite number of simulated events are considered.

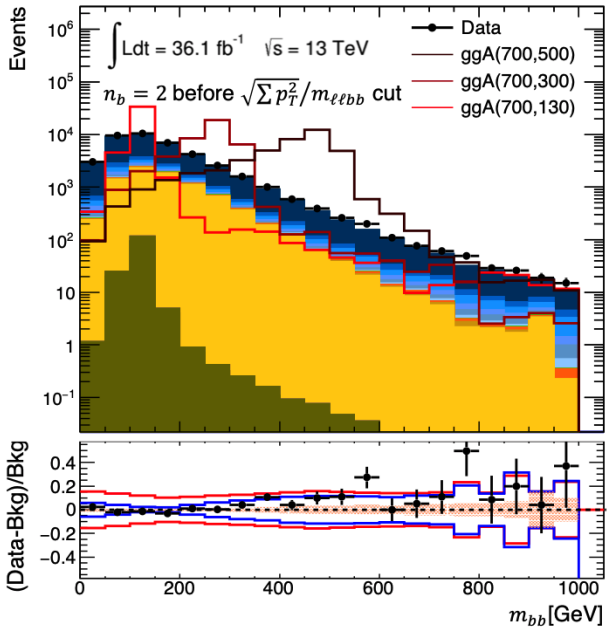

(a) m_{bb}

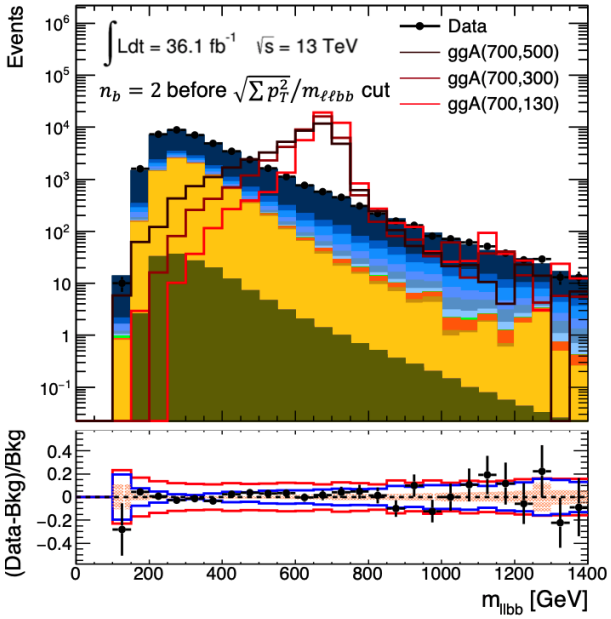

(b) $m_{\ell\ell bb}$

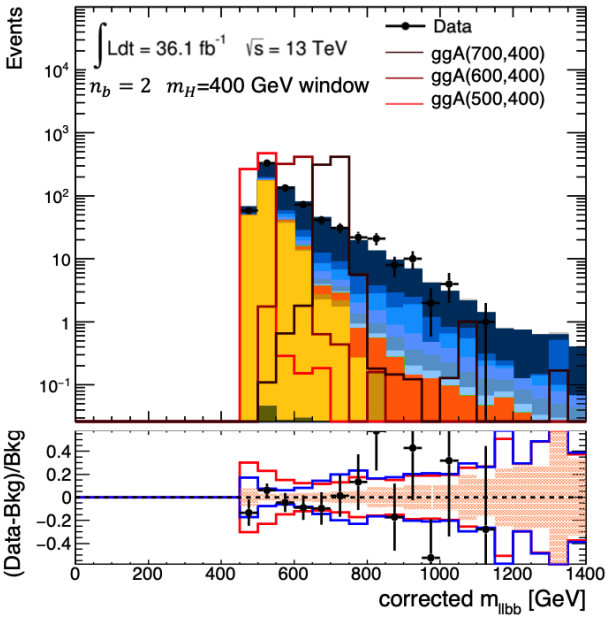

(c) $m_{\ell\ell bb}$ with mass scaling, passed $m_H = 400$ GeV window

Figure 5.10: The (a) m_{bb}, (b) $m_{\ell\ell bb}$ distributions before the $\sqrt{\Sigma p_T^2}/m_{\ell\ell bb} > 0.4$ cut and the (c) $m_{\ell\ell bb}$ distribution with mass scaling in the $n_b = 2$ category. Both $t\bar{t}$ and Z+jets scale factors are applied. For the background simulated samples, the colour code shown in Figure 3.5 has been used. At the bottom panel, the filled area represents the statistical uncertainties, while the blue line shows the combined uncertainty from statistical and shape uncertainties. The total uncertainty which combines statistical and systematic uncertainties are also shown as a red line. Figures for these distributions in the $n_b \geq 3$ category can be found in Appendix B.

5.3 Selection optimisation studies

The selection optimisation study is an important task in this search. The task is to identify variables that can discriminate between signal and background and to optimise their cut values. In this section, two of the specific selection criteria after the E_T^{miss} significance selection are introduced: a cut on the $\sqrt{\Sigma p_T^2}/m_{\ell\ell bb}$ variable and the m_{bb} window requirement for each m_H signal hypothesis. In order to determine the value for a tested variable, the optimisation takes into account only the number of signal and background events, these numbers are used to estimate a significance measure and maximise its value. The number of signal and background events in each histogram bin follows a Poisson distribution. The number of signal events is denoted by s, while the number of background events is denoted by b. For large enough values of b this is approximated by a Gaussian with standard deviation $\sqrt{b}$. A simple significance measure can be defined as [123]:

$$\sigma = s/\sqrt{b}. \tag{5.1}$$

In this search, the significance measure in use is obtained by an approximation for $s << b$, which is more precise and often called the asymptotic significance formula [124]:

$$\sigma = \sqrt{2((s+b)\ln(1+s/b)-s)}, \tag{5.2}$$

the significance is calculated for different cut values in order to find the one that maximises it. Figure 5.11 shows an example of optimisation of the $\sqrt{\Sigma p_T^2}/m_{\ell\ell bb}$ variable with one of the gluon–gluon signals. The bottom panel shows the value of the significance. The integrated number of events from the particular bin to the last bin is considered in the calculation of the significance for each bin. The location where the significance is maximum in the bottom panel indicates the optimal cut. For this particular signal, events with $\sqrt{\Sigma p_T^2}/m_{\ell\ell bb} > 0.55$ passed the selection.

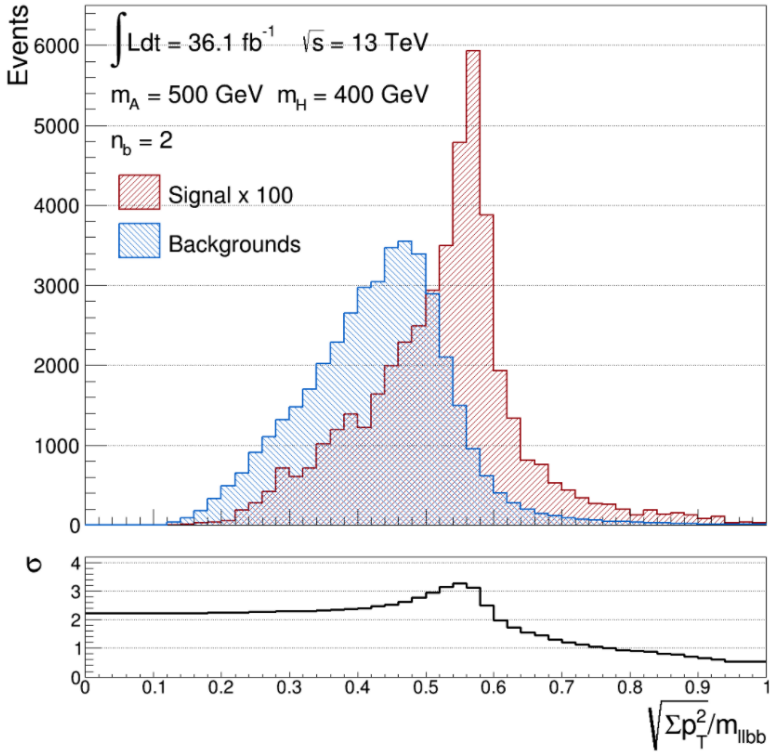

Figure 5.11: The $\sqrt{\Sigma p_T^2}/m_{\ell\ell bb}$ distribution of the backgrounds and one of the signal sample. An ability normalisation has been applied to the distribution of the signal sample. The bottom panel shows the value of σ for each bin of the distribution in the top panel. In this example, signal sample with $m_A = 500$ GeV and $m_H = 400$ GeV has been used.

b-associated production $n_b \geq 3$ category				gluon fusion samples $n_b = 2$ category			
m_A (GeV)	m_H (GeV)	Optimised value without m_{bb}	Optimised value with m_{bb}	m_A (GeV)	m_H (GeV)	Optimised value without m_{bb}	Optimised value with m_{bb}
230	130	0.16	0.38	230	130	0.43	0.43
250	130	0.16	0.34	250	130	0.41	0.40
300	130	0.17	0.28	300	130	0.37	0.35
400	130	0.24	0.24	400	130	0.37	0.26
500	130	0.18	0.24	500	130	0.43	0.47
700	130	0.13	0.13	700	130	0.47	0.49
300	200	0.35	0.38	300	200	0.42	0.43
400	200	0.17	0.38	400	200	0.37	0.39
500	200	0.25	0.38	500	200	0.34	0.41
400	300	0.29	0.42	400	300	0.52	0.51
500	300	0.30	0.36	500	300	0.40	0.40
700	300	0.25	0.36	700	300	0.35	0.38
500	400	0.53	0.50	500	400	0.55	0.54
700	500	0.28	0.36	700	500	0.50	0.43

Table 5.5: Optimised values for the $\sqrt{\Sigma p_T^2}/m_{\ell\ell bb}$ cut for the $n_b \geq 3$ and $n_b = 2$ categories with and without the m_{bb} window cuts. Only some of the signal samples are shown in this table.

The $\sqrt{\Sigma p_T^2}/m_{\ell\ell bb}$ cut has been optimised before and after the application of the m_{bb} window requirement; the optimised values are listed at Table 5.5. Without the m_{bb} window, the average cut value is about 0.4 in $n_b = 2$ category, while it is about 0.3 in $n_b \geq 3$ category. Performing the optimization again with the application of the m_{bb} window, moves the average cut only in the $n_b \geq 3$ category to 0.4. For this reason and in order to simplify the selection, a single cut value of 0.4 is chosen for both categories.

The m_{bb} window is applied after the $\sqrt{\Sigma p_T^2}/m_{\ell\ell bb}$ variable cut. The boundaries of the m_{bb} window depend on the m_H value of each signal hypothesis. The optimisation is done by extending the m_{bb} window starting from $m_H \pm 5$ GeV and going up to $m_H \pm 105$ GeV. Table 5.6 lists the optimised m_{bb} window boundaries for some of the signal hypotheses. Because eventually the signal hypotheses that are tested in this search are more than the simulated samples, see also Section 5.4, a rule is needed to define the m_{bb} window boundaries for arbitrary m_H values. For this reason, a linear function is fitted to the optimised window boundary values obtained by the available simulated points. The result of this procedure is shown in Figure 5.12. The window boundaries used for this search come from these results, and are the following:

$$0.85 \times m_H - 20 \text{ GeV} < m_{bb} < m_H + 20 \text{ GeV } (n_b = 2 \text{ category})$$

and

$$0.85 \times m_H - 25 \text{ GeV} < m_{bb} < m_H + 50 \text{ GeV } (n_b \geq 3 \text{ category}).$$

b-associated production $n_b \geq 3$ category			gluon fusion samples $n_b = 2$ category		
m_A (GeV)	m_H (GeV)	Optimised window	m_A (GeV)	m_H (GeV)	Optimised window
230	130	100 - 180	230	130	105 - 145
250	130	100 - 150	250	130	110 - 145
300	130	105 - 155	300	130	105 - 150
400	130	115 - 145	400	130	105 - 145
500	130	105 - 145	500	130	110 - 145
700	130	115 - 145	700	130	115 - 145
300	200	165 - 230	300	200	160 - 215
400	200	160 - 220	400	200	165 - 220
500	200	160 - 230	500	200	165 - 220
700	200	170 - 220	700	200	170 - 220
400	300	215 - 365	400	300	245 - 325
500	300	215 - 315	500	300	245 - 325
700	300	215 - 380	700	300	255 - 320
500	400	295 - 435	500	400	340 - 425
700	400	295 - 470	700	400	340 - 425
700	500	395 - 555	700	500	425 - 535

Table 5.6: Optimised values for the m_{bb} window for the $n_b \geq 3$ and $n_b = 2$ categories. Only some of the signal samples are shown in this table.

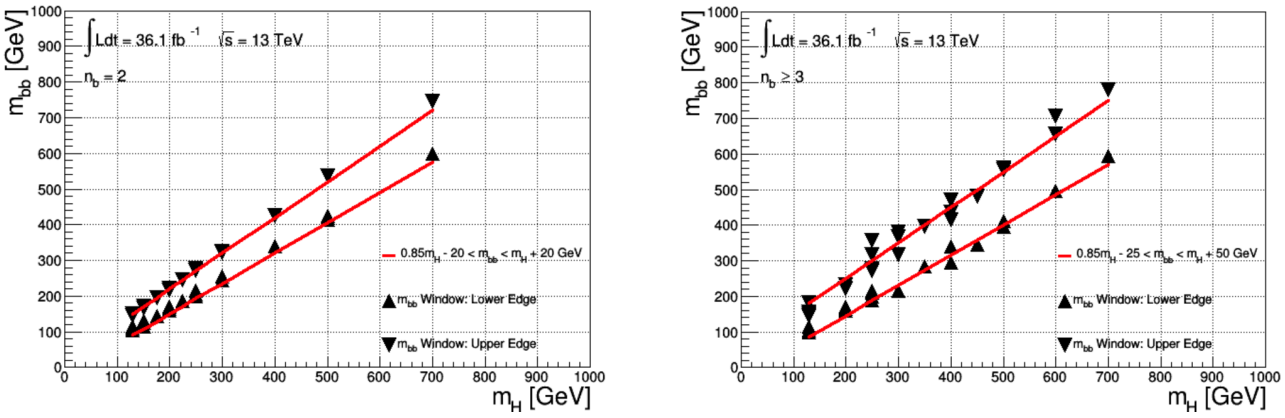

(a) $n_b = 2$ category

(b) $n_b \geq 3$ category

Figure 5.12: The m_{bb} window as a function of m_H for (a) gluon-gluon fusion signal samples in $n_b = 2$ category and (b) b-associated production signal samples in $n_b \geq 3$ category. The values of m_{bb} lower edge and upper edge are listed in Table 5.6.

5.4 Signal modelling

The experimental resolution of the $m_{\ell\ell bb}$ distribution is excellent in this search as shown in Figure 5.5. Therefore, it is necessary to estimate the signal shape at any point in the $m_A - m_H$ plane. However, due to the limitations in computational resources, only a limited number of signal points in the $m_A - m_H$ plane are generated, as shown in Figure 3.4. In order to estimate the signal shape across the whole $m_A - m_H$ plane, a functional forms are used to preform an analytical fit to the signal distribution of the generated signal samples and then interpolate the fit parameters among the different masses on the $m_A - m_H$ plane. This interpolation method has been validated in a region with more tightly spaced generated signal points along $m_A = 500$ GeV and $m_H = 200$ GeV in gluon-gluon fusion as shown in Figure 3.4. This method has the advantage that the systematic uncertainties associated with the interpolation itself can straightforwardly be assigned. In addition, the same procedure is used for the case when the natural width of the A boson is larger than the experimental mass resolution, which is true for part of the 2HDM parameter space that is of interest in this search.

There are two functions being used for analytical fits to the $m_{\ell\ell bb}$ distributions: the *ExpGaussExp* (EGE) function [125]:

$$f_{\mathrm{EGE}}(m;a,\sigma,k_L,k_H) = \begin{cases} \mathrm{e}^{\frac{1}{2}k_L^2+k_L\left(\frac{m-a}{\sigma}\right)} & \\ \mathrm{e}^{-\frac{1}{2}\left(\frac{m-a}{\sigma}\right)^2} & \text{for} \\ \mathrm{e}^{\frac{1}{2}k_H^2-k_H\left(\frac{m-a}{\sigma}\right)} & \end{cases} \begin{cases} \frac{m-a}{\sigma} \leq -k_L \\ -k_L < \frac{m-a}{\sigma} \leq k_H \\ \frac{m-a}{\sigma} > k_H \end{cases}$$

and the double-sided Crystal Ball (DSCB) function [126]:

$$f_{\mathrm{DSCB}}(m;a,\sigma,k_L,k_H,n_1,n_2) = \begin{cases} g(m;a,-\sigma,k_L,n_1)\cdot \mathrm{e}^{-\frac{1}{2}k_L^2} & \\ \mathrm{e}^{-\frac{1}{2}\left(\frac{m-a}{\sigma}\right)^2} & \text{for} \\ g(m;a,\sigma,k_H,n_2)\cdot \mathrm{e}^{\frac{1}{2}k_H^2} & \end{cases} \begin{cases} \frac{m-a}{\sigma} \leq -k_L \\ -k_L < \frac{m-a}{\sigma} \leq k_H \\ \frac{m-a}{\sigma} > k_H \end{cases}$$

where $g(m;a,\sigma,k,n) = [(|k|/n)(n/|k| - |k| + (m-a)/\sigma)]^{-n}$. these functions consist of a Gaussian core with mean a and variance σ^2, whereas the rest of the parameters (k_L, k_H, n_1, n_2) describe the tails. The EGE function uses exponential tails, whereas the DSCB use power-law based tails. It is found that the EGE function can describe the gluon-gluon fusion in the $n_b = 2$ category, while the

DSCB function describes better the b-associated production in both $n_b = 2$ and $n_b \geq 3$ categories. The tail parameters are chosen as a constant value with some dependence on the $(m_A - m_H)$. Then the core parameters is fitted with these tail parameters. As an example of the performance of the interpolation, Figure 5.13 shows a comparison for the $(m_A, m_H) = (500, 250)$ GeV mass point between the simulated distributions and the analytical functions described above. The agreement between the simulated distribution and the interpolated distribution is very good. The differences between the simulation and the interpolated shape divided by the statistical uncertainties are generally in the range from -2 to +2 in both $n_b = 2$ and $n_b \geq 3$ categories.

The parameterisation described above applies to signal samples generated with narrow-width[2] A bosons. In this search, the A boson's width is significant compared with the detector resolution in some regions of a particular parameter space of the 2HDM. The large width signals are optimised for the $A \to ZH$ signature in the context of the 2HDM. For this particular signature, the A boson width that may vary, whereas the H has narrow width. The reason is that the benchmark considered in this search is at the alignment limit, $\cos(\beta - \alpha) = 0$, as mentioned in Chapter 1. Under this scenario, the natural width of H boson is restricted. Also, the m_{bb} window selection is correlated to the narrow-width H boson, therefore the acceptance of the large width samples is expected to be the same as the narrow-width samples. The drawback of this approach is that the results cannot be used to interpret the search for the $H \to ZA$ decay. In that case, the large width of the A will lead to different distributions and different acceptance with respect to this search. In order to model the $m_{\ell\ell bb}$ shape of A bosons with large natural widths, a modified Breit–Wigner distribution is convolved with the EGE and DSCB functions [115]. The modification is the multiplication of the Breit–Wigner distribution with a log-normal distribution to account for the distortion due to the event selection. The procedure is validated by comparing the results of the convolution with those of the simulated samples of A bosons with large natural widths. Widths of up to 20% of the A boson mass are considered. An example of signal distributions with large natural widths is shown in Figure 5.14 for the same signal points used in Figure 5.13.

[2]narrow-width: In this search the narrow-width A boson is considered with Γ_A = 1 GeV

Finally, the signal efficiencies for the interpolated mass points are obtained through separate two-dimensional interpolations on the (m_A, m_H) plane using thin plate splines [127]. The uncertainties are assessed by comparing the interpolated signal yield and the generated yield for each generated signal points when that point is left out of the interpolation input. It is found that a 5.5% uncertainty on the signal acceptance due to the yield interpolation generally covers the difference between the generated and interpolated acceptances in the (m_A, m_H) plane. Therefore, this additional uncertainty is applied to each signal point in the final signal extraction. Also, the change in the signal acceptance due to the A boson's large width is studied and a flat uncertainty of 2% is placed on the signal acceptance when $(\Gamma_A/m_A) > 5\%$.

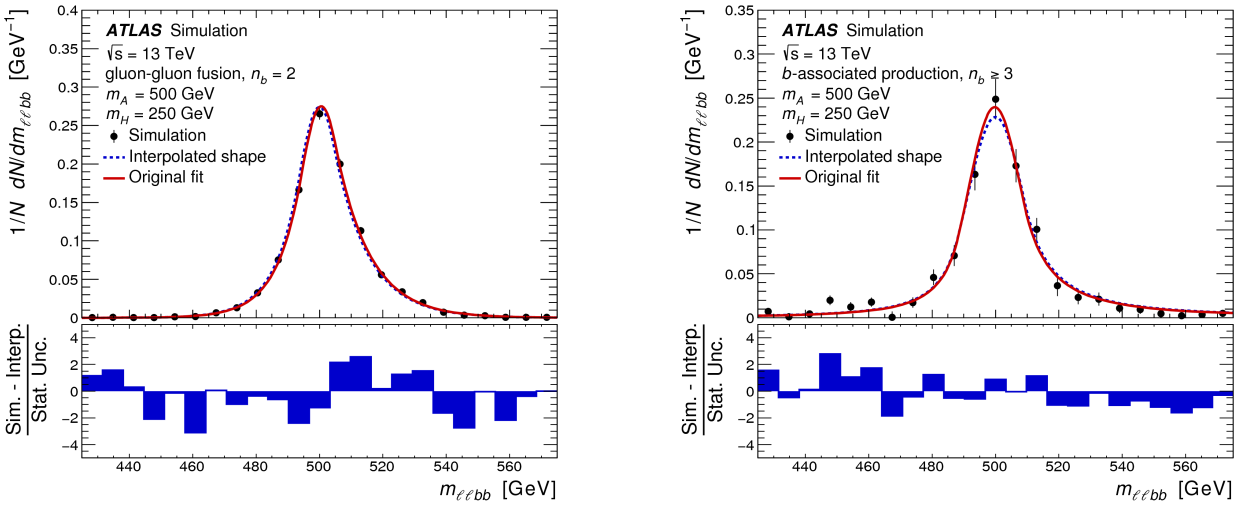

(a) (b)

Figure 5.13: Simulated signal $m_{\ell\ell bb}$ distributions (closed circles) assuming $m_A = 500$ GeV and $m_H = 250$ GeV for the following cases: (a) the gluon fusion in the $n_b = 2$ category and (b) b-associated production in the $n_b \geq 3$ category. Signal parameterisations are overlaid for comparison. The solid curves are from parameter values obtained directly from the fits to the simulated distributions, whereas the dashed curves use the interpolated parameter values. The differences between the simulation and the interpolated shape divided by the statistical uncertainties of the simulation are shown in the bottom panels. From Ref [57].

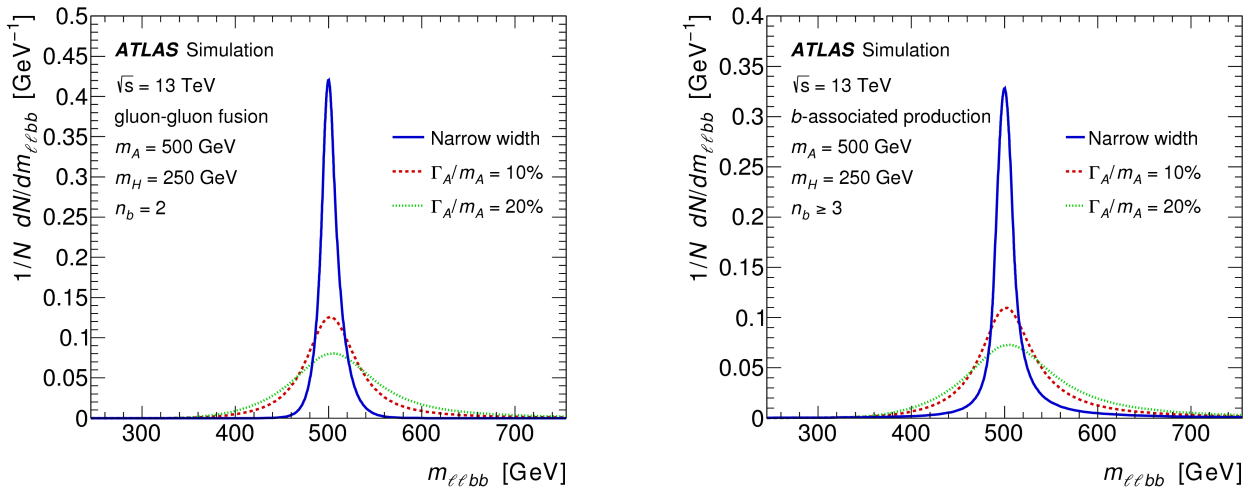

(a) (b)

Figure 5.14: The interpolated signal $m_{\ell\ell bb}$ distribution shapes assuming $m_A = 500$ GeV and $m_H = 250$ GeV and various A boson widths for the following cases: (a) gluon fusion in the $n_b = 2$ category and (b) b-associated production in the $n_b \geq 3$ category. Taken from [57]

5.5 Systematic uncertainties

The ability to constrain a new physics process is limited by both statistical and systematic uncertainties. Systematic uncertainties usually originate from a lack of complete understanding or mismeasurement of the physics objects in the detector or simulation. This section describes the systematic uncertainties considered in this search, which are divided into three groups: experimental uncertainties, background modelling uncertainties and uncertainties related to the simulation programs that were used to generate the signal events.

5.5.1 Experimental uncertainties

The experimental uncertainties are related to luminosity, pileup, physics object reconstruction and identification. There is a 2.1% uncertainty on the measured integrated luminosity of the data. This is derived by calibrating the luminosity scale with $x-y$ beam separation scans, see ref. [128] for details. This uncertainty is applied to all simulated backgrounds except Z + jets and $t\bar{t}$, as their normalisation is determined from control region data.

The uncertainty due to the pile-up re-weighting procedure of the simulated samples is also included in this search. It is estimated using the ratio of the measured over predicted inelastic cross sections in the fiducial region which is defined by the hadronic mass, M_X, with $M_X > 13$ GeV [129].

There are several sources of uncertainties related to the lepton properties: trigger, reconstruction, identification and isolation efficiencies, energy or momentum scale and energy or momentum resolution. The uncertainties related to the trigger efficiency, reconstruction efficiency, identification and isolation efficiencies have p_T and η dependence due to the calibration method used to estimate the efficiencies [130, 131]. The uncertainty of the combined efficiencies are in the range from 0.007% to 0.5%, depending on the p_T of the electron. For muons, the uncertainty range from 0.05% to 2%, depending on the muon p_T.

The uncertainty associated with the electron energy scale also depends on the electron p_T and η [132]. The total uncertainty on the electron energy scale ranges from 0.04% to 0.4% for electrons with p_T at 40 GeV. For electrons with p_T = 10 GeV, the uncertainty ranges between 0.3% and 1%. The uncertainty related to muon momentum scale and energy resolution affect the muon efficiency by 0.2% and 1.2% depending on the shape of the muon p_T.

Uncertainties associated with the jets are propagated from jet energy scale and jet energy resolution calibrations, as well as the efficiencies of jet vertex tagging and b-tagging. The total jet energy scale uncertainty ranges from 4.5% at $p_T^{jet} = 20$ GeV to 2% for jet with $p_T^{jet} = 2$ TeV [133]. The uncertainties on the jet energy resolution range from 10% - 20% at $p_T^{jet} = 20$ GeV to about 5% at $p_T^{jet} = 200$ GeV. The uncertainty coming from jet vertex tagging is approximately 1%. The uncertainties from b-tagging efficiencies are approximately 5% to 10% [134].

The main sources of uncertainty on the missing transverse energy is the propagated systematic uncertainties from all the reconstructed objects that are used to build it. An additional uncertainty is also included to account for the soft terms, defined in Section 3.6. The uncertainty originated from the energy resolution and scale of the soft term is approximately 2% on the value of missing transverse energy [135].

5.5.2 Background modelling uncertainties

Modelling uncertainties associated with the major backgrounds are one of the most important sources of systematic uncertainties. Although in the final signal extraction, the normalisation is derived from the data and the distribution shapes are taken from simulation, several quantities like the p_T of the Z boson or the top quark are generally difficult to model in the simulation since they are sensitive

to higher order corrections. The distributions of the $b\bar{b}$ system and p_T^V of the $\ell\ell$ system are compared against data in signal depleted regions and eventually, a corresponding systematic uncertainty is estimated.

For the Z+jets background, the modelling uncertainties are estimated using the region where events satisfy all the selection criteria apart from the m_{bb} window. This region is dominated by Z+jets and any potential signal processes are diluted. The disagreement between the distribution shape of data and simulation in this region can be used for the estimation of the modelling uncertainties. This method is originally developed for the standard model $Vh \to b\bar{b}$ search [24]. In the analysis of Ref. [24], the uncertainty for p_T^V, $\Delta\, p_T^V$, is parameterised using a smooth function whose parameters are fitted to data to be:

$$\Delta\, p_T^V = \begin{cases} \pm 0.2 \log_{10}(p_T^V/50\text{ GeV}), & p_T^V > 10\text{ GeV} \\ \pm 0.139, & p_T^V \leq 10\text{ GeV} \\ \pm 0.181, & p_T^V \geq 400\text{ GeV}. \end{cases}$$

For the uncertainty for m_{bb}, $\Delta\, m_{bb}$, the function takes the form:

$$\Delta\, m_{bb} = \begin{cases} \pm 0.0005 \times (m_{bb} - 100\text{GeV}), & m_{bb} < 300\text{ GeV} \\ \pm 0.1, & m_{bb} \geq 300\text{ GeV}. \end{cases}$$

These parameterisations were used for the standard model $Vh \to b\bar{b}$ search and their suitability for this particular analysis was examined separately. Figure 5.15 (a) and (b) shows the ratio

$$\frac{N(\text{Data}) - N(\text{non-Z}) - N(\text{Z+jet}) \times SF_Z}{N(\text{Z+jet}) \times SF_Z}$$

as a function of p_T^V, where the $N(\text{Data})$ is the number of data events, $N(\text{non-Z})$ is the number of events in the simulated non Z+jets sample, $N(\text{Z+jet})$ is the number of events in the simulated Z+jet sample and SF_Z is the scale factor from Table 5.4. The functional form used in the analysis of Ref. [24] is overlaid and found that it is adequate for the p_T^V distribution in the $n_b = 2$ category. For the $n_b \geq 3$ category, the statistics are not enough to derive adequate conclusions and the uncertainties are compatible with the data.

A similar approach is used to estimate the uncertainty associated with the shape of the m_{bb} distri-

bution. The functional form used in the analysis of Ref. [24] is not optimal for the m_{bb} range relevant for the $A \to ZH$ search, which is 130–600 GeV. An alternative fit was preformed with a logarithmic function. Figure 5.15 (c) and (d) shows the ratio

$$\frac{N(\text{Data}) - N(\text{non-Z}) - N(\text{Z+jet}) \times SF_Z}{N(\text{Z+jet}) \times SF_Z}$$

as a function of m_{bb} with the result of the fit as a thick red line. The alternative fit has a better performance compare to the functional form used in the analysis of Ref. [24]. The functional form eventually used in the $n_b = 2$ category. For the $n_b \geq 3$ category, the functional form of $\Delta\, m_{bb}^{n_b \geq 3}$ is the following:

$$\Delta\, m_{bb}^{n_b \geq 3} = \begin{cases} \pm 0.5 \log_{10}(m_{bb}/200\text{GeV}), & \text{for } 150 < m_{bb} < 600 \text{ GeV} \\ \pm 0.062, & \text{for } m_{bb} \leq 150 \text{ GeV} \\ \pm 0.239, & \text{for } m_{bb} \geq 600 \text{ GeV}. \end{cases}$$

The estimation of the modelling uncertainties of the $t\bar{t}$ background follows the same strategy as the one used for the Z+jets background. The following functional forms have been used for p_T^V and m_{bb} uncertainties:

$$f(p_T^V) = \begin{cases} -0.05 - \frac{8}{10000} \cdot p_T^V \text{ [GeV]}, & \text{for } p_T^V < 500 \text{ GeV} \\ -0.45, & \text{for } p_T^V \geq 500 \text{ GeV} \end{cases}$$

and

$$g(m_{bb}) = \begin{cases} 0.16 - \frac{12}{1000} \cdot m_{bb} \text{ [GeV]}, & \text{for } m_{bb} < 500 \text{ GeV} \\ -5.84, & \text{for } m_{bb} \geq 500 \text{ GeV}. \end{cases}$$

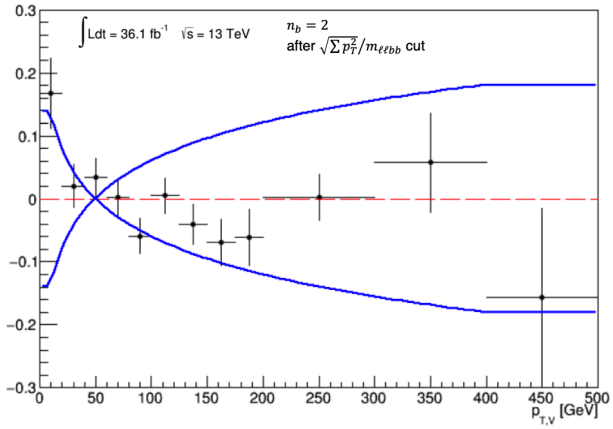

(a) $n_b = 2$ category, p_T^V

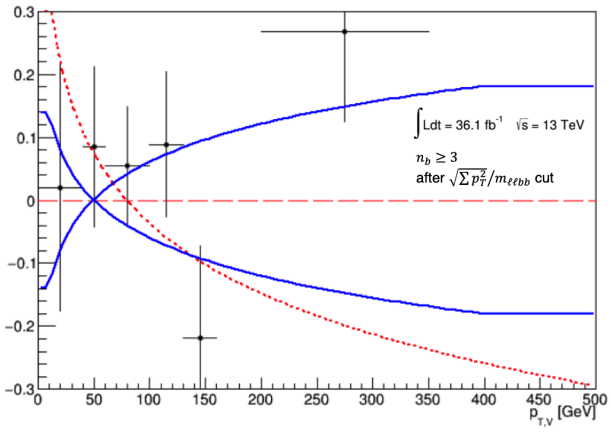

(b) $n_b \geq 3$ category, p_T^V

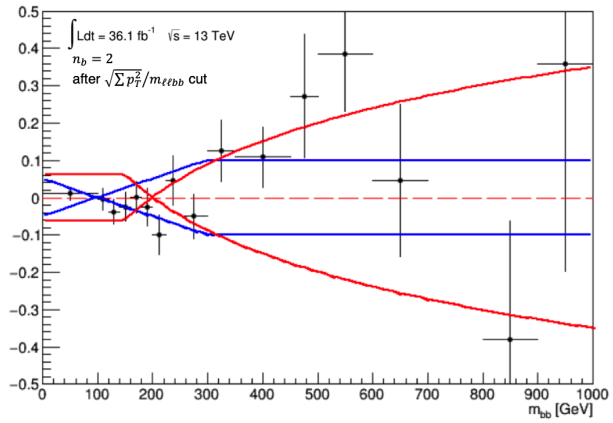

(c) $n_b = 2$ category, m_{bb}

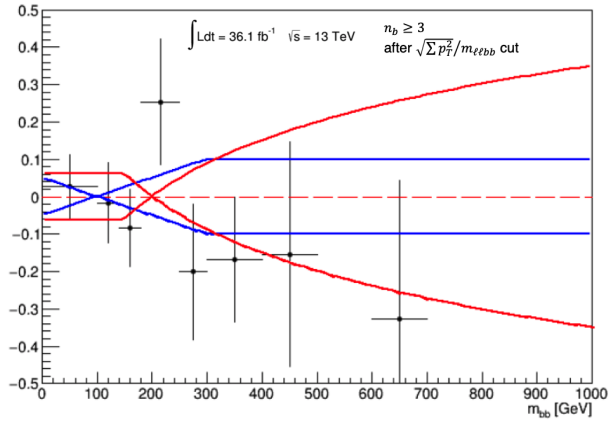

(d) $n_b \geq 3$ category, m_{bb}

Figure 5.15: The shape uncertainties derived in the $n_b = 2$ and $n_b \geq 3$ categories for the p_T^V and m_{bb} distribution of Z+jets events. The y axis shows the ratio defined in the text. This ratio as a function of p_T^V are shown in (a) $n_b = 2$ and (b) $n_b \geq 3$ categories. The ratio as a function of m_{bb} are shown in (c) $n_b = 2$ and (d) $n_b \geq 3$ categories. The thick blue line corresponds to the functional form used in the analysis of Ref. [24]. An alternative fit for m_{bb} is shown with red thick line.

The validation of these functions using a data-simulation comparison from the top control region after the $\sqrt{\Sigma p_T^2}/m_{\ell\ell bb}$ cut is shown in Figure 5.16. The plot shows the ratio (markers):

$$\frac{N(\text{Data}) - N(t\bar{t}) \times SF_{t\bar{t}}}{N(t\bar{t}) \times SF_{t\bar{t}}},$$

and compares it to the shape uncertainty functions (coloured lines), where the $N(\text{Data})$ is the number of data, $N(t\bar{t})$ is the number of simulated $t\bar{t}$ sample and $SF_{t\bar{t}}$ is the scale factor as listed in Table 5.3. The comparison gives results that are compatible with the result from the analysis of Ref. [24], apart from the p_T^V distribution in the $n_b \geq 3$ category. An alternative function has been used, shown as

dashed line in Figure 5.16 (c):

$$f(p_T^V) = \begin{cases} -0.179 - \frac{25.3}{10000} \cdot p_T^V \text{ [GeV]}, & \text{for } p_T^V < 300 \text{ GeV} \\ -0.938, & \text{for } p_T^V \geq 300 \text{ GeV}. \end{cases}$$

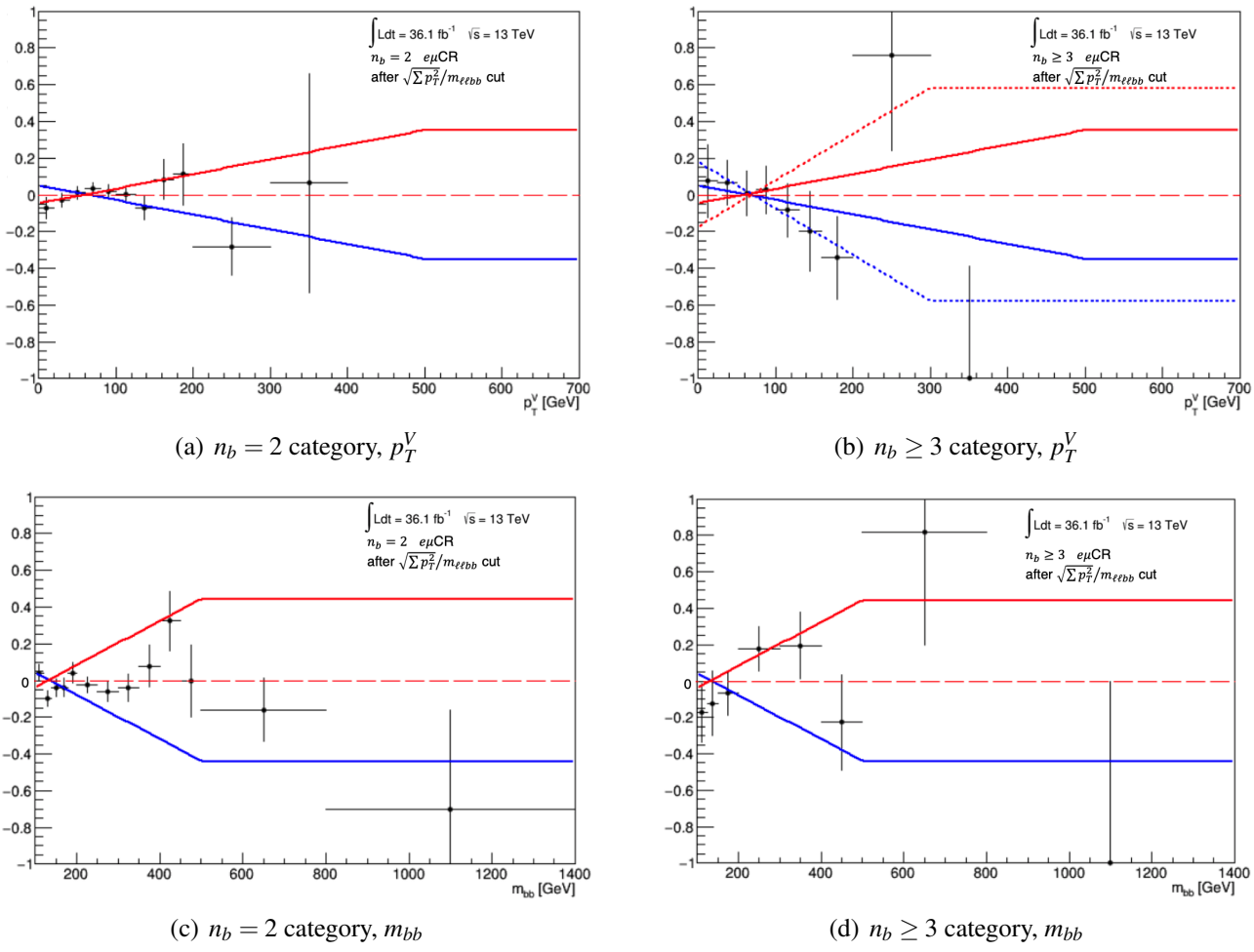

(a) $n_b = 2$ category, p_T^V

(b) $n_b \geq 3$ category, p_T^V

(c) $n_b = 2$ category, m_{bb}

(d) $n_b \geq 3$ category, m_{bb}

Figure 5.16: The shape uncertainties derived in the $n_b = 2$ and $n_b \geq 3$ categories for the p_T^V and m_{bb} distribution of $t\bar{t}$ events. The y axis shows the ratio defined in the text. This ratio as a function of p_T^V are shown in (a) $n_b = 2$ and (b) $n_b \geq 3$ categories. The ratio as a function of m_{bb} are shown in (c) $n_b = 2$ and (d) $n_b \geq 3$ categories. The thick blue and red line corresponds to the functional form used in analysis of Ref. [24]. The p_T^V systematic from that analysis does not cover the variation in the $n_b \geq 3$ category and hence alternative fit function has been used as shown with dashed line.

5.5.3 Uncertainties associated with the signal generation

The uncertainties associated with the simulated signal samples affect the acceptance of the signal events. The sources of these uncertainties are: missing higher order calculations, initial- and final-state radiation, and due to the choice of the parton distribution function (PDF). All the studies are performed with the following mass points in both gluon–gluon fusion and b-associated production: (m_A [GeV],m_H [GeV]) = (230,130), (300,130), (400,250), (500,130), (600,400), (700,200) and (800,500). No shape effect is found from these uncertainties, and hence only the effect on the normalisation is considered.

Uncertainties due to missing higher orders are estimated by varying the factorization and renormalization scale, denoted as μ_F and μ_R respectively, by a factor of 2 and 0.5. The largest difference on the signal acceptance, before the m_{bb} window is applied with respect to the nominal values, is taken as an estimate of the uncertainty. Figure 5.17 shows the acceptance uncertainties as the function of m_A. Although the uncertainties are estimated along the m_A spectrum, no significant dependence on the m_A is found. Eventually, uncertainty values of 2% and 1.5% are chosen for the signal produced via gluon-gluon fusion and b-associated production, respectively.

The uncertainties related to initial-state and final-state radiation are estimated by varying the tune parameters following the prescription described in Ref. [136]. The tune parameters are grouped into 5 difference groups as shown in Table 4 of Ref. [136]: Group "VAR1" corresponds to the effect coming from the underlying event; group "VAR2" corresponds to jet structure effects; group "VAR3a,b,c" for different aspects of extra jet production. Each group has 2 subsets, corresponding to positive and negative variations. The uncertainty is estimated by the difference on the signal acceptance between the nominal and variation from each subset. Eventually, the quadratic sum of the positive and the quadratic sum of the negative variations are used as the uncertainties due to the tune parameters, which ranges from -6% to 6% and from -8% to 8% for the signal produced via gluon-gluon fusion and b-associated production, respectively. Figure 5.18 (a) - (c) shows the acceptance uncertainties due to the tune parameters in each subset along the m_A spectrum. Figure 5.18 (d) shows the sum of the positive variations and the sum of the negative variations as the function of m_A.

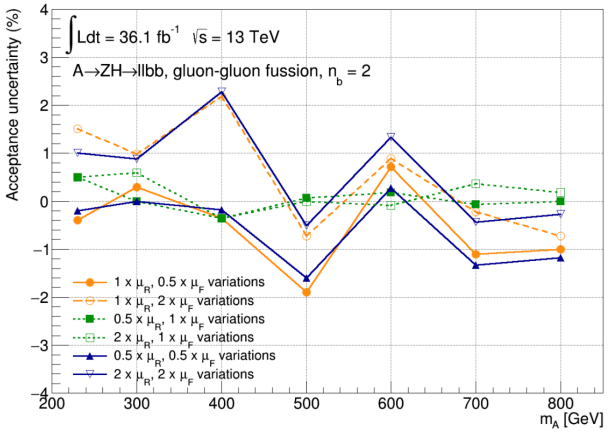

(a) $n_b = 2$ category, ggA

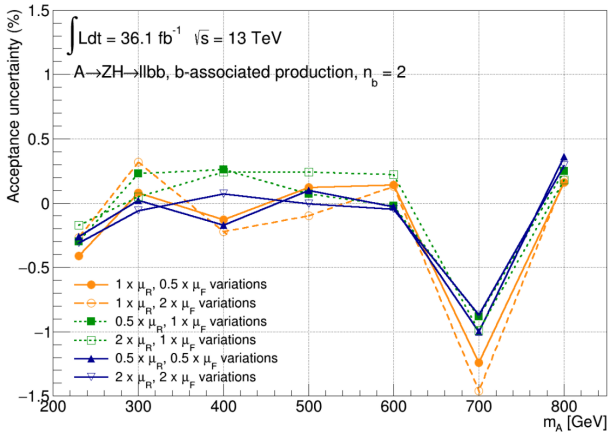

(b) $n_b = 2$ category, bbA

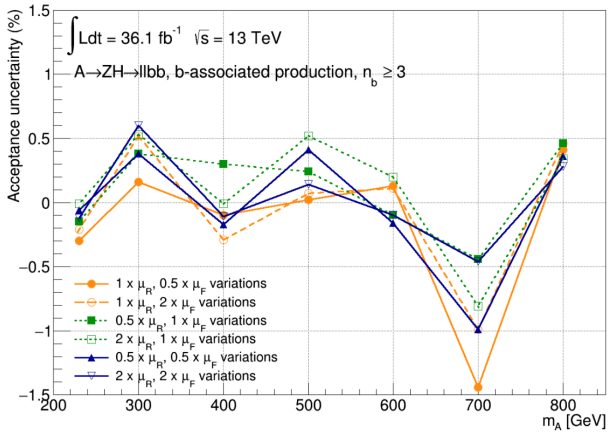

(c) $n_b \geq 3$ category, bbA

Figure 5.17: The acceptance uncertainty due to missing higher order corrections as a function of m_A for the (a) gluon-gluon fusion signal samples in $n_b = 2$ category. The uncertainties for the b-associated production signal samples in the (b) $n_b = 2$ category and the (c) $n_b \geq 3$ category.

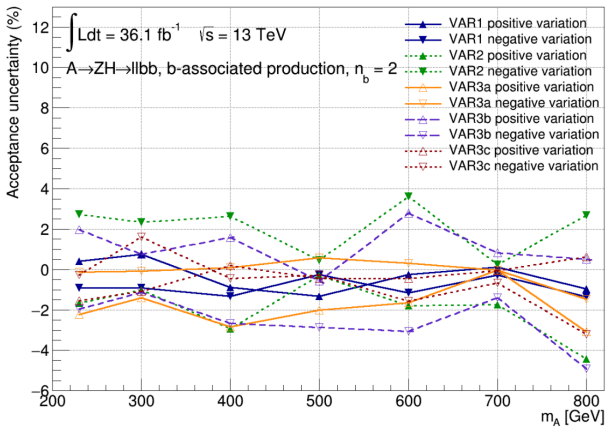

(a) $n_b = 2$ category, bbA

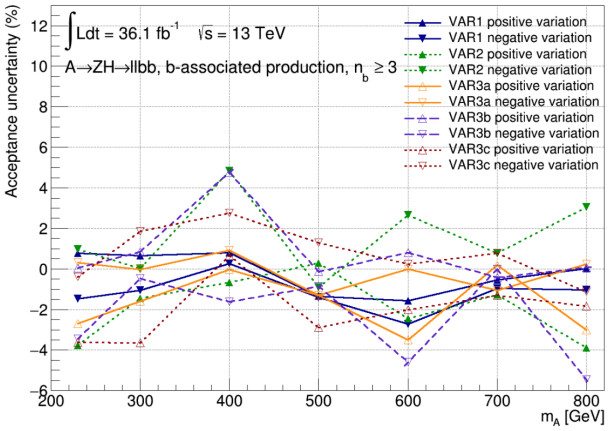

(b) $n_b \geq 3$ category, bbA

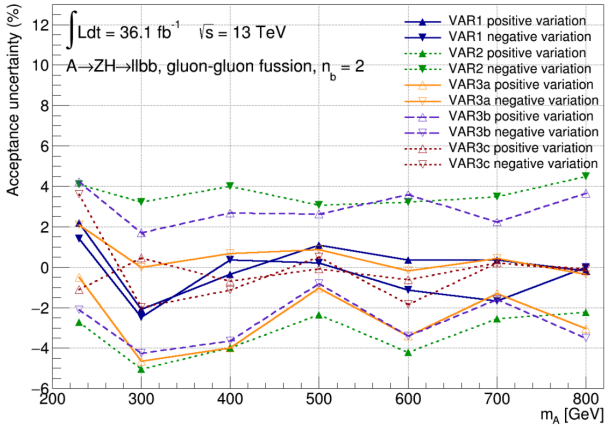

(c) $n_b = 2$ category, ggA

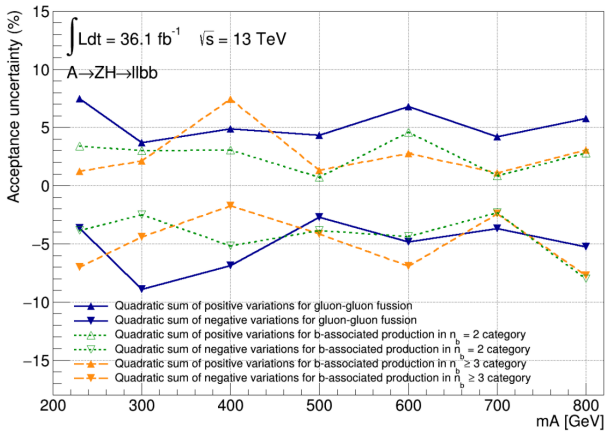

(d) Quadratic sum

Figure 5.18: The estimated acceptance uncertainty related to initial-state and final-state radiations as a function of m_A for the b-associated production signal samples in the (a) $n_b = 2$ category and (b) $n_b \geq 3$ category. The (c) uncertainty for the gluon-gluon fusion signal samples in $n_b = 2$ category. The (d) uncertainty associated with the sum of the positive variations and the sum of the negative variations as the function of m_A.

Uncertainties on the signal acceptance due to the choice of the PDF are estimated by taking the difference from the internal PDF error sets or the difference between the choice of PDF sets. In this search, the former has been used to estimate the uncertainties for the gluon-gluon fusion signal samples, while the latter has been used to estimate the uncertainties for the b-associated production signal samples; as suggested by the ATLAS PDF recommendation [137]. The LHAPDF package [138] has been used to calculate the uncertainty. The nominal PDF sets used in gluon fusion and b-associated production are NNPDF23_lo_as_0130_qed [139]and CT10nlo_nf4 [96], respectively. For gluon-gluon fusion, the standard deviation of a set of 100 PDF error sets are used to estimate the uncertainty. Eventually, the uncertainty ranges from 4% to 8%, depending on the m_A of the signal. For b-associated production, the PDF uncertainty is approximated by comparing the difference between the choice of PDF set. The study is performed by determining the relative difference to the nominal PDF set with the PDF4LHC15 [137] PDF set. Both PDF4LHC15 nominal and variation PDF set are used. No clear m_H dependence has been found. Eventually, a flat 5% uncertainty is assigned for b-associated production. Figure 5.19 shows the acceptance uncertainties as a function of m_A. In Figure 5.19(a), the overlaid red line represents the fitted function on m_H = 130 GeV signal points. The function is the following:

$$\text{PDF uncertainty}[\%] = 2.2 + 0.68 \times \frac{m_A}{100\ \text{GeV}}.$$

In Figure 5.19(b) and (c), only the maximum variation PDF4LHC15 PDF set is shown as variation set in these figures. The flat 5% uncertainty corresponds to the difference between this maximum variation PDF4LHC15 PDF set and the CT10nlo_nf4 PDF set.

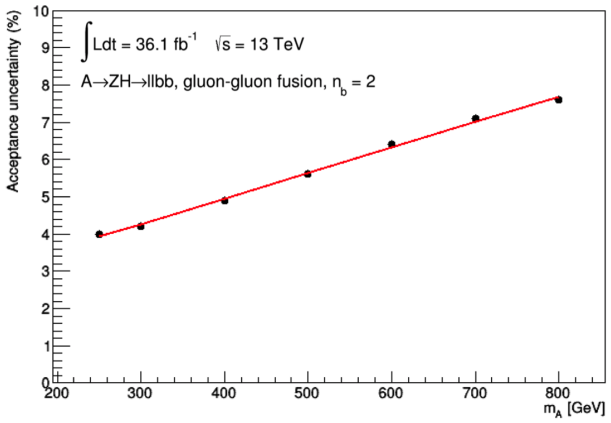

(a) $n_b = 2$ category, ggA

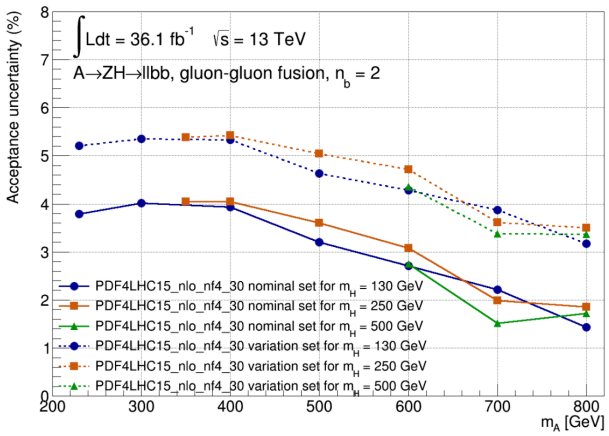

(b) $n_b = 2$ category, bbA

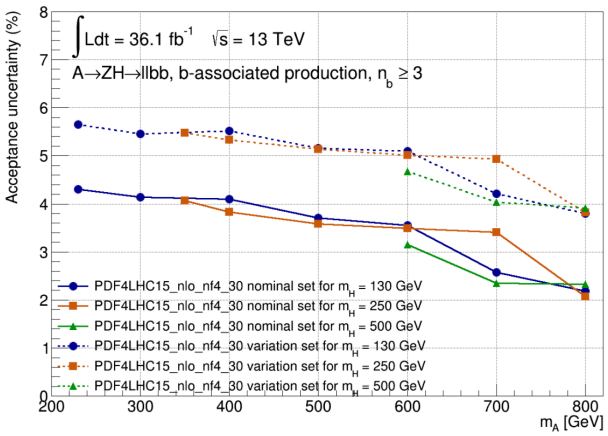

(c) $n_b \geq 3$ category, bbA

Figure 5.19: The (a) uncertainties on the signal acceptance due to the choice of the PDF for gluon-gluon fusion signal samples in the $n_b = 2$ category. The uncertainties on the b-associated produced samples in the (b) $n_b = 2$ category and the (c) $n_b \geq 3$ category.

5.6 Statistical Analysis

In order to claim a discovery or exclude the existence of a new signal process ($A \to ZH \to \ell\ell b\bar{b}$ process in this search), a statistical analysis has to be performed to quantify the evidence for or against signal production. If the evidence is found, then the significant of this evidence has to be quantified. If no clear evidence is observed, the disagreement between the data and the simulation of the process will be quantified. The statistical analysis is done using the classical statistical method known as hypothesis testing, which is based on the likelihood ratio test statistic. The consistency between observations and expectations in the search for the predicted physics processes is examined in the hypothesis testing.

In the hypothesis testing, the null hypothesis is the Standard Model background prediction, while the alternative hypothesis is the Standard Model background plus the signal for which the search is performed. If a deviation from the null hypothesis is observed, the statistical significance of the observed signal is quantified by a p-value. This is used to determine whether the signal strength is sufficient to claim a discovery. The sensitivity of an experiment can be characterised by the expected significance associated with a given signal hypothesis. In the absence of a signal, 95% confidence level limits are set on model parameters, such as the cross-section of a particular process or the mass of a particle. An upper limit excludes values of the given parameter below the quoted limit at 95% confidence level. In this case, the null hypothesis is the signal-plus-background hypothesis and the alternative hypothesis is the background-only scenario.

5.6.1 Likelihood function, test statistic and upper limits

In this search, the likelihood function is constructed using the $m_{\ell\ell bb}$ distribution, which is expected to exhibit a resonant structure if signal events are present, while background events result in a smooth falling spectrum. The shape differences in the $m_{\ell\ell bb}$ distribution between signal and background contributions are determined via binned maximum-likelihood fits of the signal-plus-background hypotheses to extract potential signal contributions based on the statistical framework described in Refs. [124, 140, 141]. For a given mass hypothesis of (m_A, m_H), the likelihood function is defined based on the product of the Poisson terms in each bin:

$$L(\mu, \vec{\alpha}, \vec{\theta} \,|\, m_A, m_H) = \prod_{i=\text{bins}} \text{Poisson}\left(N_i \,\middle|\, \left(\mu \times S_i(m_A, m_H, \vec{\theta}) + B_i(\vec{\alpha}, \vec{\theta})\right)\right) \cdot G(\vec{\theta}).$$

Here N_i is the number of observed events, $S_i(m_A, m_H, \vec{\theta})$ and $B_i(\vec{\alpha}, \vec{\theta})$ are the expected number of signal and background events in bin i, respectively. The vector $\vec{\alpha}$ represents free background scale factors, which will be described later, and $\vec{\theta}$ denotes all the nuisance parameters associated with systematic uncertainties described in Section 5.5. The function $G(\vec{\theta})$ represents the probability density function of the nuisance parameters. The parameter of interest in this search is the signal-strength parameter μ, which is the product of the fitted signal production cross section times branching ratio: $\sigma(A) \times BR(A \to ZH) \times BR(H \to bb)$ in units of pb. When $\mu = 0$, signal events are absent, whereas, $\mu = 1$ suggests that there is a signal which compatible with the assumption of the hypothesis. The binning algorithm of the $m_{\ell\ell bb}$ distribution considers signal resolution, peak positions and the statistical uncertainty related to the number of background events. For both gluon fusion and b-associated production signals in $n_b = 2$ category, the overall background statical uncertainty is required no more than 20%. For b-associated production signals in $n_b \geq 3$ category, 90% signal events are required in one signal peak bin, and the overall background statical uncertainty is required no more than 20%.

The upper limits on the parameter of interest are set, which is derived employing the test statistic $\tilde{q}_\mu$ [124]:

$$\tilde{q}_\mu = \begin{cases} -2\ln L(\mu, \hat{\hat{\theta}}(\mu))/L(\hat{\mu}, \hat{\theta}), & \text{if } 0 \leq \hat{\mu} \leq \mu \\ 0, & \text{if } \hat{\mu} > \mu \end{cases}$$

where $L(\mu, \theta)$ is the likelihood function, μ denotes the parameter of interest, and θ is the nuisance parameters. The set of parameters that represents the global maximum of the likelihood is denoted by $(\hat{\mu}, \hat{\theta})$, with the corresponding likelihood function is expressed as $L(\hat{\mu}, \hat{\theta})$. The notation $L(\mu, \hat{\hat{\theta}}(\mu))$ corresponds to the maximum likelihood for the given μ value, where $\hat{\hat{\theta}}(\mu)$ is the nuisance parameter that maximise the likelihood with this μ value. The test statistic compares the likelihood at a certain μ value to either the likelihood global maximum, where $\hat{\mu}$ is positive, or the null hypothesis likelihood, where $\hat{\mu} = 0$. The p-value is computed for a test statistic distribution in order to quantify the level of agreement and hence exclude a hypothesis based on the observed data. The p-value is defined as follow:

$$p_\mu = \int_{\tilde{q}_{\mu,obs}}^{\infty} f(\tilde{q}_\mu | \mu, \theta) d\tilde{q}_\mu,$$

where $f(\tilde{q}_\mu | \mu, \theta)$ is the probability distribution function for a test statistic. Upper limits on the signal strength are usually derived using the CL$_s$ method [142]. The ratio of p-value is used in this method:

$$p'_\mu = \frac{p_\mu}{1 - p_b},$$

where p_b is the p-value of the same test statistic assuming the background-only hypothesis, which is:

$$p_b = \int_{\tilde{q}_{\mu},obs}^{\infty} f(\tilde{q}_{\mu}|0,\hat{\hat{\theta}}(\mu = 0, obs))d\tilde{q}_{\mu}.$$

The upper limit on μ,denoted by μ^{up}, is obtained by solving $p'_{\mu^{up}} = 5\%$ in order to reject the signal hypothesis at 95% confidence-level.

If some excess of events is observed, a similar test statistic is defined:

$$q_0 = \begin{cases} -2\ln L(0,\hat{\hat{\theta}})/L(\hat{\mu},\hat{\theta}), & \text{if } \hat{\mu} \geq 0 \\ 0, & \text{if } \hat{\mu} < 0 \end{cases}.$$

In this case, the test statistic measures the compatibility between the null hypothesis, which in this case is the background-only hypothesis, and the signal strength that maximises the likelihood.

The p-value is often converted to a significance, Z, defined such that a Gaussian distributed variable found Z standard deviations above its mean has an upper-tail probability equal to p, which is given by:

$$Z = \Phi^{-1}(1-p),$$

where Φ^{-1} is the inverse of the cumulative distribution of the standard Gaussian. In high energy physics, rejection of the background-only hypothesis typically requires a significance of $Z \geq 5$ to constitute a discovery, corresponding to $p = 2.87 \times 10^{-7}$. The exclusion of the signal hypothesis occurs at a threshold p-value of p = 0.05 as mentioned above is equivalent to Z = 1.64.

5.6.2 Fit inputs and effect of systematic uncertainties

The inputs to the fits to the likelihood function includes the following: (a) the binned reconstructed A mass distribution, $m_{\ell\ell bb}$, for a given signal region (b) the number of events for the Z+jets control region and (c) the number of events in the $t\bar{t}$ control region. Signal and minor backgrounds are normalised to their respective theoretical cross sections. The normalisation of the dominant background, Z+jets and $t\bar{t}$, is constrained by the control regions. To achieve this, two free scale factors for each category are derived from the corresponding control regions. Table 5.7 shows some examples of this scale factors for Z+jets and $t\bar{t}$ backgrounds in different signal regions. Systematic uncertainties are

incorporated in the likelihood as nuisance parameters with either Gaussian or log-normal constraint terms.

	$n_b = 2$ category		$n_b \geq 3$ category	
m_H [GeV] for signal region	$Z+jets$	$t\bar{t}$	$Z+jets$	$t\bar{t}$
130	1.20 ± 0.12	0.96 ± 0.08	1.34 ± 0.26	0.93 ± 0.19
200	1.12 ± 0.09	0.96 ± 0.06	1.07 ± 0.20	1.22 ± 0.20
250	1.16 ± 0.11	0.98 ± 0.06	0.93 ± 0.21	1.50 ± 0.25
400	1.20 ± 0.12	1.05 ± 0.1	1.18 ± 0.25	1.37 ± 0.32

Table 5.7: The Z+jets and $t\bar{t}$ scale factors used in the fit with respected to different m_H hypothesis of signal region. Scale factors are estimated in the Z+jets sideband region and $t\bar{t}$ control region.

The effect of systematic uncertainties on the search is studied using the signal-strength parameter μ. Uncertainties having the largest impact depend on the choice of (m_A, m_H) signal point. Table 5.8 shows the relative uncertainties in the best-fit μ value from the leading sources of systematic uncertainty for two example mass points of both gluon fusion and b-associated production of a narrow-width A boson. In this table, the uncertainties are combined into different groups: "Data stat." and "Sim. stat." represent the statistical uncertainty for the data and simulated samples, receptively; "Total syst." represent all the systematic uncertainties introduced in Section 5.5, including several subsets: background modelling systematic uncertainties are denoted as "Bkg. model.", the systematic uncertainties due to the jet energy scale and jet energy resolution calibration are grouped into "JES/JER", the uncertainties related to the lepton properties are denoted by "Leptons", while the uncertainties due to the b-tagging are labelled as "b-tagging", and finally the signal modelling uncertainties are grouped into "Theory". The leading sources of systematic uncertainty are similar for other mass points and for larger A boson widths. For all cases, the limited size of the simulated samples has the largest impact on the search sensitivity among all the sources of systematic uncertainty. While systematic uncertainties and the statistical uncertainty of the data have comparable impact at low masses, the search sensitivity is mostly determined at high masses by the limited size of the data sample.

5.7 Results

This section presents the results of this search after the statistical analysis described in Section 5.6. In this search, fits are preformed under three scenarios: Consider only the gluon fusion signal in $n_b = 2$ category; consider the b-associated production signal in both $n_b = 2$ and $n_b \geq 3$ categories;

gluon fusion production				*b*-associated production			
(230,130) GeV		(700,200) GeV		(230,130) GeV		(700,200) GeV	
Source	$\Delta\mu/\mu$ [%]	Source	$\Delta\mu/\mu$ [%]	Source	$\Delta\mu/\mu$ [%]	Source	$\Delta\mu/\mu$ [%]
Data stat.	32	Data stat.	49	Data stat.	35	Data stat.	46
Total syst.	36	Total syst.	22	Total syst.	38	Total syst.	26
Sim. stat.	22	Sim. stat.	10	Sim. stat.	26	Sim. stat.	12
Bkg. model.	16	Bkg. model.	10	*b*-tagging	14	Bkg. model.	11
JES/JER	12	Theory	9.1	JES/JER	11	*b*-tagging	10
b-tagging	9.9	*b*-tagging	8.5	Bkg. model.	9.8	Theory	6.8
Theory	7.5	Leptons	4.2	Theory	7.0	JES/JER	6.2

Table 5.8: The effect of the most important sources of uncertainty group on the signal-strength parameter at two example mass points of $(m_A, m_H) = (230, 130)$ GeV and $(m_A, m_H) = (700, 200)$GeV for both the gluon fusion and *b*-associated production of a narrow-width A boson.

consider both gluon fusion and b-associated production signals in $n_b = 2$ category and only the b-associated production signal in $n_b \geq 3$ category. First two scenarios are used in the p-value scan and upper limit calculation across the (m_A, m_H) plane as shown in Figure 5.20 and 5.22, respectively. The third scenario is used in the upper limit calculation across the 2HDM parameter space as shown in Figure 5.23.

In each signal region, the $m_{\ell\ell bb}$ spectrum is scanned for potential excesses due to narrow-width A bosons produced via gluon-gluon fusion or *b*-associated production. The p-value is calculated across the (m_A, m_H) plane, and the results are shown in Figure 5.20. Both $n_b = 2$ and $n_b \geq 3$ categories are taken into account in the *b*-associated production, while only $n_b = 2$ category has been considered in the gluon-gluon fusion.

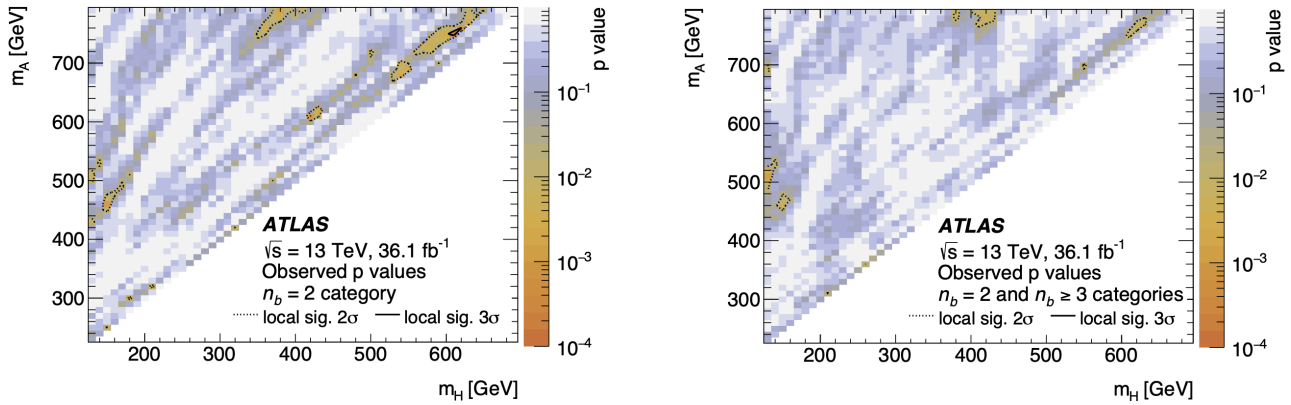

(a) gluon-gluon fusion (b) *b*-associated production

Figure 5.20: p-value scan from the test statistic q_0 for (a) gluon-gluon fusion and (b) *b*-associated production.

The largest significance excess for gluon-gluon fusion is locally 3.5σ, found at (m_A, m_H) = (750,

610) GeV, which corresponding to 2.0σ after taking into account the look-elsewhere effect, as described in Ref. [143]. For the b-associated production, the largest excess occurs at (m_A, m_H) = (510, 130) GeV with a local significance of 3.0 σ, which corresponding to 1.2σ after considering the look-elsewhere effect. The $m_{\ell\ell bb}$ spectra corresponding to m_H = 130 and 610 GeV hypothesis are shown in Figure 5.21.

The upper limits on $\sigma(A) \times BR(A \to ZH) \times BR(H \to bb)$ are calculated at 95% confidence-level using the CL_s method, which is described in Section 5.6.1. Figure 5.22 shows the upper limits for gluon-gluon fusion and b-associated production. The b-associated production has been taken into account in both $n_b = 2$ and $n_b \geq 3$, while while only $n_b = 2$ category has been considered in the gluon-gluon fusion.

In order to preform a scan in the 2HDM parameter space, a new signal model weighted by the predicted cross sections of the two processes is built for every point tested in the 2HDM parameter space. Upper limits on $\sigma(A) \times BR(A \to ZH) \times BR(H \to bb)$ with σ here including contributions from both processes are recalculated and compared with the 2HDM predictions to derive the limits in the 2HDM parameter space. The number of free parameters in 2HDM are fixed by some explicit assumptions required by the benchmark of in this search as mentioned in Chapter 1. The widths of the A and H bosons are taken from the predictions of the 2HDM and the corresponding large-width signals are used. The cross-sections for A boson production in the 2HDM are calculated using up to NNLO QCD corrections for gluon fusion and b-associated production in the five-flavour scheme as implemented in `SusHi` [144–147]. For b-associated production a cross-section in the four-flavour scheme is also calculated as described in Refs. [148, 149] and the results are combined with the five-flavour scheme calculation following Ref. [150]. The Higgs boson widths and branching ratios are calculated using `2HDMC` [151]. The procedure for the calculation of the cross-sections and branching ratios, as well as for the choice of 2HDM parameters, follows Ref. [12].

Figure 5.23 shows the observed and expected limits for the Type-I, Type-II, lepton specific and flipped 2HDMs for various $\tan\beta$ values in the (m_A, m_H) plane. Similar constraints are shown in Type-II and flipped 2HDM because the Yukawa couplings are the same for all fermions apart from leptons in these models. The same holds when comparing Type-I and lepton-specific 2HDM. However, the increased significance of the $H \to \tau\tau$ decay for $\tan\beta > 1$ in the lepton-specific model causing the difference in sensitivity between Type-I and lepton-specific 2HDMs. The loss of sensitivity in Type-I and lepton specific 2HDM for high $\tan\beta$ values is due to the fact that the gluon fusion production cross

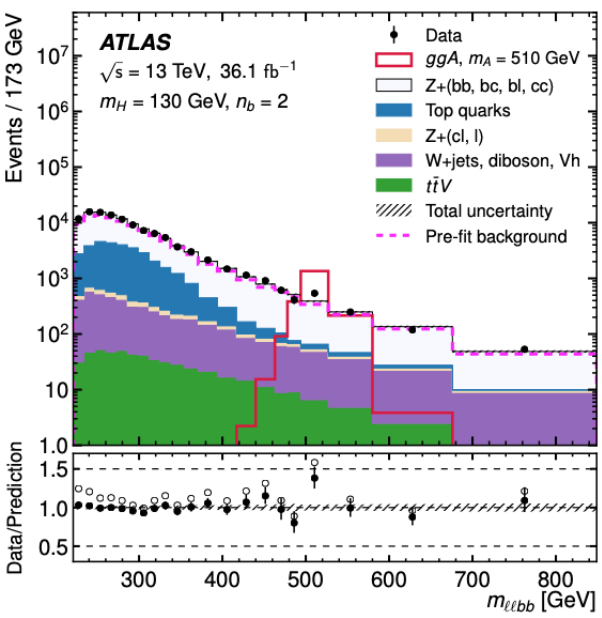

(a) $n_b = 2$ category,m_H = 130 GeV

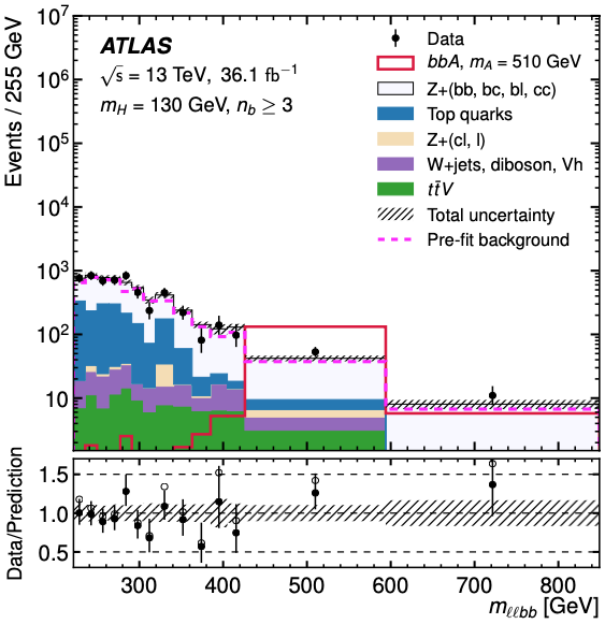

(b) $n_b \geq 3$ category,m_H = 130 GeV

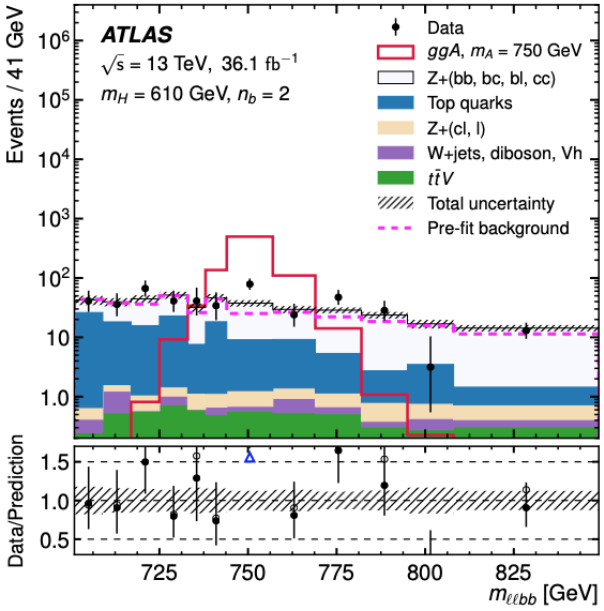

(c) $n_b = 2$ category,m_H = 610 GeV

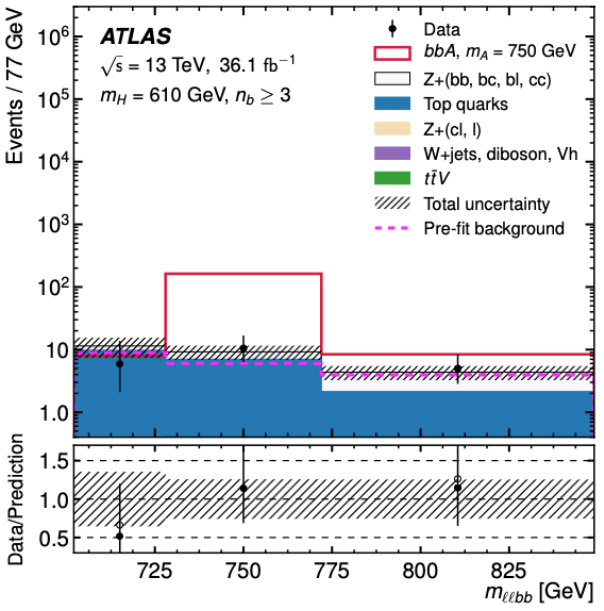

(d) $n_b \geq 3$ category,m_H = 610 GeV

Figure 5.21: The $m_{\ell\ell bb}$ distribution for the m_H = 130 GeV window in the (a) $n_b = 2$ and (b) $n_b \geq 3$ categories, and for m_H = 610 GeV hypothesis in the (c) $n_b = 2$ and (d) $n_b \geq 3$ categories. The solid dots in the bottom panels represents the ratio of the data events over the background prediction obtained from the maximum likelihood function with $\mu = 0$, while the open circles correspond to the ratio of the data to the pre-fit background prediction. The signal distributions assume $\sigma(A) \times BR(A \to ZH) \times BR(H \to bb) = 1$ pb.

section decreases with increasing $\tan\beta$. In Type-II and flipped models, the b-associated production dominates in the large $\tan\beta$ region. This is expected because in these models, the coupling of the A boson to down-type quarks is enhanced with respect to the $\tan\beta$ as shown in Table 1.2. In this model,

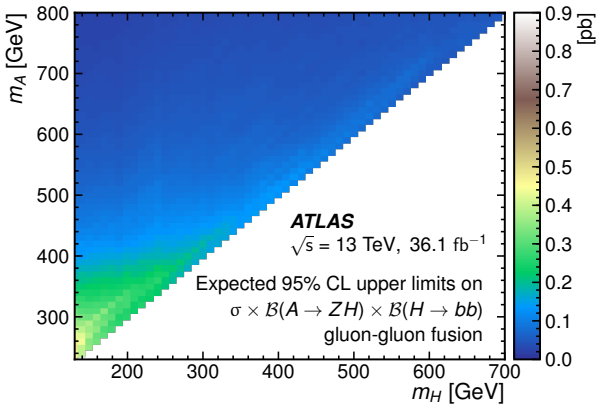

(a) gluon-gluon fusion, expected upper limits

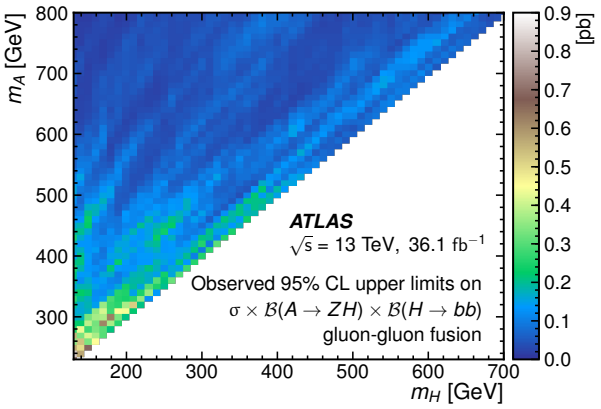

(b) gluon-gluon fusion, observed upper limits

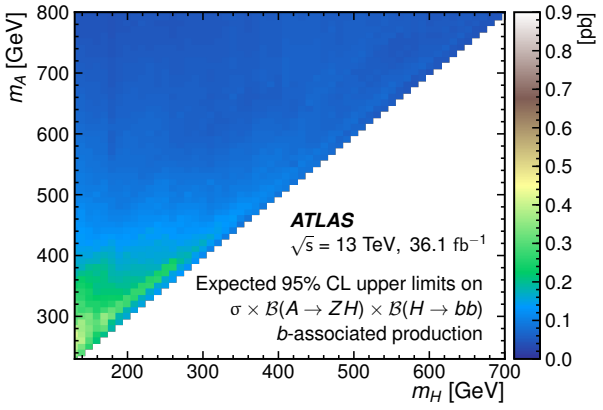

(c) b-associated production, expected upper limits

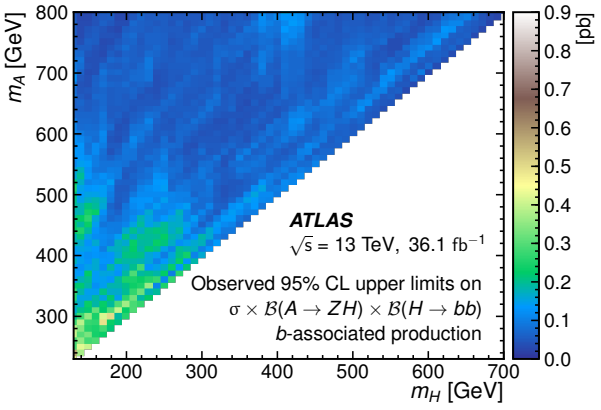

(d) b-associated production, observed upper limits

Figure 5.22: The expected and observed upper limits at 95% confidence-level on $\sigma(A) \times BR(A \to ZH) \times BR(H \to bb)$ across the (m_A, m_H) plane for gluon-gluon fusion and b-associated production.

the exclusion can reach up to $m_H \approx 400$ GeV at $\tan\beta < 10$ and $m_H \approx 600$ GeV when $\tan\beta > 20$. An exclusion up to $m_H = 350$ GeV is observed for $\tan\beta = 1$ in all examined models.

In conclusion, no significant deviation from the standard model background predictions are observed in the $ZH \to \ell\ell b\bar{b}$ final state that is considered in this search. Considering each production process separately, upper limits are set at the 95% confidence level for $\sigma(A) \times BR(A \to ZH) \times BR(H \to bb)$ of 14–830 fb for gluon fusion and 26–570 fb for b-associated production of a narrow A boson for the mass ranges 130–700 GeV of the H boson and 230–800 GeV of the A boson. Taking into account both production processes, this search tightens the constraints on the 2HDM in the case of $m_A - m_H \geq 100$ GeV, where m_A is ranging from 230 to 800 GeV up to the time this search was published. Now these limits are less stringent in comparison to the new result with respect to the analysis described in the next chapter.

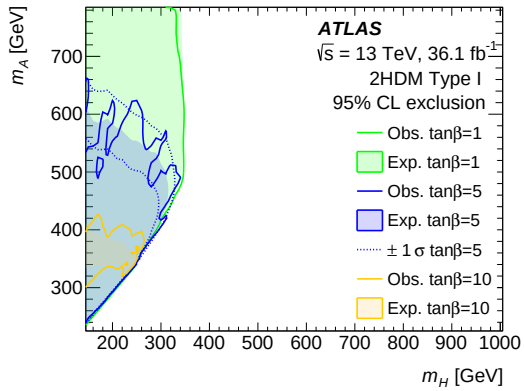

(a) Type-I 2HDM

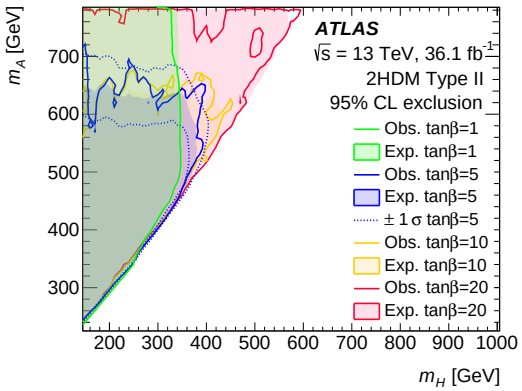

(b) Type-II 2HDM

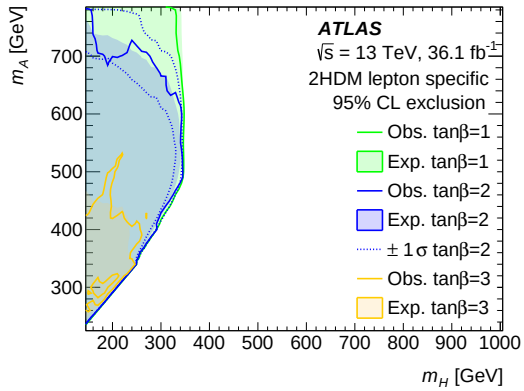

(c) lepton specific 2HDM

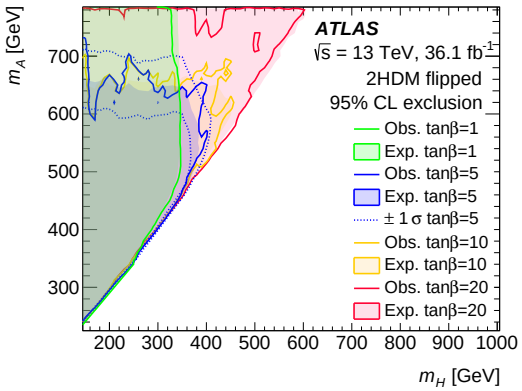

(d) flipped 2HDM

Figure 5.23: The expected and observed upper limits at 95% confidence-level on $\sigma(A) \times BR(A \to ZH) \times BR(H \to bb)$ across the (m_A, m_H) with various $tan\beta$ values for (a)Type-I, (b)Type-II, (c)lepton specific and (d)flipped 2HDM parameter space.

CHAPTER 6

Search for $A \to ZH \to \ell\ell bb$ with 139 fb^{-1}

In this chapter, the search for the $A \to ZH \to \ell\ell b\bar{b}$ with a proton-proton collision data sample collected by ATLAS detector corresponding to integrated luminosity of 139 fb^{-1} will be discussed. The result of this search has been published in The European Physical Journal C [58]. The search strategy is the same as in 36 fb^{-1} result (see Chapter 5) with the following differences: A new dataset with an updated pile up profile has been added and the choice of the simulated signal points (m_A, m_H) has changed, as mentioned in Chapter 3; new triggers with respect to the LHC data taking periods in 2017 and 2018 are added into the trigger list; a more detailed study of the generator modelling uncertainties for the Z+jets and top pair production has been performed. This chapter will focus on the elements that differ with respect to the 36 fb^{-1} analysis.

6.1 Event selection

The baseline of the event selection follows the same procedure described in Section 5.1, summarised in Figure 5.3. New triggers have been added with respect to the new data taking period. They have similar requirements to the one used in Section 5.1. In particular, the single-electron trigger requirements different from the 36 fb^{-1} analysis are detailed in the following:

- At least one electron with $p_T > 26$ GeV satisfying the Tight identification criteria with isolation requirements in the data-taking period during 2017 to 2018.

The single-muon trigger requirements are detailed in the following:

- At least one muon with $p_T > 26$ GeV in the data-taking period during 2017 to 2018, satisfying the isolation requirements introduced in Chapter 3.

As summarised in Figure 5.3, two categories are defined after the E_T^{miss} significance criterion. For the gluon fusion production, more than 95% of the events passing the selection fall into the $n_b = 2$ category. For the b-associated production, only 25%–35% fall into the $n_b \geq 3$ category, whereas the remaining events pass in the $n_b = 2$ category. The overall signal efficiencies of the $n_b = 2$ category after the $\sqrt{\Sigma p_T^2}/m_{\ell\ell bb}$ and m_{bb} window cut are 5.1%–11% and 2.5%–6.6% for gluon fusion and b-associated production, respectively. This efficiency depends on the m_A and m_H values of the signal samples. Similarly, the efficiency of the $n_b \geq 3$ category is 1.3%–3.2% for the b-associated production. Tables 6.1 and 6.2 show the signal acceptance for both gluon fusion and b-associated production in difference selection stages. In comparison with Tables 5.1 and 5.2, the overall acceptance in signal regions are sightly increased in the search introduced in this chapter.

gluon-gluon fusion				
		before	after	
mA	mH	$\sqrt{\Sigma p_T^2}/m_{\ell\ell bb}$	$\sqrt{\Sigma p_T^2}/m_{\ell\ell bb}$	signal regions
230	130	0.06112 ± 0.00043	0.05727 ± 0.00042	0.05087 ± 0.00037
250	130	0.07137 ± 0.00047	0.06608 ± 0.00046	0.05753 ± 0.00043
300	130	0.08554 ± 0.00057	0.07354 ± 0.00053	0.06286 ± 0.00049
300	200	0.09427 ± 0.00055	0.08425 ± 0.00052	0.06433 ± 0.00046
350	250	0.10509 ± 0.00059	0.09269 ± 0.00055	0.06480 ± 0.00046
400	130	0.11040 ± 0.00062	0.09213 ± 0.00056	0.07774 ± 0.00052
500	130	0.12664 ± 0.00067	0.10558 ± 0.00061	0.08941 ± 0.00056
500	200	0.14329 ± 0.00071	0.11917 ± 0.00065	0.09008 ± 0.00056
500	300	0.14961 ± 0.00073	0.12817 ± 0.00067	0.08465 ± 0.00055
500	400	0.11963 ± 0.00064	0.10322 ± 0.00060	0.06389 ± 0.00047
700	130	0.14726 ± 0.00073	0.12125 ± 0.00067	0.10514 ± 0.00062
700	200	0.15746 ± 0.00076	0.12712 ± 0.00068	0.09777 ± 0.00060
700	300	0.16702 ± 0.00079	0.13677 ± 0.00071	0.09185 ± 0.00058
700	400	0.16902 ± 0.00079	0.14281 ± 0.00073	0.08751 ± 0.00057
700	500	0.15716 ± 0.00076	0.13339 ± 0.00070	0.07755 ± 0.00054
b-associated production				
		before	after	
mA	mH	$\sqrt{\Sigma p_T^2}/m_{\ell\ell bb}$	$\sqrt{\Sigma p_T^2}/m_{\ell\ell bb}$	signal regions
230	130	0.0765 ± 0.0011	0.06104 ± 0.00095	0.04646 ± 0.00084
300	200	0.1059 ± 0.0013	0.0832 ± 0.0011	0.05204 ± 0.00090
400	200	0.1279 ± 0.0014	0.0969 ± 0.0012	0.05817 ± 0.00097
500	130	0.1326 ± 0.0015	0.0974 ± 0.0013	0.0591 ± 0.0010
500	300	0.1383 ± 0.0015	0.1082 ± 0.0013	0.05466 ± 0.00097
500	400	0.1228 ± 0.0014	0.0980 ± 0.0013	0.04487 ± 0.00088
700	200	0.1459 ± 0.0016	0.1089 ± 0.0014	0.0628 ± 0.0011
700	300	0.1466 ± 0.0016	0.1121 ± 0.0014	0.0558 ± 0.0010
700	400	0.1460 ± 0.0016	0.1142 ± 0.0015	0.05022 ± 0.00097
700	500	0.1356 ± 0.0016	0.1079 ± 0.0014	0.04343 ± 0.00091

Table 6.1: Signal acceptance before and after the $\sqrt{\Sigma p_T^2}/m_{\ell\ell bb}$ cut; and for the signal regions in $n_b = 2$ category. Only some of the signal samples are shown in this table. Only uncertainties due to the finite number of generated events in the simulated samples are considered.

gluon-gluon fusion				
mA	mH	before $\sqrt{\Sigma p_T^2}/m_{\ell\ell bb}$	after $\sqrt{\Sigma p_T^2}/m_{\ell\ell bb}$	signal regions
230	130	0.001509 ± 0.000068	0.001202 ± 0.000060	0.000733 ± 0.000047
250	130	0.002040 ± 0.000079	0.001624 ± 0.000070	0.000973 ± 0.000054
300	130	0.002597 ± 0.000098	0.002009 ± 0.000086	0.001140 ± 0.000065
300	200	0.002716 ± 0.000093	0.002292 ± 0.000086	0.001379 ± 0.000066
350	250	0.00328 ± 0.00010	0.002760 ± 0.000095	0.001463 ± 0.000069
400	130	0.00363 ± 0.00011	0.002838 ± 0.000098	0.001481 ± 0.000071
500	130	0.00431 ± 0.00012	0.00328 ± 0.00011	0.001764 ± 0.000079
500	200	0.00526 ± 0.00014	0.00400 ± 0.00012	0.002005 ± 0.000083
500	300	0.00545 ± 0.00014	0.00461 ± 0.00013	0.002270 ± 0.000089
500	400	0.00467 ± 0.00013	0.00405 ± 0.00012	0.002002 ± 0.000083
700	130	0.00523 ± 0.00014	0.00409 ± 0.00012	0.002389 ± 0.000093
700	200	0.00614 ± 0.00015	0.00467 ± 0.00013	0.002569 ± 0.000096
700	300	0.00711 ± 0.00016	0.00556 ± 0.00014	0.00278 ± 0.00010
700	400	0.00736 ± 0.00016	0.00610 ± 0.00015	0.00295 ± 0.00010
700	500	0.00753 ± 0.00017	0.00644 ± 0.00015	0.00285 ± 0.00010
b-associated production				
mA	mH	before $\sqrt{\Sigma p_T^2}/m_{\ell\ell bb}$	after $\sqrt{\Sigma p_T^2}/m_{\ell\ell bb}$	signal regions
230	130	0.02365 ± 0.00055	0.01699 ± 0.00047	0.01304 ± 0.00041
300	200	0.03898 ± 0.00073	0.03048 ± 0.00065	0.02122 ± 0.00054
400	200	0.04726 ± 0.00084	0.03437 ± 0.00072	0.02249 ± 0.00058
500	130	0.05235 ± 0.00089	0.03782 ± 0.00076	0.02183 ± 0.00058
500	300	0.06007 ± 0.00098	0.04751 ± 0.00087	0.02799 ± 0.00068
500	400	0.05380 ± 0.00092	0.04505 ± 0.00085	0.02679 ± 0.00066
700	200	0.0676 ± 0.0011	0.04868 ± 0.00091	0.02873 ± 0.00070
700	300	0.0708 ± 0.0011	0.05327 ± 0.00094	0.03117 ± 0.00071
700	400	0.0716 ± 0.0011	0.05677 ± 0.00097	0.03225 ± 0.00073
700	500	0.0668 ± 0.0011	0.05504 ± 0.00096	0.03056 ± 0.00072

Table 6.2: Signal acceptance before and after the $\sqrt{\Sigma p_T^2}/m_{\ell\ell bb}$ cut; and for the signal regions in $n_b \geq 3$ category. Only some of the signal samples are shown in this table. Only uncertainties due to the finite number of generated events in the simulated samples are considered.

6.2 Signal modelling & Background estimation

The signal modelling follows the same procedure as described in Section 5.4: the reconstructed A boson mass, $m_{\ell\ell bb}$, is modelled using EGE or DSCB functions, depending on the production mechanism. The EGE function is used for gluon-gluon fusion signals and the DSCB function is used for the b-associated production signals, whose parameters are interpolated to cover the mass points that are not simulated. The yield interpolation is also applied. The large width samples are also treated in the same way as described in Section 5.4.

The dominant background of this search is the same as mentioned in Section 5.2, which is comes from the Z+jets and $t\bar{t}$ processes. Table 6.3 shows the fraction of Z+jets and $t\bar{t}$ events estimated in different signal regions. The same strategy as in the 36 fb^{-1} analysis has been used, where in the distributions scale factors are used for the Z+jets and the $t\bar{t}$ yield. These scale factors are evaluated in the same way as explained in Section 5.2. Their values for the 139^{-1} analysis are shown in Table 6.4 and Table 6.5 for $t\bar{t}$ and Z+jets, respectively. Figure 6.1 and 6.2 shows the scale factor as a function of m_{bb} in $n_b = 2$ and $n_b \geq 3$ categories for $t\bar{t}$ and Z+jets in the corresponding regions, respectively. In this search, a new control region, denoted as $n_b = 1$ control region, that requires exactly 1 b-jet, as well as an early selection stage before the m_{bb} window and the $\sqrt{\Sigma p_T^2}/m_{\ell\ell bb}$ criteria have been added to test the background modelling which will be discussed in Section 6.2.1. The $m_{\ell\ell bb}$ distribution in $n_b = 1$ control region, $n_b = 2$ and $n_b \geq 3$ categories can be found in Appendix C.

	$n_b = 2$ category		$n_b \geq 3$ category	
m_H [GeV] for signal region	$Z + jets$	$t\bar{t}$	$Z + jets$	$t\bar{t}$
130	67.8%	26.6%	63.2%	29.0%
350	48.7%	49.3%	54.5%	38.4%
500	56.7%	40.5%	57.8%	34.4%
700	68.3%	27.9%	66.0%	23.9%

Table 6.3: Fraction of simulated Z+jets and $t\bar{t}$ events with different m_H hypothesis of signal region. Fractions are calculated by diving the number of Z+jets or $t\bar{t}$ events over number of all the simulated backgrounds.

Category:	$n_b = 1$ control region	$n_b = 2$	$n_b \geq 3$
Top control region: Before $\sqrt{\Sigma p_T^2}/m_{\ell\ell bb}$ variable cut			
Data:	40459	27902	1034
Rest:	539.11 ± 25.15	84.13 ± 4.93	8.66 ± 0.57
Top:	39954.27 ± 46.85	28036.49 ± 35.26	764.48 ± 5.97
Scale factor	0.999 ± 0.005	0.992 ± 0.006	1.341 ± 0.043
Top control region: After $\sqrt{\Sigma p_T^2}/m_{\ell\ell bb}$ variable cut			
Data:	27374	21885	773
Rest:	329.89 ± 14.33	66.82 ± 1.97	7.13 ± 0.51
Top:	27640.04 ± 38.88	22318.23 ± 31.31	555.273 ± 5.085
Scale factor	0.978 ± 0.006	0.978 ± 0.007	1.379 ± 0.052

Table 6.4: The number of events in the top control region before and after the $\sqrt{\Sigma p_T^2}/m_{\ell\ell bb}$ variable cut for the $n_b = 1$ control region, $n_b = 2$ and $n_b \geq 3$ categories along with their associated scale factors. Statistical uncertainties from the data and systematic uncertainties that are due to the finite number of simulated events are considered.

Before $\sqrt{\Sigma p_T^2}/m_{\ell\ell bb}$ variable cut			
Category:	$n_b = 1$ control region	$n_b = 2$	$n_b \geq 3$
Data:	822983	128579	3727
Z:	675559.91 ± 1236.79	77449.07 ± 181.32	1936.38 ± 20.47
Top:	42940.93 ± 50.83	28593.97 ± 36.18	1069.25 ± 8.51
Other:	14238.29 ± 49.27	3517.212 ± 14.061	221.34 ± 3.26
Z+jets Scale factor	1.134 ± 0.002	1.246 ± 0.003	1.258 ± 0.014
Z+jets ample break-up			
Zcl+Zl	188654.79 ± 863.97	794.82 ± 1.25	19.62 ± 6.54
Zcc	28272.62 ± 288.92	2717.91 ± 8.58	39.63 ± 6.38
Zbl	383904.63 ± 805.44	2039.93 ± 34.07	132.05 ± 4.22
Zbc	25863.99 ± 121.82	4714.61 ± 51.21	334.39 ± 11.81
Zbb	48863.90 ± 190.14	67181.79 ± 170.35	1410.69 ± 13.36

Table 6.5: The number of events before the $\sqrt{\Sigma p_T^2}/m_{\ell\ell bb}$ variable cut for the $n_b = 1$ control region, $n_b = 2$ and $n_b \geq 3$ categories along with their associated scale factors for Z+jets. Statistical uncertainties from the data and systematic uncertainties that are due to the finite number of simulated events are considered.

After $\sqrt{\Sigma p_T^2}/m_{\ell\ell bb}$ variable cut			
Category:	$n_b = 1$ control region	$n_b = 2$	$n_b \geq 3$
Data:	441084	78834	2305
Z:	351976.18 ± 893.94	44062.79 ± 110.43	1139.63 ± 15.53
Top:	29210.62 ± 41.55	22416.88 ± 31.66	802.97 ± 7.51
Other:	9079.32 ± 29.49	2650.43 ± 11.89	161.42 ± 2.76
Z+jets Scale factor	1.144 ± 0.003	1.220 ± 0.003	1.176 ± 0.017
Z+jets ample break-up			
Zcl+Zl	95050.87 ± 543.98	405.01 ± 0.79	5.81 ± 2.34
Zcc	15740.46 ± 186.78	1548.49 ± 5.65	26.48 ± 6.10
Zbl	200782.24 ± 670.21	1042.14 ± 20.67	73.55 ± 2.41
Zbc	13622.74 ± 75.67	2531.09 ± 31.66	188.84 ± 9.98
Zbb	26779.86 ± 115.84	38536.06 ± 103.60	844.93 ± 9.64

Table 6.6: The number of events after the $\sqrt{\Sigma p_T^2}/m_{\ell\ell bb}$ variable cut for the $n_b = 1$ control region, $n_b = 2$ and $n_b \geq 3$ categories along with their associated scale factors for Z+jets. Statistical uncertainties from the data and systematic uncertainties that are due to the finite number of simulated events are considered.

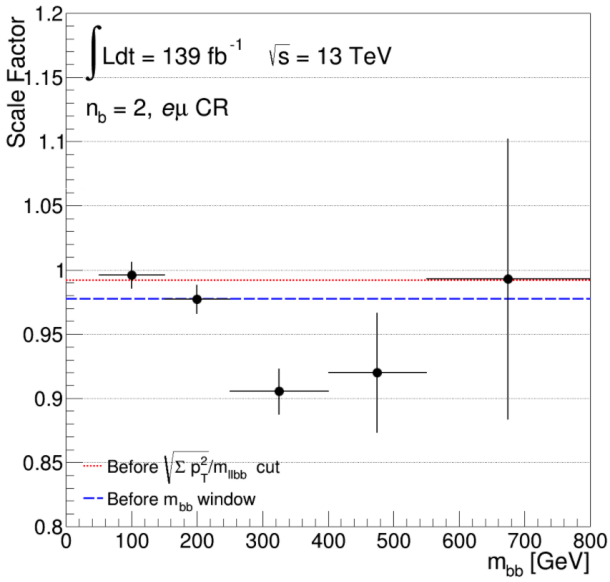

(a) $n_b = 2$ category

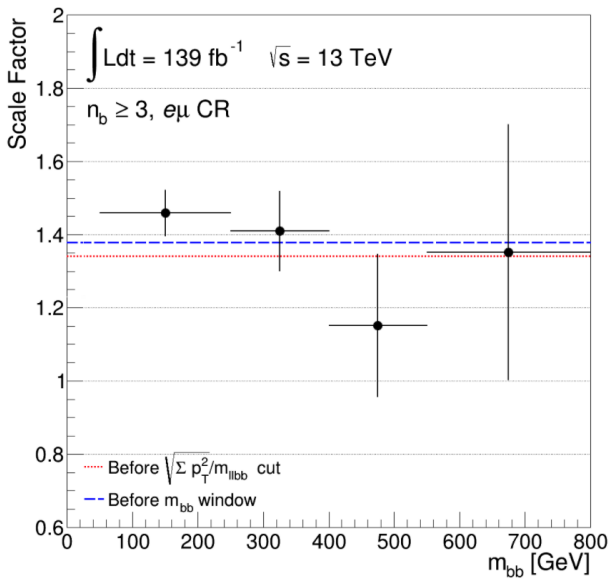

(b) $n_b \geq 3$ category

Figure 6.1: Scale factors of $t\bar{t}$ background as a function of m_{bb} in top control region of $n_b = 2$ and $n_b \geq 3$ categories after several selections stages. Statistical uncertainties from the data and systematic uncertainties that are due to the finite number of simulated events are considered.

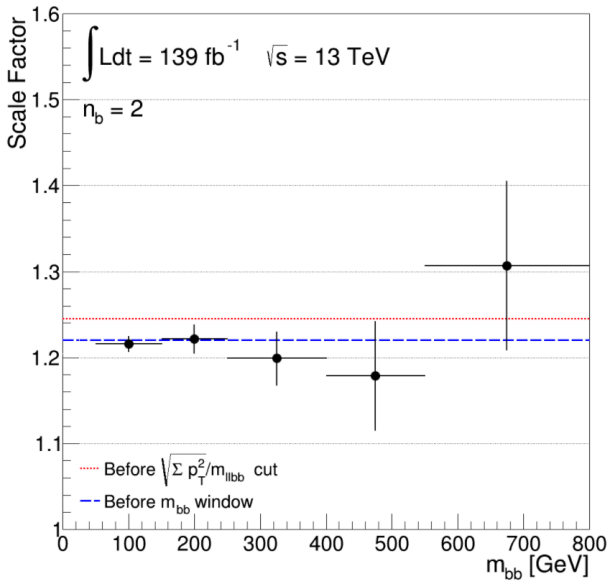

(a) $n_b = 2$ category

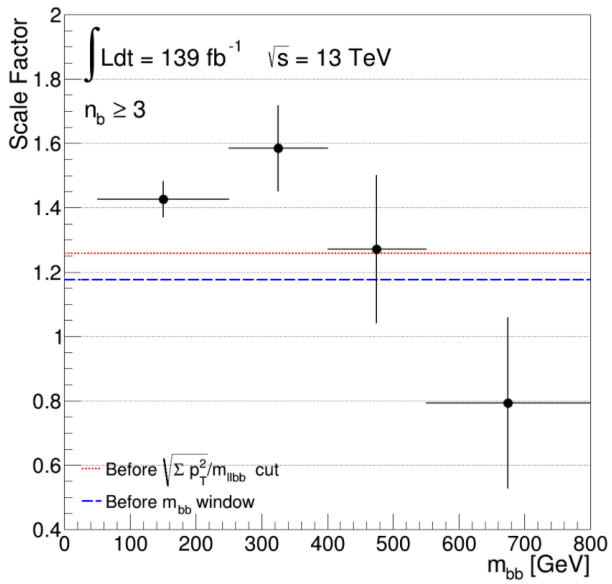

(b) $n_b \geq 3$ category

Figure 6.2: Normalisation scale factors of Z+jets background as a function of m_{bb} in $n_b = 2$ and $n_b \geq 3$ categories after several stages of selections including the m_{bb} window. Statistical uncertainties from the data and systematic uncertainties that are due to the finite number of simulated events are considered.

6.2.1 Backgound modelling

The distributions of the Z+jets simulated events have been studied for possible systematic effects. In particular, the discrepancy between the data and simulation has been corrected for the following variables: The p_T of the Z boson, denoted by p_T^Z; the m_{bb} distribution and the $\sqrt{\Sigma p_T^2}/m_{\ell\ell bb}$ distribution. The new control region, $n_b = 1$ control region, have been used to perform comparisons of the simulation against data. Corrections to the simulation have been derived from the $n_b = 1$ control region and parameterised using the variables shown in Table 6.7.

Variable	Region to derive the correction	Region where the correction is applied
p_T^Z	$n_b = 1$ control region	$n_b = 2$ category
$\sqrt{\Sigma p_T^2}/m_{\ell\ell bb}$	$n_b = 1$ control region	$n_b = 2$ category
m_{bb}	$n_b = 1$ control region	$n_b = 2$ & $n_b \geq 3$ category

Table 6.7: Summary of the corrections used in this search.

Half the size of the correction is applied as an uncertainty in the $n_b = 2$ category, while full size of the correction in the $n_b \geq 3$ category is considered as the associated uncertainty. This is because the origin of events is similar in $n_b = 1$ control region and $n_b = 2$ category. Therefore, the associated uncertainty in the $n_b = 2$ category can be reduced by using the $n_b = 1$ control region as a handle. However, due to the different origin of events between the $n_b = 1$ control region and $n_b \geq 3$ category, a conservative approach has been considered and hence a larger uncertainty has been assigned in this category.

Figure 6.3 shows the shape of the distributions for Z+jets in data versus the simulation in various regions used in this search as a function of p_T^Z, $\sqrt{\Sigma p_T^2}/m_{\ell\ell bb}$, and, m_{bb}. The shape of the Z+jets events in data is estimated by taking the data in the regions after subtracting contributions from non-Z+jets backgrounds using simulation. While subtracting the contribution from $t\bar{t}$, the corresponding scale factor as shown in Table 6.4 has been applied. The shape difference between the data and the simulation is expressed as bin-by-bin correction factors that are shown in Figure 6.3. In Figure 6.3(a) and (b), only the shape of the distribution from $n_b = 1$ and $n_b = 2$ categories have been shown. Figure 6.3(c) also show the distribution from $n_b \geq 3$ category.

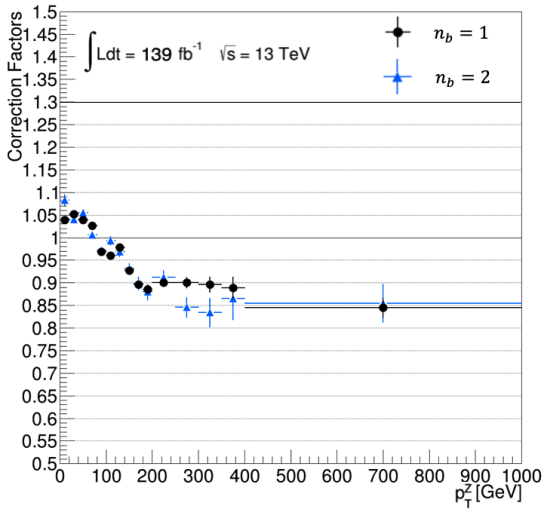

(a)

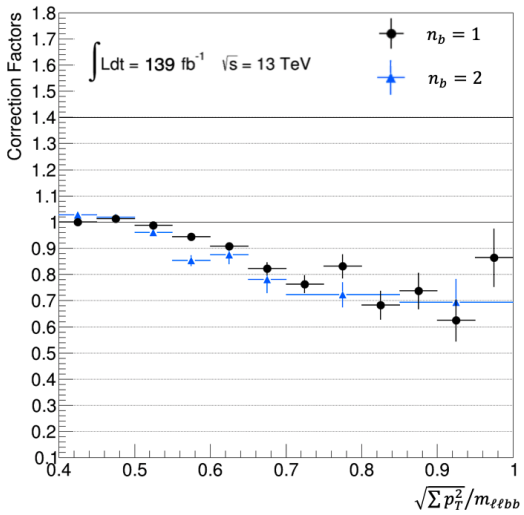

(b)

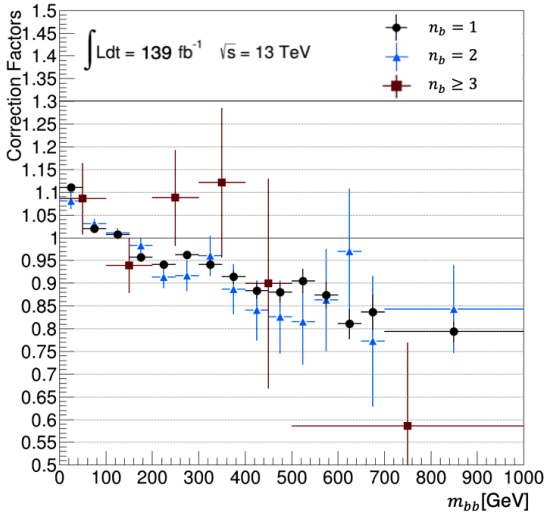

(c)

Figure 6.3: The comparison of the shape of the distributions for Z+jets in data versus the simulation in various regions used in this search as a function of p_T^Z (a), $\sqrt{\Sigma p_T^2}/m_{\ell\ell bb}$ variable (b), and, m_{bb} (c). Statistical uncertainties from the data and systematic uncertainties that are due to the finite number of simulated events are considered.

The shape correction for p_T^Z

It is well known that the p_T of the Z boson for the simulated Z+jets is modelled inaccurately in the generator, for example it has been observed in Ref. [24]. In the search described in Chapter 5, a systematic uncertainty on the p_T^Z was estimated by parameterizing the data-simulation differences in an early selection stage. Here, a correction is derived using the $n_b = 1$ control region. Subsequently, the correction is validated in two regions of the $n_b = 2$ category: The low and high m_{bb} regions, which contains the events for which the m_{bb} mass is smaller than the lower edge of the lowest m_H window and higher than the higher edge of the highest m_H window, respectively. A systematic uncertainty is derived by fitting the shape distribution in $n_b = 1$ control region to a linear function, then half of the value of this function is taken as the systematic uncertainty of the correction. Eventually, the following empeirical function is used to estimate the uncertainty associated with the p_T^Z correction:

$$f(p_T^Z) = \begin{cases} 0.0725 + (\text{-}0.0009 \cdot p_T^V \text{ [GeV]}), & \text{for } p_T^V < 190 \text{ GeV} \\ \text{-}0.1006, & \text{for } p_T^V \geq 190 \text{ GeV} . \end{cases}$$

Figures 6.4(a) and 6.4(b) show the p_T^Z distributions before the correction in $n_b = 1$ and $n_b = 2$ categories, respectively. A validation has been preformed in the $n_b = 2$ category using regions with $m_{bb} < 130$ GeV and $m_{bb} > 700$ GeV that are not considered in the signal regions. The p_T^Z distribution for these validation regions are shown in Figure 6.4(c) and 6.4(d). The corrected p_T^Z distribution in $n_b = 1$ and $n_b = 2$ categories is shown in Figure 6.4(e) and 6.4(f), respectively.

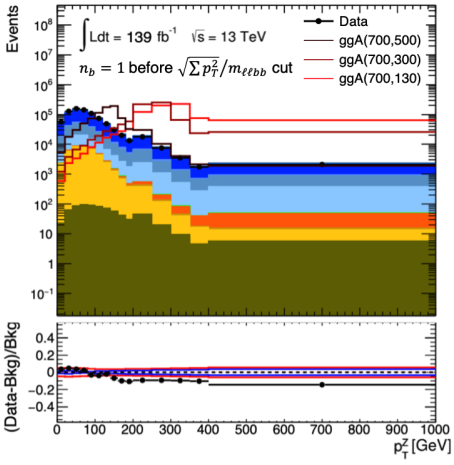

(a) $n_b = 1$, no p_T^Z correction

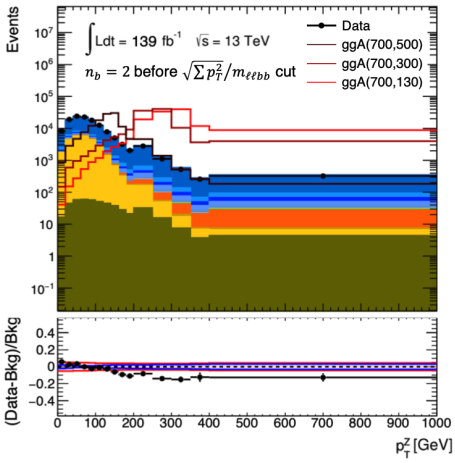

(b) $n_b = 2$, no p_T^Z correction

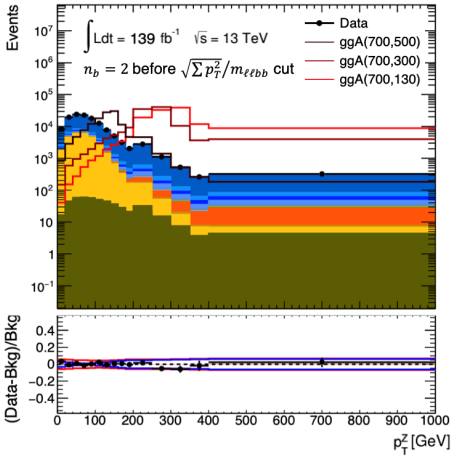

(c) $n_b = 2$ category with $m_{bb} < 130$ GeV, p_T^Z corrected

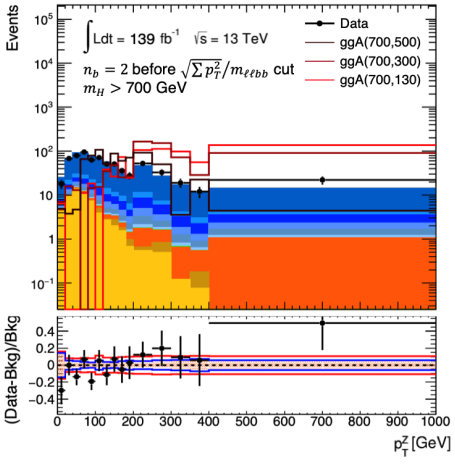

(d) $n_b = 2$ category with $m_{bb} > 700$ GeV, p_T^Z corrected

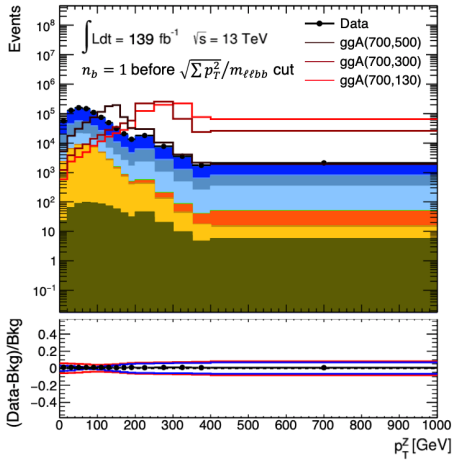

(e) $n_b = 1$, p_T^Z corrected

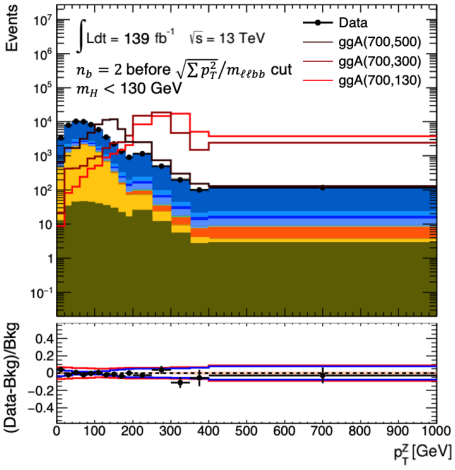

(f) $n_b = 2$, p_T^Z corrected

Figure 6.4: The p_T^Z distribution before the p_T^Z correction in the (a) $n_b = 1$ and (b) $n_b = 2$ categories. Distribution with correction applied in the $n_b = 2$ category with (c) $m_{bb} < 130$ GeV and for (d) $m_{bb} > 700$ GeV. The p_T^Z distribution after p_T^Z correction applied in the (e) $n_b = 1$ and (f) $n_b = 2$ categories. For the background simulated samples, color code shown in Figure 3.5 has been used. At the bottom panel, the filled area represent the statistical uncertainties, while the blue line shows the combined uncertainty from statistical and shape uncertainties. The total uncertainty which combines statistical and systematic uncertainties are also shown as a red line.

The shape correction for $\sqrt{\Sigma p_T^2}/m_{\ell\ell bb}$

A discrepancy in the shape of $\sqrt{\Sigma p_T^2}/m_{\ell\ell bb}$ distribution has been found in this search. There were some hints of such discrepancy which were much less significant in the 36 fb^{-1} analysis as shown in Figure 5.2(a). Several potential sources of this mismodelling were investigated, including the angular distance between the closest (b-)jet to the Z boson system, which is known to be modelled inadequately. Alternative variables were investigated, which are expected to be modelled better, such as replacing the denominator of the $\sqrt{\Sigma p_T^2}/m_{\ell\ell bb}$ variable with any jet and not only the b-jets of the events. Also, a study preformed that the $\sqrt{\Sigma p_T^2}/m_{\ell\ell bb}$ variable is modelling better by replacing the Sherpa with the Madgraph5 generator. However, MadGraph5 generator is not suitable for events with high jet multiplicity, which is important for this search. Eventually, these studies show that there is a residual uncertainty that related to the Z boson recoil p_T with respect to different jets that cannot be simply corrected by deriving a correction factor for some other variable such as the p_T^Z correction. Figure 6.5(a) and 6.5(b) shows that the p_T^Z correction cannot explain the discrepancy in the $\sqrt{\Sigma p_T^2}/m_{\ell\ell bb}$ distribution. The discrepancy mostly affect the tail of the distribution, which only contain a small amount of background events. Therefore, the impact of this discrepancy in the final result is limited.

The $\sqrt{\Sigma p_T^2}/m_{\ell\ell bb}$ correction is evaluated using the same $n_b = 1$ control region as the p_T^Z correction. The correction is only applied on the $n_b = 2$ category, since the distribution of this variable in the $n_b \geq 3$ category does not seem to have any significant discrepancy, as shown in Figure 6.5(c). A systematic uncertainty on the correction is derived by following the same procedure as the method described for the p_T^Z correction. The following empirical function is used to parameterize the uncertainty associated with the $\sqrt{\Sigma p_T^2}/m_{\ell\ell bb}$ correction:

$$f(\sqrt{\Sigma p_T^2}/m_{\ell\ell bb}) = \begin{cases} -0.1612 + [-0.2383 \cdot \ln(\sqrt{\Sigma p_T^2}/m_{\ell\ell bb})], & \text{for } \sqrt{\Sigma p_T^2}/m_{\ell\ell bb} > 0.5 \\ 0.0039, & \text{for } \sqrt{\Sigma p_T^2}/m_{\ell\ell bb} \leq 0.5 \end{cases}.$$

The $\sqrt{\Sigma p_T^2}/m_{\ell\ell bb}$ distribution with the correction applied in both $n_b = 1$ and $n_b = 2$ categories are shown in Figures 6.5(d) and 6.5(e), respectively.

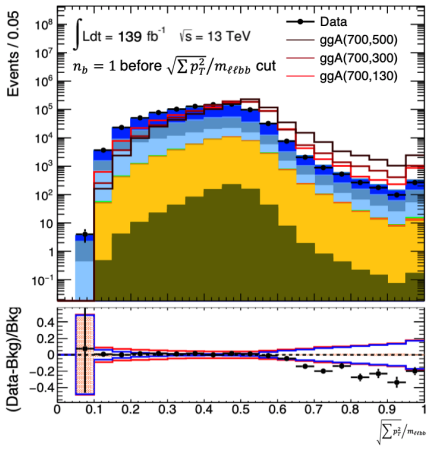

(a) $n_b = 1$, p_T^Z corrected

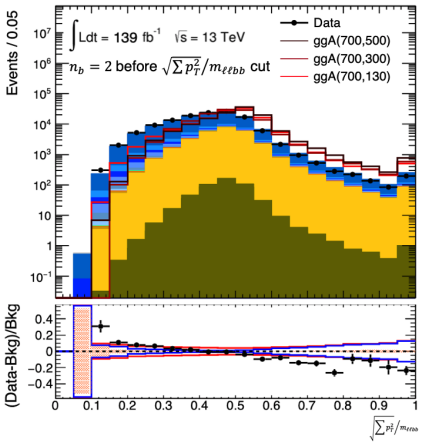

(b) $n_b = 2$, p_T^Z corrected

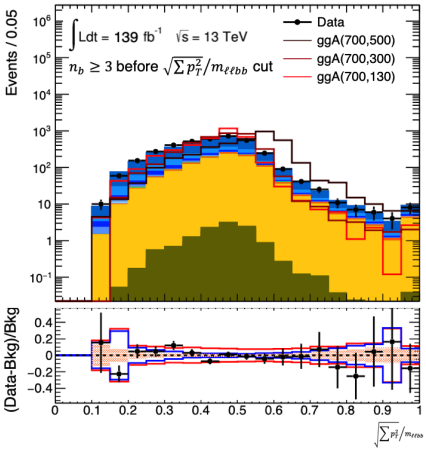

(c) $n_b \geq 3$, no correction

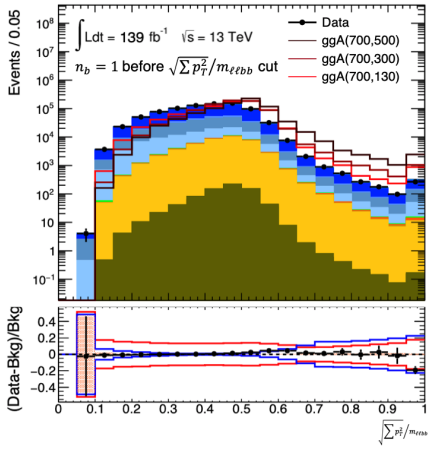

(d) $n_b = 1$, $\sqrt{\Sigma p_T^2}/m_{\ell\ell bb}$ variable corrected

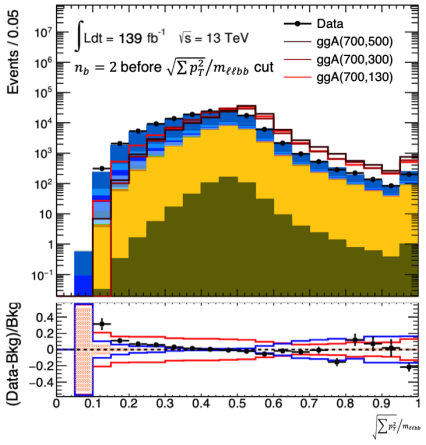

(e) $n_b = 2$, $\sqrt{\Sigma p_T^2}/m_{\ell\ell bb}$ variable corrected

Figure 6.5: The $\sqrt{\Sigma p_T^2}/m_{\ell\ell bb}$ distribution with p_T^Z correction in (a) $n_b = 1$ and (b) $n_b = 2$ (b) categories. Distribution without correction in (c) $n_b \geq 3$ category. The distributions before the $\sqrt{\Sigma p_T^2}/m_{\ell\ell bb}$ variable cut in (d) $n_b = 1$ and (e) $n_b = 2$ categories with $\sqrt{\Sigma p_T^2}/m_{\ell\ell bb}$ variable correction derived in the $n_b = 1$ control region. For the background simulated samples, color code shown in Figure 3.5 has been used. At the bottom panel, the filled area represent the statistical uncertainties, while the blue line shows the combined uncertainty from statistical and shape uncertainties. The total uncertainty which combines statistical and systematic uncertainties are also shown as a red line.

The shape correction for m_{bb}

The m_{bb} correction was introduced in order to correct the bias of the shape in the signal region with high value m_H windows. There is a slope in the m_{bb} distribution appearing after the $\sqrt{\Sigma p_T^2}/m_{\ell\ell bb}$ variable cut, as shown in Figure 6.6(a) and 6.6(b). The slope does not affect the $t\bar{t}$ normalisation since the normalisation is taken by a dedicated top control region after the m_{bb} window cut applied. However, this will affect the normalisation of the Z+jets events since their normalisation are estimated from the sideband regions. The normalisation is biased by the events in the region with lower m_{bb} since the statistics rapidly reduce as m_{bb} increases. Eventually, the applied scale factor which was derived before the m_{bb} window cannot explain the difference between data and simulated events in such low statistics region, and hence the slope appeared. Figure 6.6(a) and 6.6(b) shows the m_{jb} and m_{bb} distribution before the m_{bb} correction applied in $n_b = 1$ and $n_b = 2$ categories, respectively. Similar to the $\sqrt{\Sigma p_T^2}/m_{\ell\ell bb}$ and p_T^Z corrections, the m_{bb} correction is done by using the shape of the m_{jb} distribution from the $n_b = 1$ category. The m_{jb} and m_{bb} distributions after the correction are shown in Figure 6.6(c) and 6.6(d).

The m_{bb} correction is applied also on the $n_b \geq 3$ category. The only difference is that the associated uncertainty in the $n_b \geq 3$ category is larger than the one in the $n_b = 2$ category. The uncertainties used in both $n_b = 2$ and $n_b \geq 3$ categories are:

$$f(m_{bb}, n_b = 2) = \begin{cases} 0.02357 + (-0.00017 \cdot m_{bb}), & \text{for } m_{bb} < 609 \text{ GeV} \\ -0.07996, & \text{for } m_{bb} \geq 609 \text{ GeV} \end{cases}$$

and

$$f(m_{bb}, n_b \geq 3) = \begin{cases} 0.04714 + (-0.00034 \cdot m_{bb}), & \text{for } m_{bb} < 609 \text{ GeV} \\ -0.15992, & \text{for } m_{bb} \geq 609 \text{ GeV} \end{cases}.$$

Figure 6.6(e) and 6.6(f) shows the m_{bb} distribution in the $n_b \geq 3$ category before and after the correction, respectively.

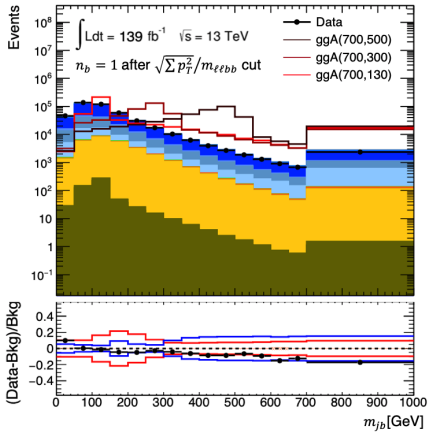

(a) $n_b = 1$, $\sqrt{\Sigma p_T^2}/m_{\ell\ell bb}$ corrected

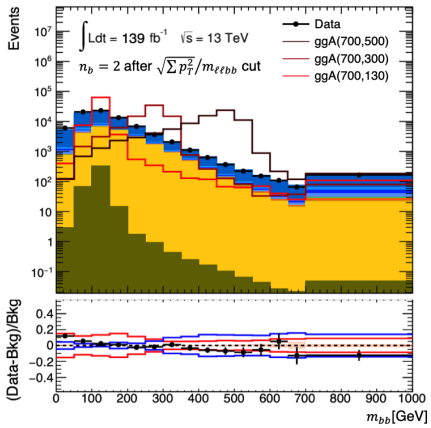

(b) $n_b = 2$, $\sqrt{\Sigma p_T^2}/m_{\ell\ell bb}$ corrected

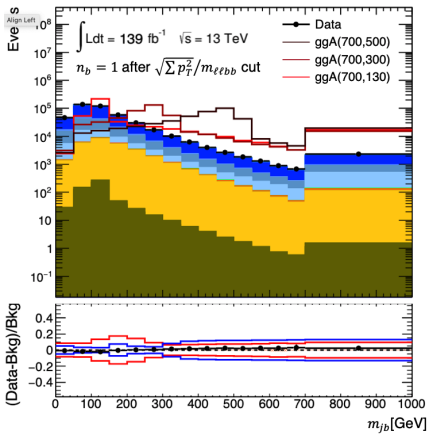

(c) $n_b = 1$, m_{jb} corrected

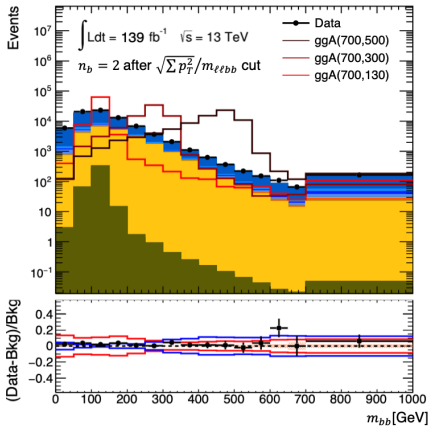

(d) $n_b = 2$, m_{bb} corrected

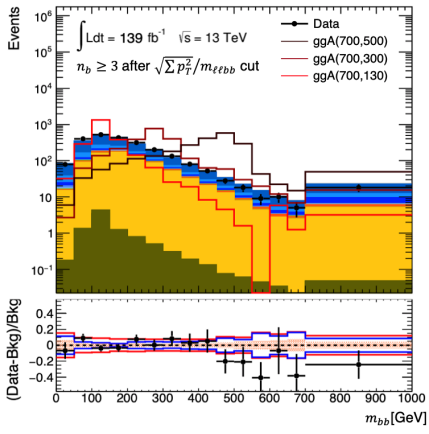

(e) $n_b \geq 3$, no m_{bb} correction

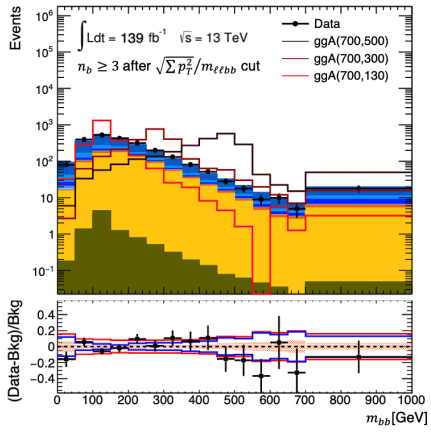

(f) $n_b \geq 3$, m_{bb} corrected

Figure 6.6: The m_{jb} and m_{bb} distributions after the $\sqrt{\Sigma p_T^2}/m_{\ell\ell bb}$ cut in different categories. (a) The m_{jb} distributions in $n_b = 1$ control region with $\sqrt{\Sigma p_T^2}/m_{\ell\ell bb}$ correction applied. (b) The m_{bb} distributions in $n_b = 2$ category with $\sqrt{\Sigma p_T^2}/m_{\ell\ell bb}$ correction applied. (c) The m_{jb} distributions in $n_b = 1$ control region with m_{jb} correction applied. (d) The m_{bb} distributions in $n_b = 2$ category with m_{bb} correction applied. (e) The m_{bb} distributions in $n_b \geq 3$ category without m_{bb} correction applied. (f) The m_{bb} distributions in $n_b \geq 3$ category with m_{bb} correction applied. For the background simulated samples, colour code shown in Figure 3.5 has been used. At the bottom panel, the filled area represent the statistical uncertainties, while the blue line shows the combined uncertainty from statistical and shape uncertainties. The total uncertainty which combines statistical and systematic uncertainties are also shown as a red line.

The $n_b = 1$ control region

As shown in Table 6.7, all the corrections are derived from the corresponding distribution in the $n_b = 1$ control region. It is important to examine the properties, for instance the signal contentment and the agreement between data and simulated backgrounds after the m_{jb} window, in the $n_b = 1$ control region. Table 6.8 shows the signal acceptance in the $n_b = 1$ control region, and Figure 6.7 shows the $m_{\ell\ell jb}$ distribution after the m_{jb} window, which is defined as: $0.85 \times m_H - 20$ GeV $< m_{jb} < m_H + 20$ GeV, in the $n_b = 1$ control region. All the corrections along with their systematic uncertainties are used, the agreement within the systematic uncertainties is good. Comparing the signal acceptance in Table 6.8 and 6.1, the signal acceptances are very similar. However, Table 6.5 and 6.6 shows that the backgrounds are 7 times larger in the $n_b = 1$ control region, and therefore it is safe to be used as a control region.

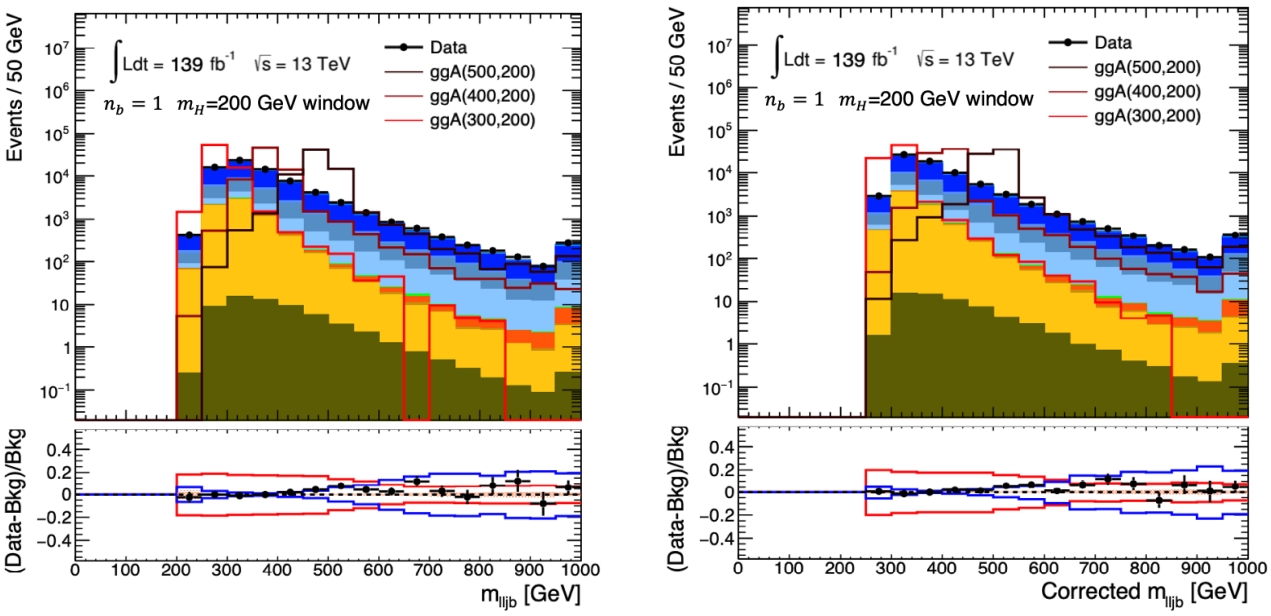

(a) $m_{\ell\ell jb}$, passed $m_H = 200$ GeV window

(b) $m_{\ell\ell jb}$ with mass scaling, passed $m_H = 200$ GeV window

Figure 6.7: The $m_{\ell\ell jb}$ distribution (a) without and (b) with the mass scaling in the signal regions after the $\sqrt{\Sigma p_T^2}/m_{\ell\ell bb}$ cut and the m_{jb} window in the $n_b = 1$ control region. All correction described in this section has been applied with their systematic uncertainties. For the background simulated samples, color code shown in Figure 3.5 has been used. At the bottom panel, the filled area represent the statistical uncertainties, while the blue line shows the combined uncertainty from statistical and shape uncertainties. The total uncertainty which combines statistical and systematic uncertainties are also shown as a red line.

gluon-gluon fusion				
mA	mH	before $\sqrt{\Sigma p_T^2}/m_{\ell\ell bb}$	after $\sqrt{\Sigma p_T^2}/m_{\ell\ell bb}$	after m_{jb} windows
230	130	0.09117 ± 0.00054	0.07082 ± 0.00048	0.04113 ± 0.00037
250	130	0.11027 ± 0.00060	0.08458 ± 0.00053	0.04707 ± 0.00040
300	130	0.13822 ± 0.00075	0.10178 ± 0.00064	0.05093 ± 0.00045
300	200	0.10431 ± 0.00059	0.08247 ± 0.00053	0.04083 ± 0.00037
350	250	0.10673 ± 0.00060	0.08508 ± 0.00054	0.04001 ± 0.00037
400	130	0.16256 ± 0.00076	0.11905 ± 0.00065	0.05569 ± 0.00045
500	130	0.17124 ± 0.00079	0.12495 ± 0.00068	0.05962 ± 0.00047
500	200	0.16575 ± 0.00078	0.12633 ± 0.00068	0.05845 ± 0.00046
500	300	0.15219 ± 0.00074	0.12056 ± 0.00066	0.05326 ± 0.00044
500	400	0.10939 ± 0.00062	0.08908 ± 0.00056	0.04072 ± 0.00038
700	130	0.17437 ± 0.00081	0.12725 ± 0.00069	0.06710 ± 0.00050
700	200	0.17511 ± 0.00081	0.13047 ± 0.00070	0.06305 ± 0.00049
700	300	0.17288 ± 0.00081	0.13423 ± 0.00071	0.05997 ± 0.00047
700	400	0.16145 ± 0.00078	0.13044 ± 0.00070	0.05658 ± 0.00046
700	500	0.15060 ± 0.00075	0.12369 ± 0.00068	0.05455 ± 0.00045
b-associated production				
mA	mH	before $\sqrt{\Sigma p_T^2}/m_{\ell\ell bb}$	after $\sqrt{\Sigma p_T^2}/m_{\ell\ell bb}$	after m_{jb} windows
230	130	0.0789 ± 0.0011	0.05746 ± 0.00094	0.03951 ± 0.00079
300	200	0.0877 ± 0.0012	0.0667 ± 0.0010	0.03512 ± 0.00077
400	200	0.1050 ± 0.0013	0.0792 ± 0.0012	0.03913 ± 0.00082
500	130	0.1170 ± 0.0015	0.0844 ± 0.0012	0.04185 ± 0.00088
500	300	0.0995 ± 0.0016	0.0776 ± 0.0012	0.03409 ± 0.00080
500	400	0.0833 ± 0.0012	0.0648 ± 0.0011	0.02950 ± 0.00072
700	200	0.1129 ± 0.0015	0.0832 ± 0.0013	0.04159 ± 0.00088
700	300	0.1092 ± 0.0014	0.0841 ± 0.0013	0.03847 ± 0.00085
700	400	0.1043 ± 0.0014	0.0829 ± 0.0012	0.03485 ± 0.00081
700	500	0.0958 ± 0.0013	0.0780 ± 0.0012	0.03450 ± 0.00078

Table 6.8: Signal acceptance before and after the $\sqrt{\Sigma p_T^2}/m_{\ell\ell bb}$ cut; and after the m_{jb} windows in $n_b = 1$ control region. Only some of the signal samples are shown in this table. Only uncertainties due to the finite number of generated events in the simulated samples are considered.

6.3 Statistical Analysis

The statistical analysis is conducted based on the statistical framework as described in Section 5.6. The likelihood function, the definition and the application of the scale factors considered in this search is exactly the same as the one mentioned in Section 5.6. Table 6.9 shows some examples of the scale factors for Z+jets and $t\bar{t}$ backgrounds in different signal regions. The Z+jets scale factors are derived from the Z+jets sideband region, while the $t\bar{t}$ scale factors are derived from the $t\bar{t}$ control region. The detailed event selection and the definitions of the signal and control regions are described in Section 5.1. Compare to Table 5.7, the agreement of the scale factors in the corresponding regions between the searches is very well.

	$n_b = 2$ category		$n_b \geq 3$ category	
m_H [GeV] for signal region	$Z+jets$	$t\bar{t}$	$Z+jets$	$t\bar{t}$
130	1.216 ± 0.009	0.996 ± 0.010	1.43 ± 0.05	1.46 ± 0.06
350	1.199 ± 0.031	0.905 ± 0.018	1.58 ± 0.13	1.41 ± 0.11
500	1.18 ± 0.06	0.92 ± 0.05	1.27 ± 0.23	1.15 ± 0.20
700	1.307 ± 0.098	0.99 ± 0.11	0.79 ± 0.27	1.35 ± 0.35

Table 6.9: The Z+jets and $t\bar{t}$ scale factors used in the fit with respected to different m_H hypothesis of signal region. Scale factors are estimated in the Z+jets sideband region and $t\bar{t}$ control region.

The effect of systematic uncertainties on the search is studied using the signal-strength parameter μ for hypothesised signal production. As mentioned in Section 6.2.1, the systematic uncertainties associated with the corrections are considered as the new source of shape systematic uncertainties within the "Bkg. model." group. Table 6.10 shows the relative uncertainties in the best-fit μ value from the leading sources of systematic uncertainty for two example mass points of both gluon fusion and b-associated production of a narrow-width A boson. In this table, the uncertainties are combined into different groups and the short-hands are introduced in Section 5.6. The leading sources of systematic uncertainty are similar for other mass points studied and for larger A boson widths. For all cases, the limited size of the simulated samples has the largest impact on the search sensitivity among all the sources of systematic uncertainty. While systematic uncertainties and the statistical uncertainty of the data have comparable impact at low masses, the search sensitivity is mostly determined at high masses by the limited size of the data sample.

gluon fusion production				*b*-associated production			
(230,130) GeV		(700,200) GeV		(230,130) GeV		(700,200) GeV	
Source	$\Delta\mu/\mu$ [%]	Source	$\Delta\mu/\mu$ [%]	Source	$\Delta\mu/\mu$ [%]	Source	$\Delta\mu/\mu$ [%]
Data stat.	37	Data stat.	75	Data stat.	50	Data stat.	76
Total syst.	63	Total syst.	25	Total syst.	50	Total syst.	23
Sim. stat.	17	Sim. stat.	1.9	Sim. stat.	14	Sim. stat.	1.9
Sig. interp.	4.7	Sig. interp.	2.8	Sig. interp.	8.1	Sig. interp	6.4
Bkg. model.	17	Bkg. model.	11	Bkg. model.	9.5	Bkg. model.	9.5
JES/JER	19	JES/JER	11	JES/JER	9.2	JES/JER	9.0
b-tagging	2.7	*b*-tagging	5.4	*b*-tagging	4.1	*b*-tagging	5.1
Theory	2.6	Theory	3.3	Theory	2.2	Theory	1.8

Table 6.10: The effect of the most important sources of uncertainty group on the signal-strength parameter at two example mass points of $(m_A, m_H) = (230, 130)$ GeV and $(m_A, m_H) = (700, 200)$ GeV for both the gluon fusion and *b*-associated production of a narrow-width A boson [58].

6.4 Results

As mentioned in Section 5.7, fits in this search are also preformed under three scenarios: Consider only the gluon fusion signal in $n_b = 2$ category; consider the b-associated production signal in both $n_b = 2$ and $n_b \geq 3$ categories; consider both gluon fusion and b-associated production signals in $n_b = 2$ category and only the b-associated production signal in $n_b \geq 3$ category. First two scenarios are used in the p-value scan and upper limit calculation across the (m_A, m_H) plane as shown in Figure 6.8 and 6.10, respectively. In this search, the upper limit calculated from the large width samples are also preformed, as shown in Figure 6.11 and 6.12. The third scenario is used in the upper limit calculation across the 2HDM parameter space as shown in Figure 6.14.

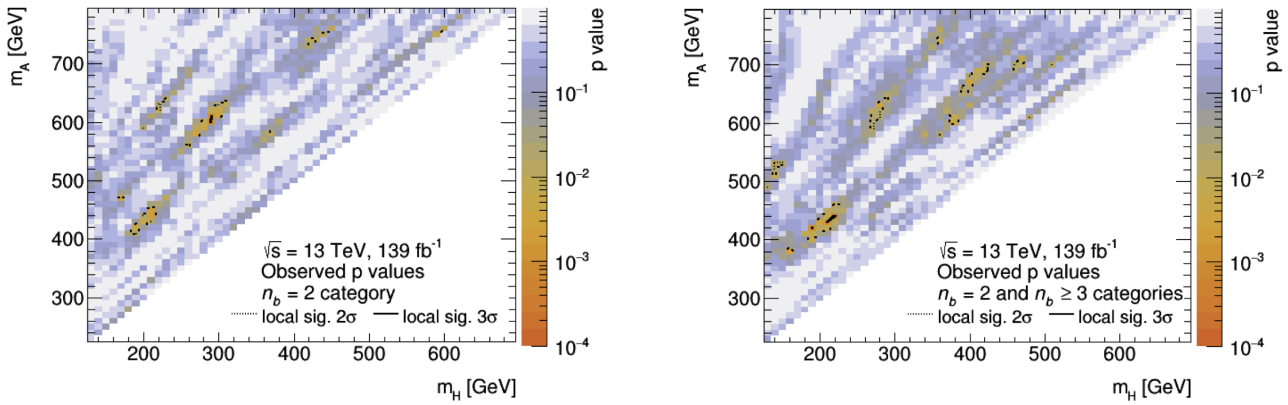

(a) gluon-gluon fusion (b) *b*-associated production

Figure 6.8: p-value scan from the test statistic q_0 for (a) gluon-gluon fusion and (b) *b*-associated production.

The largest significance excess for gluon-gluon fusion is locally 3.1σ, found at (m_A, m_H) = (610,

290) GeV, which corresponding to 1.3σ after taking into account the look-elsewhere effect. For the b-associated production, the largest excess occurs at (m_A,m_H) = (440,220) GeV with a local significance of 3.1 σ, which corresponding to 1.3σ after considering the look-elsewhere effect. The $m_{\ell\ell bb}$ spectra corresponding to m_H = 130 and 610 GeV hypothesis are shown in Figure 6.9.

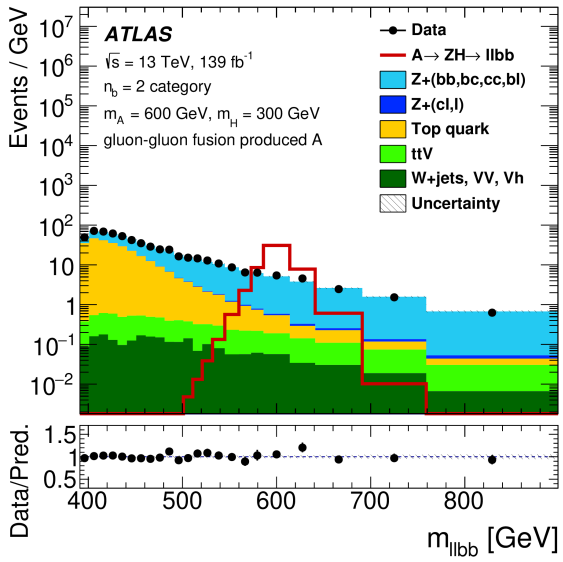

(a) $n_b = 2$ category,m_H = 300 GeV

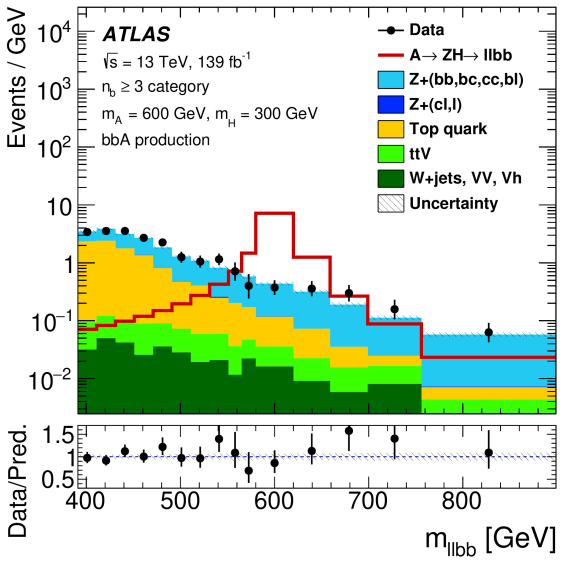

(b) $n_b \geq 3$ category,m_H = 300 GeV

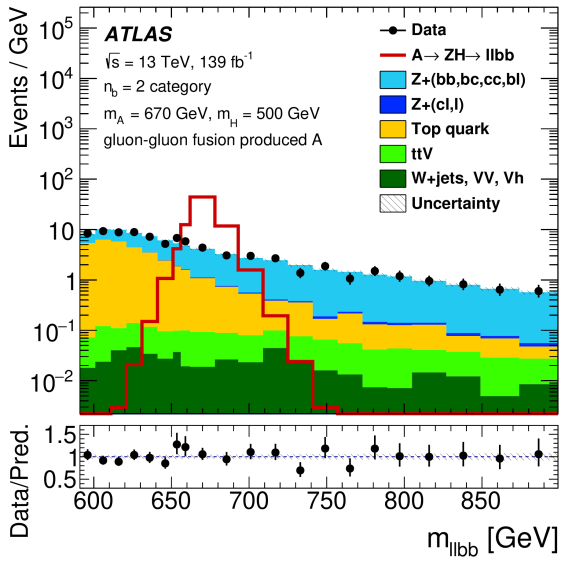

(c) $n_b = 2$ category,m_H = 500 GeV

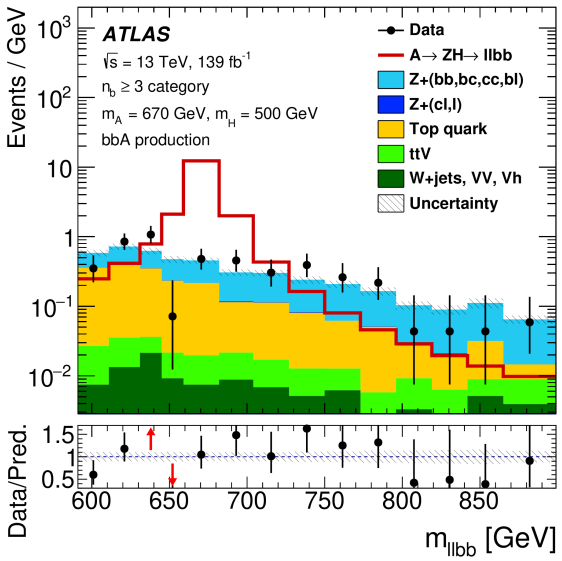

(d) $n_b \geq 3$ category,m_H = 500 GeV

Figure 6.9: Distribution of $m_{\ell\ell bb}$ for m_H = 300 GeV hypothesis in the (a) $n_b = 2$ and (b) $n_b \geq 3$ categories, and for m_H = 500 GeV hypothesis in the (c) $n_b = 2$ and (d) $n_b \geq 3$ categories. The solid dots in the bottom panels represent the ratio of the data to background prediction obtained from the Maximum Likelihood Function with $\mu = 0$. The signal distributions are presented under the assumption of $\sigma(A) \times B(A \to ZH) \times B(H \to bb)$ = 1 pb.

The upper limits on $\sigma(A) \times B(A \to ZH) \times B(H \to bb)$ are calculated at 95% confidence-level

based on the CL_s method which described in Section 5.6.1. Figure 6.10 shows the upper limits for gluon-gluon fusion and b-associated production. In this figure, upper limits are calculated using the narrow-width A bosons. The expected and observed upper limits for gluon fusion produced narrow-width A bosons in the $n_b = 2$ category are shown in Figures 6.10(a) and 6.10(b), respectively. For the b-associated production of narrow-width A bosons, the expected and observed limits for the combination of the $n_b = 2$ and $n_b \geq 3$ categories are shown in Figures 6.10(c) and 6.10(d), respectively. The upper limits for gluon fusion vary from 6.2 fb for (m_A,m_H) = (780, 129) GeV to 380 fb for (m_A,m_H) = (250, 150) GeV. This is to be compared with the corresponding expected limits of 15 fb and 240 fb for these two signal hypotheses. For the b-associated production the upper limit varies from 6.8 fb for (m_A,m_H) = (760, 220) GeV to 210 fb for (m_A,m_H) = (230, 130) GeV, whereas the corresponding expected limits are 15 fb and 160 fb, respectively. Compare to the result from Section 5.7, the upper limits for gluon fusion are improved from the range of 14-830 fb to the reange of 6.2-380 fb, while the limits for b-associated production are improved from 26-570 fb to 6.8-210 fb. The improvement is expected due to the increased luminosity and the improved generator modelling uncertainties of the backgrounds in the search described in this chapter.

Upper limits are also calculated for signal assumptions with large natural widths of the A boson in comparison with the experimental mass resolution, which is needed for the interpretation in the context of the 2HDM. The upper limit degrades with the increasing natural width with respect to the narrow A boson width upper limits that were discussed earlier. In particular, a gluon–gluon produced A boson with natural width of 10% with respect to its mass degrades the upper limits on average by a factor of approximately 3. This factor becomes approximately 4 when the natural width increases 20%. The b-associated produced A bosons have worse experimental mass resolution and the degradation of the limit is on average smaller: the upper limits are degraded by a factor of about 1.9 and 2.3 for a natural width of 10% and 20%, respectively. Figure 6.13 shows the upper limits for a fixed choice of $m_H = 130$ GeV. In this figure, upper limit calculated using narrow-width, natural width of 10% and 20% with respect to the A boson mass are shown for both gluon–gluon produced and b-associated produced A bosons in 6.13(a) and 6.13(b), respectively.

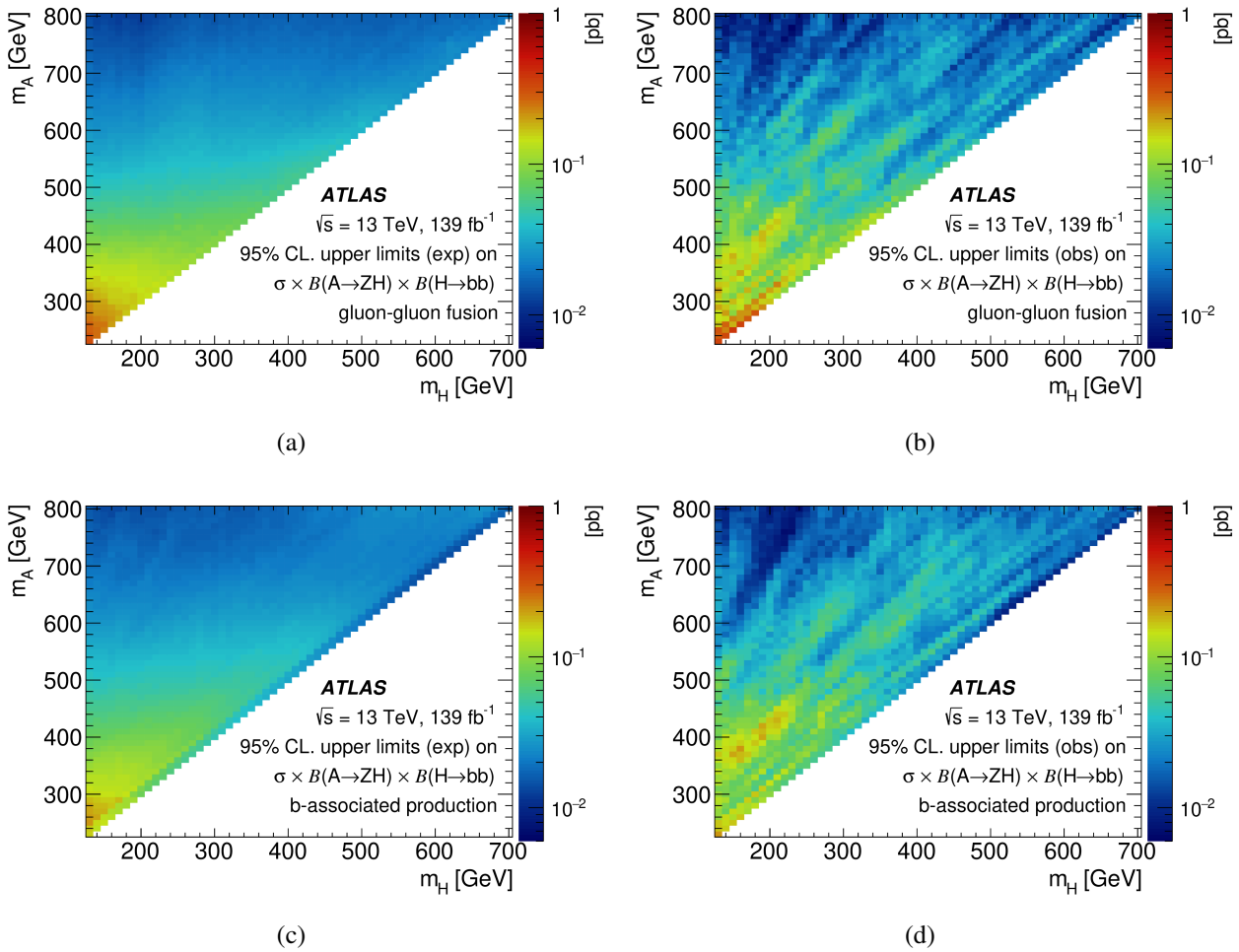

Figure 6.10: Upper bounds at 95% CL on the production cross-section times the branching ratio $B(A \to ZH) \times B(H \to bb)$ in pb for (a, b) gluon fusion and (c, d) b-associated production. The expected upper limits are shown in (a) and (c) and the observed upper limits are shown in (b) and (d).

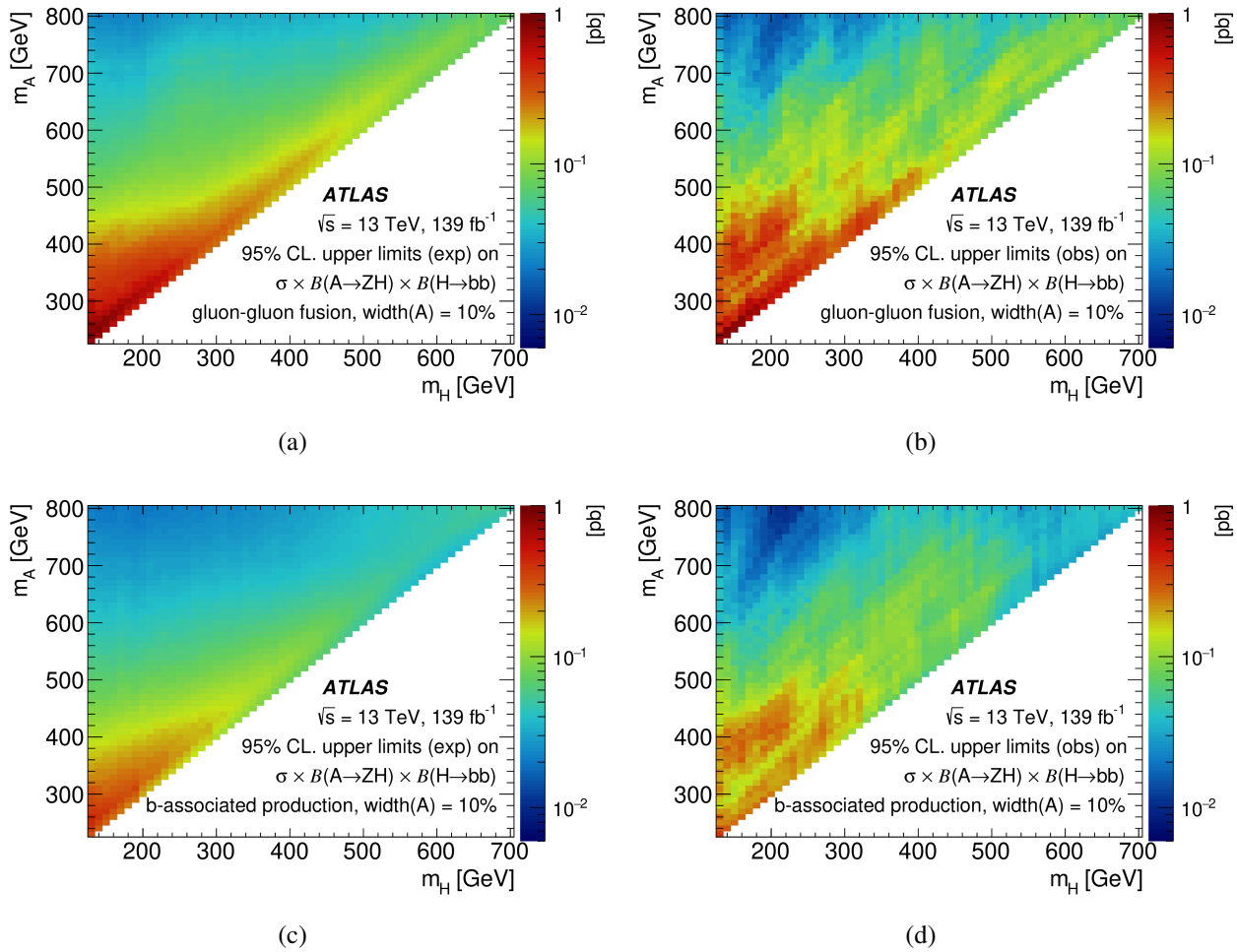

Figure 6.11: Upper bounds at 95% CL on the production cross-section times the branching ratio $B(A \to ZH) \times B(H \to bb)$ in pb for (a, b) gluon fusion and (c, d) b-associated production with natural width of 10% with respect to the A. The expected upper limits are shown in (a) and (c) and the observed upper limits are shown in (b) and (d).

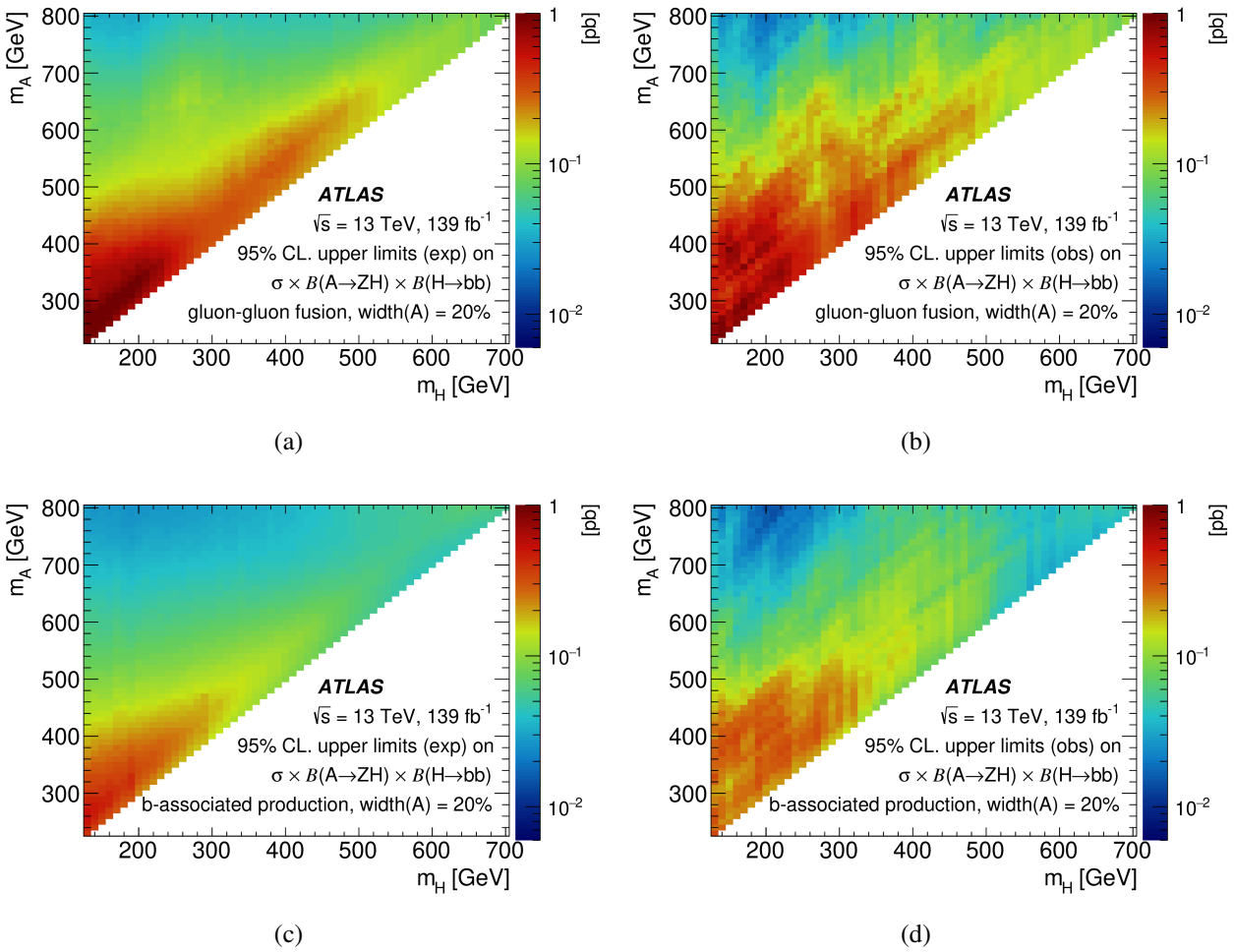

Figure 6.12: Upper bounds at 95% CL on the production cross-section times the branching ratio $B(A \to ZH) \times B(H \to bb)$ in pb for (a, b) gluon fusion and (c, d) b-associated production with natural width of 20% with respect to the A. The expected upper limits are shown in (a) and (c) and the observed upper limits are shown in (b) and (d).

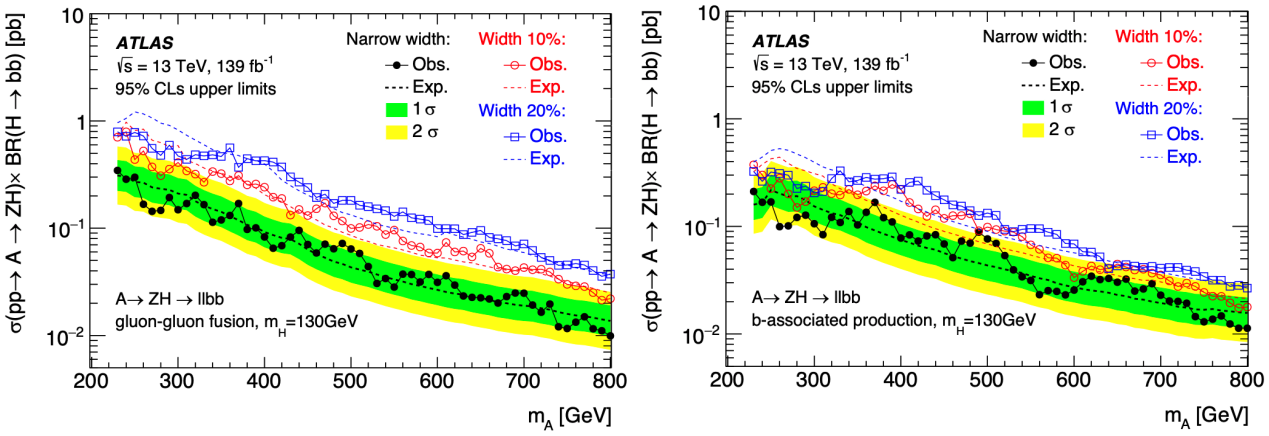

(a) (b)

Figure 6.13: Observed and expected upper limits at 95% CL on the production cross section times the branching ratio $B(A \to ZH) \times B(H \to bb)$ in pb as a function of m_A for a fixed choice of $m_H = 130$ GeV. The upper limits are shown for an A boson with narrow width with respect to the experimental mass resolution, and for a natural width of 10% and 20% with respect with its mass. The plots refer to an A boson produced via (a) gluon fusion and (b) b-associated production.

The results with natural A boson widths that are comparable or larger with respect to the experimental mass resolution are used for the interpretation of the search in the context of the CP-conserving 2HDM. The choices of the 2HDM benchmark and the methodology of calculate the cross-sections for A boson production are the same as mentioned in Section 5.7. The interpretation of the search in the 2HDM is performed on (m_A, m_H) plane, as shown in Figure 6.14. In this plot, colour shaded areas and solid lines indicate expected and observed exclusions for various $\tan\beta$ values, respectively. There is one plot for each of the four 2HDM types. Similarly to the result from Chapter 5, the constraints are similar for the type-I and lepton-specific 2HDM because they only differ in the lepton Yukawa couplings. The search excludes the type-I and lepton-specific 2HDM parameter space up to $m_H \lesssim 350$ GeV for $\tan\beta = 1$ but the sensitivity degrades for larger $\tan\beta$ values: For $\tan\beta = 10$ the exclusion is up to $m_H \lesssim 320$ GeV and $m_A \lesssim 550$ GeV. Type-II and flipped are dominated by b-associated produced A bosons as $\tan\beta$ increases, although gluon fusion is still important for $\tan\beta \approx 1$. Similarly to type-I and lepton-specific, they show similar constraints because the only differ in the lepton Yukawa couplings. The contribution due to the b-associated signal production increases the sensitivity at large $\tan\beta$ values, which excludes $m_H \lesssim 650$ GeV for $\tan\beta = 20$. The search sensitivity degrades at lower $\tan\beta$ values, excluding up to $m_H \lesssim 350$ GeV for $\tan\beta = 1$.

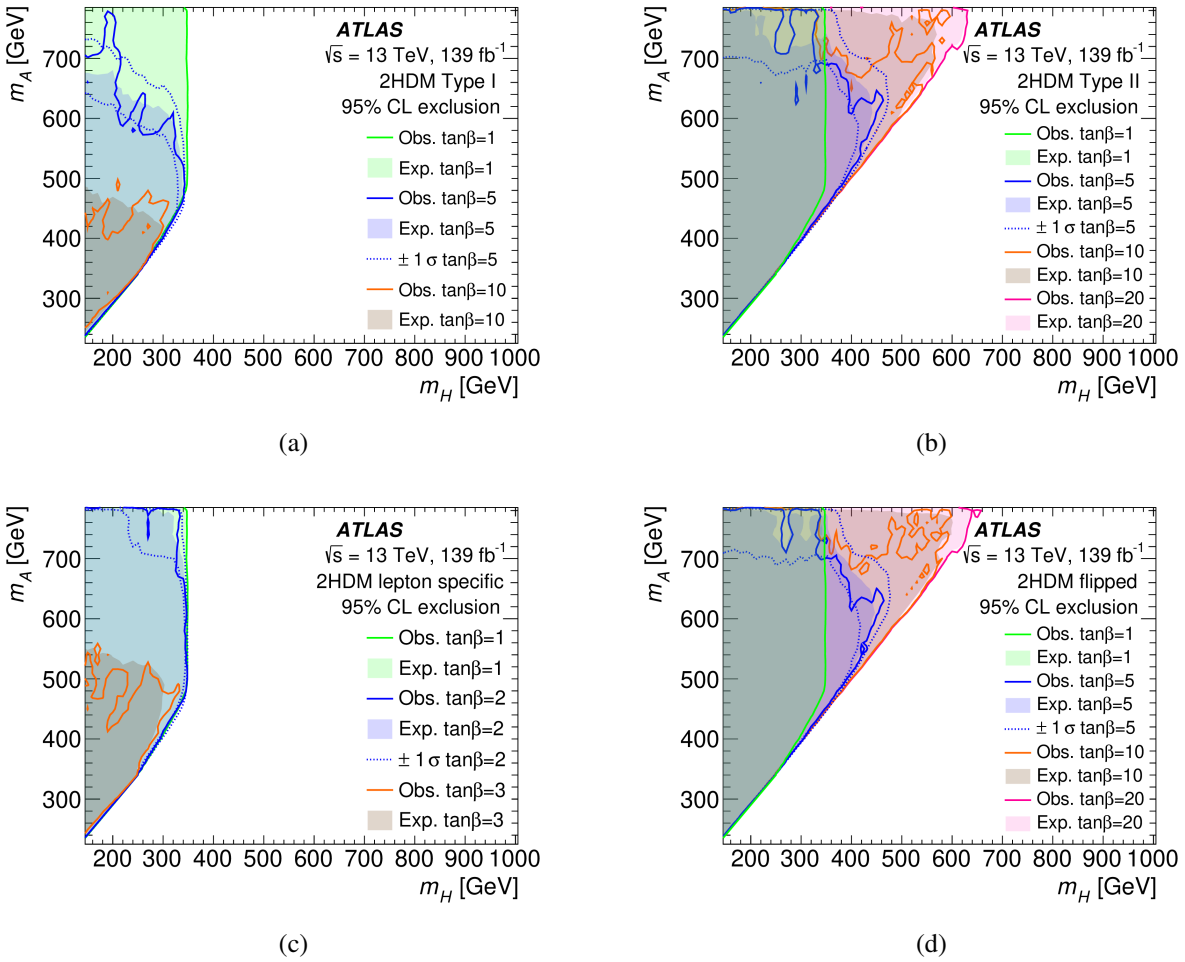

Figure 6.14: Observed and expected 95% CL exclusion regions in the (m_A,m_H) plane for various $\tan\beta$ values for (a) type I, (b) type II, (c) lepton-specific and (d) flipped 2HDM.

In conclusion, no significant deviation from the standard model background predictions are observed in the final state that is considered in this search. Considering each production process separately, upper limits are set at the 95% confidence level for $\sigma(A) \times B(A \to ZH) \times B(H \to bb)$ of 6.2–380 fb for gluon fusion and 6.8–210 fb for b-associated production of a narrow A boson for the mass ranges 130–700 GeV of the H boson and 230–800 GeV of the A boson. Taking into account both production processes, this search further tightens the constraints on the 2HDM parameter space comparing to the result shown in Section 5.7, especially for low $\tan\beta$ values in the high m_A regions.

CHAPTER 7

Conclusion

In this thesis, searches for heavy Higgs bosons A decaying into a Z boson another heavy Higgs boson H and is presented in the $\ell\ell bb$ final state, using 36.1 fb^{-1} and 139 fb^{-1} of proton-proton collision data at center-of-mass energy of $\sqrt{s} = 13$ TeV recorded by ATLAS detector at the LHC. Both gluon fusion production and b-associated production of the A boson are considered. The observed data are found to be compatible with the standard model prediction, with no significant excess observed.

No significant excess from the standard model background prediction are observed in the $ZH \to \ell\ell bb$ final state which is considered in the searches described in this thesis. Considering each production process separately, upper limits are set on the product $\sigma(A) \times BR(A \to ZH) \times BR(H \to bb)$ with 95% confidence-level across the (m_A,m_H) plane. For the search with integrated luminosity of 36.1 fb^{-1}, the upper limits range from 14 fb to 830 fb and from 26 fb to 570 fb for the gluon fusion production and b-associated production of a narrow-width A boson, respectively. In the search with integrated luminosity of 139 fb^{-1}, the upper limits range from 6.2 fb to 380 fb and from 6.8 fb to 210 fb for the gluon fusion production and b-associated production of a narrow-width A boson, respectively. Taking into account both production processes, the search also tightens the constraints on difference types of 2HDMs in the past of the parameter space with a large mass splitting between m_A and m_H by taking into account both production processes. These constraints are established for Type-I, Type-II, lepton-specific and flipped 2HDMs in the (m_A,m_H) plane with different $\tan\beta$ values.

As the LHC physics program continues, this channel remains a smoking gun of new physics beyond the standard model. The Run-III operation of LHC is planned to start at the beginning of March 2022, with a goal of delivering instantaneous luminosity of about 300 fb^{-1} of data at the center-of-mass energy of 14 TeV until the end of 2024. After that, the high luminosity LHC is scheduled to come into operation at the end of 2027 with an expected total integrated luminosity of about 3000 fb^{-1}

in around a decade. All of these further extend the discovery potential at the LHC and improve the sensitivity to the rare processes will provide a more complete picture of the elementary particles. For the $A \to ZH$ searches, the constraints on the 2HDM phase space will be further tightened by analyse the data collected from these high luminosity machines. Also, they provide an opportunity to search for some rare processes such as t-associated production or searches away from the weak decoupling limit, for example $ZH \to \ell\ell WW/ZZ/hh$ final states. This channel remains a viable option for searching new physics beyond the Standard Model in the upcoming high luminosity era of particle physics.

Bibliography

[1] ATLAS Collaboration, "Observation of a new particle in the search for the Standard Model Higgs boson with the ATLAS detector at the LHC," *Phys. Lett. B*, vol. 716, no. 1, pp. 1–29, 2012.

[2] CMS Collaboration, "Observation of a new boson at a mass of 125 GeV with the CMS experiment at the LHC," *Phys. Lett. B*, vol. 716, no. 1, pp. 30–61, 2012.

[3] F. Englert and R. Brout, "Broken Symmetry and the Mass of Gauge Vector Mesons," *Phys. Rev. Lett.*, vol. 13, pp. 321–323, 1964. DOI: 10.1103/PhysRevLett.13.321.

[4] P. W. Higgs, "Broken Symmetries and the Masses of Gauge Bosons," *Phys. Rev. Lett.*, vol. 13, pp. 508–509, 1964. DOI: 10.1103/PhysRevLett.13.508.

[5] P. W. Higgs, "Spontaneous Symmetry Breakdown without Massless Bosons," *Phys. Rev.*, vol. 145, pp. 1156–1163, 1966. DOI: 10.1103/PhysRev.145.1156.

[6] M. Thomson, *Modern particle physics*. New York: Cambridge University Press, 2013, ISBN: 9781107034266. [Online]. Available: http://www-spires.fnal.gov/spires/find/books/www?cl=QC793.2.T46::2013.

[7] P. Langacker, *The standard model and beyond*. 2010, ISBN: 9781420079067.

[8] A. Purcell, "Go on a particle quest at the first CERN webfest. Le premier webfest du CERN se lance à la conquête des particules," no. BUL-NA-2012-269. 35/2012, p. 10, Aug. 2012. [Online]. Available: https://cds.cern.ch/record/1473657.

[9] S. L. Glashow, "Partial Symmetries of Weak Interactions," *Nucl. Phys.*, vol. 22, pp. 579–588, 1961. DOI: 10.1016/0029-5582(61)90469-2.

[10] S. Weinberg, "A Model of Leptons," *Phys. Rev. Lett.*, vol. 19, pp. 1264–1266, 1967. DOI: 10.1103/PhysRevLett.19.1264.

[11] A. Salam, "Weak and Electromagnetic Interactions," *Conf. Proc. C*, vol. 680519, pp. 367–377, 1968. DOI: 10.1142/9789812795915_0034.

[12] LHC Higgs Cross Section Working Group, "Handbook of LHC Higgs Cross Sections: 4. Deciphering the Nature of the Higgs Sector," 2016. DOI: 10.23731/CYRM-2017-002. arXiv: 1610.07922 [hep-ph].

[13] ATLAS Collaboration, "Evidence for the spin-0 nature of the Higgs boson using ATLAS data. Evidence for the spin-0 nature of the Higgs boson using ATLAS data," *Phys. Lett. B*, vol. 726, no. CERN-PH-EP-2013-102. CERN-PH-EP-2013-102, 120–144. 25 p, Jul. 2013. [Online]. Available: http://cds.cern.ch/record/1559925.

[14] CMS Collaboration, "Study of the Mass and Spin-Parity of the Higgs Boson Candidate via Its Decays to Z Boson Pairs. On the mass and spin-parity of the Higgs boson candidate via its decays to Z boson pairs," *Phys. Rev. Lett.*, vol. 110, no. CMS-HIG-12-041. CMS-HIG-12-041. CERN-PH-EP-2012-372, 081803. 15 p, Dec. 2012. [Online]. Available: http://cds.cern.ch/record/1502670.

[15] CMS Collaboration, "Precise determination of the mass of the Higgs boson and tests of compatibility of its couplings with the standard model predictions using proton collisions at 7 and 8 TeV," *Eur. Phys. J.*, vol. C75, no. 5, p. 212, 2015. DOI: 10.1140/epjc/s10052-015-3351-7. arXiv: 1412.8662 [hep-ex].

[16] ATLAS Collaboration, "Measurement of the Higgs boson mass from the $H \to \gamma\gamma$ and $H \to ZZ^* \to 4\ell$ channels with the ATLAS detector using 25 fb^{-1} of pp collision data," *Phys. Rev.*, vol. D90, no. 5, p. 052 004, 2014. DOI: 10.1103/PhysRevD.90.052004. arXiv: 1406.3827 [hep-ex].

[17] Particle Data Group, "Review of Particle Physics," *PTEP*, vol. 2020, no. 8, p. 083C01, 2020. DOI: 10.1093/ptep/ptaa104.

[18] ATLAS Collaboration, "Measurement of the Higgs boson coupling properties in the $H \to ZZ^* \to 4\ell$ decay channel at $\sqrt{s}$ = 13 TeV with the ATLAS detector," *JHEP*, vol. 03, p. 095, 2018. DOI: 10.1007/JHEP03(2018)095. arXiv: 1712.02304 [hep-ex].

[19] ATLAS Collaboration, "Measurements of Higgs boson properties in the diphoton decay channel with 36 fb^{-1} of pp collision data at $\sqrt{s} = 13$ TeV with the ATLAS detector," *Phys. Rev. D*, vol. 98, p. 052 005, 2018. DOI: 10.1103/PhysRevD.98.052005. arXiv: 1802.04146 [hep-ex].

[20] CMS Collaboration, "Measurements of properties of the Higgs boson decaying into the four-lepton final state in pp collisions at $\sqrt{s} = 13$ TeV," *JHEP*, vol. 11, p. 047, 2017. DOI: 10.1007/JHEP11(2017)047. arXiv: 1706.09936 [hep-ex].

[21] CMS Collaboration, "A measurement of the Higgs boson mass in the diphoton decay channel," *Phys. Lett. B*, vol. 805, p. 135 425, 2020. DOI: 10.1016/j.physletb.2020.135425. arXiv: 2002.06398 [hep-ex].

[22] ATLAS Collaboration, "Cross-section measurements of the Higgs boson decaying into a pair of τ-leptons in proton-proton collisions at $\sqrt{s} = 13$ TeV with the ATLAS detector," *Phys. Rev. D*, vol. 99, p. 072 001, 2019. DOI: 10.1103/PhysRevD.99.072001. arXiv: 1811.08856 [hep-ex].

[23] CMS Collaboration, "Observation of the Higgs boson decay to a pair of τ leptons with the CMS detector," *Phys. Lett.*, vol. B779, pp. 283–316, 2018. DOI: 10.1016/j.physletb.2018.02.004. arXiv: 1708.00373 [hep-ex].

[24] ATLAS Collaboration, "Observation of $H \to b\bar{b}$ decays and VH production with the ATLAS detector," *Phys. Lett.*, vol. B786, pp. 59–86, 2018. DOI: 10.1016/j.physletb.2018.09.013. arXiv: 1808.08238 [hep-ex].

[25] CMS Collaboration, "Observation of Higgs boson decay to bottom quarks," *Phys. Rev. Lett.*, vol. 121, no. 12, p. 121 801, 2018. DOI: 10.1103/PhysRevLett.121.121801. arXiv: 1808.08242 [hep-ex].

[26] ATLAS Collaboration, "A search for the dimuon decay of the Standard Model Higgs boson with the ATLAS detector," *Phys. Lett. B*, vol. 812, p. 135 980, 2021. DOI: 10.1016/j.physletb.2020.135980. arXiv: 2007.07830 [hep-ex].

[27] CMS Collaboration, "Evidence for Higgs boson decay to a pair of muons," *JHEP*, vol. 01, p. 148, 2021. DOI: 10.1007/JHEP01(2021)148. arXiv: 2009.04363 [hep-ex].

[28] ATLAS Collaboration, "Search for the Decay of the Higgs Boson to Charm Quarks with the ATLAS Experiment," *Phys. Rev. Lett.*, vol. 120, no. 21, p. 211 802, 2018. DOI: 10.1103/PhysRevLett.120.211802. arXiv: 1802.04329 [hep-ex].

[29] CMS Collaboration, "A search for the standard model Higgs boson decaying to charm quarks," *JHEP*, vol. 03, p. 131, 2020. DOI: 10.1007/JHEP03(2020)131. arXiv: 1912.01662 [hep-ex].

[30] ATLAS Collaboration, "Observation of Higgs boson production in association with a top quark pair at the LHC with the ATLAS detector," *Phys. Lett.*, vol. B784, pp. 173–191, 2018. DOI: 10.1016/j.physletb.2018.07.035. arXiv: 1806.00425 [hep-ex].

[31] CMS Collaboration, "Measurement of the Higgs boson production rate in association with top quarks in final states with electrons, muons, and hadronically decaying tau leptons at $\sqrt{s} =$ 13 TeV," Nov. 2020. arXiv: 2011.03652 [hep-ex].

[32] G. L. Kane and M. A. Shifman, "Introduction to 'the supersymmetric world: The Beginnings of the theory'," Feb. 2001. arXiv: hep-ph/0102298.

[33] R. D. Peccei and H. R. Quinn, "CP Conservation in the Presence of Instantons," *Phys. Rev. Lett.*, vol. 38, pp. 1440–1443, 1977. DOI: 10.1103/PhysRevLett.38.1440.

[34] R. D. Peccei and H. R. Quinn, "Constraints Imposed by CP Conservation in the Presence of Instantons," *Phys. Rev. D*, vol. 16, pp. 1791–1797, 1977. DOI: 10.1103/PhysRevD.16.1791.

[35] S. Weinberg, "A New Light Boson?" *Phys. Rev. Lett.*, vol. 40, pp. 223–226, 1978. DOI: 10.1103/PhysRevLett.40.223.

[36] F. Wilczek, "Problem of Strong P and T Invariance in the Presence of Instantons," *Phys. Rev. Lett.*, vol. 40, pp. 279–282, 1978. DOI: 10.1103/PhysRevLett.40.279.

[37] G. C. Branco, P. M. Ferreira, L. Lavoura, M. N. Rebelo, M. Sher, and J. P. Silva, "Theory and phenomenology of two-Higgs-doublet models," *Phys. Rept.*, vol. 516, pp. 1–102, 2012. DOI: 10.1016/j.physrep.2012.02.002. arXiv: 1106.0034 [hep-ph].

[38] J. F. Gunion and H. E. Haber, "The CP conserving two Higgs doublet model: The Approach to the decoupling limit," *Phys. Rev.*, vol. D67, p. 075 019, 2003. DOI: 10.1103/PhysRevD.67.075019. arXiv: hep-ph/0207010 [hep-ph].

[39] N. Craig, J. Galloway, and S. Thomas, "Searching for Signs of the Second Higgs Doublet," May 2013. arXiv: 1305.2424 [hep-ph].

[40] S. L. Glashow and S. Weinberg, "Natural conservation laws for neutral currents," *Phys. Rev. D*, vol. 15, pp. 1958–1965, 7 Apr. 1977. DOI: 10.1103/PhysRevD.15.1958. [Online]. Available: https://link.aps.org/doi/10.1103/PhysRevD.15.1958.

[41] ATLAS Collaboration, "Beyond Standard Model Higgs boson searches at a High-Luminosity LHC with ATLAS," 2013.

[42] ATLAS Collaboration, "Combined measurements of Higgs boson production and decay using up to 80 fb^{-1} of proton-proton collision data at $\sqrt{s} = 13$ TeV collected with the ATLAS experiment," *Phys. Rev. D*, vol. 101, no. 1, p. 012 002, 2020. DOI: 10.1103/PhysRevD.101.012002. arXiv: 1909.02845 [hep-ex].

[43] ATLAS Collaboration, "Search for a CP-odd Higgs boson decaying to Zh in pp collisions at $\sqrt{s}$ = 13 TeV with the ATLAS detector," Mar. 2016.

[44] D. Eriksson, J. Rathsman, and O. Stal, "2HDMC: Two-Higgs-Doublet Model Calculator Physics and Manual," *Comput. Phys. Commun.*, vol. 181, pp. 189–205, 2010. DOI: 10.1016/j.cpc.2009.09.011. arXiv: 0902.0851 [hep-ph].

[45] ATLAS Collaboration, "Searches for heavy ZZ and ZW resonances in the $\ell\ell qq$ and $\nu\nu qq$ final states in pp collisions at $\sqrt{s} = 13$ TeV with the ATLAS detector," *JHEP*, vol. 03, p. 009, 2018. DOI: 10.1007/JHEP03(2018)009. arXiv: 1708.09638 [hep-ex].

[46] ATLAS Collaboration, "Search for WW/WZ resonance production in $\ell\nu qq$ final states in pp collisions at $\sqrt{s} = 13$ TeV with the ATLAS detector," *JHEP*, vol. 03, p. 042, 2018. DOI: 10.1007/JHEP03(2018)042. arXiv: 1710.07235 [hep-ex].

[47] ATLAS Collaboration, "Search for diboson resonances in hadronic final states in 139 fb^{-1} of pp collisions at $\sqrt{s} = 13$ TeV with the ATLAS detector," *JHEP*, vol. 09, p. 091, 2019. DOI: 10.1007/JHEP09(2019)091. arXiv: 1906.08589 [hep-ex].

[48] CMS Collaboration, "Search for a heavy Higgs boson decaying to a pair of W bosons in proton-proton collisions at $\sqrt{s} = 13$ TeV," *JHEP*, vol. 03, p. 034, 2020. DOI: 10.1007/JHEP03(2020)034. arXiv: 1912.01594 [hep-ex].

[49] CMS Collaboration, "Search for a new scalar resonance decaying to a pair of Z bosons in proton-proton collisions at $\sqrt{s} = 13$ TeV," *JHEP*, vol. 06, p. 127, 2018. DOI: 10.1007/JHEP06(2018)127. arXiv: 1804.01939 [hep-ex].

[50] ATLAS Collaboration, "Combination of searches for Higgs boson pairs in pp collisions at $\sqrt{s}$ =13 TeV with the ATLAS detector," *Phys. Lett. B*, vol. 800, p. 135 103, 2020. DOI: 10.1016/j.physletb.2019.135103. arXiv: 1906.02025 [hep-ex].

[51] CMS Collaboration, "Combination of searches for Higgs boson pair production in proton-proton collisions at $\sqrt{s} = 13$ TeV," *Phys. Rev. Lett.*, vol. 122, no. 12, p. 121 803, 2019. DOI: 10.1103/PhysRevLett.122.121803. arXiv: 1811.09689 [hep-ex].

[52] CMS Collaboration, "Search for a heavy pseudoscalar Higgs boson decaying into a 125 GeV Higgs boson and a Z boson in final states with two tau and two light leptons at $\sqrt{s} = 13$ TeV," *JHEP*, vol. 03, p. 065, 2020. DOI: 10.1007/JHEP03(2020)065. arXiv: 1910.11634 [hep-ex].

[53] ATLAS Collaboration, "Search for heavy Higgs bosons decaying into two tau leptons with the ATLAS detector using pp collisions at $\sqrt{s} = 13$ TeV," *Phys. Rev. Lett.*, vol. 125, no. 5, p. 051 801, 2020. DOI: 10.1103/PhysRevLett.125.051801. arXiv: 2002.12223 [hep-ex].

[54] CMS Collaboration, "Search for beyond the standard model Higgs bosons decaying into a $b\bar{b}$ pair in pp collisions at $\sqrt{s} = 13$ TeV," *JHEP*, vol. 08, p. 113, 2018. DOI: 10.1007/JHEP08(2018)113. arXiv: 1805.12191 [hep-ex].

[55] CMS Collaboration, "Search for additional neutral MSSM Higgs bosons in the $\tau\tau$ final state in proton-proton collisions at $\sqrt{s} = 13$ TeV," *JHEP*, vol. 09, p. 007, 2018. DOI: 10.1007/JHEP09(2018)007. arXiv: 1803.06553 [hep-ex].

[56] CMS Collaboration, "Search for neutral resonances decaying into a Z boson and a pair of b jets or τ leptons," *Phys. Lett. B*, vol. 759, pp. 369–394, 2016. DOI: 10.1016/j.physletb.2016.05.087. arXiv: 1603.02991 [hep-ex].

[57] ATLAS Collaboration, "Search for a heavy Higgs boson decaying into a Z boson and another heavy Higgs boson in the $\ell\ell bb$ final state in pp collisions at $\sqrt{s} = 13$ TeV with the ATLAS detector," *Phys. Lett. B*, vol. 783, no. arXiv:1804.01126, 392–414. 23 p, Apr. 2018. DOI: 10.1016/j.physletb.2018.07.006. [Online]. Available: https://cds.cern.ch/record/2311387.

[58] ATLAS Collaboration, "Search for a heavy Higgs boson decaying into a Z boson and another heavy Higgs boson in the $\ell\ell bb$ and $\ell\ell WW$ final states in pp collisions at $\sqrt{s} = 13$ TeV with the ATLAS detector," no. arXiv:2011.05639, Nov. 2020. [Online]. Available: https://arxiv.org/abs/2011.05639.

[59] C. Bambi and A. D. Dolgov, *Introduction to Particle Cosmology*, ser. UNITEXT for Physics. Springer, 2015, ISBN: 9783662480779. DOI: 10.1007/978-3-662-48078-6.

[60] A. D. Sakharov, "Violation of CP Invariance, C asymmetry, and baryon asymmetry of the universe," *Pisma Zh. Eksp. Teor. Fiz.*, vol. 5, pp. 32–35, 1967. DOI: 10.1070/PU1991v034n05ABEH002497.

[61] G. C. Dorsch, S. J. Huber, K. Mimasu, and J. M. No, "Echoes of the Electroweak Phase Transition: Discovering a second Higgs doublet through $A_0 \to ZH_0$," *Phys. Rev. Lett.*, vol. 113, no. 21, p. 211 802, 2014. DOI: 10.1103/PhysRevLett.113.211802. arXiv: 1405.5537 [hep-ph].

[62] LEP Collaboration, "Search for the standard model Higgs boson at LEP," *Phys. Lett.*, vol. B565, pp. 61–75, 2003. DOI: 10.1016/S0370-2693(03)00614-2. arXiv: hep-ex/0306033 [hep-ex].

[63] O. S. Brüning, P. Collier, P. Lebrun, S. Myers, R. Ostojic, J. Poole, and P. Proudlock, *LHC Design Report*, ser. CERN Yellow Reports: Monographs. Geneva: CERN, 2004. [Online]. Available: https://cds.cern.ch/record/782076.

[64] ATLAS Collaboration, "The ATLAS Experiment at the CERN Large Hadron Collider," *JINST*, vol. 3, S08003, 2008. DOI: 10.1088/1748-0221/3/08/S08003.

[65] CMS Collaboration, "The CMS Experiment at the CERN LHC," *JINST*, vol. 3, S08004, 2008. DOI: 10.1088/1748-0221/3/08/S08004.

[66] LHCb Collaboration, "The LHCb Detector at the LHC," *JINST*, vol. 3, S08005, 2008. [Online]. Available: http://cds.cern.ch/record/1129809.

[67] ALICE Collaboration, "Performance of the ALICE Experiment at the CERN LHC," *Int. J. Mod. Phys. A*, vol. 29, no. CERN-PH-EP-2014-031. CERN-PH-EP-2014-031, 1430044. 120 p, Feb. 2014. [Online]. Available: http://cds.cern.ch/record/1648854.

[68] E. Mobs, "The CERN accelerator complex. Complexe des accélérateurs du CERN," Jul. 2016. [Online]. Available: https://cds.cern.ch/record/2197559.

[69] L. R. Evans and P. Bryant, "LHC Machine," *JINST*, vol. 3, S08001. 164 p, 2008. [Online]. Available: http://cds.cern.ch/record/1129806.

[70] ATLAS Collaboration. (2021). Luminosity Public Results Run2, [Online]. Available: https://twiki.cern.ch/twiki/bin/view/AtlasPublic/LuminosityPublicResultsRun2.

[71] ATLAS Collaboration, "Performance of pile-up mitigation techniques for jets in pp collisions at $\sqrt{s} = 8$ TeV using the ATLAS detector. Performance of pile-up mitigation techniques for jets in pp collisions at $\sqrt{s} = 8$ TeV using the ATLAS detector," *Eur. Phys. J. C*, vol. 76, no. CERN-PH-EP-2015-206. CERN-PH-EP-2015-206, 581. 54 p, Oct. 2015. [Online]. Available: http://cds.cern.ch/record/2058295.

[72] Stanford ATLAS Group. (2021). Particle Collision & Detection:LHC and Particle Collision, [Online]. Available: http://stanford.edu/group/stanford_atlas/pictures/collision/.

[73] ATLAS Collaboration, "ATLAS Insertable B-Layer Technical Design Report," Tech. Rep. CERN-LHCC-2010-013. ATLAS-TDR-19, Sep. 2010. [Online]. Available: https://cds.cern.ch/record/1291633.

[74] ATLAS Collaboration, "ATLAS Liquid Argon Calorimeter Phase-II Upgrade: Technical Design Report," CERN, Geneva, Tech. Rep., Sep. 2017. [Online]. Available: https://cds.cern.ch/record/2285582.

[75] ATLAS Collaboration, "Technical Design Report for the Phase-II Upgrade of the ATLAS Tile Calorimeter," CERN, Geneva, Tech. Rep., Sep. 2017. [Online]. Available: https://cds.cern.ch/record/2285583.

[76] ATLAS Collaboration, "ATLAS muon spectrometer: Technical design report," 1997.

[77] ATLAS Collaboration, *ATLAS level-1 trigger: Technical Design Report*, ser. Technical Design Report ATLAS. Geneva: CERN, 1998. [Online]. Available: https://cds.cern.ch/record/381429.

[78] P. Jenni, M. Nessi, M. Nordberg, and K. Smith, *ATLAS high-level trigger, data-acquisition and controls: Technical Design Report*, ser. Technical Design Report ATLAS. Geneva: CERN, 2003. [Online]. Available: https://cds.cern.ch/record/616089.

[79] WLCG Collaboration. (2021). Worldwide LHC Computing Grid, [Online]. Available: https://wlcg-public.web.cern.ch.

[80] GridPP Collaboration. (2021). Grid PP, [Online]. Available: https://www.gridpp.ac.uk/.

[81] ATLAS Collaboration, *ATLAS Computing: technical design report*, ser. Technical Design Report ATLAS. Geneva: CERN, 2005. [Online]. Available: https://cds.cern.ch/record/837738.

[82] LHCb Collaboration, "GAUDI: The software architecture and framework for building LHCb data processing applications," 2000. DOI: 10.1016/S0010-4655(01)00254-5. [Online]. Available: http://cds.cern.ch/record/467678.

[83] S. Agostinelli *et al.*, "GEANT4: A Simulation toolkit," *Nucl. Instrum. Meth.*, vol. A506, pp. 250–303, 2003. DOI: 10.1016/S0168-9002(03)01368-8.

[84] ATLAS Collaboration, "The ATLAS Simulation Infrastructure. The ATLAS Simulation Infrastructure," *Eur. Phys. J. C*, vol. 70, no. arXiv:1005.4568. CERN-PH-EP-2010-044, 823–874. 53 p, May 2010. DOI: 10.1140/epjc/s10052-010-1429-9. [Online]. Available: https://cds.cern.ch/record/1267853.

[85] ATLAS Collaboration, "The ATLAS Simulation Infrastructure," *Eur. Phys. J.*, vol. C70, pp. 823–874, 2010. DOI: 10.1140/epjc/s10052-010-1429-9. arXiv: 1005.4568 [physics.ins-det].

[86] ATLAS Collaboration. (2021). Luminosity summary plots for 2015 pp data taking, [Online]. Available: https://twiki.cern.ch/twiki/bin/view/AtlasPublic/LuminosityPublicResultsRun2#2015_pp_Collisions.

[87] ATLAS Collaboration. (2021). Luminosity summary plots for 2016 pp data taking, [Online]. Available: https://twiki.cern.ch/twiki/bin/view/AtlasPublic/LuminosityPublicResultsRun2#Luminosity_summary_plots_for_AN3.

[88] J. Alwall, M. Herquet, F. Maltoni, O. Mattelaer, and T. Stelzer, "MadGraph 5 : Going Beyond," *JHEP*, vol. 06, p. 128, 2011. DOI: 10.1007/JHEP06(2011)128. arXiv: 1106.0522 [hep-ph].

[89] J. Alwall, R. Frederix, S. Frixione, V. Hirschi, F. Maltoni, O. Mattelaer, H. Shao, T. Stelzer, P. Torrielli, and M. Zaro, "The automated computation of tree-level and next-to-leading order differential cross sections, and their matching to parton shower simulations," *JHEP*, vol. 07, p. 079, 2014. DOI: 10.1007/JHEP07(2014)079. arXiv: 1405.0301 [hep-ph].

[90] T. Sjöstrand, S. Ask, J. R. Christiansen, R. Corke, N. Desai, P. Ilten, S. Mrenna, S. Prestel, C. O. Rasmussen, and P. Z. Skands, "An Introduction to PYTHIA 8.2," *Comput. Phys. Commun.*, vol. 191, pp. 159–177, 2015. DOI: 10.1016/j.cpc.2015.01.024. arXiv: 1410.3012 [hep-ph].

[91] T. Gleisberg, S. Hoeche, F. Krauss, M. Schonherr, S. Schumann, F. Siegert, and J. Winter, "Event generation with SHERPA 1.1," *JHEP*, vol. 02, p. 007, 2009. DOI: 10.1088/1126-6708/2009/02/007. arXiv: 0811.4622 [hep-ph].

[92] R. D. Ball, V. Bertone, S. Carrazza, C. S. Deans, L. Del Debbio, S. Forte, A. Guffanti, N. P. Hartland, J. I. Latorre, J. Rojo, and M. Ubiali, "Parton distributions for the LHC Run II," *JHEP*, vol. 04, no. arXiv:1410.8849. EDINBURGH 2014-15. IFUM-1034-FT. CERN-PH-TH-2013-253. OUTP-14-11P. CAVENDISH-HEP-14-11, 040. 138 p, Oct. 2014. DOI: 10.1007/JHEP04(2015)040. [Online]. Available: https://cds.cern.ch/record/1966481.

[93] P. Nason, "A New method for combining NLO QCD with shower Monte Carlo algorithms," *JHEP*, vol. 11, p. 040, 2004. DOI: 10.1088/1126-6708/2004/11/040. arXiv: hep-ph/0409146 [hep-ph].

[94] S. Frixione, P. Nason, and C. Oleari, "Matching NLO QCD computations with Parton Shower simulations: the POWHEG method," *JHEP*, vol. 11, p. 070, 2007. DOI: 10.1088/1126-6708/2007/11/070. arXiv: 0709.2092 [hep-ph].

[95] S. Alioli, P. Nason, C. Oleari, and E. Re, "A general framework for implementing NLO calculations in shower Monte Carlo programs: the POWHEG BOX," *JHEP*, vol. 06, p. 043, 2010. DOI: 10.1007/JHEP06(2010)043. arXiv: 1002.2581 [hep-ph].

[96] H. L. Lai, M. Guzzi, J. Huston, Z. Li, P. M. Nadolsky, J. Pumplin, and C. P. Yuan, "New parton distributions for collider physics," *Phys. Rev.*, vol. D82, p. 074 024, 2010. DOI: 10.1103/PhysRevD.82.074024. arXiv: 1007.2241 [hep-ph].

[97] T. Sjostrand, S. Mrenna, and P. Z. Skands, "PYTHIA 6.4 Physics and Manual," *JHEP*, vol. 05, p. 026, 2006. DOI: 10.1088/1126-6708/2006/05/026. arXiv: hep-ph/0603175 [hep-ph].

[98] P. Z. Skands, "Tuning Monte Carlo Generators: The Perugia Tunes," *Phys. Rev.*, vol. D82, p. 074 018, 2010. DOI: 10.1103/PhysRevD.82.074018. arXiv: 1005.3457 [hep-ph].

[99] ATLAS Collaboration, "Measurement of the Z/γ^* boson transverse momentum distribution in pp collisions at $\sqrt{s} = 7$ TeV with the ATLAS detector," *JHEP*, vol. 09, p. 145, 2014. DOI: 10.1007/JHEP09(2014)145. arXiv: 1406.3660 [hep-ex].

[100] ATLAS Collaboration, "Summary of ATLAS Pythia 8 tunes," CERN, Geneva, Tech. Rep. ATL-PHYS-PUB-2012-003, Aug. 2012. [Online]. Available: https://cds.cern.ch/record/1474107.

[101] A. D. Martin, W. J. Stirling, R. S. Thorne, and G. Watt, "Parton distributions for the LHC," *Eur. Phys. J.*, vol. C63, pp. 189–285, 2009. DOI: 10.1140/epjc/s10052-009-1072-5. arXiv: 0901.0002 [hep-ph].

[102] ATLAS Collaboration, "Early Inner Detector Tracking Performance in the 2015 data at $\sqrt{s}$ = 13 TeV," CERN, Geneva, Tech. Rep. ATL-PHYS-PUB-2015-051, Dec. 2015. [Online]. Available: https://cds.cern.ch/record/2110140.

[103] ATLAS Collaboration, "Vertex Reconstruction Performance of the ATLAS Detector at $\sqrt{s} =$ 13 TeV," CERN, Geneva, Tech. Rep. ATL-PHYS-PUB-2015-026, Jul. 2015. [Online]. Available: https://cds.cern.ch/record/2037717.

[104] D0 Collaboration, "Observation of Single Top Quark Production," *Phys. Rev. Lett.*, vol. 103, p. 092 001, 2009. DOI: 10.1103/PhysRevLett.103.092001. arXiv: 0903.0850 [hep-ex].

[105] ATLAS Collaboration, "Electron reconstruction and identification in the ATLAS experiment using the 2015 and 2016 LHC proton-proton collision data at $\sqrt{s} = 13$ TeV," Feb. 2019. arXiv: 1902.04655. [Online]. Available: http://cds.cern.ch/record/2657964.

[106] ATLAS Collaboration, "Muon reconstruction performance of the ATLAS detector in proton–proton collision data at $\sqrt{s}$=13 TeV. Muon reconstruction performance of the ATLAS detector in proton–proton collision data at $\sqrt{s}$=13 TeV," *Eur. Phys. J. C*, vol. 76, no. CERN-EP-2016-033. CERN-EP-2016-033, 292. 45 p, Mar. 2016. DOI: 10.1140/epjc/s10052-016-4120-y. [Online]. Available: https://atlas.web.cern.ch/Atlas/GROUPS/PHYSICS/PAPERS/PERF-2015-10/.

[107] M. Cacciari, G. P. Salam, and G. Soyez, "The anti-k_t jet clustering algorithm," *JHEP*, vol. 04, p. 063, 2008. DOI: 10.1088/1126-6708/2008/04/063. arXiv: 0802.1189 [hep-ph].

[108] ATLAS Collaboration, "Topological cell clustering in the ATLAS calorimeters and its performance in LHC Run 1. Topological cell clustering in the ATLAS calorimeters and its performance in LHC Run 1," *Eur. Phys. J. C*, vol. 77, no. CERN-PH-EP-2015-304, 490. 87 p, Mar. 2016. DOI: 10.1140/epjc/s10052-017-5004-5. [Online]. Available: http://atlas.web.cern.ch/Atlas/GROUPS/PHYSICS/PAPERS/PERF-2014-07/.

[109] ATLAS Collaboration, "Tagging and suppression of pileup jets with the ATLAS detector," CERN, Geneva, Tech. Rep. ATLAS-CONF-2014-018, May 2014. [Online]. Available: https://cds.cern.ch/record/1700870.

[110] ATLAS Collaboration, "Jet reconstruction and performance using particle flow with the ATLAS Detector. Jet reconstruction and performance using particle flow with the ATLAS Detector," *Eur. Phys. J. C*, vol. 77, no. CERN-EP-2017-024. 7, 466. 67 p, Mar. 2017. DOI: 10.1140/epjc/s10052-017-5031-2. [Online]. Available: http://atlas.web.cern.ch/Atlas/GROUPS/PHYSICS/PAPERS/PERF-2015-09/.

[111] ATLAS Collaboration, "Measurements of b-jet tagging efficiency with the ATLAS detector using $t\bar{t}$ events at $\sqrt{s} = 13$ TeV," *JHEP*, vol. 08, no. arXiv:1805.01845, 089. 49 p, May 2018. DOI: 10.1007/JHEP08(2018)089. arXiv: 1805.01845. [Online]. Available: http://atlas.web.cern.ch/Atlas/GROUPS/PHYSICS/PAPERS/PERF-2016-05/.

[112] A. Hocker *et al.*, "TMVA - Toolkit for Multivariate Data Analysis," Mar. 2007. arXiv: physics/0703039.

[113] ATLAS Collaboration. (2021). Expected flavour tagging performance in release 21, [Online]. Available: https://twiki.cern.ch/twiki/bin/viewauth/AtlasProtected/BTaggingBenchmarksRelease21#AntiKt4EMTopoJets.

[114] ATLAS Collaboration, "Performance of missing transverse momentum reconstruction for the ATLAS detector in the first proton-proton collisions at at $\sqrt{s}$= 13 TeV," CERN, Geneva, Tech. Rep. ATL-PHYS-PUB-2015-027, Jul. 2015. [Online]. Available: http://cds.cern.ch/record/2037904.

[115] ATLAS Collaboration, "Search for a heavy CP-odd Higgs Boson decaying to a Z boson and a heavy CP-even Higgs boson H with $A \to ZH \to \ell\ell bb$ produced in 13 TeV Collisions with the ATLAS Detector," CERN, Geneva, Tech. Rep. ATL-COM-PHYS-2016-1737, Nov. 2016. [Online]. Available: https://cds.cern.ch/record/2235744.

[116] ATLAS Collaboration, "Calibration of light-flavour jet b-tagging rates on ATLAS proton-proton collision data at $\sqrt{s} = 13$ TeV," CERN, Geneva, Tech. Rep. ATLAS-CONF-2018-006, Apr. 2018. [Online]. Available: https://cds.cern.ch/record/2314418.

[117] ATLAS Collaboration, "Early Inner Detector Tracking Performance in the 2015 data at $\sqrt{s}$ = 13 TeV," Tech. Rep., 2015.

[118] G. Borisov and C. Mariotti, "Fine tuning of track impact parameter resolution of the DELPHI detector," Aug. 1995. [Online]. Available: https://cds.cern.ch/record/2627372.

[119] M. Leyton, "Minimum Bias and Underlying Event Measurements with ATLAS," pp. 11–19, 2012. DOI: 10.3204/DESY-PROC-2012-03/1. arXiv: 1202.2090 [hep-ex].

[120] ATLAS Collaboration, "Early Inner Detector Tracking Performance in the 2015 data at $\sqrt{s}$ = 13 TeV," CERN, Geneva, Tech. Rep. ATL-PHYS-PUB-2015-051, Dec. 2015. [Online]. Available: http://cds.cern.ch/record/2110140.

[121] ATLAS Collaboration, "Modelling of Track Reconstruction Inside Jets with the 2016 ATLAS $\sqrt{s} = 13$ TeV pp dataset," CERN, Geneva, Tech. Rep. ATL-PHYS-PUB-2017-016, Jul. 2017. [Online]. Available: https://cds.cern.ch/record/2275639.

[122] ATLAS Collaboration, "Operation of the ATLAS trigger system in Run 2," *JINST*, vol. 15, no. 10, P10004, 2020. DOI: 10.1088/1748-0221/15/10/P10004. arXiv: 2007.12539 [physics.ins-det].

[123] L. Lista, *Statistical Methods for Data Analysis in Particle Physics*. Springer, 2017, vol. 941. DOI: 10.1007/978-3-319-62840-0.

[124] G. Cowan, K. Cranmer, E. Gross, and O. Vitells, "Asymptotic formulae for likelihood-based tests of new physics," *Eur. Phys. J. C*, vol. 71, p. 1554, 2011. DOI: 10.1140/epjc/s10052-011-1554-0. arXiv: 1007.1727 [physics.data-an], Erratum: Eur. Phys. J. C **73** (2013) 2501.

[125] S. Das, "A simple alternative to the Crystal Ball function," 2016. arXiv: 1603.08591 [hep-ex].

[126] M. Oreglia, "A Study of the Reactions $\psi' \to \gamma\gamma\psi$," *SLAC-R-0236*, 1980. [Online]. Available: http://www.slac.stanford.edu/cgi-wrap/getdoc/slac-r-236.pdf.

[127] J. Duchon, "Interpolation des fonctions de deux variables suivant le principe de la flexion des plaques minces," fre, *ESAIM: Mathematical Modelling and Numerical Analysis - Modélisation Mathématique et Analyse Numérique*, vol. 10, no. R3, pp. 5–12, 1976. [Online]. Available: https://eudml.org/doc/193284.

[128] ATLAS Collaboration, "Luminosity determination in pp collisions at $\sqrt{s}$ = 8 TeV using the ATLAS detector at the LHC," *Eur. Phys. J. C*, vol. 76, no. 12, p. 653, 2016. DOI: 10.1140/epjc/s10052-016-4466-1. arXiv: 1608.03953 [hep-ex].

[129] ATLAS Collaboration, "Measurement of the Inelastic Proton-Proton Cross Section at $\sqrt{s} = 13$ TeV with the ATLAS Detector at the LHC," *Phys. Rev. Lett.*, vol. 117, no. 18, p. 182 002, 2016. DOI: 10.1103/PhysRevLett.117.182002. arXiv: 1606.02625 [hep-ex].

[130] ATLAS Collaboration, "Electron reconstruction and identification in the ATLAS experiment using the 2015 and 2016 LHC proton-proton collision data at $\sqrt{s} = 13$ TeV," *Eur. Phys. J. C*, vol. 79, 639. 40 p, Feb. 2019. DOI: 10.1140/epjc/s10052-019-7140-6. arXiv: 1902.04655. [Online]. Available: https://atlas.web.cern.ch/Atlas/GROUPS/PHYSICS/PAPERS/PERF-2017-01.

[131] ATLAS Collaboration, "Muon reconstruction performance of the ATLAS detector in proton–proton collision data at $\sqrt{s}$=13 TeV. Muon reconstruction performance of the ATLAS detector in proton–proton collision data at $\sqrt{s}$=13 TeV," *Eur. Phys. J. C*, vol. 76, no. CERN-EP-2016-033. CERN-EP-2016-033, 292. 45 p, Mar. 2016. DOI: 10.1140/epjc/s10052-016-4120-y. [Online]. Available: https://atlas.web.cern.ch/Atlas/GROUPS/PHYSICS/PAPERS/PERF-2015-10/.

[132] ATLAS Collaboration, "Electron and photon energy calibration with the ATLAS detector using 2015–2016 LHC proton-proton collision data," *JINST*, vol. 14, no. 03, P03017, 2019. DOI: 10.1088/1748-0221/14/03/P03017. arXiv: 1812.03848 [hep-ex].

[133] ATLAS Collaboration, "Jet energy scale measurements and their systematic uncertainties in proton-proton collisions at $\sqrt{s} = 13$ TeV with the ATLAS detector. Jet energy scale measurements and their systematic uncertainties in proton-proton collisions at $\sqrt{s} = 13$ TeV with the ATLAS detector," *Phys. Rev. D*, vol. 96, no. CERN-EP-2017-038. 7, 072002. 36 p, Mar. 2017. DOI: 10.1103/PhysRevD.96.072002. [Online]. Available: https://atlas.web.cern.ch/Atlas/GROUPS/PHYSICS/PAPERS/PERF-2016-04/.

[134] ATLAS Collaboration, "Optimisation of the ATLAS *b*-tagging performance for the 2016 LHC Run," CERN, Geneva, Tech. Rep. ATL-PHYS-PUB-2016-012, Jun. 2016. [Online]. Available: https://cds.cern.ch/record/2160731.

[135] ATLAS Collaboration, "Expected performance of missing transverse momentum reconstruction for the ATLAS detector at $\sqrt{s} = 13$ TeV," CERN, Geneva, Tech. Rep. ATL-PHYS-PUB-2015-023, Jul. 2015. [Online]. Available: https://cds.cern.ch/record/2037700.

[136] ATLAS Collaboration, "ATLAS Run 1 Pythia8 tunes," CERN, Geneva, Tech. Rep. ATL-PHYS-PUB-2014-021, Nov. 2014. [Online]. Available: https://cds.cern.ch/record/1966419.

[137] J. Butterworth *et al.*, "PDF4LHC recommendations for LHC Run II," 2015. arXiv: 1510.03865 [hep-ph].

[138] A. Buckley, J. Ferrando, S. Lloyd, K. Nordström, B. Page, M. Rüfenacht, M. Schönherr, and G. Watt, "LHAPDF6: parton density access in the LHC precision era," *Eur. Phys. J. C*, vol. 75, p. 132, 2015. DOI: 10.1140/epjc/s10052-015-3318-8. arXiv: 1412.7420 [hep-ph].

[139] R. D. Ball *et al.*, "Parton distributions for the LHC Run II," *JHEP*, vol. 04, p. 040, 2015. DOI: 10.1007/JHEP04(2015)040. arXiv: 1410.8849 [hep-ph].

[140] L. Moneta, K. Belasco, K. S. Cranmer, S. Kreiss, A. Lazzaro, D. Piparo, G. Schott, W. Verkerke, and M. Wolf, "The RooStats Project," *PoS*, vol. ACAT2010, p. 057, 2010. arXiv: 1009.1003 [physics.data-an].

[141] W. Verkerke and D. Kirkby, *The RooFit toolkit for data modeling*, 2003. arXiv: physics/0306116 [physics.data-an].

[142] A. L. Read, "Presentation of search results: The CLs technique," *Journal of Physics G: Nuclear and Particle Physics*, vol. 28, no. 10, pp. 2693–2704, 2002. DOI: 10.1088/0954-3899/28/10/313.

[143] O. Vitells and E. Gross, "Estimating the significance of a signal in a multi-dimensional search," *Astroparticle Physics*, vol. 35, pp. 230–234, 2011.

[144] R. V. Harlander, S. Liebler, and H. Mantler, "SusHi: A program for the calculation of Higgs production in gluon fusion and bottom-quark annihilation in the Standard Model and the MSSM," *Comput. Phys. Commun.*, vol. 184, pp. 1605–1617, 2013. DOI: 10.1016/j.cpc.2013.02.006. arXiv: 1212.3249 [hep-ph].

[145] R. Harlander and P. Kant, "Higgs production and decay: Analytic results at next-to-leading order QCD," *JHEP*, vol. 12, p. 015, 2005. DOI: 10.1088/1126-6708/2005/12/015. arXiv: hep-ph/0509189.

[146] R. V. Harlander and W. B. Kilgore, "Higgs boson production in bottom quark fusion at next-to-next-to leading order," *Phys. Rev. D*, vol. 68, p. 013 001, 2003. DOI: 10.1103/PhysRevD.68.013001. arXiv: hep-ph/0304035.

[147] R. V. Harlander and W. B. Kilgore, "Next-to-next-to-leading order Higgs production at hadron colliders," *Phys. Rev. Lett.*, vol. 88, p. 201 801, 2002. DOI: 10.1103/PhysRevLett.88.201801. arXiv: hep-ph/0201206.

[148] S. Dawson, C. B. Jackson, L. Reina, and D. Wackeroth, "Exclusive Higgs boson production with bottom quarks at hadron colliders," *Phys. Rev. D*, vol. 69, p. 074 027, 2004. DOI: 10.1103/PhysRevD.69.074027. arXiv: hep-ph/0311067.

[149] S. Dittmaier, M. Kramer 1, and M. Spira, "Higgs radiation off bottom quarks at the Tevatron and the CERN LHC," *Phys. Rev. D*, vol. 70, p. 074 010, 2004. DOI: 10.1103/PhysRevD.70.074010. arXiv: hep-ph/0309204.

[150] R. Harlander, M. Kramer, and M. Schumacher, "Bottom-quark associated Higgs-boson production: reconciling the four- and five-flavour scheme approach," 2011. arXiv: 1112.3478 [hep-ph].

[151] D. Eriksson, J. Rathsman, and O. Stal, "2HDMC: Two-Higgs-doublet model calculator physics and manual," *Comput. Phys. Commun.*, vol. 181, pp. 189–205, 2010. DOI: 10.1016/j.cpc.2009.09.011. arXiv: 0902.0851 [hep-ph].

APPENDIX A

Additional plots for Calibration of Light Flavour Jet b-tagging Efficiency in ATLAS

In this appendix, additional figures for Chapter 4 with different MV2c10 working points are shown. Figure A.1 shows the calibrated light jet mis-tag efficiency with respected to $\sigma^{MC}(d_0)$ and $\sigma^{MC}(z_0)$. Figure A.2 shows the combined calibration scale factors with its components, distribution in both calorimeter jets and particle flow jets are shown. The combined calibration scale factors with components of systematic uncertainties are shown in figure A.3 for distribution in both calorimeter jets and particle flow jets. The combined calibration scale factors with total systematic uncertainties are shown in figure A.4 for distribution in both calorimeter jets and particle flow jets. Lastly, the combined calibration scale factors from adjusted simulation and negative-tag method for both calorimeter jets and particle flow jets are shown in figure A.5.

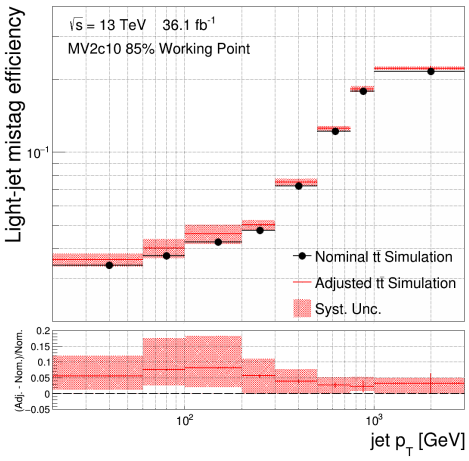

(a) Calibration on d_0 with MV2c10 85% working point

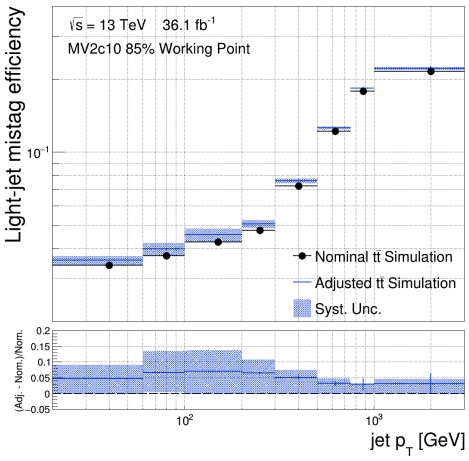

(b) Calibration on z_0 with MV2c10 85% working point

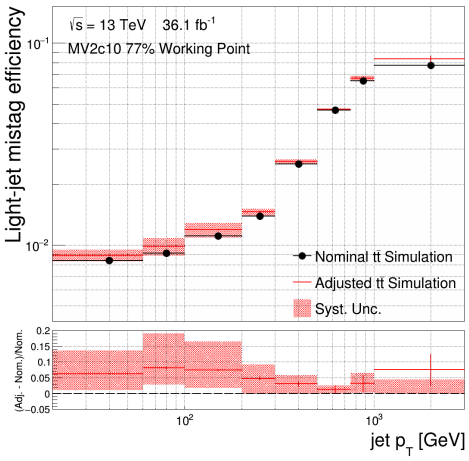

(c) Calibration on d_0 with MV2c10 77% working point

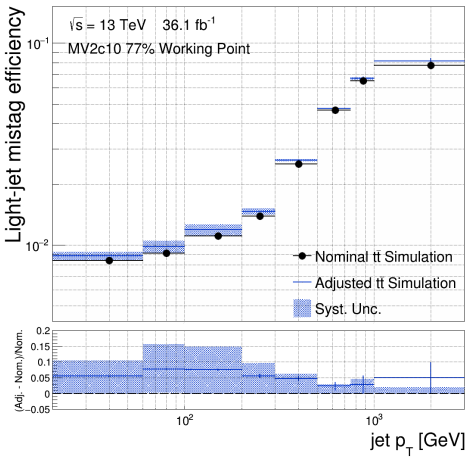

(d) Calibration on z_0 with MV2c10 77% working point

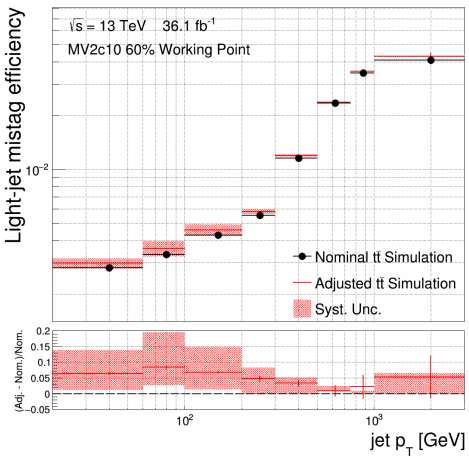

(e) Calibration on d_0 with MV2c10 60% working point

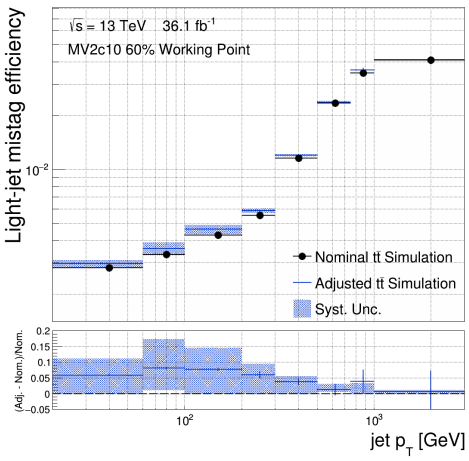

(f) Calibration on z_0 with MV2c10 60% working point

Figure A.1: The calibrated light jet mis-tag efficiency with respected to $\sigma^{MC}(d_0)$ and $\sigma^{MC}(z_0)$. Distribution with MV2c10 85%, 77% and 60% working points are shown.

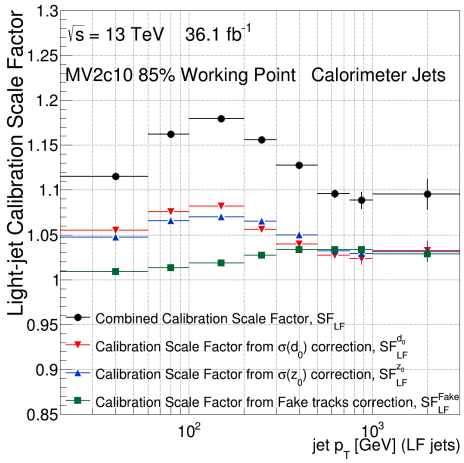

(a) Calorimeter jets with MV2c10 85% working point

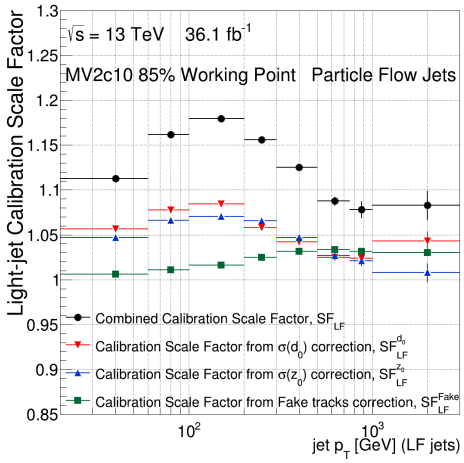

(b) Particle flow jets with MV2c10 85% working point

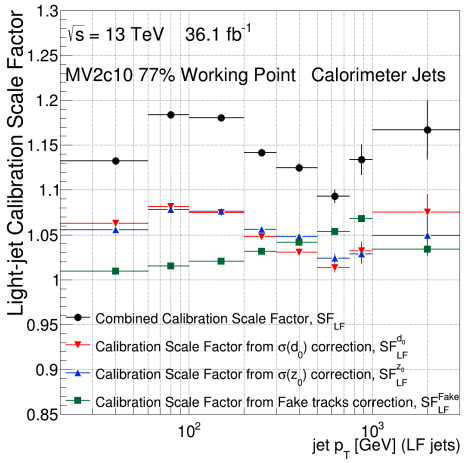

(c) Calorimeter jets with MV2c10 77% working point

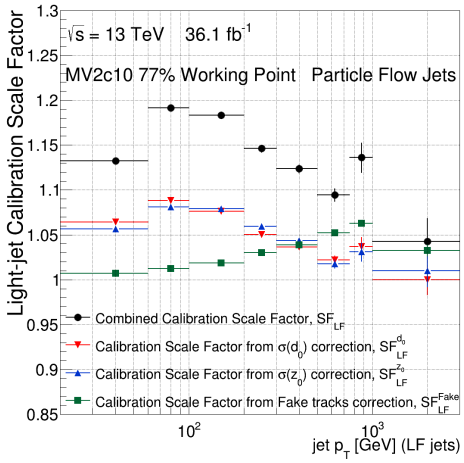

(d) Particle flow jets with MV2c10 77% working point

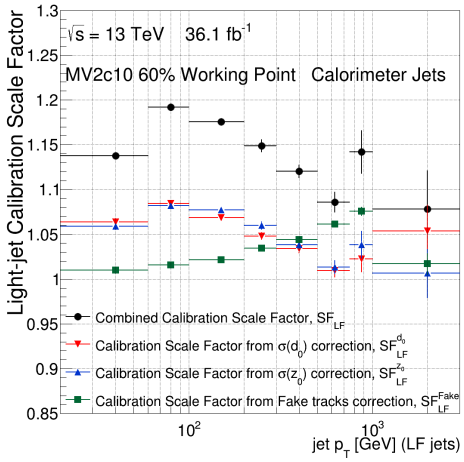

(e) Calorimeter jets with MV2c10 60% working point

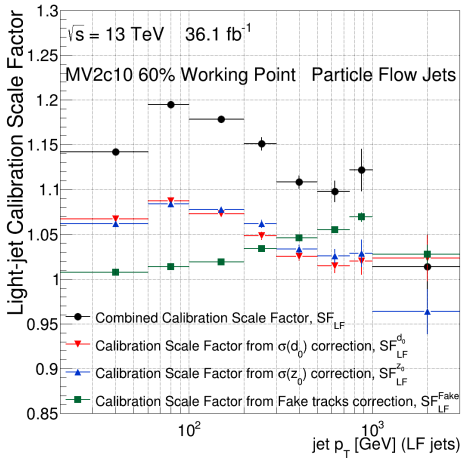

(f) Particle flow jets with MV2c10 60% working point

Figure A.2: The combined calibration scale factor with its components as mentioned in Eq. 4.7. Distributions in both calorimeter and particle flow jets with MV2c10 85%, 77% and 60% working points are shown.

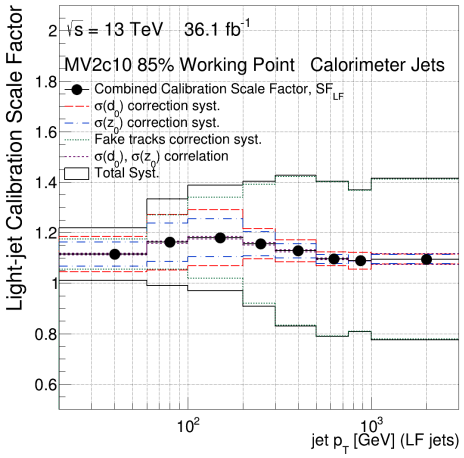

(a) Calorimeter jets with MV2c10 85% working point

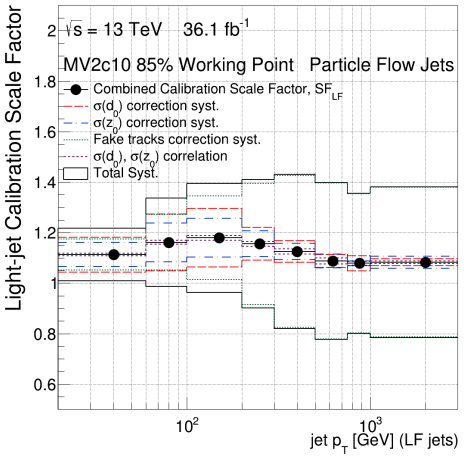

(b) Particle flow jets with MV2c10 85% working point

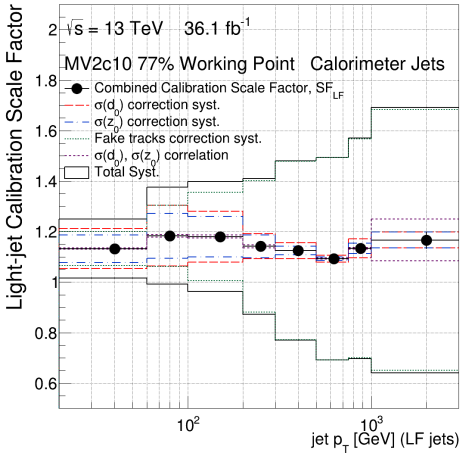

(c) Calorimeter jets with MV2c10 77% working point

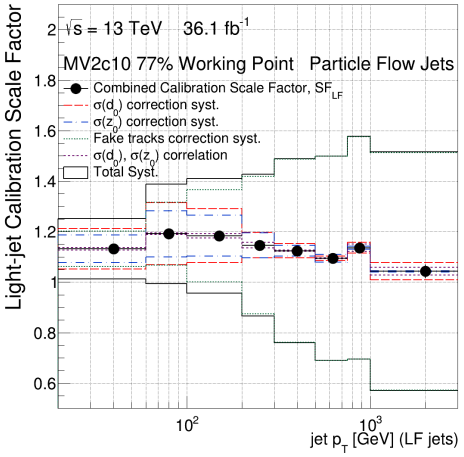

(d) Particle flow jets with MV2c10 77% working point

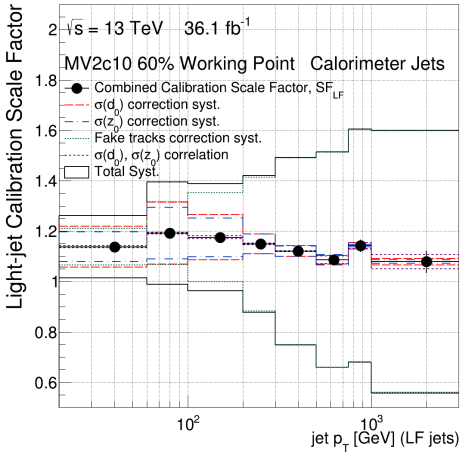

(e) Calorimeter jets with MV2c10 60% working point

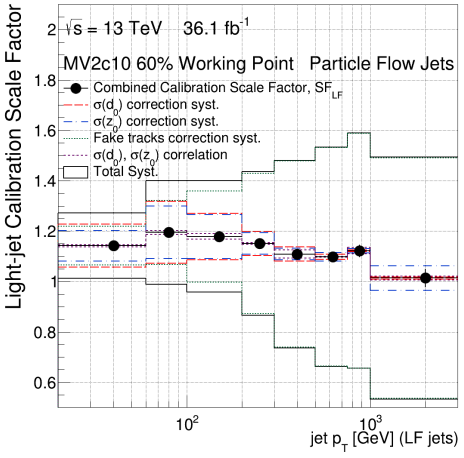

(f) Particle flow jets with MV2c10 60% working point

Figure A.3: The combined calibration scale factor with components of systematic uncertainties. Distributions of calorimeter and particle flow jets with MV2c10 85%, 77% and 60% working points are shown.

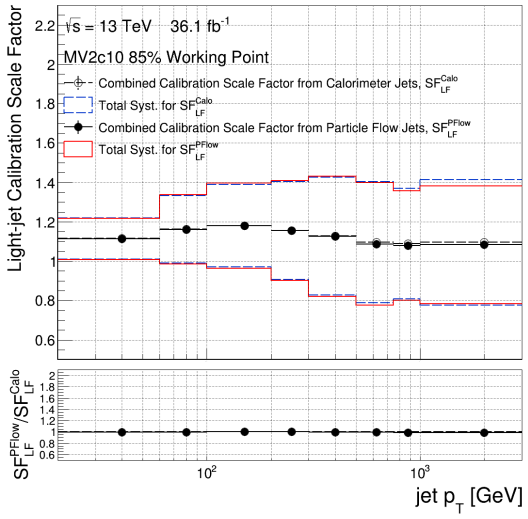

(a) MV2c10 85% working point

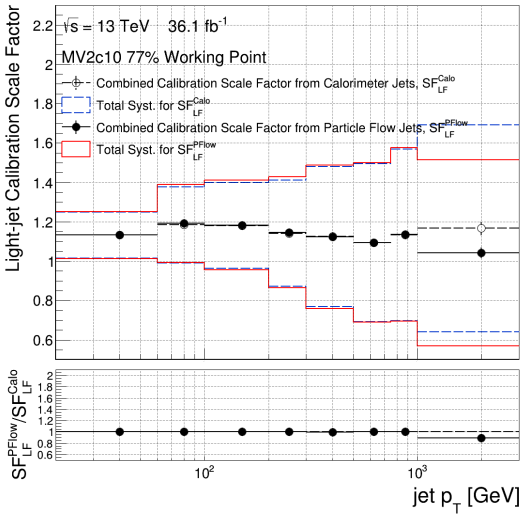

(b) MV2c10 77% working point

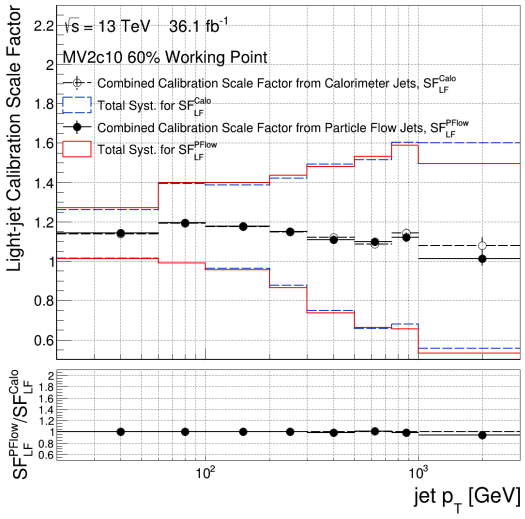

(c) MV2c10 60% working point

Figure A.4: The combined calibration scale factor for calorimeter and particle flow jets with total systematic uncertainties. The difference between the calibration scale factor for calorimeter and particle flow jets are shown in the bottom panel. Distributions with MV2c10 85%, 77% and 60% working points are shown.

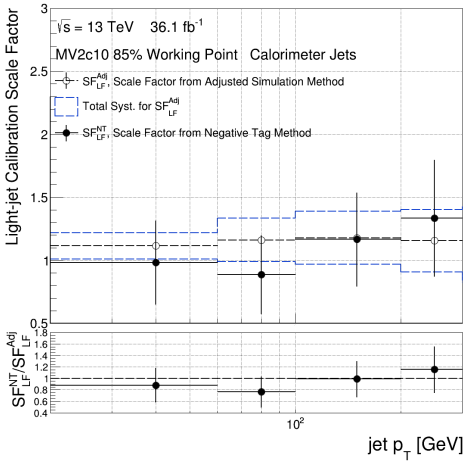

(a) Calorimeter jets with MV2c10 85% working point

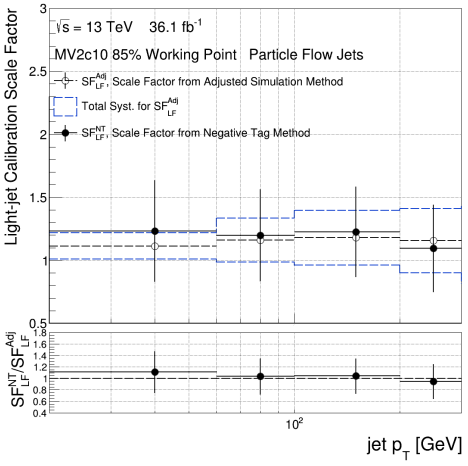

(b) Particle flow jets with MV2c10 85% working point

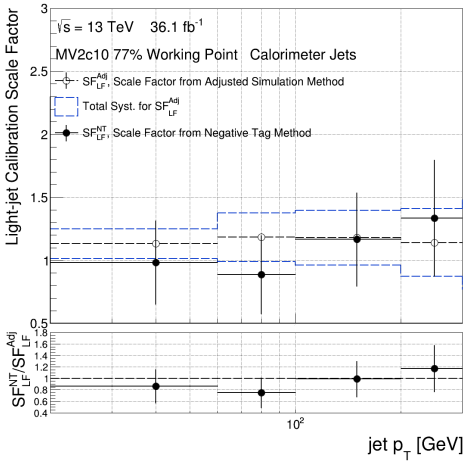

(c) Calorimeter jets with MV2c10 77% working point

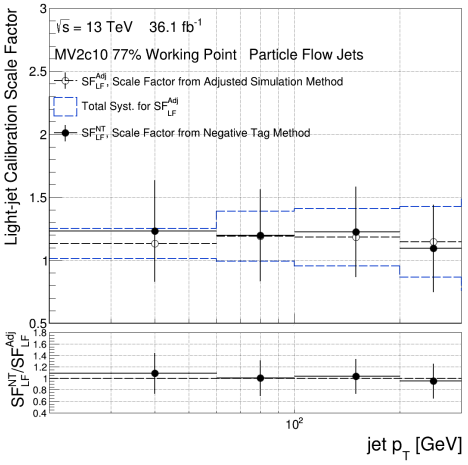

(d) Particle flow jets with MV2c10 77% working point

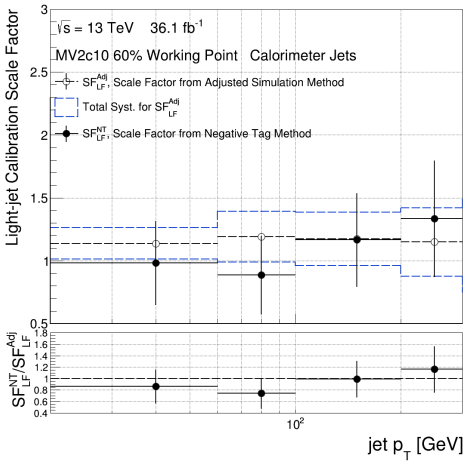

(e) Calorimeter jets with MV2c10 60% working point

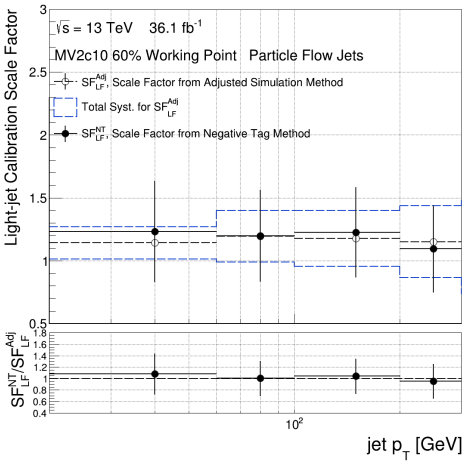

(f) Particle flow jets with MV2c10 60% working point

Figure A.5: The light jet calibration scale factors from adjusted simulation and negative-tag method for calorimeter and particle flow jets. The difference between the results of two methods is shown in the bottom panel. Distributions with MV2c10 85%, 77% and 60% working points are shown.

APPENDIX B

Additional plots for Search for $A \to ZH \to \ell\ell bb$ with 36 fb^{-1}

Additional plots for Chapter 5 are shown in this appendix. Figure B.1 shows the E_T^{miss} significance and the E_T^{miss} distribution after the E_T^{miss} significance cut for the events that contain at least 3 b-jets and at least 2 jets. Figure B.2 shows the $\sqrt{\Sigma p_T^2}/m_{\ell\ell bb}$ distribution and the $m_{\ell\ell bb}$ distribution after the $\sqrt{\Sigma p_T^2}/m_{\ell\ell bb}$ cut in $n_b \geq 3$ category. Figure B.3 shows the $m_{\ell\ell bb}$ distribution in the signal regions after the $\sqrt{\Sigma p_T^2}/m_{\ell\ell bb}$ cut and the m_{bb} window in the $n_b \geq 3$ category. Figure B.4 shows the m_{bb}, $m_{\ell\ell bb}$ distributions before the $\sqrt{\Sigma p_T^2}/m_{\ell\ell bb} > 0.4$ cut and the $m_{\ell\ell bb}$ with mass scaling for the top control region in the $n_b \geq 3$ category. Figure B.5 shows the m_{bb}, $m_{\ell\ell bb}$ distributions before the $\sqrt{\Sigma p_T^2}/m_{\ell\ell bb} > 0.4$ cut and the $m_{\ell\ell bb}$ distribution with mass scaling in the $n_b \geq 3$ category.

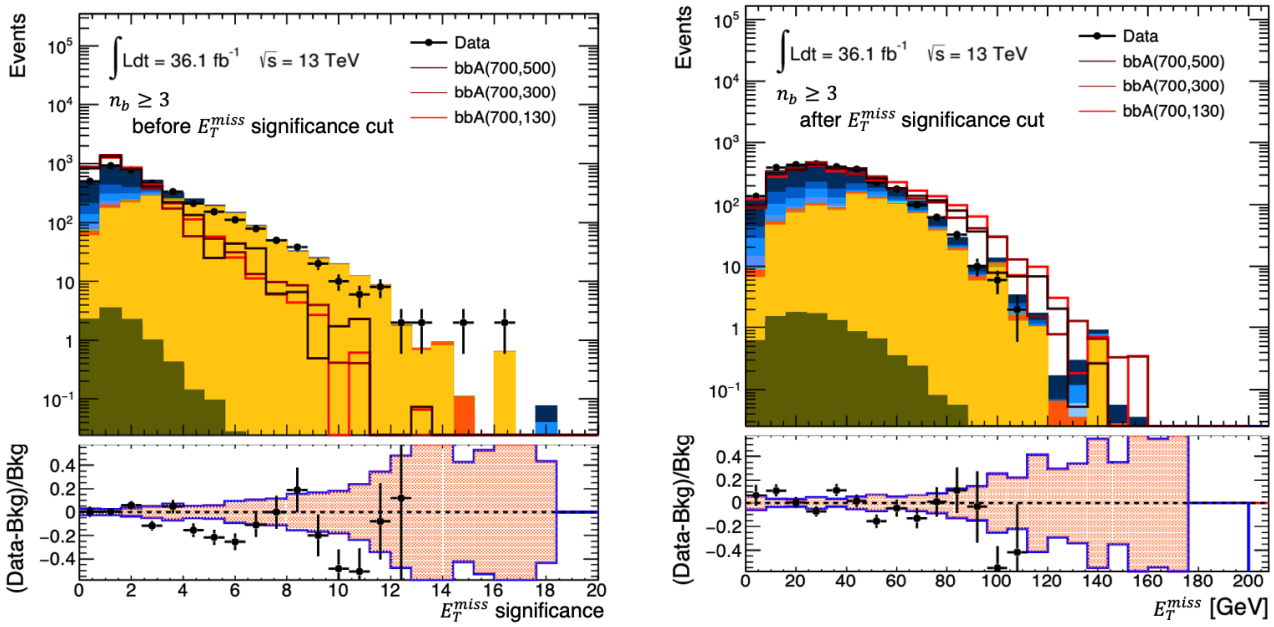

(a) E_T^{miss} significance

(b) E_T^{miss} after E_T^{miss} significance cut

Figure B.1: The (a) E_T^{miss} significance and the (b) E_T^{miss} distribution after the E_T^{miss} significance cut. Only events that contain at least 3 b-jets and at least 2 jets, with only the statistical uncertainty shown. For the background simulated samples, color code shown in figure 3.5 has been used. At the bottom panel, the filled area represents the statistical uncertainties, while the blue line shows the combined uncertainty from statistical and shape uncertainties.

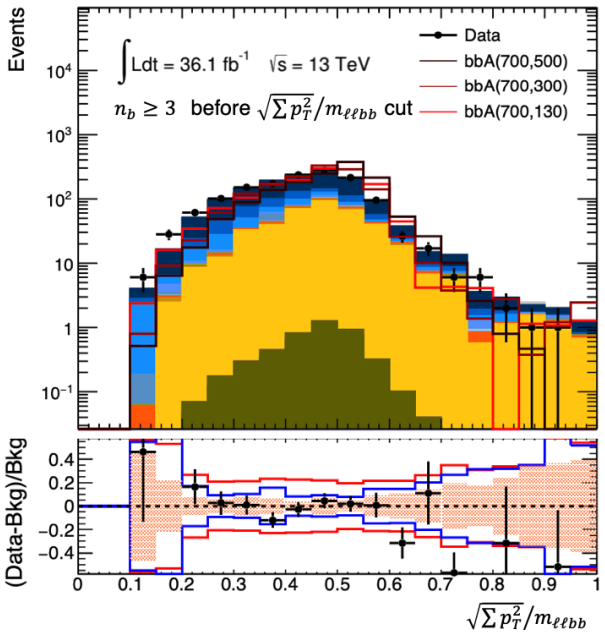

(a) $\sqrt{\Sigma p_T^2}/m_{\ell\ell bb}$

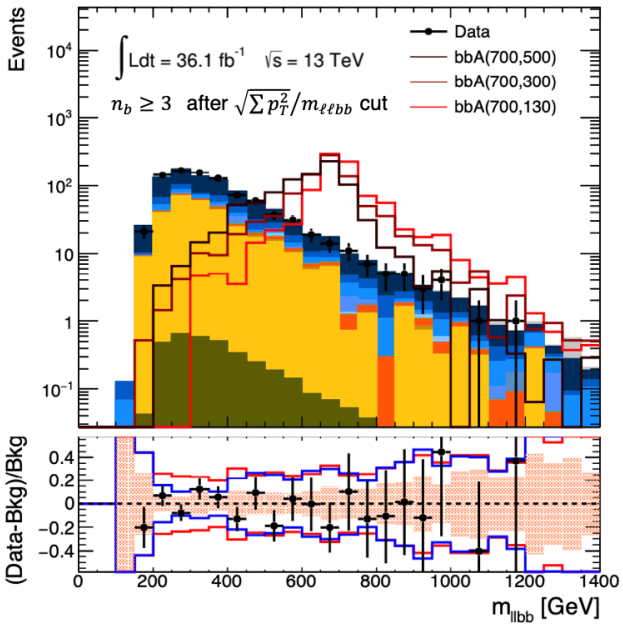

(b) $m_{\ell\ell bb}$ after $\sqrt{\Sigma p_T^2}/m_{\ell\ell bb}$ cut

Figure B.2: The (a) $\sqrt{\Sigma p_T^2}/m_{\ell\ell bb}$ distribution and the (b) $m_{\ell\ell bb}$ distribution after the $\sqrt{\Sigma p_T^2}/m_{\ell\ell bb}$ cut. Only events in $n_b \geq 3$ category are shown. For the background simulated samples, color code shown in Figure 3.5 has been used. At the bottom panel, the filled area represents the statistical uncertainties, while the blue line shows the combined uncertainty from statistical and shape uncertainties. The total uncertainty which combines statistical and systematic uncertainties is also shown as a red line.

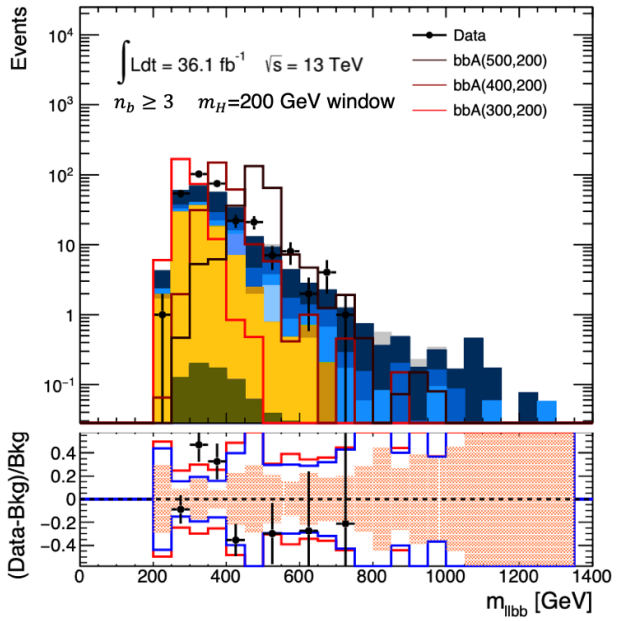

(a) $m_{\ell\ell bb}$, passed $m_H = 200$ GeV window

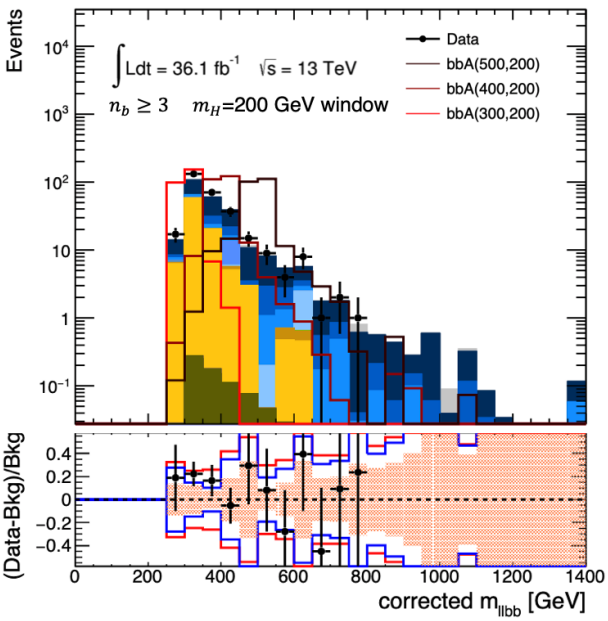

(b) $m_{\ell\ell bb}$ with mass scaling, passed $m_H = 200$ GeV window

Figure B.3: The $m_{\ell\ell bb}$ distribution (a) without and (b) with the mass scaling in the signal regions after the $\sqrt{\Sigma p_T^2}/m_{\ell\ell bb}$ cut and the m_{bb} window in the $n_b \geq 3$ category. For the background simulated samples, color code shown in Figure 3.5 has been used. At the bottom panel, the filled area represents the statistical uncertainties, while the blue line shows the combined uncertainty from statistical and shape uncertainties. The total uncertainty which combines statistical and systematic uncertainties is also shown as a red line.

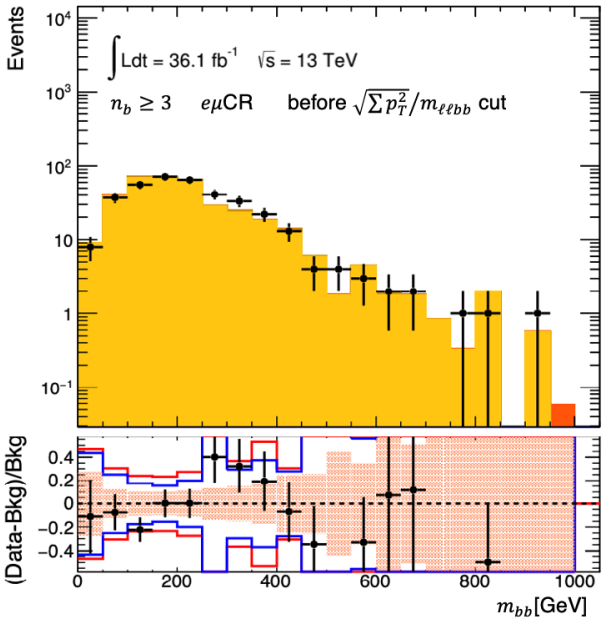

(a) m_{bb}

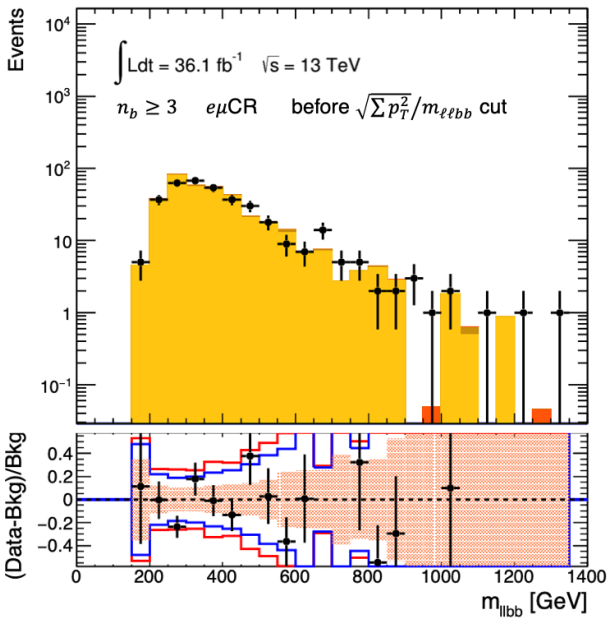

(b) $m_{\ell\ell bb}$

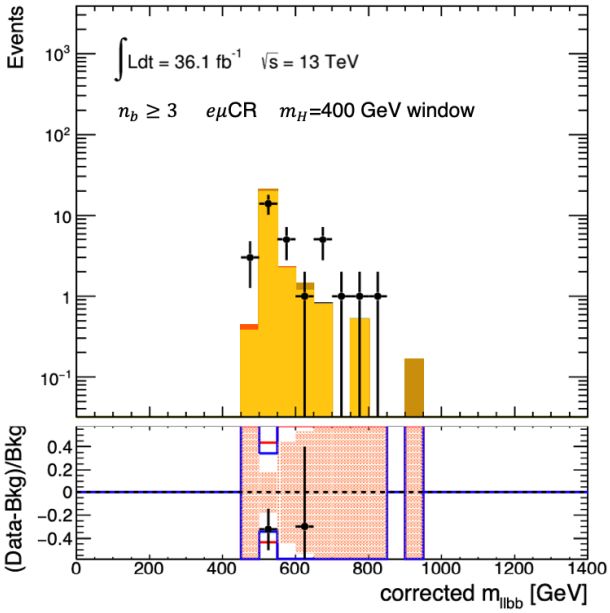

(c) $m_{\ell\ell bb}$ with mass scaling, passed $m_H = 400$ GeV window

Figure B.4: The (a) m_{bb}, (b) $m_{\ell\ell bb}$ distributions before the $\sqrt{\Sigma p_T^2}/m_{\ell\ell bb} > 0.4$ cut and the (c) $m_{\ell\ell bb}$ with mass scaling for the top control region in the $n_b \geq 3$ category. For the background simulated samples, color code shown in Figure 3.5 has been used. At the bottom panel, the filled area represents the statistical uncertainties, while the blue line shows the combined uncertainty from statistical and shape uncertainties. The total uncertainty which combines statistical and systematic uncertainties is also shown as a red line.

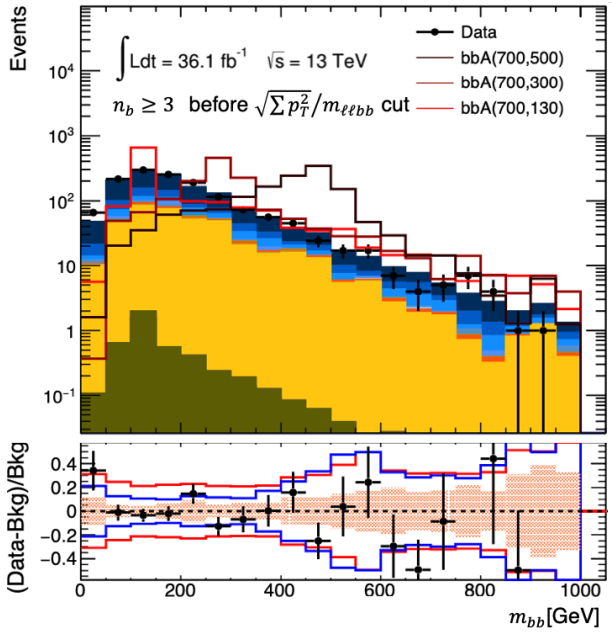

(a) m_{bb}

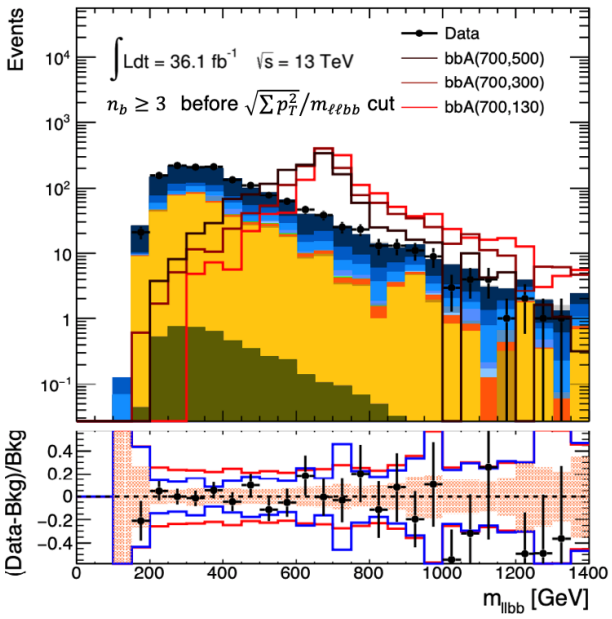

(b) $m_{\ell\ell bb}$

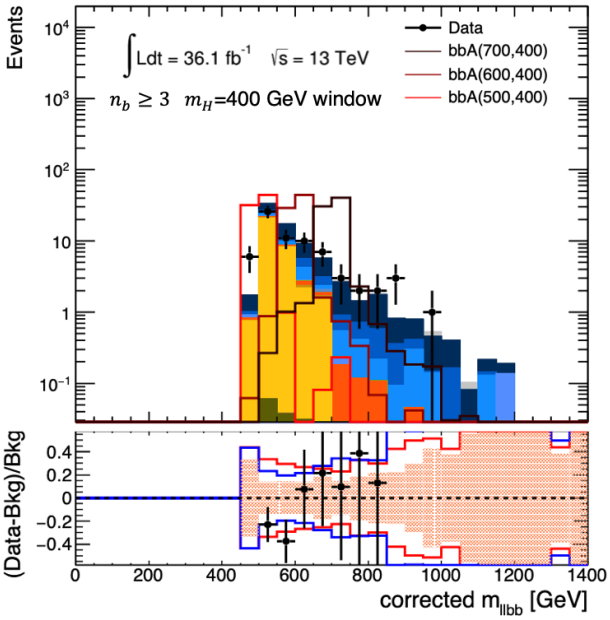

(c) $m_{\ell\ell bb}$ with mass scaling, passed $m_H = 400$ GeV window

Figure B.5: The (a) m_{bb}, (b) $m_{\ell\ell bb}$ distributions before the $\sqrt{\Sigma p_T^2}/m_{\ell\ell bb} > 0.4$ cut and the (c) $m_{\ell\ell bb}$ distribution with mass scaling in the $n_b \geq 3$ category. Both $t\bar{t}$ and Z+jets scale factors are applied. For the background simulated samples, the color code shown in Figure 3.5 has been used. At the bottom panel, the filled area represents the statistical uncertainties, while the blue line shows the combined uncertainty from statistical and shape uncertainties. The total uncertainty which combines statistical and systematic uncertainties is also shown as a red line.

APPENDIX C

Additional plots for Search for $A \to ZH \to \ell\ell bb$ with 139 fb^{-1}

Additional plots for Chapter 5 are shown in this appendix. Figure C.1 shows the $m_{\ell\ell jb}$ distribution in different selection stage in the $n_b = 1$ control region. Figure C.2 shows the $m_{\ell\ell bb}$ distribution in the $n_b = 2$ category. The $\sqrt{\Sigma p_T^2}/m_{\ell\ell bb}$ distribution, m_{bb} distribution and the $m_{e\mu bb}$ distribution in the top control region for the $n_b = 2$ category are shown in figure C.3. Figure C.4 shows the $m_{\ell\ell bb}$ distribution in the $n_b \geq 3$ category. The $\sqrt{\Sigma p_T^2}/m_{\ell\ell bb}$ distribution, m_{bb} distribution and the $m_{e\mu bb}$ distribution in the top control region for the $n_b \geq 3$ category are shown in figure C.5.

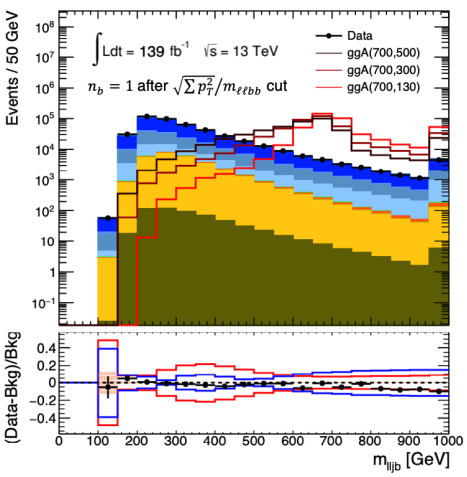

(a) $\sqrt{\Sigma p_T^2}/m_{\ell\ell bb}$ corrected

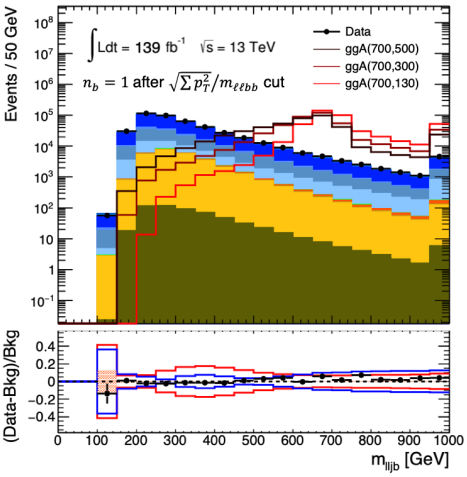

(b) m_{jb} corrected

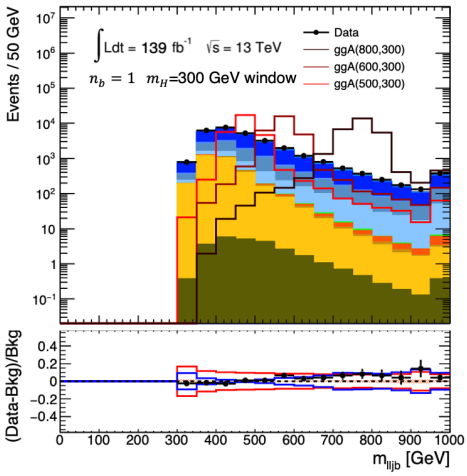

(c) m_H = 300 GeV window

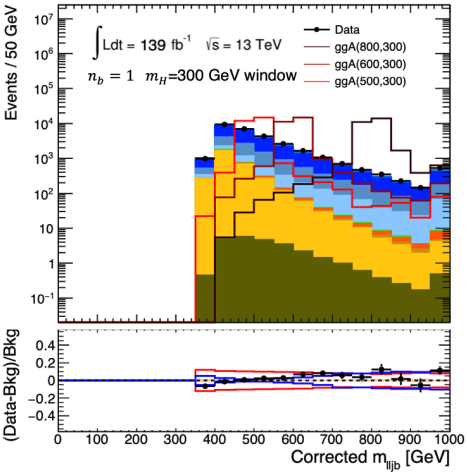

(d) m_H = 300 GeV window, mass scaling applied

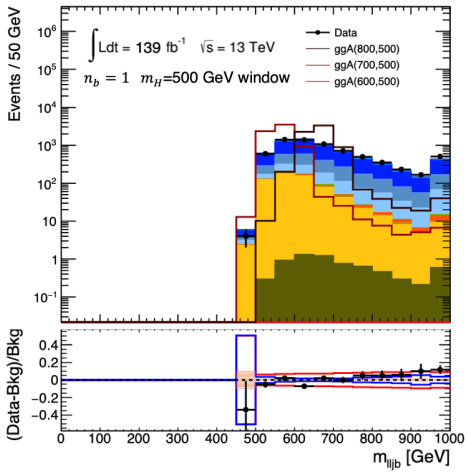

(e) m_H = 500 GeV window

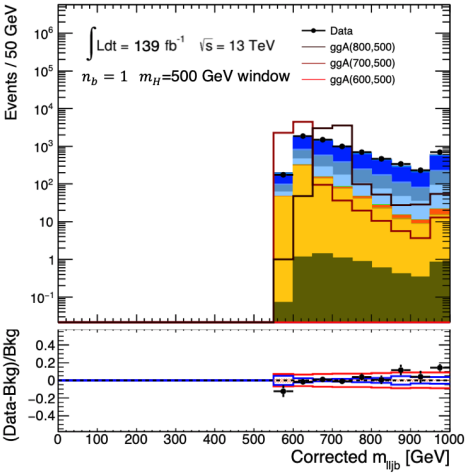

(f) m_H = 500 GeV window, mass scaling applied

Figure C.1: The $m_{\ell\ell jb}$ distribution with (a) $\sqrt{\Sigma p_T^2}/m_{\ell\ell bb}$ correction and (b) m_{jb} correction after the $\sqrt{\Sigma p_T^2}/m_{\ell\ell bb}$ cut in the $n_b = 1$ control region. $m_{\ell\ell jb}$ distribution with and without mass scaling in the signal regions are also shown. At the bottom panel, the filled area represent the statistical uncertainties, while the blue line shows the combined uncertainty from statistical and shape uncertainties. The total uncertainty which combines statistical and systematic uncertainties are also shown as a red line.

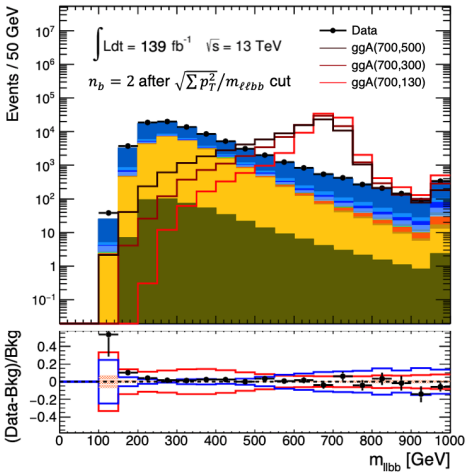

(a) $\sqrt{\Sigma p_T^2}/m_{\ell\ell bb}$ corrected

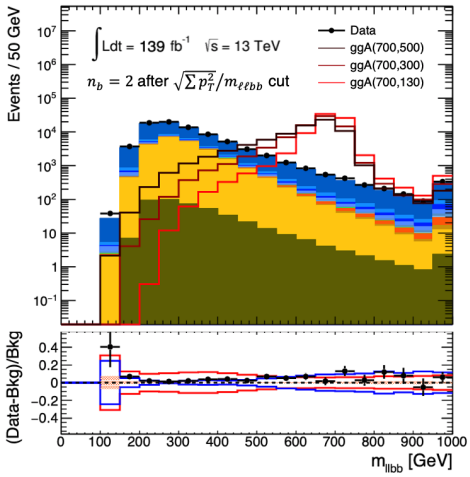

(b) m_{bb} corrected

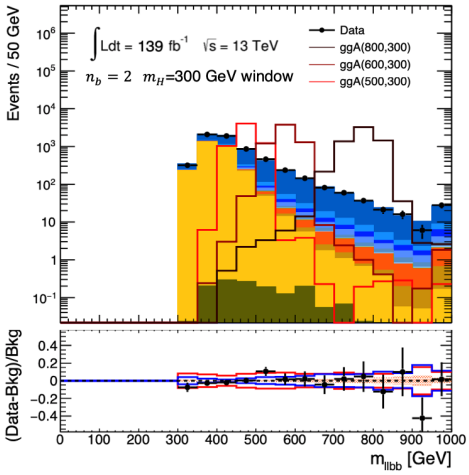

(c) m_H = 300 GeV window

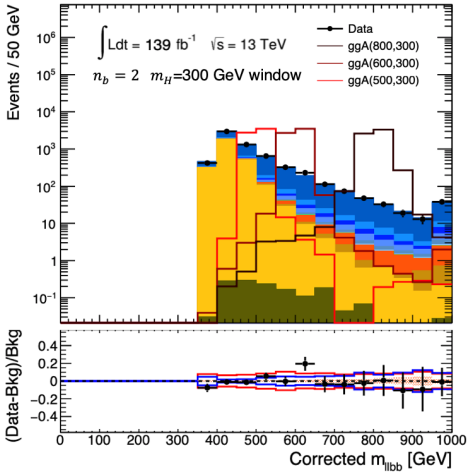

(d) m_H = 300 GeV window, mass scaling applied

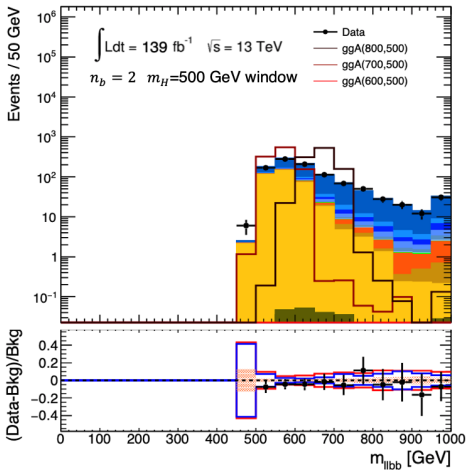

(e) m_H = 500 GeV window

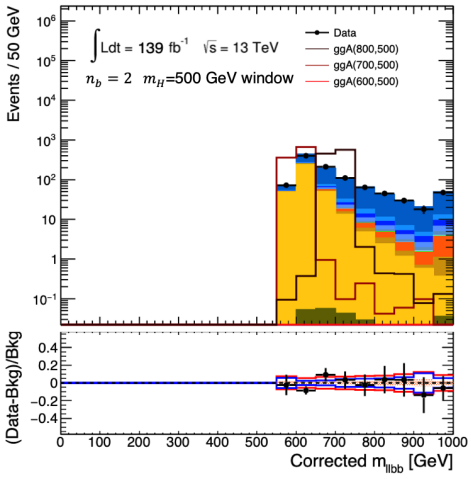

(f) m_H = 500 GeV window, mass scaling applied

Figure C.2: The $m_{\ell\ell bb}$ distribution with (a) $\sqrt{\Sigma p_T^2}/m_{\ell\ell bb}$ correction and (b) m_{bb} correction after the $\sqrt{\Sigma p_T^2}/m_{\ell\ell bb}$ cut in the $n_b = 2$ category. $m_{\ell\ell bb}$ distribution with and without mass scaling in the signal regions are also shown. At the bottom panel, the filled area represent the statistical uncertainties, while the blue line shows the combined uncertainty from statistical and shape uncertainties. The total uncertainty which combines statistical and systematic uncertainties are also shown as a red line.

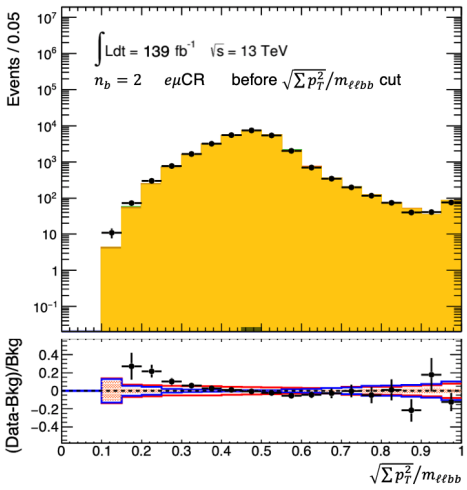

(a) before $\sqrt{\Sigma p_T^2}/m_{\ell\ell bb}$ cut

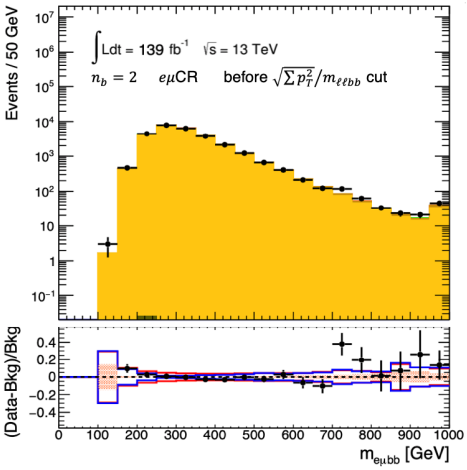

(b) before $\sqrt{\Sigma p_T^2}/m_{\ell\ell bb}$ cut

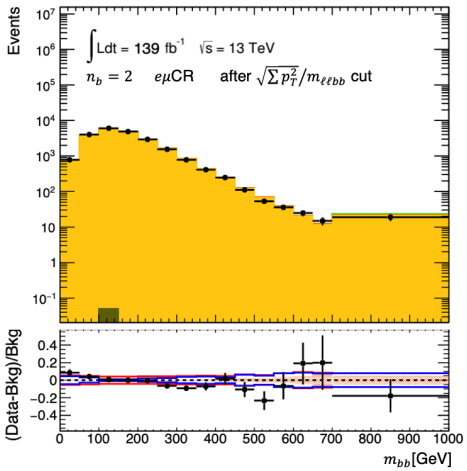

(c) after $\sqrt{\Sigma p_T^2}/m_{\ell\ell bb}$ cut

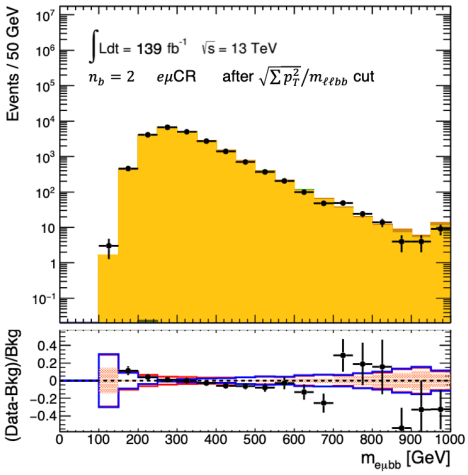

(d) after $\sqrt{\Sigma p_T^2}/m_{\ell\ell bb}$ cut

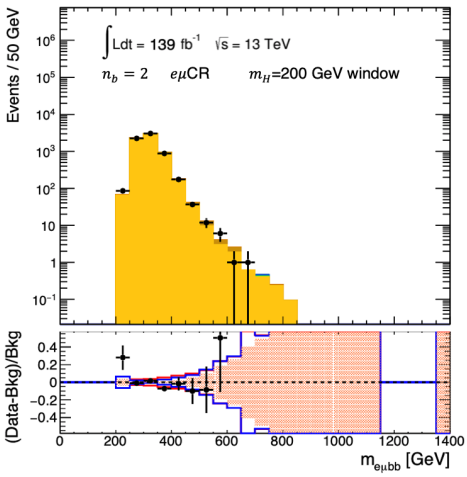

(e) m_H = 200 GeV window

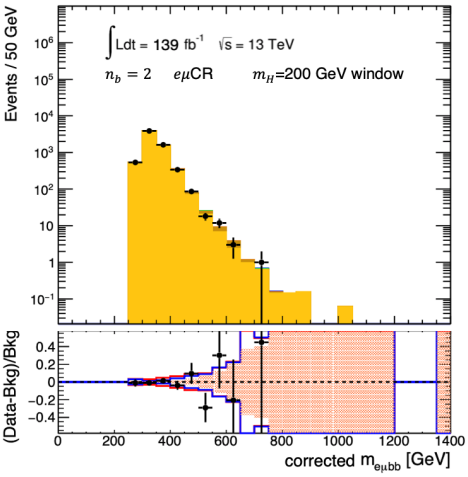

(f) m_H = 200 GeV window, mass scaling applied

Figure C.3: The (a) $\sqrt{\Sigma p_T^2}/m_{\ell\ell bb}$ distribution and (b) the $m_{e\mu bb}$ distribution before the $\sqrt{\Sigma p_T^2}/m_{\ell\ell bb}$ cut, the (c) m_{bb} distribution and (d) the $m_{e\mu bb}$ distribution after the $\sqrt{\Sigma p_T^2}/m_{\ell\ell bb}$ cut in the top control region of the $n_b = 2$ category. The $m_{e\mu bb}$ distribution with m_{bb} window in the top control region of the $n_b = 2$ category also shown. At the bottom panel, the filled area represent the statistical uncertainties, while the blue line shows the combined uncertainty from statistical and shape uncertainties. The total uncertainty which combines statistical and systematic uncertainties are also shown as a red line.

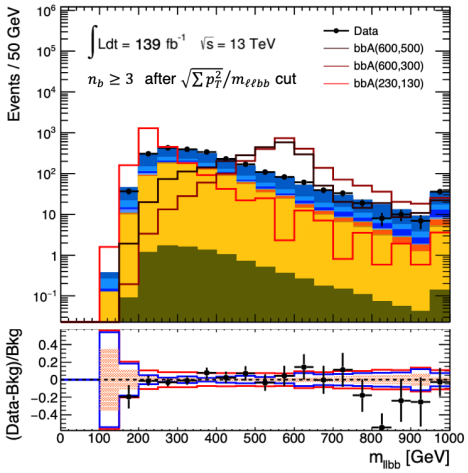

(a) no correction

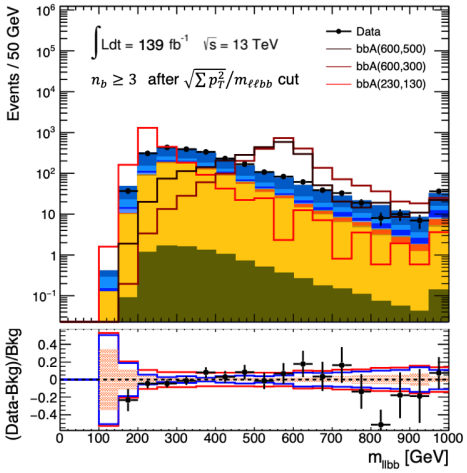

(b) m_{bb} corrected

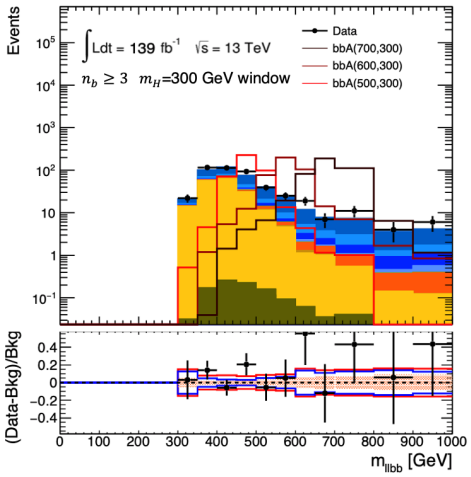

(c) m_H = 300 GeV window

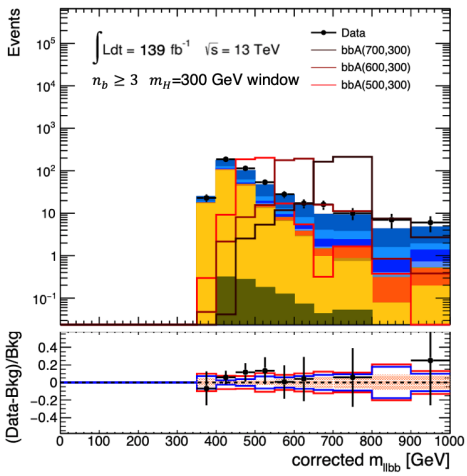

(d) m_H = 300 GeV window, mass scaling applied

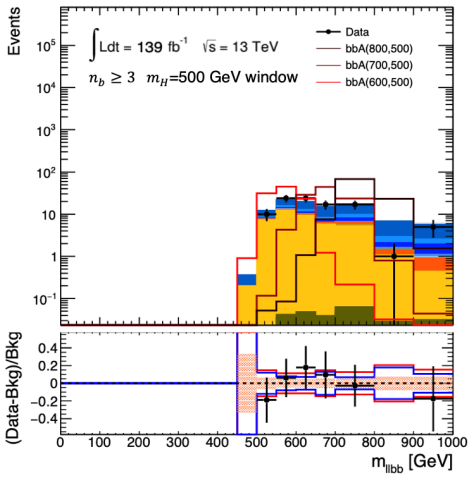

(e) m_H = 500 GeV window

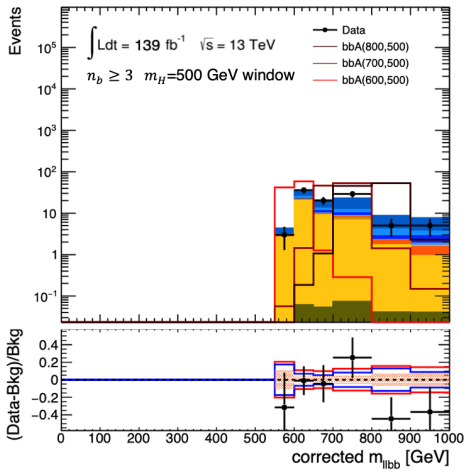

(f) m_H = 500 GeV window, mass scaling applied

Figure C.4: The $m_{\ell\ell bb}$ distribution (a) without and (b) with the m_{bb} correction after the $\sqrt{\Sigma p_T^2}/m_{\ell\ell bb}$ cut in the $n_b \geq 3$ category. $m_{\ell\ell bb}$ distribution with and without mass scaling in the signal regions are also shown. At the bottom panel, the filled area represent the statistical uncertainties, while the blue line shows the combined uncertainty from statistical and shape uncertainties. The total uncertainty which combines statistical and systematic uncertainties are also shown as a red line.

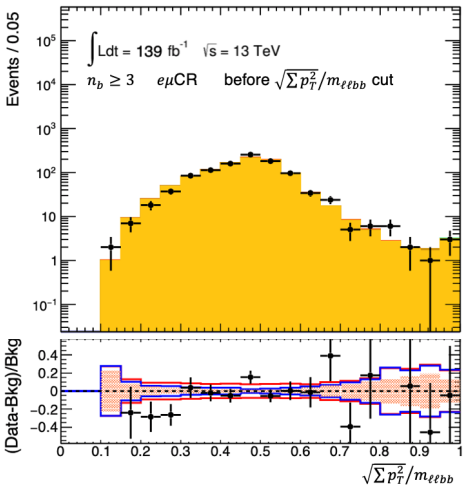

(a) before $\sqrt{\Sigma p_T^2}/m_{\ell\ell bb}$ cut

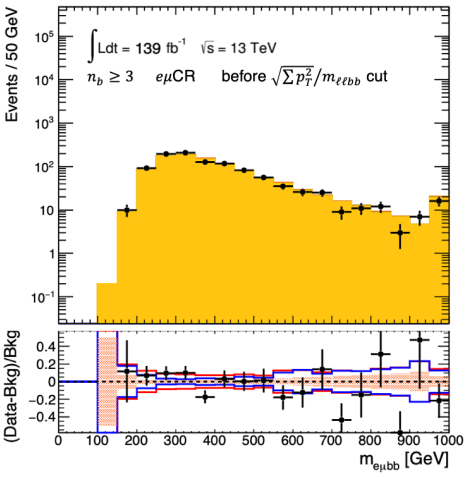

(b) before $\sqrt{\Sigma p_T^2}/m_{\ell\ell bb}$ cut

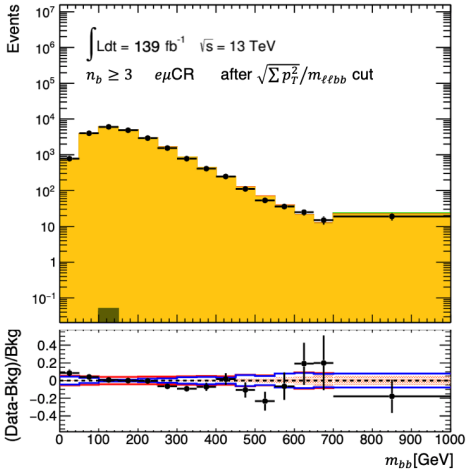

(c) after $\sqrt{\Sigma p_T^2}/m_{\ell\ell bb}$ cut

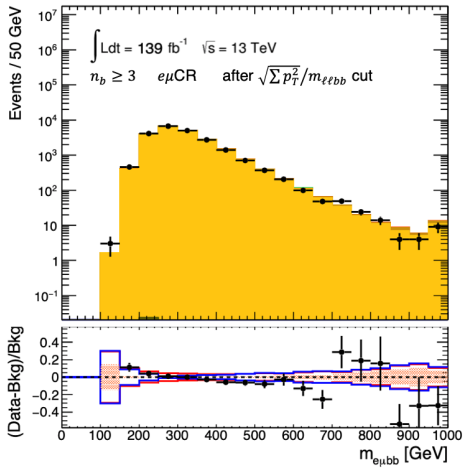

(d) after $\sqrt{\Sigma p_T^2}/m_{\ell\ell bb}$ cut

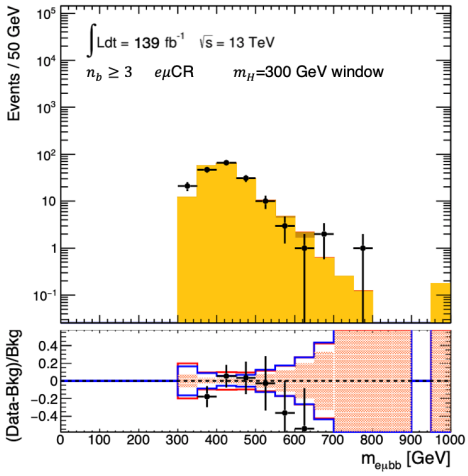

(e) m_H = 200 GeV window

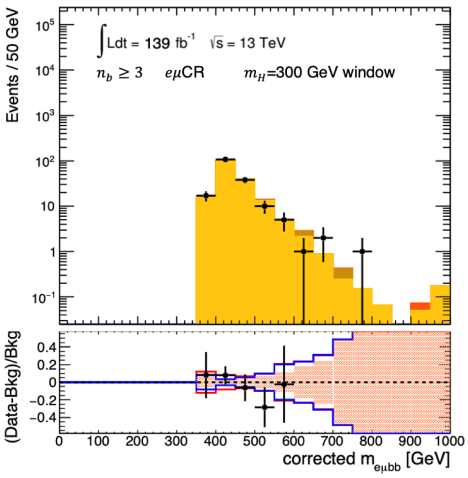

(f) m_H = 200 GeV window, mass scaling applied

Figure C.5: The (a) $\sqrt{\Sigma p_T^2}/m_{\ell\ell bb}$ distribution and (b) the $m_{e\mu bb}$ distribution before the $\sqrt{\Sigma p_T^2}/m_{\ell\ell bb}$ cut, the (c) m_{bb} distribution and (d) the $m_{e\mu bb}$ distribution after the $\sqrt{\Sigma p_T^2}/m_{\ell\ell bb}$ cut in the top control region of the $n_b \geq 3$ category. The $m_{e\mu bb}$ distribution with m_{bb} window in the top control region of the $n_b \geq 3$ category also shown. At the bottom panel, the filled area represent the statistical uncertainties, while the blue line shows the combined uncertainty from statistical and shape uncertainties. The total uncertainty which combines statistical and systematic uncertainties are also shown as a red line.

List of Figures

List of Tables